

Potential of Microdroplet Lasers for Optofluidic Biosensing Applications

by

Mehdi Aas

A Thesis Submitted to the
Graduate School of Sciences and Engineering
in Partial Fulfillment of the Requirements for
the Degree of

Doctor of Philosophy

in

Physics

Koç University

September, 2015

Koc University
Graduate School of Sciences and Engineering

This is to certify that I have examined this copy of a doctoral dissertation by

Mehdi Aas

and have found that it is complete and satisfactory in all respects,
and that any and all revisions required by the final
examining committee have been made.

Committee Members:




Alper Kiraz, Ph.D.(Advisor)



Pavel Zemánek, Ph.D.



Alexandr Jonáš, Ph.D.



Selcuk Aktürk, Ph.D.



Melikhan Tanyeri, Ph.D.

Date:

September 2015

ABSTRACT

Dye-doped microdroplets can host lasing whispering gallery modes (WGMs). The sensitivity of laser emission wavelength, lasing threshold, lasing differential efficiency or even lasing beam spatial profile to the physical properties of microdroplets such as size, shape, relative refractive index of the droplet with respect to its surrounding medium, cavity Q-factor, or molecular binding/unbinding inside their constructive material can be used in sensing applications. To this end the necessity of control and manipulation of lasing microdroplets with minimum perturbation in their performance during the study suggests the utilization of advantages of optical forces as non-contact remote manipulation tools. In this thesis firstly we demonstrate lasing from optically manipulated dye-doped emulsion and aerosol droplets. We study their lasing properties such as lasing stability in time and dependence of the lasing WGMs on the physical properties of the microdroplets such as size, refractive index and dye concentration. Moreover, we use optical forces as deforming tools to stretch the microdroplet lasers for tuning their lasing emission. To do this a dual-beam trap is used to stretch the optically pumped dye-doped droplets of oil dispersed in water. Subsequently, resonant path lengths of WGMs propagating in the droplet are modified, leading to shifts in the microlaser emission wavelengths. Using this technique, we present all-optical, almost reversible spectral tuning of the lasing WGMs and show that the direction of tuning depends on the position of the pump beam focus on the droplet. In addition, we study the effects of temperature changes on the spectral position of lasing WGMs and demonstrate that droplet heating leads to red-tuning of the droplet lasing wavelength.

In the biosensing side of this thesis, we study microdroplet biolasers that exploit active liquid optical resonators formed by surface-supported aqueous microdroplets containing purified yellow fluorescent protein or a suspension of live *E. coli* bacterial cells expressing the fluorescent protein. We first demonstrate lasing in fluorescent protein solutions at concentrations as low as 49 μM . Subsequently, we show that a single fluorescent bacterial cell of micrometre size confined in a droplet-based cavity can serve as a laser gain medium.

Aqueous droplet microcavities allow the maintenance of the bacterial cells under conditions compatible with unimpeded growth. Therefore, our results also suggest a direct route to microscopic sources of laser light with self-regenerating gain media.

Fluorescence resonance energy transfer (FRET) from a donor to an acceptor chromophore is used as an atomic scale ruler to measure the conformational changes in biomolecules. Incorporating FRET into a laser cavity can increase the sensitivity of FRET-based biochemical sensors due to the nonlinear dependence of the lasing output on the FRET parameters. In order to obtain a fundamental understanding of the sensing capabilities by FRET lasing in microdroplets we carry out a comprehensive theoretical analysis of optofluidic FRET lasers on a simpler counterparts of microdroplet lasers called Fabry-Pérot microcavity using a rate equation model. We compare conceptually distinct cases of donor and acceptor molecules diffusing freely in bulk solution versus molecules connected by a fixed-length linker and show that the latter arrangement is especially well-suited for sensing of low-concentration analytes. By comparing FRET lasing-based sensors with conventional FRET sensors, we show that for optimal pump fluence and FRET-pair concentration, FRET lasing can lead to more than 100-fold enhancement in detection sensitivities of conformational changes in the Förster radius range. We study the dependence of the sensitivity enhancement on the cavity Q-factor. We show that the highest enhancements can be obtained for Q-factors between $10^4 - 10^6$, and enhancement values decrease for Q-factors above 10^6 due to the radiative energy transfer in the cavity.

Finally, we demonstrate FRET lasing from self-assembled tetrahedral DNA complexes labeled with Cy3 and Cy5 dyes and suspended as a gain medium in aqueous microdroplet cavities deposited on a superhydrophobic surface. Threshold fluence and differential efficiency are characterized for DNA complexes containing 1Cy3-3Cy5 and 3Cy3-1Cy5. We demonstrate that at a constant Cy5 concentration, average threshold fluence is reduced 3 to 8 times and average differential efficiency is enhanced 6 to 30 times for 3Cy3-1Cy5 as compared to 1Cy3-3Cy5. Using 3Cy3-1Cy5 nanostructures, FRET lasing is observed at very low concentrations down to $\sim 1\mu\text{M}$. This work shows that optofluidic microlasers based on droplet resonators can be combined with DNA nanotechnology to explore applications in bio/chemical sensing and novel photonic devices.

ÖZETÇE

Boya katkılı mikro damlacıklar, lazer olarak kullanılabilen fısıldayan galeri kiplerini taşıyabilmektedir. Lazer çıkış dalgaboyu, lazer eşiği, lazer verimliliği ve hatta lazer ışık spotunun şekli; damlacıkların şu fiziksel özelliklerine hassas bir şekilde bağlıdır: Damlacıkların boyutu, şekli, damlacıkların kırılma indisi ile ortamın kırılma indisi arasındaki fark, kovuk kalite faktörü ve damlacık malzemesinde moleküler bağlanma veya bağların açılması gibi. Bu hassas ilişki, algılama uygulamalarının kullanılmasına olanak sağlamaktadır. Bu bağlamda lazer olarak kullanılan damlacıkların uygulama sırasında en az bozulmayla hareket ettirilebilmesi için, optik kuvvetlerin fiziksel temasa ihtiyaç duymama avantajından faydalanmak gerekmektedir. Bu tezde öncelikle optik kuvvetlerle yönlendirilen boya katkılı sıvıda veya havada asıltı şeklindeki damlacıklardan lazer ışığı elde edilmiştir. Zamana göre lazer kararlılığı ve damlacığın fiziksel özelliklerine göre lazer ışığı dalgaboyundaki değişim gözlemlenmiştir. Dahası, optik kuvvetler kullanılarak damlacık şekli deformasyona uğratılmış, böylelikle lazer dalgaboyu ayarlanabilmiştir. Bu deney için su içerisinde boya katkılı yağ damlacıklar optik olarak uyarılmış ve çift ışıklı tuzaklama yöntemiyle şekilleri deformasyona uğratılmıştır. Böylelikle ışığın damlacık içinde aldığı yol değiştiğinden lazer dalgaboyunda kaymalar meydana gelmektedir. Bu teknik kullanılarak, lazer dalgaboyu ayarlanması sadece optiğe dayanan, neredeyse tamamen tersine çevrilebilir bir şekilde gösterilmiştir. Ayrıca dalgaboyundaki ayarlamaların yönünün, pompa lazerinin odağının damlacık üzerindeki konumuna bağlı olduğu görülmüştür. Bunlara ek olarak sıcaklık değişiminin dalgaboyu kayması üzerindeki etkisi incelenmiş ve damlacığın sıcaklığının artmasıyla lazer dalgaboyunda kırmızıya kayma gözlemlenmiştir.

Tezin biyo-algılama kısmında mikrodamlacıklarbiyolazer olarak kullanılmıştır. Bu damlacıklar sarı floresan proteinler ya da floresan protein içeren canlı *E. Coli* bakterileri içermektedir. İlk olarak 49 μM kadar düşük derişimlerdeki proteinler kullanılarak lazer özelliği gösterilmiştir. Daha sonra damlacık içerisine yerleştirilen tek bir bakterinin floresan özelliği ile lazer kazanç ortamı olarak kullanılabileceği gösterilmiştir. Su içerisindeki damlacık

mikrokovuklar, bu bakterilerin engelsiz büyüme ortamına yerleştirilebilmesi için uygun zemin hazırlamaktadır. Bu sebeple bu sonuçlar, lazer ışığının mikroskobik ölçekte kendi kendini yenileyebilen bir şekilde üretilmesine zemin hazırlamaktadır.

Floresan rezonans enerji transferi (FRET) verici ile alıcı kromoforlar arasındaki mesafenin atomik boyutlarda ölçülmesine, böylelikle biyomoleküllerdeki uyumlu değişikliklerin fark edilmesine olanak sağlamaktadır. FRET ile lazer sistemini birleştirmek, FRET parametrelerinin lazer çıkışı üzerindeki doğrusal olmayan etkileri sayesinde FRET tabanlı biyokimyasal algılayıcıların hassasiyetini arttırmaktadır. Damlacıklar ile birleştirilen FRET lazerlerinin algılayıcı özelliklerinin daha iyi anlaşılması için kapsamlı bir teorik çalışma yapılmıştır. Bu çalışmada oran denklemi modeli kullanılarak Fabry-Pérot kovukları için FRET lazerleri incelenmiştir. Alıcı ve verici moleküllerin çözelti içerisinde başka bir etki olmadan difüzyon ile hareket edebildikleri durum ile birbirlerine uzunluğu sabit bir molekül ile bağlı alıcı ve verici moleküllerin durumu karşılaştırılmıştır. Sonuçta ikinci durumun, düşük derişimlerde algılama uygulamaları için daha uygun olduğu sonucuna ulaşılmıştır. FRET lazer algılayıcıları ile bilinen FRET algılayıcıları karşılaştırılmış, uygun pompa ve FRET çifti derişimleri şartları altında, Förster mesafesi bölgesinde oluşan derişimlerde algılama hassasiyetinde 100 kata varan iyileşmelerin görüleceği gösterilmiştir. Algılama hassasiyetinin iyileşmesinin kovuk kalite faktörü ile ilişkisi de araştırılmıştır. 10^4 ile 10^6 arasındaki kalite faktörleri için en yüksek iyileşmenin görüleceği gösterilmiştir. 10^6 'dan daha yüksek kalite faktörlerinin, kovuk içindeki ışımsal enerji transferi sebebiyle iyileştirmeyi düşürdüğü gösterilmiştir. Son olarak tetrahedral şeklindeki DNA yapılarının FRET lazer özelliği gösterilmiştir. Bu yapılar Cy3 ve Cy5 boyaları ile etiketlenmiş ve damlacık içine yerleştirilmiştir. Bu damlacıklar da süperhidrofobik yüzeyler üzerinde tutulmaktadır. 1Cy3-3Cy5 ve 3Cy3-1Cy5 DNA yapıları için lazerin eşik akışı ve diferansiyel verimi karakterize edilmiştir. Sabit Cy5 derişimi altında 1Cy3-3Cy5 ile karşılaştırıldığında 3Cy3-1Cy5 için ortalama eşik akışı 3 ila 8 kat azalırken diferansiyel verim 6 ila 30 kat artmıştır. 3Cy3-1Cy5 nanoyapıları kullanılarak $1\text{ }\mu\text{M}$ 'e kadar düşük seviyelerde lazer gözlemlenmiştir. Bu çalışma gösteriyor ki, biyo-kimyasal algılama uygulamaları ve fotonik alet yapımı, damlacık rezonatör tabanlı opto-akışkan mikrolazerler DNA teknolojisi ile birleştirilerek daha derin bir şekilde keşfedilebilecektir.

Keywords: Optofluidics, Dye Laser, Biosensing, Microdroplet, Optical Trapping, Optical Stretching, Whispering Gallery Modes, FRET, Bacteria Laser.

ACKNOWLEDGMENTS

Firstly, I would like to express my sincere gratitude to my advisor Prof. Alper Kiraz for the continuous support of my Ph.D study, for his immense knowledge on the research topic and for his great motivation and diligence. Besides my advisor, I would like to thank the rest of my thesis committee: Prof. Pavel Zemánek, Assoc. Prof. Selcuk Aktürk, Dr. Melikhan Tanyeri and Dr. Alexandr Jonáš, for their insightful comments and encouragement. My sincere thanks also goes to Dr. Alexandr Jonáš for his great guidance and meticulous scientific approach for solving the problems. Also, I would like to thank Prof. Zemánek and Prof. Xudong Fan and their research team members, specifically Dr. Oto Brzobohatý, Dr. Jan Ježek, Dr. Zdeněk Pilát, and Dr. Martin Šiler and Qiushu Chen for their valuable collaborations. I thank my labmates Dr. Mehdi Yavüz Yüce, Dr. Yasin Karadag, Dr. Asuman Aşıkoğlu, Dr. Ahmet Can Erten, Dr. Suman Anand, Mustafa Eryürek, Selcuk Çakmak, Ersan Özelci, Vahid Pourreza, Baran Yalçın, Oğuz Kayılhoğlu and Adil Mustafa in Koç University for the stimulating discussions and for all the fun we have had in the last four years. Last but not the least, I would like to thank my parents for supporting me spiritually throughout my life in general.

This work was partially supported by the Scientific and Technological Research Council of Turkey (TÜBİTAK) under Grant Numbers of 111T059 and 114F253.

TABLE OF CONTENTS

List of Tables	xiii
List of Figures	xiv
Nomenclature	xxvi
Chapter 1: Introduction	1
1.1 Microdroplets as Optical Cavities for Whispering Gallery Modes	1
1.2 Spatial Confinement of Micro-objects by Optical Forces	2
1.3 Microdroplets as Optofluidic Lasers	2
1.4 Optical Tuning of Emulsion Droplet Lasers	3
1.5 Biosensing with Optofluidic Lasers	5
1.5.1 Biolasing from Suspended Fluorescent Proteins and <i>E-Coli</i> Bacteria in Micordorplets	5
1.5.2 Biosensing with Fluorescence Resonance Energy Transfer (FRET) . .	7
1.5.3 FRET for Efficient Laser Pumping	7
1.5.4 Optofluidic FRET Lasers as High Sensitivity Biosensors	8
1.5.5 Droplets as Optofluidic FRET Lasers	9
1.6 Thesis Goals and Outline	9
Chapter 2: Theory of Microsphere Resonators and Lasing Microdroplets	13
2.1 Maxwell Equations in Spherical Coordinate System	14
2.2 Resonant Frequencies of a Spherical Cavity	16
2.3 A Discussion on Optical Size Parameter	18
2.4 Quality Factor	20
2.5 Optical Forces at Dielectric Interfaces	22
2.6 Optical Stretching of Deformable Dielectric Objects	23

2.7	Optical Tweezers	25
Chapter 3:	Lasing from Optically Manipulated Microdroplets	26
3.1	Experimental Setup	26
3.2	Lasing from Optically Manipulated Emulsion Droplets	28
3.2.1	Materials and Methods	28
3.2.2	Results and Discussions	29
3.3	Lasing from Optically Manipulated Aerosol Droplets	35
3.3.1	Materials and Methods	35
3.3.2	Results and Discussions	36
Chapter 4:	Spectral Tuning of Lasing Emission from Dye-doped Emul- sion Droplet Lasers Using Optical Stretching	40
4.1	Experimental Setup	40
4.2	Microfluidic Chip Fabrication	44
4.3	Immersion Oil/Water Emulsion System	45
4.4	Surfactants and Surface Tension Engineering	46
4.4.1	Structure of Surfactant Phases in Water	46
4.4.2	Classification of Surfactants	47
4.4.3	Critical Micelle Concentration and Minimum Surface Tension	48
4.4.4	Characterization and Adjustment of Interfacial Tension of Emulsion Droplets	48
4.5	Simulations of WGM Tuning by Droplet Stretching	49
4.6	Observation of Tunable Dye Lasing in Optically Stretched Microdroplets . . .	52
4.7	Influence of Thermal Effects on WGM Tuning	54
Chapter 5:	In Vitro and in Vivo Biolasing of Fluorescent Proteins Sus- pended in Liquid Microdroplet Cavities	60
5.1	Materials and Methods	60
5.1.1	Expression, Isolation, and Purification of Venus Yellow Fluorescent Protein	60

5.1.2	Generation of Liquid Microdroplets Supported by Superhydrophobic Surfaces	61
5.2	Experimental Setups	61
5.3	Characterization of Venus Fluorescent Protein and Venus-Expressing Bacterial Cells	64
5.4	Observation of Lasing from Aqueous Solutions of Venus Fluorescent Protein .	66
5.5	Observation of Lasing in Suspensions of Bacteria Expressing Venus Fluorescent Protein	69
5.5.1	Dependence of Full Width at Half Maximum of Whispering Gallery Modes on the Pump Fluence and Venus Photobleaching	72
5.6	Discussion	73
Chapter 6: Simulation of Optofluidic FRET Lasers for Biosensing Purposes		75
6.1	Mechanisms of Nonradiative Energy Transfer Between Dye Molecules	75
6.1.1	FRET Between an Isolated Pair of Donor/Acceptor	76
6.1.2	FRET for Ensemble of Acceptors Around a Donor	77
6.2	Rate Equation Model	79
6.3	Threshold Behavior in Bulk FRET Lasers	84
6.4	Threshold Behavior in Molecularly Linked FRET Pair Lasers	88
6.5	Sensitivity of Detection of Conformational Changes in Linked FRET Pair Biocomplexes	91
6.6	Effect of Q-factor on Conformational Sensitivities in Linked FRET Pair Biocomplexes	96
6.7	Sensitivity of Detection of Conformational Changes in 1D – 3A and 3D – 1A Biocomplexes	101
6.8	Concentration Sensitivity of FRET Laser Biosensors	104
Chapter 7: FRET Lasing from Self-assembled DNA Tetrahedral Nanostructures Suspended in Optofluidic Droplet Resonators		109
7.1	Materials and Methods	109

7.2	Experimental Setup	110
7.3	Results and discussions	110
Chapter 8:	Conclusion	115
Appendix A:	MATLAB Codes of Simulation of Optical Stretcher	120
A.1	Optical Force Calculation of a Single Ray	120
A.2	Stretching Force Calculation of a Gaussian Beam	122
A.3	Calculation of WGM Tuning Versus Stretching Laser Power	124
Appendix B:	Determination of Intracellular Concentration of Venus Fluorescent Protein	126
Appendix C:	MATLAB Codes for Simulation of Optofluidic FRET Lasers	128
C.1	FRET Laser Rate Equations for ode15s Solver	128
C.2	Lasing Threshold Calculation of Bulk Dye-Pair Solutions	129
C.3	Lasing Threshold Calculation of Linked Dye-Pair Solutions	133
C.4	Output Energy Calculation of FRET Lasers	137
Bibliography		140
VITA		153

LIST OF TABLES

4.1	CPP and HLB number meanings for surfactants [94]	47
6.1	Descriptions and numerical values of the constants used in the rate equation model [116]	108

LIST OF FIGURES

2.1	Effective optical potential and radial distribution of field intensity for an immersion oil emulsion microdroplet shown in Fig. 3.2 with radius $a = 13.5 \mu\text{m}$ and refractive index of $\eta_1 = 1.506$ surrounded by water with refractive index of $\eta_2 = 1.334$	18
2.2	(a) Radiation pressure of a plane wave in reflection from a mirror, (b) Stretching and scattering forces of a plane wave in transmission through a dielectric object with refractive index higher than its surrounding medium $\eta_1 > \eta_2$, (c) Consecutive refractions and reflections from the surface of a dielectric object, (d) Optical restoring force by intensity gradient of a tightly focused beam on a sphere in the axial direction , (e) Optical gradient force of a plane wave with vertical gradient intensity on a sphere in the lateral direction.	24
3.1	Experimental setup for microdroplet lasing studies. The inset shows the detail of an optically trapped droplet with the pump laser beam positioned on the droplet rim. D1, D2 - dichroic mirrors, F - band-pass filter, FM - flippable mirror, L1, L2 - lenses, M - mirror, PBS - polarizing beam splitter, WP - lambda-half wave plate.	27
3.2	Laser emission spectra from an optically manipulated emulsion droplet (diameter $27 \mu\text{m}$; denoted by a dashed circle). Arrows indicate a stationary reference droplet resting on the bottom surface of the sample chamber. The trapped droplet is first translated in the plane of the figure between (a)-(b) and subsequently out of the figure plane between (b)-(c).	29

3.3	Dependence of the droplet emission intensity on the input pump power. Intensities of both a lasing mode at ~ 620 nm and non-resonant fluorescence background in the immediate vicinity of the mode are shown. Inset identifies respective spectral locations for the measured intensity values. Droplet diameter for this measurement was $31\text{ }\mu\text{m}$	31
3.4	Dependence of the lasing wavelength on the droplet size and the dye concentration inside the droplet. Tags of individual spectra provide the droplet size, the dye concentration, and the wavelength of the most intense lasing peak. For both studied dye concentrations, droplets of approximately equal size were analyzed (see color coding of the spectra). Average pump power and exposure time for each frame in this measurement were 0.7 mW and 6 ms , respectively.	32
3.5	Normalized absorption (dotted line) and emission spectra of DiI(3) dye dissolved in immersion oil/chloroform mixture. The emission spectra are shown at two different levels of dye photobleaching (dashed line - initial dye emission, solid line - dye emission after 400 ms exposure with a 532 nm pulsed green laser with $\sim 300\text{ }\mu\text{W}$ average power).	33
3.6	Effect of photobleaching on the droplet lasing spectra. 1st, 9th, and 19th frames of spectra acquired from a $\sim 34\text{ }\mu\text{m}$ diameter droplet are shown. Average pump power was 1.8 mW and exposure time for each of the frames was 10 ms	35
3.7	Power-dependent emission spectra recorded from a $9.4\text{ }\mu\text{m}$ diameter glycerol/water droplet at three different excitation powers: (a) $12.2\text{ }\mu\text{W}$, (b) $42.3\text{ }\mu\text{W}$, and (c) $76.2\text{ }\mu\text{W}$. WGM A and WGM B denote lasing WGMs. Inset: Optical microscope image of the trapped lasing droplet.	37
3.8	Power-dependent intensities of the lasing WGMs and background emissions in a $9.4\text{ }\mu\text{m}$ diameter glycerol/water aerosol droplet.	38

3.9	(a) Lasing spectra recorded from 6 different aerosols with diameters 7.7, 8.4, 9.0, 9.6, 10.1, and 11.0 μm (bottom to top) at constant pump laser power of 60 μW . (b) Free spectral ranges of 34 lasing aerosols as a function of the mean lasing wavelength, $\bar{\lambda}$	38
4.1	(a) Schematics of experimental setup for spectral tuning of droplet-based microlasers by optical stretching. The inset shows the geometry of the single- and dual-beam optical traps and the pump beam. (b) Droplet excitation geometry - view along z -axis, in the propagation direction of the pump beam. (c) A sample lasing spectrum of a 49 μm diameter droplet with stretching power of 100 mW.	41
4.2	(a) Schematic of a prolate spheroid resulting from optical stretching of an originally spherical droplet of identical volume indicated by the red circle. (b) Simulation results showing the tuning of equatorial- and polar-plane WGMs for a 50 μm diameter immersion oil droplet in water as a function of $P_{stretch}$	51
4.3	(a) Spectral tuning of lasing WGMs of a 47 μm diameter droplet in off-axis excitation geometry (see Fig. 4.1(b)) in the presence of surfactant (droplet interfacial tension $\gamma \approx 1.5 \text{ mN/m}$). The white vertical line indicates blue drift caused by droplet dissolution. (b) Dissolution-corrected WGM tuning for the central peak in (a) as a function of the stretching laser power, $P_{stretch}$. (c) Spectral tuning of lasing WGMs of a 49 μm diameter droplet in on-axis excitation geometry (see Fig. 4.1(b)) in the presence of surfactant (droplet interfacial tension $\gamma \approx 1.5 \text{ mN/m}$). (d) Dissolution-corrected WGM tuning for the central peak in (c) as a function of the stretching laser power, $P_{stretch}$. Intensity values in arbitrary units increase from black to white in (a) and (c).	53

4.4	(a) Spectral tuning of lasing WGMs of a 44 μm diameter droplet in off-axis excitation geometry (see Fig. 4.1(b)) without surfactant (droplet interfacial tension $\gamma \approx 13.1 \text{ mN/m}$). (b) Dissolution-corrected WGM tuning for the central peak in (a) as a function of the stretching laser power, $P_{stretch}$. (c) Spectral tuning of lasing WGMs of a 55 μm diameter droplet in on-axis excitation geometry (see Fig. 4.1(b)) without surfactant (droplet interfacial tension $\gamma \approx 13.1 \text{ mN/m}$). (d) Dissolution-corrected WGM tuning for the central peak in (c) as a function of the stretching laser power, $P_{stretch}$. Intensity values in arbitrary units increase from black to white in (a) and (c).	55
4.5	(a) Frequency-splitting of WGMs of a 42 μm diameter droplet observed with on-center excitation geometry (see Fig. 4.1(b)). Light intensity in arbitrary units increases from black to white. (b) Dissolution-corrected spectral positions λ_B, λ_R , and λ_0 for WGM1, WGM2 labeled in (a) during two consecutive droplet tuning cycles. (c) Details of changes of spectral position λ_0 for WGM1, WGM2 labeled in (a) within a single droplet tuning cycle. (d) Changes of spectral position λ_0 for WGM1, WGM2 labeled in (a) as a function of the stretching laser power $P_{stretch}$ within a single droplet tuning cycle.	58
5.1	Experimental setup for fluorescence spectroscopy of surface-supported lasing microdroplets. D-dichroic mirror, DL-diode laser module, FM-flippable mirror, L1-L4-lenses, M-mirror, PBS-polarizing beam splitter, PD-photodetector, and WP- $\lambda/2$ wave plate.	62
5.2	A bunch of ~ 400 pulses from the pump laser beam with the pulse repetition rate of 80 MHz after transmission through a rotating chopper wheel with $\sim 155 \mu\text{m}$ diameter pinhole.	62

5.3	(a) DIC image of a surface-supported glycerol-water microdroplet with suspended <i>E. coli</i> bacteria expressing Venus fluorescent protein, (b) Fluorescence image of the same microdroplet as shown in (a). (c) DIC image of a surface-supported glycerol-water microdroplet without bacteria. (d) Fluorescence image of the same microdroplet as shown in (c). The scale bar is 10 μm	63
5.4	Venus-expressing <i>E. coli</i> cells as the laser gain medium. (a) Image of aqueous suspension of BL21-strain of <i>E. coli</i> bacterial cells expressing Venus variant of the yellow fluorescent protein under white light illumination (left) and UV light illumination (right). (b) Pseudocolor fluorescence image of BL21 cells expressing Venus fluorescent protein. Scale bar is 5 μm . (c) Absorption spectrum of aqueous suspension of BL21 cells expressing Venus fluorescent protein. (d) Excitation and emission spectra of purified Venus fluorescent protein suspended in 50 mM phosphate buffer.	65
5.5	Lasing of Venus fluorescent protein in surface-supported microdroplets. (a) Experimental geometry for observation of lasing from the solution of purified Venus fluorescent protein contained in a surface-supported glycerol-water microdroplet acting as a liquid optical resonant cavity. (b) Example of droplet emission spectrum recorded with a pump beam fluence below the lasing threshold. Black dashed line shows the bulk emission spectrum of Venus fluorescent protein solution (no cavity modes). (c) Example of droplet emission spectrum recorded with a pump beam fluence near the lasing threshold. (d) Example of droplet emission spectrum recorded with a pump beam fluence above the lasing threshold. (e) Intensity of the lasing and reference spectral peaks indicated in part (d) as a function of the pump laser fluence. Symbols denote experimental data, solid lines denote linear fits to the data. Droplet radius is 3.2 μm	67

5.6	Lasing of fluorescent <i>E. coli</i> bacterial cells in surface-supported microdroplets. (a) Experimental geometry for observation of lasing from live <i>E. coli</i> bacterial cells expressing Venus fluorescent protein. The bacteria are suspended and freely mobile in glycerol-water microdroplets standing on a superhydrophobic surface. The figure is not drawn to scale. (b) Example of lasing emission spectrum recorded from suspended <i>E. coli</i> bacterial cells (solid line). For comparison, emission spectrum of purified bulk solution of Venus fluorescent protein is also shown (dashed black line). Inset is the image of the actual droplet [radius $8.4\ \mu\text{m}$] used for spectral recording that contains ~ 7 bacterial cells. Circle indicates location of the excitation beam spot on the droplet. The scale bar is $5\ \mu\text{m}$	69
5.7	Dynamics of lasing from suspended <i>E. coli</i> bacterial cells. (a) Time series of emission spectra recorded from a bacteria-containing droplet of $6.8\ \mu\text{m}$ radius with a constant pump fluence. The number of bacterial cells in the droplet was ~ 10 . (b)-(e), Droplet emission spectra for frames 1, 8, 15, and 23 indicated by white horizontal lines in part (a). Due to bacteria diffusion and active motion into and out of the excitation volume, droplet emission pattern in different frames switches between lasing and non-lasing emission mode.	70
5.8	(a) FWHM of the lasing WGM studied in Fig. 5.5 as a function of the pump laser fluence (squares). (b) FWHM of the reference WGM studied in Fig. 5.5 as a function of the pump laser fluence (squares). In both figure parts, circles denote the intensity above background of the lasing WGM.	72

6.1	(a) Schematic diagram of molecular energy levels for a pair of donor and acceptor dyes showing the lowest three singlet energy levels and their sub-levels for each dye. All relevant electronic transitions that are included in our rate equation model are identified by absorption and emission cross sections specified on the arrows with appropriate transition direction. Non-radiative FRET is assumed to happen between S_{1d} and S_{1a} energy bands. Definitions of individual symbols are given in the text. (b) A simplified Fabry-Pérot laser cavity with two identical output couplers and linked donor/acceptor pairs representing FRET-based active medium. (c) Schematics of molecular constructs with a constant donor-acceptor distance containing one donor linked to three acceptors (1D – 3A) or three donors linked to one acceptor (3D – 1A).	80
6.2	Total output emission energy E_{Dout} , E_{Aout} from bulk solutions of R6G/AB7 FRET pair as a function of the pump fluence, Φ_P . (a) Donor lasing with fixed acceptor concentration $[A] = 0.1$ mM and varying donor concentration $[D] = 1$ to 0.1 mM. (b) Donor lasing with fixed acceptor concentration $[A] = 1$ mM and varying donor concentration $[D] = 1$ to 0.1 mM. (c) Acceptor lasing with fixed donor concentration $[D] = 0.1$ mM and varying acceptor concentration $[A] = 1$ to 0.05 mM. (d) Acceptor lasing with fixed donor concentration $[D] = 1$ mM and varying acceptor concentration $[A] = 1$ to 0.1 mM.	84

6.3	Gain Q-switching in optofluidic FRET lasers. (a) Total output emission energy E_{Dout} from the donor as a function of Φ_P . Insets show the time profiles of the donor emission power before reaching the lasing threshold at $\Phi_P = 0.2 \mu\text{J}/\text{mm}^2$, shortly after crossing the threshold at $\Phi_P = 0.8 \mu\text{J}/\text{mm}^2$ (a single output pulse), and well above the threshold at $\Phi_P = 1.3 \mu\text{J}/\text{mm}^2$ (three output pulses corresponding to the third ripple in the output energy curve). (b) Total output emission energy E_{Aout} from the acceptor as a function of Φ_P . Insets show the time profiles of the acceptor emission power before reaching the lasing threshold at $\Phi_P = 0.03 \mu\text{J}/\text{mm}^2$, shortly after crossing the threshold at $\Phi_P = 0.2 \mu\text{J}/\text{mm}^2$ (a single output pulse), and well above the threshold at $\Phi_P = 0.8 \mu\text{J}/\text{mm}^2$ (two output pulses corresponding to the second ripple in the output energy curve).	86
6.4	Threshold Φ_P of bulk FRET lasing of (a) donor and (b) acceptor as a function of acceptor concentration $[A]$ for several fixed donor concentrations $[D]$. Threshold Φ_P of bulk FRET lasing for (c) donor and (d) acceptor as a function of donor concentration $[D]$ for several fixed acceptor concentrations $[A]$. Solid and dashed curves in (a)-(d) indicate calculations performed assuming active (k_F calculated using Eq. 6.15) and inactive ($k_F = 0$) FRET channels, respectively. The figure legends for (a) and (c) are shown in (b) and (d), respectively.	87
6.5	Total output emission energy E_{Dout} , E_{Aout} from molecularly linked FRET pair R6G/AB7 (denoted as D-A) as a function of Φ_P for different $[D-A]$ values and linker lengths R . In (a), no lasing is observed in donor emission. Plot legend shown in (b) applies to all sub-figures (a)-(f).	89
6.6	(a) Donor lasing threshold as a function of $[D-A]$ for different linker lengths R . (b) Acceptor lasing threshold as a function of $[D-A]$ for different linker lengths R	90
6.7	(a) Donor lasing threshold as a function of linker length R for different $[D-A]$ values. (b) Acceptor lasing threshold as a function of linker length R for different $[D-A]$ values.	90

6.8	Performance of FRET-based biosensors using spontaneous fluorescence emission for $[D - A] = 5 \mu\text{M}$. Donor (solid curves) and acceptor (dashed curves) fluorescence emission energy from linked donor/acceptor pairs versus R at different values of Φ_P for excitation pulsewidth of (a) $\Delta t = 5 \text{ ns}$ and (b) $\Delta t = 50 \mu\text{s}$. Donor emission sensitivity to linker length ($\Omega_D(R)$) versus R for FRET emission from linked donor/acceptor pairs at different values of Φ_P for excitation pulsewidth of (c) $\Delta t = 5 \text{ ns}$ and (d) $\Delta t = 50 \mu\text{s}$. Acceptor emission sensitivity to linker length ($\Omega_A(R)$) versus R for FRET emission from linked donor/acceptor pairs at different values of Φ_P for excitation pulsewidth of (e) $\Delta t = 5 \text{ ns}$ and (f) $\Delta t = 50 \mu\text{s}$. In all these calculations lasing is prevented by assuming $Q = 1$	92
6.9	Behavior of FRET lasing-based biosensor for changing linker length R . Total output energy of (a) donor and (b) acceptor versus Φ_P for different values of R . Total output energy of (c) donor and (d) acceptor versus R for different values of Φ_P . The linker length sensitivity for (e) donor, $\Omega_D(R)$, versus R and (f) acceptor, $\Omega_A(R)$, versus R , calculated for FRET lasing emission from linked donor/acceptor pairs at different values of Φ_P and a constant value of donor/acceptor complex concentration, $[D - A] = 5 \mu\text{M}$. The sensitivity enhancement factor for (g) donor and (h) acceptor as a function of linker length at different Φ_P values. In all simulations, excitation pulse width was set to $\Delta t = 5 \text{ ns}$ and the cavity Q-factor was 10^6	95
6.10	Effect of the cavity Q-factor on emission sensitivities of donor, $\Omega_D(R)$, and acceptor, $\Omega_A(R)$, for linked 1D – 1A donor/acceptor complexes at different values of Φ_P and a fixed concentration, $[D - A] = 5 \mu\text{M}$. In (a), (c) and (e) for donor and in (b) for acceptor no lasing is observed.	97
6.11	Effect of the cavity Q-factor on sensitivity enhancement factors for donor, $\Pi_D(R)$, and acceptor $\Pi_A(R)$ versus R in linked 1D – 1A donor/acceptor complexes at different values of Φ_P and a fixed complex concentration of $[D - A] = 5 \mu\text{M}$	98

6.12 Behavior of FRET lasing-based biosensor using 1D – 3A linked dye complexes with changing R . Total output energy of (a) donor and (b) acceptor versus Φ_P for different values of R . Total output energy of (c) donor and (d) acceptor versus R for different values of Φ_P . The emission sensitivity for (e) donor, $\Omega_D(R)$, and (f) acceptor $\Omega_A(R)$, versus R calculated for FRET lasing emission from linked donor/acceptor complexes at different values of Φ_P . Sensitivity enhancement factors for (g) donor, $\Pi_D(R)$, and (h) acceptor $\Pi_A(R)$, versus R calculated for linked donor/acceptor complexes at different values of Φ_P . In all calculations, 1D – 3A linked dye complexes are assumed to have equal link distances between the donor and acceptor molecules. Effective donor concentration is $[D] = 3 \mu\text{M}$, effective acceptor concentration is $[A] = 9 \mu\text{M}$	102
6.13 Behavior of FRET lasing-based biosensor using 3D – 1A linked dye complexes with changing R . Total output energy of (a) donor and (b) acceptor versus Φ_P for different values of R . Total output energy of (c) donor and (d) acceptor versus R for different values of Φ_P . The emission sensitivity for (e) donor, $\Omega_D(R)$ and (f) acceptor, $\Omega_A(R)$, versus R calculated for FRET lasing emission from linked donor/acceptor complexes at different values of Φ_P . Sensitivity enhancement factors for (g) donor, $\Pi_D(R)$, and (h) acceptor $\Pi_A(R)$, versus R calculated for linked donor/acceptor complexes at different values of Φ_P . In all calculations, 3D – 1A linked dye complexes are assumed to have equal link distances between the acceptor and donor molecules. Effective donor concentration is $[D] = 27 \mu\text{M}$, effective acceptor concentration is $[A] = 9 \mu\text{M}$	103

6.14	Behavior of FRET lasing-based biosensor with changing concentration of linked complex [D-A]. Total output energy of (a) donor and (b) acceptor versus Φ_P for different values of [D-A]. Total output energy of (c) donor and (d) acceptor versus [D-A] for different values of Φ_P . The complex concentration sensitivity of (e) donor and (f) acceptor versus [D-A] calculated for FRET lasing emission from linked donor/acceptor pairs at different values of Φ_P . The complex concentration sensitivity enhancement factor for (g) donor and (h) acceptor versus [D-A] for FRET lasing emission from linked donor/acceptor pairs at different values of Φ_P . In all calculations, R is assumed to be equal to R_0	105
6.15	Behavior of a single dye laser for changing concentration of the gain medium [D]. (a) Total output energy from a single dye, R6G, for $Q_0 = 10^6$ versus Φ_P for different values of [D], (b) Total output energy from a single dye, R6G, for $Q_0 = 10^6$ with solid lines and for $Q_0 = 1$ with dashed lines versus [D] for different values of Φ_P . (c) Concentration sensitivity of emission from a single dye for $Q_0 = 10^6$ with solid lines and for $Q_0 = 1$ with dashed line versus [D] at different values of Φ_P . (d) Concentration sensitivity enhancement factor for single dye versus [D] relative to the nonlasing emission at different values of Φ_P	106
7.1	(a) Lasing spectrum of a 15.6 μm diameter droplet doped with 1Cy3-3Cy5 and (b) lasing spectrum of a 16.4 μm diameter droplet doped with 3Cy3-1Cy5 DNA complexes with identical Cy5 concentration of 25 μM at a pump fluence of 58 mJ/cm^2 . (c) Integral intensity of the lasing peaks as a function of the pump fluence for the droplet spectra shown in (a) (circles) and (b) (squares). Line fits to both experimental data sets give the lasing threshold fluences of 20 mJ/cm^2 and 11 mJ/cm^2 , and differential efficiencies of 310 cm^2/mJ and 3200 cm^2/mJ , respectively.	111

7.2	(a) Average lasing threshold fluence and (b) average lasing differential efficiency for droplets with diameters 14-17 μm containing 1Cy3-3Cy5 (circles) and 3Cy3-1Cy5 (squares) DNA complexes as a function of Cy5 concentration varying between 0.8 μM and 75 μM	113
B.1	(a) Background image (left) and histogram of normalized pixel intensity values in this image (right). (b) Fluorescence image of 1.5 μM Venus solution (left) and histogram of normalized pixel intensity values in this image (right). (c) Fluorescence image of Venus-expressing BL21 <i>E. coli</i> cells adhering to cover slip surface (left) and histogram of normalized pixel intensity values over 100 cells selected in the image (right). Acquisition time for all images was 200 ms. Histograms are normalized such that the sum of frequencies of all bins is equal to 1.	127

NOMENCLATURE

FRET	Fluorescence Resonance Energy Transfer
WGM	Whispering Gallery Mode
Cy3	Cyanine 3
Cy5	Cyanine 5
R6G	Rhodamine 6G
R700	Rhodamine 700
AB7	Acid Blue 7
DiI(3)	1,1-Dioctadecyl-3,3,3,3-tetramethylindo carbocyanine perchlorate
Q	Quality Factor
x	Optical size parameter
k_0	Wavenumber in vacuum
λ	Wavelength of light in vacuum
D	Electric Displacement vector
B	Magnetic induction vector
H	Magnetic field vector
E	Electric field strength vector
ϵ_0	Permittivity of vacuum
ϵ_r	Dielectric constant
μ_0	Permeability of vacuum
ω	Angular frequency of light
η	Refractive index
c	Light speed in vacuum
Z_0	Electromagnetic impedance
\hat{L}	Angular momentum operator
ψ_l, χ_l	Riccati-Bessel differential equation solutions

$Y_{lm}(\theta, \phi)$	Spherical harmonics
$\mathbf{X}_{lm}, \mathbf{Y}_{lm}, \mathbf{Z}_{lm}$	Vector spherical harmonics
m	Azimuthal mode number in spherical harmonic functions
l	Angular mode number in spherical harmonic functions
n	Radial quantum number for WGMs
$P_m^l(\cos \theta)$	Legendre functions
$j_l(x)$	Spherical Bessel function
$n_l(x)$	Spherical Neumann function
TE	Transvers Electric polarization
TM	Transvers Magnetic polarization
\hbar	Reduced Planck's constant
p	Light linear momentum
V_{eff}	Effective optical potential
E_{eff}	Effective optical energy
$\Delta\omega$	Resonant mode linewidth
τ	Cavity decay time
Q_{rad}	Radiative Q-factor from curvature losses
Q_{mat}	Q-factor originated from bulk Rayleigh scattering and cavity material absorption
Q_{cont}	Q-factor originated from environmental contamination losses
$Q_{s.s}$	Q-factor originated from residual surface inhomogeneities
Q_r	Q-factor originated from radiative out-coupling
Q_s	Q-factor originated from absorptive losses
γ_1, γ_2	Attenuation constants of droplet and surrounding medium
f_{me}	Fraction of the mode energy outside of the sphere
$r_0 = a, D$	Droplet radius and diameter
σ	RMS size of inhomogeneities on the droplet surface
B	Correlation length of inhomogeneities on the droplet surface
$d\mathbf{P}$	Directional power of a ray
$d\mathbf{S}$	Cross section vector of a ray canal in ray direction
$\langle I(\mathbf{r}) \rangle$	Average intensity of light in ray-optics regime

$d\mathbf{F}$	Rate of transported linear momentum by a ray
R, \mathcal{R}	Reflection coefficient
$f_l(r)$	Radial part of solution for the wave equation
NA	Numerical Aperture of an objective lens
PBS	Polarizing Beam Splitter
WP	$\lambda/2$ Wave Plate
ρ	Density of mass
$g_0(\lambda)$	Dye gain spectrum
$\beta(a, \lambda)$	Efficiency of light out-coupling from a droplet
$A(a, \lambda)$	Effective cross-section of a lasing WGM
$P_{out}(a, \lambda)$	Out-coupled laser power from a droplet
PDMS	Polydimethylsiloxane
FM	Flippable Mirror
UV	Ultra Violet
CPP	Critical Packing Parameter
HLB	Hydrophile-Lipophile Balance parameter
SDS	Sodium Dodecyl Sulfate
CMC	Critical Micelle Concentration
γ	Interfacial surface tension
AOT	Docusate sodium salt
C_e, C_p	Stretched droplet circumferences in equatorial and polar plane
c_B	Average interacellular concentration
V_B	<i>E. coli</i> cell volume
ν_B	Normalized fluorescence intensity of cells
c_V	Venus concentration
ν_V	Normalized fluorescence intensity of Venus
d_B	Bacteria cell thickness
d_V	Thickness of the Venus layer in sample chamber
α_n	Roots of Airy function
α_s	Optical absorption coefficient

δ	Thermal coefficient of refractive index
β	Thermal expansion coefficient
$P_{stretch}$	Dual beam stretching laser power
k_{F0}	FRET rate between a single donor/acceptor pair
k_F	FRET rate from donor to surrounding acceptors
R_0	Förster Radius
τ_d, τ_a	Donor and acceptor lifetimes
κ	Dipole orientation factor
N_A	Avogadro's number
φ_D^0	Donor fluorescence quantum yield in absence of energy transfer
φ_D	Donor fluorescence quantum yield in presence of energy transfer
ϵ_A	Molar absorption coefficient of acceptor dye
$I_D(\lambda)$	Normalized fluorescence spectrum of donor dye
φ_{FRET}	FRET efficiency
$\rho(t)$	Probability of finding a donor at excited state
N	Number of acceptor molecules surrounded a donor
N_a, N_d	Total concentration of acceptor and donor
R_g	Effective range of the dipole-dipole interaction
$I_p(t)$	Pump intensity
n_a, n_d	Densities of acceptor and donor molecules at excited state
q_a, q_d	Photon densities for single lasing line at acceptor and donor dyes
ΔT	Temperature difference
S_{0d}, S_{0a}	Ground states of energy for donor and acceptor dyes
S_{1d}, S_{1a}	First excited singlet states of energy for donor and acceptor dyes
S_{2d}, S_{2a}	Second excited singlet states of energy for donor and acceptor dyes
$P_{Dout}(t)$	Total out-coupled lasing emission power at donor lasing wavelength
$P_{Aout}(t)$	Total out-coupled lasing emission power at acceptor lasing wavelength
E_{Dout}	Total out-coupled lasing emission energy at donor lasing wavelength
E_{Aout}	Total out-coupled lasing emission energy at acceptor lasing wavelength
σ_{pd}	Donor absorption cross section at the pump wavelength

σ_{pa}	Acceptor absorption cross section at the pump wavelength
σ_{edd}	Donor stimulated emission cross section at λ_d
σ_{eaa}	Acceptor stimulated emission cross section at λ_a
σ_{ead}	Acceptor stimulated emission cross section at λ_d
σ_{add}	Donor absorption cross section at λ_d
σ_{1dd}	Excited state absorption cross section of donor molecules at λ_d
σ_{1aa}	Excited state absorption cross section of acceptor molecules at λ_a
σ_{1ad}	Excited state absorption cross section of acceptor molecules at λ_d
σ_{aad}	Acceptor absorption cross section at λ_d
σ_{aaa}	Acceptor absorption cross section at λ_a
τ_{cd}	Fluorescence lifetime of cavity at λ_d
τ_{ca}	Fluorescence lifetime of cavity at λ_a
λ_d	Donor lasing wavelength
λ_a	Acceptor lasing wavelength
Q_0	Empty cavity Q-factor
F	Fraction of mode volume occupied by the dye molecules
d	Depth of the electromagnetic mode
d_p	Penetration depth of the electromagnetic mode
w	Width of the electromagnetic mode
l	Length of the electromagnetic mode
V	Volume of the electromagnetic mode
V_p	Volume of the pumped region in laser gain medium
Δt	Pump laser pulsewidth
h	Planck's constant
Φ_P	Pulse energy fluence
CET	Cavity-enhanced Energy Transfer
$\Omega_D(R)$	Sensitivity of emission energy to conformational changes in donor
$\Omega_A(R)$	Sensitivity of emission energy to conformational changes in acceptor
Π_D	FRET sensitivity enhancement factor in donor
Π_A	FRET sensitivity enhancement factor in acceptor

ρ_a	Concentration of acceptor molecules
$\rho_{a1/2}$	Characteristic acceptor concentration with half of CET

Chapter 1

INTRODUCTION

1.1 Microdroplets as Optical Cavities for Whispering Gallery Modes

Acoustic or electromagnetic wave resonances of round shape objects are called Whispering Gallery Modes (WGMs). Whispering-Gallery Modes were first observed and explained for the case of acoustic waves propagating in the gallery of St Paul's Cathedral in London in 1878 by Lord Rayleigh. It was found that a whispering close to the edge of the inner side of the vault could be heard relatively easily by a person standing at the opposite side of the dome. The phenomenon was named as "Whispering Gallery" and explained by traveling whispers with a series of specularly reflected sound waves that construct chords of the circular gallery.

The analogy of WGM for sound waves can happen for electromagnetic waves in optical microresonators if the photon returns in phase after each round trip around the resonator [1, 2, 3]. They have been produced in microscopic glass spheres or disks [4, 5], with applications in lasing [6], optomechanical cooling [7], frequency comb generation [8] and sensing [9]. The light waves are almost perfectly guided around the resonator by optical total internal reflection that makes Q-factors more than 10^{10} achievable [10]. Such high-Q cavities are a prerequisite for low-threshold lasing which is attractive in the development of integrated tunable organic light sources [11] and in biological and chemical sensing.

Among different kinds of WGM resonators, cavities based on liquid microdroplets represent a very important category, due to their simplicity, easy fabrication, and very high quality. At the microscale, shape of liquids is dictated by the liquid surface tension that tends to minimize liquid surface area, thus transforming a small liquid parcel into a perfect spherical droplets. Liquid droplets have been long recognized and studied for their peculiar optical properties [12]. Such spherical droplets with exceptionally smooth surfaces can

act as optical cavities hosting WGMs that are confined to the small volumes close to their surfaces [13].

1.2 Spatial Confinement of Micro-objects by Optical Forces

In order to manipulate microdroplets as tiny liquid objects we can use different tools such as mechanical tweezers, electrostatic forces and optical forces. The idea of using forces of optical waves to manipulate objects originates from the concept of radiation pressure proposed by Johannes Kepler back in 1619. He used this concept to explain the direction of a comet tail that always points away from the sun. The radiation pressure of light was first discovered theoretically by James C. Maxwell in 1873 based on his electromagnetic theory, and measured experimentally by Lebedev [14], and Nichols and Hull in 1901 [15]. In 1970, Arthur Ashkin published a paper [16] showing that one can use a focused laser beam to accelerate and trap micrometer-sized transparent particles. Few years later he demonstrated optical levitation of liquid droplets and dielectric microspheres in air [17, 18]. Using the gradient force of a single strongly focused laser beam Ashkin et al. [19] demonstrated stable trapping of dielectric particles which did not rely on any other external force. This technique became known as optical tweezers and it was soon used to trap and manipulate viruses and bacteria and became a standard tool in biophysics. Moreover, the laser radiation pressure was used to trap and cool atoms [20, 21, 22], which led to important discoveries in atomic, molecular and optical physics such as the realization of Bose-Einstein condensation, degenerate Fermi gas and a new generation of atomic clocks.

1.3 Microdroplets as Optofluidic Lasers

Optofluidics is a research and technology area that combines the advantages of microfluidics and optics. Lasers with liquid gain medium based on microfluidics technology are called optofluidic lasers. Microdroplets as perfect optofluidic resonators that contain gain medium can host lasing WGMs. First demonstration of lasing from liquid droplets dates back to 1984; in these pioneering experiments, lasing was observed in dye-doped free-falling ethanol droplets in air [23, 24]. Since then, numerous additional demonstrations of lasing in liquid droplets surrounded by air (aerosol droplets) or another liquid (emulsion droplets) have followed. In particular, lasing has been observed in electrodynamically or ultrasoni-

cally trapped dye or quantum-dot doped aerosol droplets [25, 26, 27], or dye-doped aerosol droplets supported by a superhydrophobic surface [28]. In parallel with the advances in techniques of droplet generation with microfluidic chips, these emulsion droplets surrounded by a suitable host liquid have also been studied as micro-lasers [29].

In order to fully exploit the potential of lasing WGMs in microdroplets, it is necessary to stabilize the droplet position over extended time periods. The position stabilization of droplets of water and other polar liquids can be effectively realized by depositing them on a superhydrophobic surface [28].

As a prerequisite to confine the light inside a microdroplet-based optical cavity, its index of refraction must be higher than the refractive index of the host medium. The requirement of the refractive index contrast also means that the droplets can be manipulated with a single-beam optical trap (optical tweezers) [19]. Optical tweezers have been used to manipulate emulsion or aerosol droplets for micro-spectroscopy and chemical analysis applications [30, 31], and atmospheric chemistry and physics or health science up to now [32, 33].

Despite these efforts, however, lasing in optically manipulated aerosol or emulsion droplets has not been demonstrated yet; optically manipulated micro-lasers presented in the literature so far have always used solid spherical microcavities [34, 35]

1.4 Optical Tuning of Emulsion Droplet Lasers

Tunability of shape, size, and composition is an important advantage of reconfigurable optofluidic components based on microdroplets. The most straightforward way of tuning spectral position of WGMs of airborne droplets relies on controlled changes of the liquid cavity size using evaporation/condensation [36], electrowetting [37], or photothermal effect [38]. Adjustment of resonant frequency of a microdroplet optical cavity can also be achieved by controlled deformation of the microdroplet which lifts the degeneracy of WGMs with different azimuthal mode numbers. Frequency splitting of the azimuthal WGMs then depends on the extent of the microdroplet deformation [39, 40].

For microdroplets surrounded by a solid elastomer, tuning has been achieved by mechanical shape deformation [41] or by changing the refractive index of liquid crystal droplets in external electric field [42]. However, for the case of microdroplets surrounded by another

liquid in microfluidic channels, reversible spectral tuning has not been shown yet, despite different demonstrations of optical functionality of emulsion droplets including dye lasing [29, 43]. In order to address the issue of spectral tuning, researchers have demonstrated multicolor dye lasing in microfluidic channels by fast switching between consecutive droplets doped with different dye molecules [44]. Recently, emission wavelength tuning by continuous decrease of the droplet size due to dissolving of benzyl alcohol microdroplets in water has also been demonstrated [45]. Nevertheless, such dissolution-based tuning of the lasing emission wavelength is irreversible.

As shown by Guck *et al.*, transparent dielectric micro-objects suspended in a liquid can be deformed by the forces of light [46]. At the object surface where the material properties (in particular, the dielectric constant) change abruptly, transfer of momentum from light to the object occurs. Such surface momentum transfer then leads to surface stresses that can cause deformation of the illuminated object, with the amount of deformation directly proportional to the incident light power. Optically induced deformation of soft micro-objects (lipid vesicles, living cells) has been successfully demonstrated using a pair of counter-propagating laser beams in the so-called optical stretcher geometry [46]. Optical stretcher uses the dual-beam optical trap configuration [16, 47, 48] which consists of two precisely aligned, slightly divergent counter-propagating laser beams emitted, for example, from optical fibers. Because of the Gaussian transversal intensity profile of both beams, high refractive index objects (e.g. oil droplets suspended in water) are pulled toward the beams axis and, subsequently, move along this axis to the location where the radiation pressures of both beams just balance each other. At this position, the objects are stably confined and their stretching in the optical field of the two beams can be studied.

Optical stretcher represents a convenient, all-optical method for tuning the emission spectra of lasing microdroplets via controlled droplet deformation that leads to frequency-splitting of degenerate WGMs of originally spherical droplets. However, the magnitude of optical stretching forces is rather small in comparison with the typical interfacial tension forces acting between two immiscible liquids in emulsions. In order to achieve sufficient droplet deformations without using prohibitively high stretching laser powers, interfacial tension has to be lowered by several orders of magnitude. This can be accomplished by using various mixtures of surfactant molecules and inorganic salts for the emulsion preparation.

Emulsions with ultra-low interfacial tension have been used by Møller *et al.* [49] and Ward *et al.* [50] in the single beam and multiple beam optical tweezers, respectively, to observe large deformations of the emulsion droplets with moderate trapping powers. Despite the above demonstrations, optical stretcher geometry has not been employed yet for light-induced tuning of the emission spectra of lasing microdroplets.

1.5 Biosensing with Optofluidic Lasers

Optofluidic lasers have recently emerged as a promising technology for developing novel photonic devices and highly sensitive biochemical sensors [51, 52, 53]. Optofluidic lasers integrate optical microcavities and gain media into liquid environments contained within suitable microfluidic circuits or chips. On the photonic device side, they exploit flexibility of material characteristics and geometrical shape of liquids for creating miniaturized light sources embedded directly on a chip. On the biosensing side, optofluidic lasers take advantage of a fully-biocompatible aqueous working environment. Analytes under study, which form laser gain media, can be directly placed within the optical mode volume. Thus, amplified lasing emission rather than ordinary spontaneous fluorescence is used as the sensing signal. Due to the optical feedback provided by the cavity, a small change in the gain medium induced by underlying biological processes is significantly amplified, leading to a dramatic change in the laser output characteristics.

1.5.1 Biolasing from Suspended Fluorescent Proteins and E-Coli Bacteria in Microdroplets

Green fluorescent protein (GFP) and its engineered color variants such as yellow fluorescent protein (YFP) or cyan fluorescent protein (CFP) are widely used experimental tools that have revolutionized cell and molecular biology research [54]. The tremendous potential of fluorescent proteins in life sciences stems from the possibility of fusing them genetically to a number of important cellular components in both prokaryotic and eukaryotic organisms without affecting the structure, function, or cellular location of the fluorescently labeled target molecule [55]. Combined with advanced microscopy techniques such as Förster resonance energy transfer (FRET), fluorescent protein-based probes allow understanding of numerous biological phenomena at the molecular level, including highly selective and sensitive quantitative detection of molecular components in complex environments (e.g., cell

cytoplasm and membranes), visualization of protein expression and degradation in cells, and dynamics of molecular interactions [56].

In a typical live-cell experiment, the intensity of spontaneous light emission from optically pumped fluorescent proteins expressed in cells is detected and evaluated. While this procedure is straightforward to implement, the level of the spontaneous fluorescence signal can be too low to collect a sufficiently high number of photons before the fluorophore photobleaches. Amplified stimulated emission from fluorescent protein molecules placed inside a suitable optical cavity can lead to lasing of the protein and, subsequently, a significant increase in the fluorescence intensity. Such biolasers can be used to implement new ways of biological sensing and analysis that benefit from the high sensitivity of stimulated emission to small perturbations in the laser cavity and the gain medium and from the specificity of attachment of fluorescent proteins to selected cellular components which allows targeted studies of well-defined intracellular processes [53].

Gain media based on fluorescent proteins expressed in living cells can be regenerated following photobleaching of the fluorophore; hence, biolasers are in principle self-healing. Furthermore, specific molecular recognition and selfassembly can provide additional functionality and programmatic control of photonic components based on biological molecules. The first demonstrations of biolasing employed GFP-expressing live mammalian cells or *E. coli* bacteria placed inside a FabryPérot resonator [57, 58]. Recently, an optofluidic ring resonator (OFRR) was used for observation of in vitro lasing from aqueous solutions of fluorescent proteins. This scheme was based on indirect pumping of lasing emission via FRET and employed genetically encoded fluorescent protein pairs linked by a peptide with adjustable length, thus allowing the study of proteinprotein or proteindrug interactions [59]. Biological molecules other than fluorescent proteins have also been recently tested as laser gain media. In these demonstrations, lasing was achieved with luciferin solution contained within an OFRR [60] or flavin mononucleotide dissolved in glycerolwater microdroplets supported by a superhydrophobic surface [61]. However, unlike fluorescent proteins, these small fluorescent organic compounds cannot be readily expressed and regenerated in living cells and selectively fused to other cellular proteins without external coupling agents.

1.5.2 *Biosensing with Fluorescence Resonance Energy Transfer (FRET)*

A very important physical phenomena at the molecular level that is used for biosensing purposes is fluorescence (Förster) resonance energy transfer (FRET). FRET is a mechanism of energy transfer between two light-sensitive chromophores where a donor chromophore is initially in its electronic excited state and transfers its energy to an acceptor chromophore through nonradiative dipole-dipole coupling. The efficiency of this energy transfer is inversely proportional to the sixth power of the distance between donor and acceptor (making FRET extremely sensitive to small changes in distance) and to the spectral overlap of donor emission with acceptor absorption. Hence, FRET between a pair of donor and acceptor chromophores that have sufficient spectral overlap can be used as a precise ruler to measure the distance between the two chromophores with atomic-scale resolution. Working range of FRET is limited to chromophore spacings less than 10 nm which is the typical size of large biomolecules such as proteins and nucleic acids. Therefore, FRET is commonly used in biological and biochemical sensing for studying conformational changes or quantifying interactions between different biomolecules and molecular complexes in live cells [62, 63]. When biomolecules labeled with the donor and acceptor dyes undergo a conformational change or binding/unbinding process, the distance between the donor and acceptor changes, resulting in a change in the donor and acceptor emission intensity which constitutes the FRET signal.

1.5.3 *FRET for Efficient Laser Pumping*

In addition to sensing applications, FRET has also been employed as an alternative mechanism for pumping laser gain media [64, 65]. In these demonstrations, donor and acceptor molecules are mixed together in a liquid or solid host matrix. Subsequently, the donor molecules are directly pumped using an external source of energy. Excited donor molecules then transfer their energy to acceptor molecules that emit coherent laser light. Typically, the distances between the donor and acceptor molecules are randomly distributed and determined statistically by the donor and acceptor concentrations. By using FRET as indirect pumping mechanism in dye lasers the effective absorption cross section from the pump beam increases by increasing donor concentration. So in a fixed concentration of acceptor by increasing the donor concentration, the acceptor molecules can be pumped more efficiently. Efficient acceptor pumping translates to lower lasing threshold that lowers the bleaching

rate of dyes and extends the dye laser lifetime.

1.5.4 *Optofluidic FRET Lasers as High Sensitivity Biosensors*

Lasers with suitable pair of FRET chromophores (donor and acceptor) placed inside the mode volume of optofluidic resonators to form laser gain medium can be called optofluidic FRET lasers. In such lasers changes in FRET efficiency brought about by modulation of the separation distance between the donor and acceptor molecules will translate into modulation of the laser output energy. The unique position of biolasers in sensing applications derives from the high sensitivity of the nonlinear optical processes associated with lasing to minute perturbations of the gain medium and/or the laser cavity [53]. In combination with advanced biotechnologies based on self-recognition and self-assembly of biological molecules (proteins, polynucleotides, or DNA), the sensing potential of lasers with biological gain media has been demonstrated in highly specific discrimination between DNA molecules with a single base-pair mismatch [66] or analysis of DNA melting [67]. Recent experiments demonstrated that the same underlying biological process or the same change of FRET efficiency can result in changes of the lasing emission intensity from the donor and/or the acceptor that are orders of magnitude larger than those observed in conventional FRET based on spontaneous fluorescence [66, 68, 59, 67]. Furthermore, besides intensity and polarization of the emitted light, laser output consists of many more parameters that can be monitored and serve as a measurement signal, such as the lasing threshold, lasing efficiency, and lasing mode spatial profile. Therefore, optofluidic FRET lasers provide a powerful complementary technology to analyze minute changes in biomolecules that may otherwise remain indistinguishable with conventional FRET.

Optofluidic FRET lasers also open the door for developing new types of sources of coherent light. With recent advances in nanotechnology and biotechnology, the number and position of the donor and acceptor molecules located within the laser mode volume can be precisely controlled and modulated with sub-nanometer spatial resolution. Therefore, overall FRET efficiency is no longer dependent upon the bulk concentrations of the donor and acceptor molecules, and high FRET efficiencies can be maintained even at the single-molecular level [69, 70]. Recently, lasing from a single-layer gain medium containing orders of magnitude fewer gain molecules than the conventional bulk active media has been demon-

strated [71]. Therefore, it is imaginable that lasing from only a few gain molecules might be achievable [72, 71], in which the FRET pumping mechanism is strongly preferable to the direct optical excitation in order to achieve higher pumping efficiency [72].

1.5.5 Droplets as Optofluidic FRET Lasers

In order to perform biosensing with optofluidic lasers various experimental strategies of creating optical resonators for integrated optofluidic lasers have been explored. Typically, the resonator is formed from a solid-state material; this includes miniaturized versions of conventional Fabry-Pérot cavities [57], distributed-feedback grating resonators [73], and optofluidic ring resonators (OFRRs) based on thin-wall capillaries that can support whispering gallery modes (WGMs) with extremely high quality factors (Q-factors) of $\sim 10^7$ and small modal volumes localized in the proximity of the resonator surface [66, 67, 74]. While all these approaches provide functional optical cavities, they require microfabrication and/or alignment steps which bring additional experimental challenges to the process of creating a working optofluidic sensor.

In the simplest possible approach as we discussed earlier, liquid droplets without any additional external solid structures can be used to build the alternative self-assembled ring resonators hosting high-Q WGMs [24, 12, 36]. In contrast to the OFRR where WGMs residing inside the capillary wall interact with the analyte only through evanescent mode coupling, in a liquid droplet resonator, analytes are placed directly into the cavity. Thus, the analyte molecules that are located near the droplet surface can interact with the peak WGM fields, achieving very strong light-matter coupling. Moreover, aqueous microdroplets provide natural environmental conditions for biological molecules and live cells. These features make microdroplets ideally suited for sensing of biological species [75]. However, droplet-based cavities have only found a limited use in practical sensing application to date, mostly because of the difficulties with controlling and stabilizing the droplets.

1.6 Thesis Goals and Outline

The main aims of this thesis are to generate and manipulate lasing microdroplets and simulate and experimentally characterize their laser emission to demonstrate their advantages and potential as high sensitivity optofluidic biosensors. To this end in chapter 2 we started

with the solution of Maxwell equations for a spherical dielectric resonator to have a fundamental physical and mathematical description of the WGM structures in the microdroplet lasers and their dependence on different physical parameters. Moreover, in chapter 2 a brief description of optical forces is given since they have been used as suitable tools for droplet manipulation.

In chapter 3 we show manipulation of optically pumped dye-doped emulsion and aerosol microdroplet lasers by a single beam optical trap. We characterize the droplet emission spectrum as a function of the droplet size and show that the droplet lasing wavelength can be tuned over an interval larger than 30 nm by adjusting the droplet radius. Moreover, we investigate the effects of droplet size and dye concentration on the spectral position of lasing wavelength and show how these parameters can be used for the emission wavelength tuning. We also study shifting of the average lasing wavelength to the blue side of the spectrum due to dye photobleaching. For emulsion droplet lasers we show high stability of the laser emission spectra during prolonged optical manipulation of the droplets within an immiscible host liquid.

In chapter 4 we show further capabilities of optical forces in combination with microdroplet lasers by introducing tunable optofluidic microlasers based on active optical resonant cavities formed by optically stretched, dye-doped emulsion droplets confined in a dual-beam optical trap. To achieve tunable dye lasing, optically pumped droplets of oil dispersed in water are stretched by light in the dual-beam trap. Subsequently, resonant path lengths of whispering gallery modes (WGMs) propagating in the droplet are modified, leading to shifts in the microlaser emission wavelengths. Using this technique, we present all-optical, almost reversible spectral tuning of the lasing WGMs and show that the direction of tuning depends on the position of the pump beam focus on the droplet. In addition, we study the effects of temperature changes on the spectral position of lasing WGMs and demonstrate that droplet heating leads to red-tuning of the droplet lasing wavelength.

In chapter 5 we introduce optofluidic droplet-based biolasers with the gain medium effectively formed by an individual micron-sized bacterial cell suspended in the droplet liquid or solutions of purified Venus fluorescent protein. The glycerol-water microdroplets supported by a superhydrophobic surface serve as optical cavities for the amplification of stimulated emission from the Venus variant of yellow fluorescent protein expressed in the

bacteria or from its purified solution. We study the dynamics of lasing from these laser gain media and provide experimental evidence for lasing from a single Venus-expressing bacterial cell. The lasing bacteria suspended in a droplet can be provided with all nutrients required for steady growth, which may allow for extending the operation time of this biologically controlled source of laser light by active regeneration of the gain medium.

Lasers are complicated physical systems with too many effective parameters. In order to obtain a better understanding about the performances of optofluidic lasers as biosensors, in chapter 6 we carry out a comprehensive theoretical analysis of optofluidic FRET lasers based on a Fabry-Pérot microcavity using a rate equation model. We compare conceptually distinct cases of donor and acceptor molecules diffusing freely in bulk solution versus molecules connected by a fixed-length linker and show that the latter arrangement is especially well-suited for sensing of low-concentration analytes. By comparing FRET lasing-based sensors with conventional FRET sensors, we show that for optimal pump fluence and FRET-pair concentration, FRET lasing can lead to more than 100-fold enhancement in detection sensitivities of conformational changes in the Förster radius range. We also show that for optimal experimental conditions, donor and acceptor emission intensities become over 20-fold more sensitive to FRET-pair concentration changes in the presence of FRET lasing. Moreover, we study the dependence of the sensitivity enhancement on the cavity Q-factor. We show that the highest enhancements can be obtained for Q-factors between $10^4 - 10^6$, and enhancement values decrease for Q-factors above 10^6 due to the radiative energy transfer in the cavity.

Following the theoretical studies in chapter 6 about biosensing with optofluidic FRET lasers based on Fabry-Pérot cavities, in chapter 7 we demonstrate FRET lasing from self-assembled tetrahedral DNA complexes labeled with Cy3 and Cy5 dyes as donor and acceptor pair that are suspended as a gain medium in aqueous microdroplet cavities deposited on a superhydrophobic surface. Threshold fluence and differential efficiency are characterized for DNA complexes containing 1Cy3-3Cy5 and 3Cy3-1Cy5. It is shown that with a fixed concentration of Cy5, lasing threshold for 3Cy3-1Cy5 is 2 to 8 times less than 1Cy3-3Cy5 complexes that reveals more efficient pumping of lasing chromophores with FRET mechanism. Here, the geometry of the laser cavity is different than what we considered in theoretical studies in chapter 6 but in general the behavior of the laser emission by changing

the laser parameters follows the same trends in both systems.

Chapter 2

THEORY OF MICROSPHERE RESONATORS AND LASING MICRODROPLETS

The light wave behavior in interaction with spherical microresonators can be categorized by a relative parameter called size parameter or dimensionless sphere radius that is the ratio of the sphere circumference to the wavelength of light: $x = 2\pi a/\lambda = k_0 a$, where a is the radius of the sphere, and λ and $k_0 = 2\pi/\lambda$ are the wavelength and wavenumber of light in vacuum, respectively. Light scattering by an isolated droplet is usually called Mie scattering. When the size parameter ranges from a few tens to several hundreds and with λ located in the visible range, a will be around few to tens of micrometers. When $x \ll 1$, light scattering is called Rayleigh scattering and the droplet diameters for visible light will be well below one micrometer.

The solution to Maxwell's equations known as the Lorenz-Mie solution, the Lorenz-Mie-Debye solution or Mie scattering, describes the scattering of electromagnetic plane waves by a homogeneous sphere. The solution takes the form of infinite series of spherical multipole partial waves. The term "Mie theory" is sometimes used for the collection of solutions and methods other than spheres like cylinders where the solution can be separated to radial and angular portions [1, 2]. Generally Mie scattering covers the situations where the size of the scattering particles is comparable to the wavelength of the light, rather than much smaller or much larger. For the case of the laser beam of an arbitrary wavefront shape the same approach can be applied within the framework of so-called generalised Lorenz-Mie theory (GLMT). The only difference is in the complexity of the infinite series and the number of expansion coefficients, which have to be evaluated [76]

The Maxwell equations can describe the WGMs for any resonator but for spherical resonators the wave equations can be modified to the shape of Schrödinger equation so that the optical resonance modes can be treated like electronic states in an atom. Hence, we will analyze the modes by analogy with the Quantum Mechanics of electrons in atoms.

2.1 Maxwell Equations in Spherical Coordinate System

Aerosol or emulsion droplets are dielectric spheres surrounded by another dielectric medium. To find the optical resonance frequencies of a droplet, we begin with the Maxwell equations in spherical coordinate system. The time dependent Maxwell equations for a nonmagnetic and charge-free medium are

$$\nabla \cdot \mathbf{D}(\mathbf{r}, t) = 0 \quad (2.1)$$

$$\nabla \cdot \mathbf{B}(\mathbf{r}, t) = 0 \quad (2.2)$$

$$\nabla \times \mathbf{E}(\mathbf{r}, t) + \frac{\partial \mathbf{B}(\mathbf{r}, t)}{\partial t} = 0 \quad (2.3)$$

$$\nabla \times \mathbf{H}(\mathbf{r}, t) - \frac{\partial \mathbf{D}(\mathbf{r}, t)}{\partial t} = 0 \quad (2.4)$$

where

$$\mathbf{D}(\mathbf{r}, t) = \epsilon_0 \epsilon_r \mathbf{E}(\mathbf{r}, t) \quad (2.5)$$

$$\mathbf{B}(\mathbf{r}, t) = \mu_0 \mathbf{H}(\mathbf{r}, t) \quad (2.6)$$

are the constitutive relations with μ_0 , ϵ_0 , and ϵ_r as vacuum permeability and permittivity, and dielectric constant, respectively. Assuming a harmonic time dependence for electric and magnetic field strengths $\mathbf{E}(\mathbf{r}, t) = e^{-i\omega t} \mathbf{E}(\mathbf{r})$ and $\mathbf{H}(\mathbf{r}, t) = e^{-i\omega t} \mathbf{H}(\mathbf{r})$, we can use Eqs. 2.1 to 2.4 to obtain

$$(\nabla^2 + \omega^2 \epsilon_0 \epsilon_r \mu_0) \mathbf{E}(\mathbf{r}) = 0 \quad (2.7)$$

$$(\nabla^2 + \omega^2 \epsilon_0 \epsilon_r \mu_0) \mathbf{H}(\mathbf{r}) = 0 \quad (2.8)$$

$$\mathbf{H}(\mathbf{r}) = \frac{-i}{\omega \mu_0} \nabla \times \mathbf{E}(\mathbf{r}) \quad (2.9)$$

$$\mathbf{E}(\mathbf{r}) = \frac{i}{\omega \epsilon_0 \epsilon_r} \nabla \times \mathbf{H}(\mathbf{r}) \quad (2.10)$$

By introducing $\eta = \sqrt{\epsilon_r}$, $k_0 = \omega/c$, $k = \omega\eta/c$, $Z_0 = \sqrt{\mu_0/\epsilon_0}$ and $c = 1/\sqrt{\mu_0\epsilon_0}$ as the refractive index, vacuum wavenumber, dielectric wavenumber, electromagnetic impedance, and speed of light, we rewrite the time independent Maxwell equations as the following

$$(\nabla^2 + k^2) \mathbf{E}(\mathbf{r}) = 0 \quad (2.11)$$

$$(\nabla^2 + k^2) \mathbf{H}(\mathbf{r}) = 0 \quad (2.12)$$

$$\mathbf{H}(\mathbf{r}) = \frac{-i}{k_0 Z_0} \nabla \times \mathbf{E}(\mathbf{r}) \quad (2.13)$$

$$\mathbf{E}(\mathbf{r}) = \frac{iZ_0}{k_0\eta^2(r)} \nabla \times \mathbf{H}(\mathbf{r}) \quad (2.14)$$

In the framework of classical electrodynamics we can use Hansen's method [77] to solve the vectorial Helmholtz equations (2.11) and (2.12). In this method solutions of these two equations have angular dependence described by vector spherical harmonics [78] defined as

$$\begin{aligned} \mathbf{X}_{lm} &= \nabla Y_{lm} \times \mathbf{r} / \sqrt{l(l+1)} \\ \mathbf{Y}_{lm} &= r \nabla Y_{lm} \sqrt{l(l+1)} \\ \mathbf{Z}_{lm} &= \hat{r} Y_{lm} \end{aligned}$$

where l is a non-negative integer, m is an integer that $-l < m < l$, and Y_{lm} 's are the standard spherical harmonics:

$$Y_{lm}(\theta, \phi) = \sqrt{\frac{2l+1}{4\pi} \frac{(l-m)!}{(l+m)!}} P_m^l(\cos\theta) e^{im\phi} \quad (2.15)$$

where $P_m^l(\cos\theta)$ are the Legendre functions. In this picture, each WGM mode with transverse electric field (TE) (namely $\mathbf{r} \cdot \mathbf{E} = 0$) is shown by $\{\mathbf{E}_{lm}^{TE}(\mathbf{r}), \mathbf{H}_{lm}^{TE}(\mathbf{r})\}$ and each WGM mode in transverse magnetic field (TM) (namely $\mathbf{r} \cdot \mathbf{H} = 0$) is shown by $\{\mathbf{E}_{lm}^{TM}(\mathbf{r}), \mathbf{H}_{lm}^{TM}(\mathbf{r})\}$. The mode number l indicates the order of spherical harmonic and describes the orbital momentum distribution. Angular momentum operator is defined by $\hat{L} = -i\mathbf{r} \times \nabla$ and it is straightforward to show that $L^2 Y_{lm} = l(l+1)Y_{lm}$. The m is called the azimuthal mode number and takes $2l+1$ values from $-l$ to l . The solutions for both of polarizations can be written as the following [13]

$$\mathbf{E}_{lm}^{TE}(\mathbf{r}) = \frac{E_0 f_l(\eta(r)k_0 r)}{k_0 r} \mathbf{X}_{lm} \quad (2.16)$$

$$\mathbf{H}_{lm}^{TE}(\mathbf{r}) = \frac{E_0}{ic\mu_0} \left(\frac{f'_l(\eta(r)k_0 r)}{k^2 r} \mathbf{Y}_{lm} + \sqrt{l(l+1)} \frac{f_l(\eta(r)k_0 r)}{k_0^2 r^2} \mathbf{Z}_{lm} \right) \quad (2.17)$$

$$\mathbf{E}_{lm}^{TM}(\mathbf{r}) = \frac{E_0}{\eta^2} \left(\frac{f'_l(\eta(r)k_0 r)}{k^2 r} \mathbf{Y}_{lm} + \sqrt{l(l+1)} \frac{f_l(\eta(r)k_0 r)}{k_0^2 r^2} \mathbf{Z}_{lm} \right) \quad (2.18)$$

$$\mathbf{H}_{lm}^{TM}(\mathbf{r}) = -\frac{iE_0 f_l(\eta(r)k_0 r)}{\mu_0 c k_0 r} \mathbf{X}_{lm} \quad (2.19)$$

where E_0 is electric field amplitude, $\eta(r)$ is the refractive index at radius r , $f'_l(\rho) = \frac{df_l(\rho)}{d\rho}$, and $f_l(r)$ is the solution of the radial part of the wave equations (2.11) and (2.12) known

as Riccati-Bessel radial equation

$$\frac{d^2 f_l(r)}{dr^2} + \left[\eta(r)^2 k^2 - \frac{l(l+1)}{r^2} \right] f_l(r) = 0 \quad (2.20)$$

where its solutions have the general form of $f_l(\rho) = A_l \psi_l(\rho) + B_l \chi_l(\rho)$, where $\psi_l(\rho) = \rho j_l(\rho)$ and $\chi_l(\rho) = \rho n_l(\rho)$. Here j_l and n_l are spherical Bessel and Neumann functions. For $r < a$ when $r \rightarrow 0$ the solution for radial part should be finite, hence $B_l = 0$ whereas for $r > a$, A_l and B_l are nonzero and we can write the solutions as

$$\begin{cases} f_l(\eta k_0 r) = \psi_l(\eta k_0 r) & \text{for } r < a \\ f_l(k_0 r) = A_l \psi_l(k_0 r) + B_l \chi_l(k_0 r) & \text{for } r > a \end{cases} \quad (2.21)$$

We can rewrite Eq. 2.20 as

$$\left[-\frac{d^2 f_l(r)}{dr^2} + V_{\text{eff}}(r) \right] f_l(r) = k^2 f_l(r) \quad (2.22)$$

where

$$V_{\text{eff}}(r) = \left\{ [1 - \eta(r)^2] k^2 + \frac{l(l+1)}{r^2} \right\} \quad (2.23)$$

Eq. 2.22 is similar to Schrödinger equation of a particle in a pocket-like pseudo-potential V_{eff} . This pseudopotential takes into account the refractive index discontinuity at the surface of the sphere and its curvature. This effective-potential method described by Nussenzveig [79] provides good physical conception about the properties of the WGMs which emerge as quasi-bound states of light. The number of peaks in the radial distribution of the field inside the sphere (Fig. 2.1) results into the definition of a radial mode number n . The lowest-lying mode with $n = 1$ is confined close to the bottom of the potential well, i.e. as close as possible to the surface of the sphere, and is expected to happen at the maximum value of the angular momentum which is $l \approx \eta ka = \eta x$. These modes are leaky and light trapped into these modes can escape out of the sphere by tunneling across the potential barrier which extends as far as ηa .

2.2 Resonant Frequencies of a Spherical Cavity

In order to determine the field distribution inside and outside of sphere the boundary conditions for the tangential components of the fields on the surface of the sphere should be

satisfied. Hence, using equations. 2.16 to 2.19 we get

$$\begin{cases} \psi_l(\eta k_0 a) = A_l \psi_l(k_0 a) + B_l \chi_l(k_0 a) \\ P \psi'_l(\eta k_0 a) = A_l \psi'_l(k_0 a) + B_l \chi'_l(k_0 a) \end{cases} \quad (2.24)$$

where for TE polarization $P = \eta$ and for TM polarization $P = 1/\eta$. To find the exact solutions for Eq. 2.24, determination of constants A_l and B_l results in complex frequency values. The radiative leakage of the energy is rather small for the resonators with diameters very larger than λ . Hence, as a good approximation we can assume that the radiative part of field outside the sphere is negligible; so the resonance condition can be found as the following

$$P \frac{\psi'_l(\eta x)}{\psi_l(\eta x)} = \frac{\chi'_l(x)}{\chi_l(x)} \quad (2.25)$$

where $x = 2\pi a/\lambda$ is the size parameter. And by transforming the spherical Bessel and Neumann functions hidden in Eq. 2.25 to there cylindrical counterparts we obtain

$$P \frac{J'_\nu(\eta x)}{J_\nu(\eta x)} = \frac{N'_\nu(x)}{N_\nu(x)} \quad (2.26)$$

where $\nu = l + 1/2$. Eq. 2.26 is called characteristic equation and in fact it determines the relation between the wave number k and radius of the sphere a . The roots of this equation build an infinite set of wave vectors (eigenfrequencies) for a given radius of the sphere which lead to introduction of radial mode number n . In general if the sphere (with refractive index $\eta = \eta_1$) is located inside another medium with a refractive index different than the refractive index of vacuum, η_2 , P is defined as

$$P = \begin{cases} \frac{\eta_1}{\eta_2} & \text{for } TE \\ \frac{\eta_2}{\eta_1} & \text{for } TM \end{cases} \quad (2.27)$$

In general the roots of characteristic equation, Eq. 2.26, should be found numerically. In order to obtain analytical expressions for the resonance positions Lam et al. [80] used an asymptotic expansion of the Bessel and Neumann functions for $\nu \gg 1$ and they found an analytical approximation for the position of modes as the following:

$$\begin{aligned} \eta_1 x_{n,l} = & \nu + 2^{-1/3} \alpha_n \nu^{1/3} - \frac{P}{((\frac{\eta_1}{\eta_2})^2 - 1)^{1/2}} + \left(\frac{3}{10} 2^{-2/3} \right) \alpha_n^2 \nu^{-1/3} \\ & - \frac{2^{-1/3} P \left((\frac{\eta_1}{\eta_2})^2 - 2P^2/3 \right)}{\left((\frac{\eta_1}{\eta_2})^2 - 1 \right)^{3/2}} \alpha_n \nu^{-2/3} + O(\nu^{-1}) \end{aligned} \quad (2.28)$$

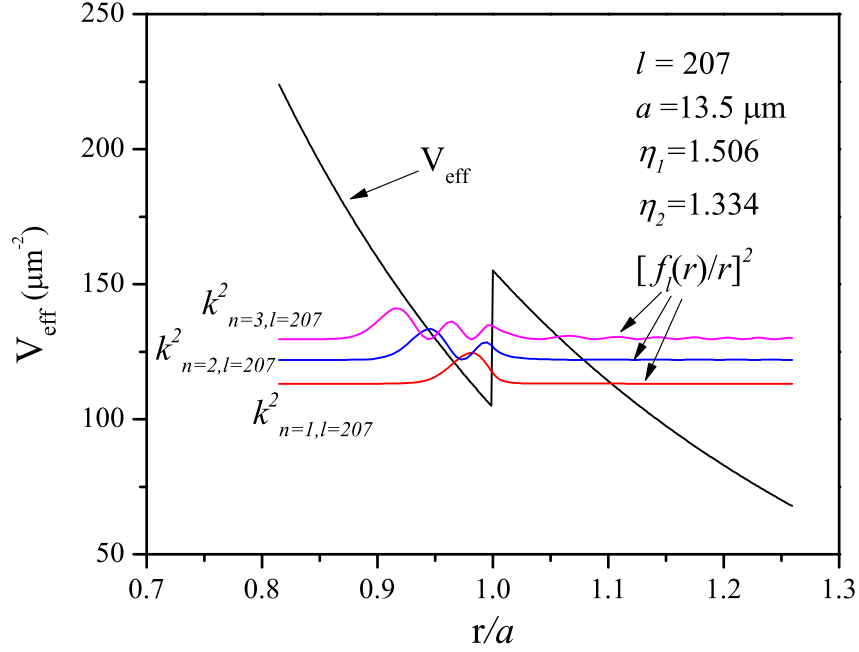


Figure 2.1: Effective optical potential and radial distribution of field intensity for an immersion oil emulsion microdroplet shown in Fig. 3.2 with radius $a = 13.5 \mu\text{m}$ and refractive index of $\eta_1 = 1.506$ surrounded by water with refractive index of $\eta_2 = 1.334$

where α_n 's are the roots of Airy function. The index n for the roots of Airy function shows the radial mode number in the sphere so that the $n = 1$ is related to the closest radial mode to the surface of the droplet. We will use Eq. 2.28 later for some other applications.

2.3 A Discussion on Optical Size Parameter

In Eq. 2.22 where the effective optical potential defined by Eq. 2.23, the effective optical energy also can be defined by $E_{\text{eff}} = k^2$. The effective potential describes the light behavior inside the dielectric microsphere. Its first term is negative and leads to dielectric confinement of light, while the second term is a centripetal repulsive term. The sum of these two terms builds a potential well in which photons can be confined. In Fig. 2.1 we have plotted the effective potential for an oil emulsion droplet in water with radius $a = 13.5 \mu\text{m}$ (see Fig. 3.2) with the central lasing peak at 616 nm, $l = 207$, $\eta_1 = 1.506$, $\eta_2 = 1.334$, and $k_0 = 10.2 \mu\text{m}^{-1}$.

By changing the independent variable in Eq. 2.22 from r to $k_0 r$, we can create a di-

dimensionless length parameter which at the surface of sphere ($x = k_0 a$) is known as optical size parameter. For given refractive indices η_1 and η_2 , the optical size parameter identifies dimensionless resonance frequencies that are independent of droplet radius. Hence, for a droplet with a constant radius, we can determine series of resonance wave numbers or wavelengths that have identities of radial quantum number, n , and angular momentum quantum number, l . The azimuthal quantum number does not appear in the optical size because in a perfect sphere, azimuthal modes are degenerate and their wavelengths are the same.

In Fig. 2.1 the bounded states of potential well exist just for a limited range of effective energy that determines the limits of allowed optical size parameter for a droplet. Consequently the limited number of resonance modes can be trapped inside this potential well. The lower limit of the effective energy to have bounded states is the bottom of potential well when we approach from inside of the droplet to its surface i.e. $V_{\text{eff}}(r \rightarrow a^-; \eta = \eta_1) = k_0^2$ that results in $(k_0^2)_{\text{min}} = l(l+1)/(a^2 \eta_1^2)$ or $(k_0 a)_{\text{min}} = \sqrt{l(l+1)}/\eta_1$ and also the upper limit to have bounded states in the well is the summit of potential when we approach from outside of the droplet to its surface i.e. $V_{\text{eff}}(r \rightarrow a^+; \eta = \eta_2) = k_0^2$ that results in $(k_0^2)_{\text{max}} = l(l+1)/(a^2 \eta_2^2)$ or $(k_0 a)_{\text{max}} = \sqrt{l(l+1)}/\eta_2$. So the confinement condition for optical sizes to have bounded states (i.e. resonance frequencies) is:

$$\frac{\sqrt{l(l+1)}}{\eta_1} < k_0 a < \frac{\sqrt{l(l+1)}}{\eta_2} \quad (2.29)$$

For very large l values Eq. 2.29 can be approximated by:

$$\frac{l+1/2}{\eta_1} < x < \frac{l+1/2}{\eta_2} \quad (2.30)$$

For example the possible range of values for x for the oil droplet shown in Fig. 3.2 is $137.78 < x < 155.55$. Since the electromagnetic wave functions can penetrate into the classically forbidden region the real resonance positions in optical size parameter will never be at the exact top or bottom of this range. Physically, l is the number of wavelengths that fit the resonant light path near the internal sphere surface so that the wave returns in phase to build standing WGMs. On the other hand the optical size is the droplet circumference divided by the free space wavelength, and therefore it will not be an integer. For example in Fig. 2.1, the radial field intensity distribution for three of the lowest order radial mode numbers with fixed angular momentum number and TE polarization are shown; their approximate optical size parameters were found using Eq. 2.28 and these values were used to obtain more precise

values using an appropriate root finder in MATLAB. The numerically calculated values are $x_{n=1,l=207} = 143.6137$, $x_{n=2,l=207} = 149.1083$, and $x_{n=3,l=207} = 153.7182$, respectively.

2.4 Quality Factor

Optical modes in a whispering gallery resonator are inherently dissipative due to a mechanism similar to quantum tunneling. Strictly speaking, total internal reflection does not take place at a curved boundary between two distinct media, and light inside a whispering gallery resonator cannot be totally trapped, even with theoretically ideal conditions. Such a loss channel has been known in fiber optics waveguide theory as tunneling ray attenuation [81].

The Q-factor of a resonator is proportional to the decay time of the waves. The decay time itself is inversely proportional to both the surface scattering rate and the wave absorption in the resonance medium.

As we know a freely decaying mode loses energy exponentially. The quality factor Q is defined as the ratio of total energy over its loss in one angular cycle:

$$Q = 2\pi \frac{\text{stored energy}}{\text{dissipated energy per cycle}} = \frac{\omega}{\Delta\omega} = \omega\tau \quad (2.31)$$

where ω , $\Delta\omega$, and τ are resonance frequency, linewidth (FWHM) and cavity decay time associated with the considered resonance, respectively.

For an isolated resonator that is not coupled to any other waveguide or nearby object, we can identify four independent contributions to its intrinsic factor Q_0 :

$$Q_0^{-1} = Q_{rad}^{-1} + Q_{mat}^{-1} + Q_{cont}^{-1} + Q_{s.s}^{-1} \quad (2.32)$$

The first term Q_{rad} denotes radiative losses that is due to the surface curvature and corresponds to the escape of energy through the potential barrier. As we found out in the previous section the roots of the resonance equation are complex values. From the theory of simple lossy harmonic resonators it can be shown that the radiative Q-factor of the resonance modes are half of the ratio of the real to imaginary parts of the resonance size parameters found as the poles of Eq. 2.26 [13]:

$$Q_{rad} = -\frac{\text{Re}[x]}{2\text{Im}[x]} \quad (2.33)$$

Relying on Eq. 2.26 for the resonance poles is possible but not physically informative. As an alternative analytical method, Treussart, using a semi-classical (WKB) approximation

for the Riccati-Bessel radial solutions, found an expression for Q_{rad} as the following [82]:

$$(Q_{rad})_{\text{WKB}} \approx xe^{2\nu \left[-\sqrt{1 - \left(\frac{x}{\nu}\right)^2} + \text{argcosh}\left(\frac{\nu}{x}\right) \right]} \quad (2.34)$$

In another approach Khoshsima used tunneling probability assuming the resonator as a photonic atom to find a slightly different expression for Q_{rad} [83]:

$$(Q_{rad})_{\text{tunneling}} = 2\eta_1 [(\eta_1 x)^2 - L^2]^{\frac{1}{2}} e^{-2[L^2 - (\eta_2 x)^2]^{\frac{1}{2}}} \left[\frac{L + [L^2 - (\eta_2 x)^2]^{\frac{1}{2}}}{\eta_2 x} \right]^{2L} \quad (2.35)$$

where $L = \sqrt{l(l+1)}$.

Using Eq. 2.28 in Eqs. 2.34 or 2.35 we can develop an expression for Q_{rad} of TE and TM modes in terms of the radial order n . This approximation shows that Q_{rad} decreases with increasing n . Furthermore for the fixed mode numbers, the Q-factor associated with TE polarization is slightly higher than Q-factor of TM polarization. Also Q_{rad} increases exponentially with increasing droplet diameter D so that for $D/\lambda > 15$, $Q_{rad} > 10^{11}$.

Q_{mat} is due to the absorption and bulk Rayleigh scattering in the microresonator material that can be approximated by [13]

$$Q_{mat} \approx \frac{2\pi\eta_1}{\gamma_1\lambda} \quad (2.36)$$

where γ_1 is the attenuation constant in m^{-1} . For example for water droplets in air and in the visible spectrum, γ_1 increases monotonously from 0.06 m^{-1} in $\lambda = 400 \text{ nm}$ to 2 m^{-1} in $\lambda = 800 \text{ nm}$ [84] that corresponds to $Q_{mat} = 3.6 \times 10^8$ to 5×10^6 .

Q_{cont} is due to the losses that are produced by the interaction of the evanescent field of the mode with the environmental contamination. In fact the absorption of the surrounding medium limits the measured Q-factor. In the case of glass microspheres, it has been shown that ultimate Q-factor of a freshly made microsphere is around 10^{11} that degrades by time to 10^9 due to the water adsorption [85]. In case of droplets covered by another medium, Q_{cont} can be calculated by [83]:

$$Q_{cont} \approx \frac{2\pi\eta_2}{\gamma_2\lambda f_{me}} \quad (2.37)$$

where f_{me} is the fraction of the mode energy outside of the sphere (i.e. in the evanescent field) and γ_2 is the attenuation constant for the surrounding medium.

$Q_{s,s}$ is associated with scattering losses due to the residual surface inhomogeneities. Calculations based on the model of Rayleigh scattering by molecular-sized surface clusters [86]

under grazing incidence and total internal reflection results in the following approximation [85]:

$$Q_{s.s} \approx \frac{\lambda^2 D}{2\pi^2 \sigma^2 B} \quad (2.38)$$

where σ and B are the RMS size and the correlation length of inhomogeneities. If we assume that the magnitudes of σ and B for liquid droplets are similar to the numerical values reported for glass surfaces with $\sigma \approx 0.3$ nm and $B \approx 3$ nm, the $Q_{s.s}$ for glass sphere with diameter around $20\mu\text{m}$ in visible range will be around $Q_{s.s} = 10^7$. In the case of droplets, thermally induced capillary ripples and also molecular discreteness may cause the surface roughness in the liquid-air or liquid-liquid interfaces.

2.5 Optical Forces at Dielectric Interfaces

In the ray-optics picture of electromagnetic waves, propagating waves can be treated as a bundle of individual rays that are like localized canals of light power and each of these rays has appropriate direction, intensity and polarization state. In this ray-optics picture each ray propagating in a straight line can lose its energy by absorption or scattering during the propagation or it can refract, reflect or change its polarization at the interfaces with other media. The power of each ray is

$$d\mathbf{P} = \langle I(\mathbf{r}) \rangle d\mathbf{S} \quad (2.39)$$

where $\langle I(\mathbf{r}) \rangle$ is the time averaged intensity of light ray at point \mathbf{r} and $d\mathbf{S}$ is the surface element vector of ray canal in the ray direction. The time average intensity can be rendered as time averaged Poynting vector $\langle I(\mathbf{r}) \rangle = \frac{1}{2} \epsilon_0 c E^2$ where E is the amplitude of the electric field. In Eq. 2.39, we showed the ray power as a vector in the direction of energy flow perpendicular to the surface element whereas the power is a scalar parameter and this representation is merely to simplify the notations. The rate of transported linear momentum for a ray propagating in a medium with refractive index η is given by [87]

$$d\mathbf{F} = \frac{\eta}{c} d\mathbf{P} = \frac{\eta}{c} \langle I(\mathbf{r}) \rangle d\mathbf{S} \quad (2.40)$$

where c is the speed of light in vacuum. In Fig. 2.2(a) the normal incidence and reflection of a ray from a mirror is illustrated. The conservation of momentum leads to a radiation force \mathbf{F} on the mirror if we equalize momentum rate before and after incidence upon the

mirror as the following:

$$\mathbf{F} = \frac{\eta}{c} (\mathbf{P}_i - \mathbf{P}_r) = \frac{\eta}{c} (\langle I_i(\mathbf{r}) \rangle - \langle I_r(\mathbf{r}) \rangle) \mathbf{S} \quad (2.41)$$

where \mathbf{P}_i and \mathbf{P}_r are the total incident and reflected power from the mirror surface S . For a perfect reflector $\mathbf{P}_i = -\mathbf{P}_r$ so that $F = \frac{2\eta}{c} P_i$. As an example for incident power light of 1 W in vacuum, the force is 6.7 nN, which is very tiny and was almost useless before invention of the laser. A laser beam in contrast to the incoherent light sources can be focused onto a small particle with 1 μm diameter. For example for a cube of 10 μm side length with density of 1 g/cm^3 due to the small mass of the particle, the radiation force of a 1 W laser is around 700 times larger than the particle weight, therefore optical force can induce a tremendous acceleration on the particle.

2.6 Optical Stretching of Deformable Dielectric Objects

The behavior of optical forces at the interface of transparent materials is a little bit different. As depicted in Fig. 2.2(b) the momentum conservation for the first interface between an object and its surrounding medium assuming $R = \left(\frac{\eta_2 - \eta_1}{\eta_2 + \eta_1} \right)^2$ as the Fresnel reflection coefficient for the normal incidence of light is

$$\mathbf{F}_1 = \frac{1}{c} (\eta_2 \mathbf{P}_{i1} - \eta_2 \mathbf{P}_{r1} - \eta_1 \mathbf{P}_{t1}) \quad (2.42)$$

which we can rewrite in the scalar form as

$$\begin{aligned} F_1 &= \frac{1}{c} (\eta_2 P_{i1} + \eta_2 P_{r1} - \eta_1 P_{t1}) \\ &= \frac{1}{c} [\eta_2(1 + R) - \eta_1(1 - R)] P_{i1} \\ &= \frac{2\eta_2}{c} \left[\frac{(\eta_2 - \eta_1)}{(\eta_2 + \eta_1)} \right] P_{i1} \end{aligned} \quad (2.43)$$

In Eq. 2.43 if the refractive index of the object is higher than the refractive index of its surrounding medium (i.e. $\eta_2 < \eta_1$ as it is assumed in Fig. 2.2(b)) the optical force \mathbf{F}_1 will be negative which means the force pulls the interface toward the incident beam, against the direction of light propagation. The optical force \mathbf{F}_2 at the second interface where the light travels from a higher refractive index medium to a lower one is

$$F_2 = \frac{2\eta_1}{c} \left[\frac{(\eta_1 - \eta_2)}{(\eta_2 + \eta_1)} \right] P_{i2} \quad (2.44)$$

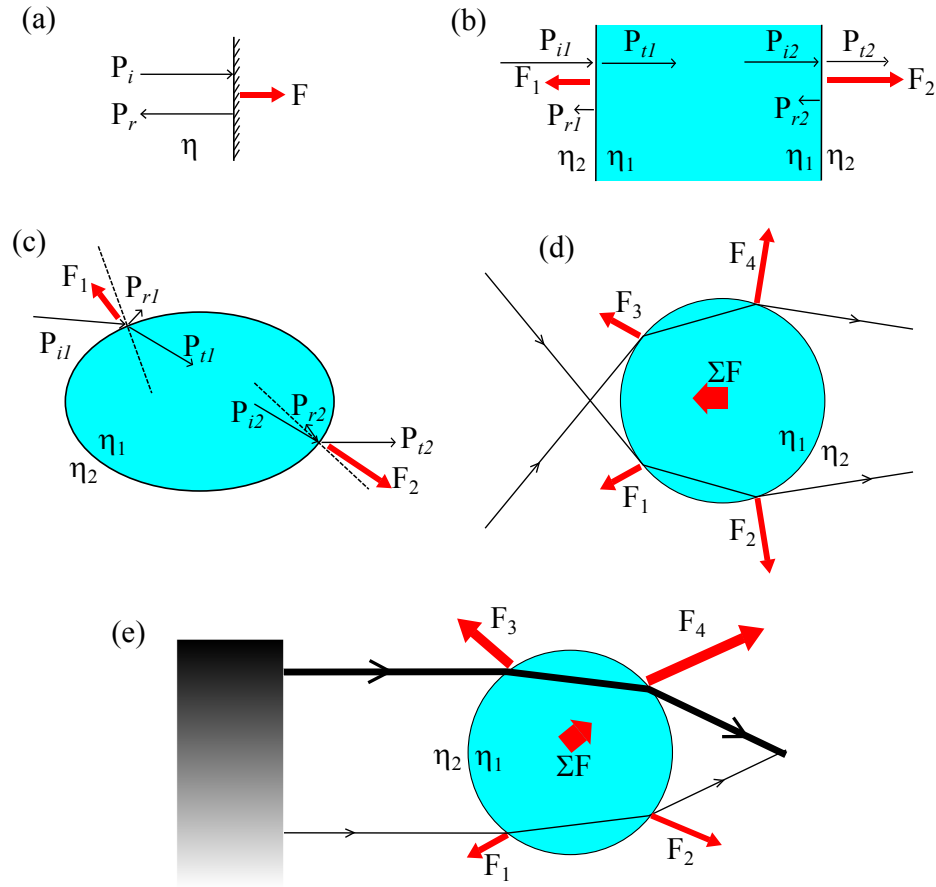


Figure 2.2: (a) Radiation pressure of a plane wave in reflection from a mirror, (b) Stretching and scattering forces of a plane wave in transmission through a dielectric object with refractive index higher than its surrounding medium $\eta_1 > \eta_2$, (c) Consecutive refractions and reflections from the surface of a dielectric object, (d) Optical restoring force by intensity gradient of a tightly focused beam on a sphere in the axial direction, (e) Optical gradient force of a plane wave with vertical gradient intensity on a sphere in the lateral direction.

and it will push the interface in the light propagation direction. This means that a transparent object with a refractive index higher than its surrounding medium will always experience a stretching force. This is the basic of an optical stretcher that we used as a tool to stretch the emulsion droplets in chapter 4. For normal incidence of plane waves upon a planar surface as shown in Fig. 2.2(b), it can be shown with some mathematical operations that for the positive values of refractive indices, always $|F_1| < |F_2|$, so that the total net force on the object is a pushing (scattering) force that pushes the object in the light propagation direction. In order to cancel out this scattering forces, in building up an optical stretcher

two symmetric counter-propagating beam are used to fix the microparticle position.

The light rays incident upon a microparticle with an arbitrary shape refract and change their direction according to the Snell's law and follow several other sequential refraction or total internal reflection to lose their energy to zero (see Fig. 2.2(c)). This process can be done automatically by finding direction and position of a ray at each refraction or reflection in 3D coordinate using a recursive computer code and one can use such a 3D ray-tracing to calculate the distribution of the forces on the surface of the object. We used this method to calculate the amount of forces acting on the left and right side of an ellipsoidal object between two counter-propagating Gaussian beam to find the stretching forces in chapter 4.

2.7 Optical Tweezers

The basics of optical tweezers or optical trapping by a single beam can be understood by Fig. 2.2(d) and (e). In Fig. 2.2(d) the mechanism of canceling out of the scattering forces in axial direction using a tightly focused beam is depicted. Here \mathbf{F}_1 and \mathbf{F}_3 are the forces that emerge from the first refraction of two tightly focused rays from the front surface of the object and \mathbf{F}_2 and \mathbf{F}_4 are the forces that emerge from the second refraction of transmitted rays from the rear surface of the object. When the object is slightly out of the focal point, the sum of the optical forces on the particle can cancel out the scattering forces and build a restoring force and hold the particle in the trap in the axial direction. In Fig. 2.2(e) the mechanism of optical trapping in transversal direction using a light intensity gradient in transversal direction is demonstrated. This transversal gradient is a representation of intensity gradient in half of a Gaussian beam wave front. Here \mathbf{F}_1 and \mathbf{F}_3 are the forces that come out of first refraction from the front surface of object and \mathbf{F}_2 and \mathbf{F}_4 are the forces that come out of the refraction of transmitted light in the rear surface of the object. In this figure the directions of \mathbf{F}_1 with \mathbf{F}_3 and \mathbf{F}_2 with \mathbf{F}_4 are symmetric relative to the horizontal axis crossing the center of object. However, sum of these forces takes a component toward the higher intensity region of the beam. Similar effect happens for a particle in a highly focused beam; when the particle tries to move out of the focused beam, the force resulting from intensity gradient pulls back the particle to the beam axis-the location of the highest optical intensity- and builds the lateral part of the trap.

Chapter 3

LASING FROM OPTICALLY MANIPULATED MICRODROPLETS

In this chapter we demonstrate lasing in dye-doped immersion oil microdroplets emulsified in water and glycerol-water aerosol microdroplets that are manipulated by a single beam optical trap. We show that the laser emission spectrum can be tuned by changing the dye concentration and the droplet size. The presented optically manipulated fluidic microlasers are disposable and can be easily combined with microfluidic chip technology. This makes them especially attractive for on-chip applications in chemical and biological analysis and sensing.

3.1 Experimental Setup

Experimental setup for the observation of lasing from optically trapped emulsion and aerosol microdroplets is shown in Figure 3.1. A continuous wave solid state infrared laser with 1064 nm wavelength and 300 mW maximum power (CrystaLaser) was used for microdroplet trapping. This laser was sent through a beam expander and reflected from two dichroic mirrors D1, D2 before being focused into the sample chamber by a water immersion microscope objective (Nikon, NA=1.2, 60x). In order to change the position of the optical trap in the objective focal plane, the first lens of the beam expander could be steered in x and y directions (perpendicular to the beam axis). The overall transmission of all optical elements in the trapping beam path was measured to be about 20%, resulting in the average trapping power of ~ 60 mW at the specimen. For the emulsion immersion oil droplets we used the full power of the trapping laser beam available at the specimen. However, for aerosol droplets the full trapping power resulted in multiple droplet trapping in a ring shaped trap because of optical binding effects. Thus, based on similar experiments by Mc Gloin [33], the power of the trapping beam was attenuated to 3.5 mW at the focus of the microscope objective for stable single particle on-axis trapping of aerosols with diameters ranging between 5-10 μm .

Fluorescently-stained trapped droplets were pumped with a 532 nm green beam obtained

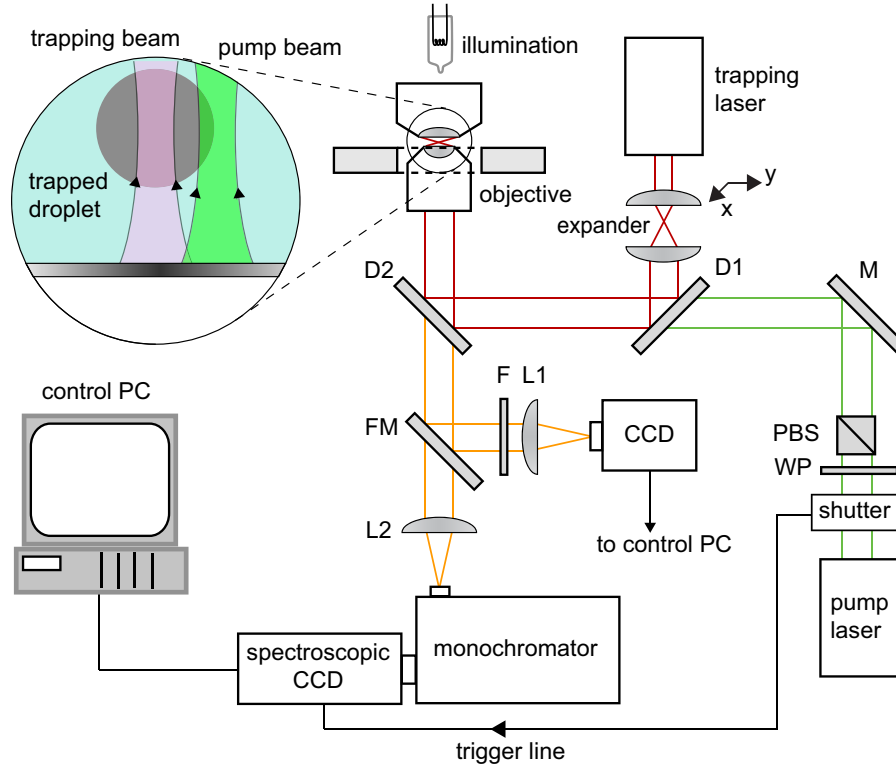


Figure 3.1: Experimental setup for microdroplet lasing studies. The inset shows the detail of an optically trapped droplet with the pump laser beam positioned on the droplet rim. D1, D2 - dichroic mirrors, F - band-pass filter, FM - flippable mirror, L1, L2 - lenses, M - mirror, PBS - polarizing beam splitter, WP - lambda-half wave plate.

after second harmonic generation from a home-built passively Q-switched Nd – YVO₄ laser beam (20 ns pulse width and 33 kHz repetition rate). The pump laser was focused by the same microscope objective as the trapping laser, after being transmitted through the dichroic mirror D1 and reflected from the dichroic mirror D2. Before the experiments, the droplet position was adjusted by moving the optical trap in the focal plane so that the focal spot of the pump laser lied near the droplet's rim for the maximal efficiency of the WGM excitation. Fluorescence from a trapped microdroplet was collected using the same microscope objective as used for focusing the trapping and pump beams, and dispersed by a monochromator (focal length 500 mm; Acton Research) on the chip of a cooled CCD detector (Pixis 100; Princeton Instruments). In order to prevent fast photobleaching of dye molecules in the droplet, a shutter was added to the pump laser beam path; this shutter was only opened during the spectrum acquisition time and provided trigger signal for the

spectroscopic detector to synchronize the data recording. The light in the imaging path of the microscope could be diverted to an ordinary CCD camera via a flippable mirror to observe the sample.

3.2 Lasing from Optically Manipulated Emulsion Droplets

3.2.1 Materials and Methods

The emulsion system selected for our study consisted of microdroplets of dye-doped microscope immersion oil ($\eta = 1.515$, $\rho = 1.02 \text{ g/cm}^3$, Merck) dispersed in deionized water ($\eta = 1.334$, $\rho = 1.00 \text{ g/cm}^3$). This emulsion system of virtually immiscible liquids provides a high refractive index contrast together with a low density contrast between the droplet and the surrounding medium. This implies a good confinement of WGMs inside the trapped microdroplet, strong optical trapping force, and a small buoyancy that further facilitates the optical trapping of the droplets. In addition, hydrophobic nature of the immersion oil also prevents sticking of the microdroplets to the surfaces of regular cover glasses that were used to make the sample chamber. The dye DiI(3) (1,1'-Dioctadecyl-3,3,3',3'-tetramethylindo carbocyanine perchlorate, Sigma Aldrich) that has a hydrophilic chromophore and hydrophobic side chains was selected as the laser active medium. This dye has its excitation peak at $\sim 560 \text{ nm}$ and emission peak at $\sim 575 \text{ nm}$ (see also Fig. 3.5), and is well suited for the efficient excitation of the WGMs due to its surfactant nature that ensures its localization at the oil-water interface where WGMs also reside [88]. In our experiments DiI(3) was dissolved in chloroform with different concentrations and the dye solution was subsequently added to the immersion oil in 1 to 9 ratio. Final concentration of the dye in the droplets ranged from 0.1 to 1 mM. Addition of chloroform (refractive index 1.444) to the droplet liquid caused a small decrease of the droplet refractive index to the value of 1.506. Microdroplets were obtained by mixing the dye-doped immersion oil with water in 1 to 50 ratio, and shaking the obtained mixture by hand. Droplets produced this way had a large size distribution with diameters ranging from < 1 up to $\sim 100 \text{ }\mu\text{m}$ and the emulsions were stable over ~ 10 hours. Prepared emulsions were subsequently loaded into a small capillary container made of two cover glasses attached to each other by double-sided tape. After loading, microdroplets were observed to float freely within the capillary container, thanks to their small buoyancy. The droplets did not stick to the walls of the sample

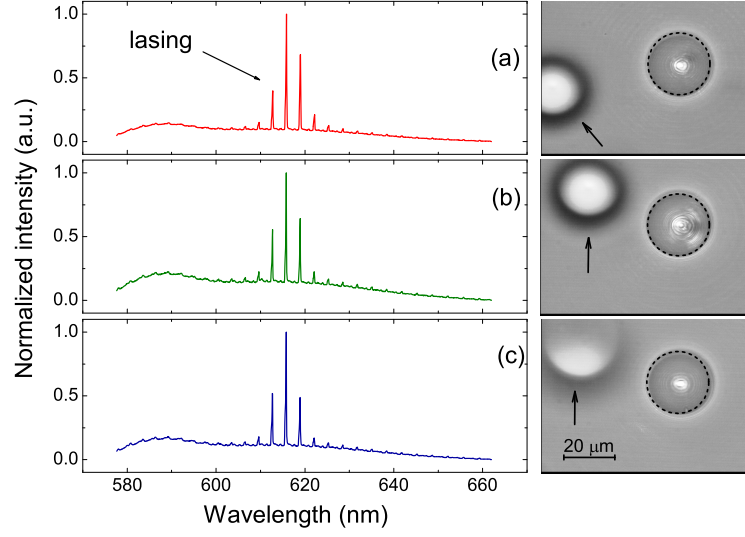


Figure 3.2: Laser emission spectra from an optically manipulated emulsion droplet (diameter $27 \mu\text{m}$; denoted by a dashed circle). Arrows indicate a stationary reference droplet resting on the bottom surface of the sample chamber. The trapped droplet is first translated in the plane of the figure between (a)-(b) and subsequently out of the figure plane between (b)-(c).

chamber and could be readily trapped in all three dimensions.

The radius a of the trapped droplets was calculated from the measured WGM spacing $\Delta\lambda$, mean lasing wavelength λ , and known refractive indices of the droplet ($\eta_1 = 1.506$) and host ($\eta_2 = 1.334$) liquids, using the asymptotic formula of Chylek *et al.* [89]:

$$a = \frac{\lambda^2}{2\pi\eta_2\Delta\lambda} \frac{\arctan([\eta_1/\eta_2]^2 - 1)^{1/2}}{[\eta_1/\eta_2]^2 - 1)^{1/2}}. \quad (3.1)$$

All droplet sizes presented in the following sections were determined from Eq. 3.1.

3.2.2 Results and Discussions

Figure 3.2 illustrates lasing from an optically trapped and manipulated droplet. In this figure, emission spectra and corresponding images of a $27 \mu\text{m}$ diameter droplet with 1 mM dye concentration are presented for different positions of the trapped droplet with respect to the sample chamber. All spectra are normalized by the same reference value - the overall maximum of emission intensity recorded at different droplet positions. Mean power of the pump beam used for recording the spectra was 1 mW (well above the lasing threshold - see below) and the data was acquired over the total trapping time of 10 min. A group of WGMs

with large intensities centered at around 615 nm can be observed in the fluorescence spectra recorded at various droplet positions; these are the WGMs that exhibit lasing. Spectral region of droplet lasing is shifted from the emission maximum of the bulk dye solution at ~ 575 nm towards the red end of the fluorescence spectrum to the location of the secondary emission peak of the dye (see Fig. 3.5). Here, the overall gain of the active medium given by an interplay between the spectral profile of the dye emission and the attenuation due to the dye self-absorption reaches maximum.

In order to demonstrate the stability of optical confinement, sample chamber was translated past the trapped lasing droplet. Since the droplet was confined on the axis of a stationary trapping beam, its position in the field of view was fixed. Consequently, its displacement with respect to the sample chamber could be inferred from the image of a reference droplet resting on the sample chamber surface. In Figs. 3.2(a) and 3.2(b), the trapped droplet is located approximately in contact with the bottom surface of the sample chamber while its transversal position along the surface changes. In Fig. 3.2(c), the trapped droplet is lifted ~ 50 μm above its location in Fig. 3.2(b), as indicated by defocusing of the reference droplet image. Comparison of the spectra corresponding to successive positions of the droplet in the sample chamber shows that the lasing modes are located at exactly the same wavelengths for all studied droplet positions. This implies that no change is observed in the size or the refractive index of the microdroplet over the whole duration of its manipulation.

In general, lasing can be observed only if the net gain of the active medium is larger than the cavity losses, which requires sufficiently high pumping. In order to determine the threshold pump power necessary for the droplet lasing, we analyzed a series of emission spectra recorded from a single optically trapped droplet with gradually increasing pump power. In Figure 3.3, the results of quantitative analysis of such spectral series acquired from a 31 μm diameter droplet with 1 mM dye concentration are presented. Here, the intensities of both a lasing WGM at 620 nm and non-resonant fluorescence background in the immediate vicinity of the lasing WGM are shown as a function of the pump power. As illustrated by the graph, the intensities of the lasing WGM and the background grow with a different slope once the threshold pump power is exceeded which is indicative of the lasing onset. The value of the threshold pump power was estimated from the intersection

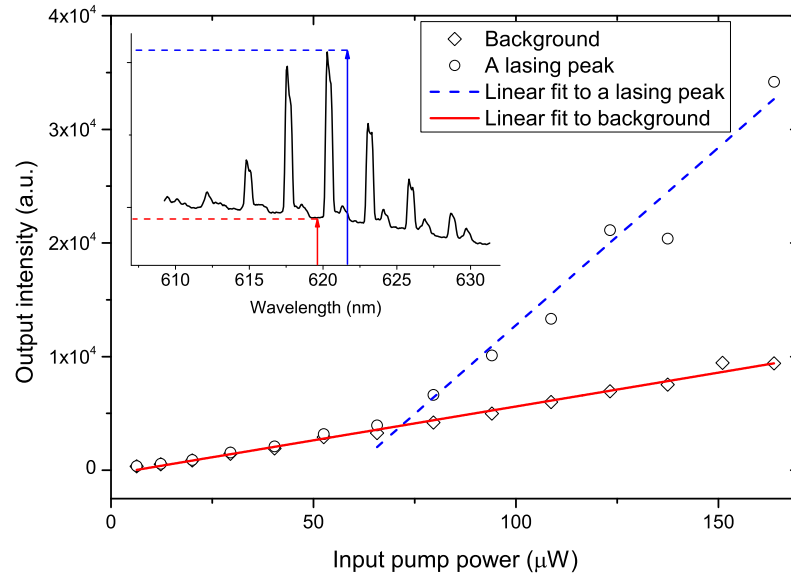


Figure 3.3: Dependence of the droplet emission intensity on the input pump power. Intensities of both a lasing mode at ~ 620 nm and non-resonant fluorescence background in the immediate vicinity of the mode are shown. Inset identifies respective spectral locations for the measured intensity values. Droplet diameter for this measurement was $31 \mu\text{m}$.

of line fits to the background and lasing peak intensities, respectively. For the presented case, lasing threshold was around $70 \mu\text{W}$, measured in the sample plane. It should be mentioned that due to the very short exposure time for each spectrum in the series (5 ms), the influence of photobleaching on the measured emission intensities could be neglected; this is confirmed by the linear growth of background emission intensity over the whole range of the studied pump powers. Lasing threshold was investigated for different sizes of droplets. As an example, for droplets with 26 and $40 \mu\text{m}$ diameters, threshold power of ~ 140 and $\sim 35 \mu\text{W}$ was measured, respectively. The lower threshold power required for lasing in larger droplets can be attributed to their higher Q-factors [45].

Overall shape of the microdroplet lasing spectra depends on the absorption and emission profiles of the used dye, the concentration of the dye in the droplet, and the droplet size [45]. In order to elucidate the influence of these parameters on the droplet emission spectra, we carried out experiments with microdroplets of different sizes doped with different dye concentrations. The results of these experiments are summarized in Fig. 3.4 which reveals concentration- and size-dependent tuning of the average lasing wavelength. For the sake of

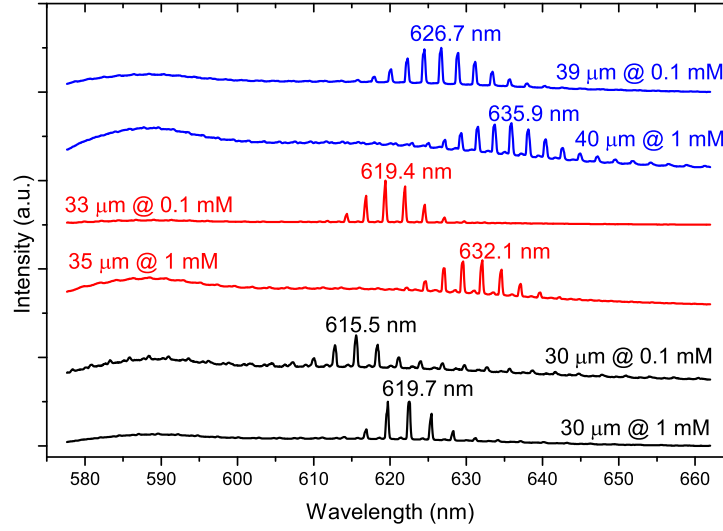


Figure 3.4: Dependence of the lasing wavelength on the droplet size and the dye concentration inside the droplet. Tags of individual spectra provide the droplet size, the dye concentration, and the wavelength of the most intense lasing peak. For both studied dye concentrations, droplets of approximately equal size were analyzed (see color coding of the spectra). Average pump power and exposure time for each frame in this measurement were 0.7 mW and 6 ms, respectively.

clarity wavelength of the most intense lasing peak is given for each spectrum. In Fig. 3.4, pairs of spectra acquired from droplets of approximately equal sizes and dye concentrations differing by a factor of 10 are presented. Comparison of the spectra within each pair shows that the position of the most intense lasing peak is shifted to longer wavelengths for higher dye concentration. Such concentration-dependent shift of the lasing wavelength can be attributed to dye self-absorption. Figure 3.5 shows the normalized absorption and emission spectra of DiI(3) dye dissolved in chloroform/immersion oil mixtures at 1.25 μM and 1 mM concentrations, respectively. Absorption spectrum of the dye was acquired from a dilute dye solution placed in a spectroscopic cuvette. For recording emission spectra, a droplet of size similar to that used in the lasing experiments was pumped with the pulsed green beam the focus of which was placed at the droplet center so that the WGMs were not efficiently excited. Emission spectra were acquired both from a freshly generated droplet and from the same droplet after prolonged exposure to the green beam (400 ms). Prolonged irradiation with the green light caused photobleaching of the dye molecules and, thus, effectively lowered the dye concentration in the droplet (see below). Analysis of the absorption and emission

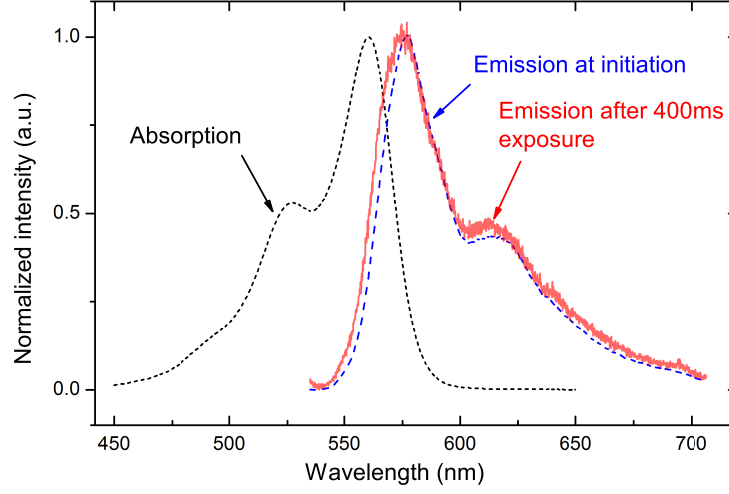


Figure 3.5: Normalized absorption (dotted line) and emission spectra of DiI(3) dye dissolved in immersion oil/chloroform mixture. The emission spectra are shown at two different levels of dye photobleaching (dashed line - initial dye emission, solid line - dye emission after 400 ms exposure with a 532 nm pulsed green laser with $\sim 300 \mu\text{W}$ average power).

spectra of DiI(3) reveals a spectral overlap at wavelengths immediately contiguous to the spectral region where the lasing modes are located. Consequently, part of the light emitted at shorter wavelengths is reabsorbed again by the dye molecules. Self-absorption phenomenon becomes more significant with increasing dye concentration and causes a shift of the effective emission maximum of the dye to the red end of the spectrum [90]. This tendency is clearly illustrated by comparing the emission spectra of a fresh droplet with high dye concentration (dashed line) and a partially photobleached droplet with low dye concentration (solid line). For a constant concentration of the fluorescent dye in the droplet, the position of the most intense lasing peak shifts to shorter wavelengths with decreasing droplet size. This trend can be qualitatively explained by considering the combined effect of the dye gain spectrum $g_0(\lambda)$, the efficiency of out-coupling of light from the droplet $\beta(a, \lambda)$, and the effective cross-section of the lasing WGMs $A(a, \lambda)$. The lasing power $P_{out}(a, \lambda)$ coupled out of the droplet scales as [91]

$$P_{out}(a, \lambda) \sim \frac{A(a, \lambda)}{\lambda^3} g_0(\lambda) \beta(a, \lambda). \quad (3.2)$$

While g_0 is independent of the droplet size, both β and A change with the droplet radius a . As argued by Tang *et al.* in [45], for the studied experimental situation, the maximum of the

product of $\beta(a, \lambda)$ and $A(a, \lambda)/\lambda^3$ shifts to the blue end of the spectrum for smaller droplets. Hence, optimal conditions for droplet lasing at a particular dye concentration that are given by the spectral position of the maximum of Eq. 3.2 occur at shorter wavelengths. When comparing the lasing spectra obtained with different dye concentrations, the sizes of the droplets used in the comparison were not identical. Thus, in principle, both concentration and size variations contributed to the observed differences in the spectral position of the lasing maximum. However, since the relative size differences within the studied droplet pairs were small (less than 6%), the effect of the concentration change was dominant.

Upon prolonged exposure to pump light, dye molecules inside the droplet undergo photobleaching that decreases the effective concentration of absorbing chromophores in the droplet. This in turn leads to changes of the emission spectral profile of the dye. In Fig. 3.5, normalized emission spectra of droplets containing 1 mM DiI(3) solution excited with 532 nm pulsed laser beam with $\sim 300 \mu\text{W}$ average power are presented. These spectra were acquired immediately after the start of the experiment, during the first 5 ms exposure with the green beam (dashed line), and after 400 ms exposure with the green beam when partial photobleaching had taken place (solid line). Lowering of dye concentration due to photobleaching causes a decrease of self-absorption and, thus, an overall blue shift in the observed emission spectrum.

This observation is consistent with Fig. 3.4 where a decrease of the dye concentration causes shift of the lasing emission maximum to the blue end of the spectrum. As a result of the photobleaching process, the droplet emission profile evolves in time. Figure 3.6 illustrates quantitatively the dynamics of photobleaching. The spectra of Fig. 3.6 were recorded from a single droplet of diameter $\sim 34 \mu\text{m}$ with the initial dye concentration 1 mM and the average pump power of 1.8 mW. As expected, the overall intensity of the spectra decreases with increasing frame number (bottom to top). Moreover, as the photobleaching progresses, spectral location of the most intense lasing peak moves to shorter wavelengths; in the presented spectral series, the maximal lasing intensity shifts from peak labeled C to B to A between the 1st, 9th and 19th frame, respectively. This trend is a direct consequence of the blue shift in the overall dye emission spectrum due to photobleaching, as shown in Fig. 3.5. However, while the location of the lasing maximum changes in time, the spectral positions of individual WGMs remain constant. This indicates that the droplet size and refractive index

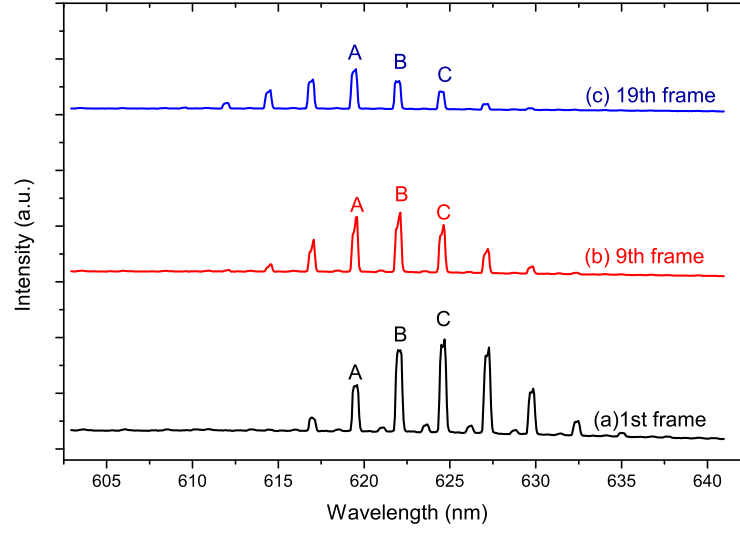


Figure 3.6: Effect of photobleaching on the droplet lasing spectra. 1st, 9th, and 19th frames of spectra acquired from a $\sim 34 \mu\text{m}$ diameter droplet are shown. Average pump power was 1.8 mW and exposure time for each of the frames was 10 ms.

do not change during the experiment. Thus, prolonged confinement of the droplet in the optical trap does not influence its optical parameters; we observed stable WGM structures from droplets that were trapped for up to several hours. It should be mentioned that the bleaching rate at a fixed pump power depends strongly on the droplet size; it is possible to acquire more spectra from bigger droplets before they bleach. For example, with 1 mM dye concentration at 1.8 mW average pump power and 5 ms acquisition time, the droplets with the diameter of $\sim 26 \mu\text{m}$, $\sim 31 \mu\text{m}$, and $\sim 53 \mu\text{m}$ bleach after acquiring 50, 100, and 200 spectral frames, respectively.

3.3 Lasing from Optically Manipulated Aerosol Droplets

3.3.1 Materials and Methods

A compact ultrasonic nebulizer (JIH50; Beuer) was used for generating liquid aerosols out of 39% w/w glycerol/water solution (refractive index $\eta_1 = 1.38$, density $\rho = 1.099 \text{ g/cm}^3$) doped with 1 mM Rhodamine B dye. The nebulizer was attached to a closed glass sample chamber that prevented external air flow from disturbing the stability of the trapped aerosol particles and maintained approximately constant ambient humidity during the experiments.

A cover glass treated with Ar/O₂ plasma was attached at the bottom of the sample chamber. Plasma cleaning of cover glasses ensured a good hydrophilicity of their surface, thus preventing accumulation of large sessile droplets that otherwise disturb the trapping and pump beams focused into the chamber. The trapping and pump beams were focused at the same plane approximately 20 μm above the upper surface of the cover glass that formed the bottom part of the sample chamber. The pump beam spot size was measured that was 9.8 μm in diameter.

During the experiments, initial diameters of the trapped droplets were generally around 5 μm . Larger droplets were then obtained by fusion of the trapped droplets with others that were attracted to the trapping region. Trapped droplet diameters were estimated from microscope images and independently determined from the observed WGM free-spectral range (FSR), mean lasing wavelength $\bar{\lambda}$, and known refractive indices of the droplet ($\eta_1 = 1.38$) and air ($\eta_2 = 1.00$), using Eq. 3.1.

3.3.2 Results and Discussions

Fig. 3.7 shows fluorescence emission spectra recorded from a trapped 9.4 μm diameter glycerol/water aerosol droplet at 12.2 μW , 42.3 μW , and 76.2 μW pump laser powers in (a), (b), and (c), respectively. Non-lasing WGMs of the aerosol particle were observed in Fig. 3.7(a) when the pump power was lower than the lasing threshold. These WGMs are superimposed on a broad non-resonant background emission from the dye-doped thin solution layer formed on the cover glass during the experiment. In general, droplet WGMs can be characterized using radial, azimuthal, and angular mode numbers, and polarization (TE or TM) [45]. The WGMs that belong to the same mode family with identical radial mode number and polarization are indicated in Fig. 3.7(a). Spectral separation between two such consecutive WGMs gives the FSR which is equal to 10.7 nm. In order to observe lasing, the cavity losses must be smaller than the net cavity gain. Pump power and the amount of dye in the aerosol particle are critical to satisfy this condition. As shown in Fig. 3.7(b,c), two WGMs denoted as A and B exhibit lasing around $\lambda = 608$ nm and $\lambda = 618$ nm upon crossing the threshold pump powers of 19 μW and 21 μW . Owing to the very low volatility of glycerol and approximately stabilized relative humidity in the sample chamber, the spectral positions of lasing WGMs display only a minimal drift $\Delta\lambda = 0.06$ nm over the

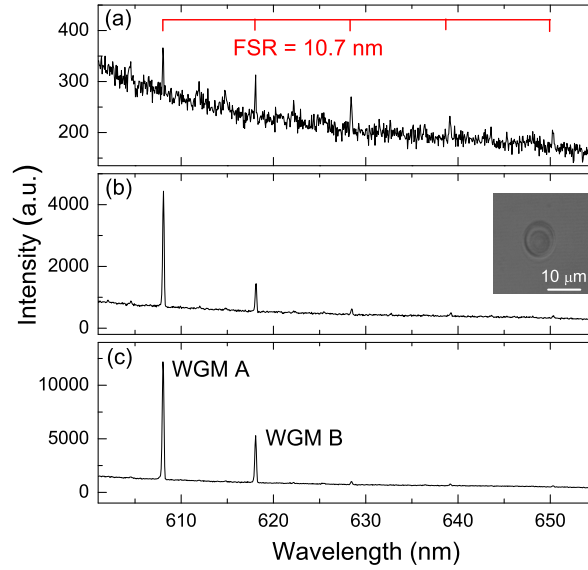


Figure 3.7: Power-dependent emission spectra recorded from a $9.4 \mu\text{m}$ diameter glycerol/water droplet at three different excitation powers: (a) $12.2 \mu\text{W}$, (b) $42.3 \mu\text{W}$, and (c) $76.2 \mu\text{W}$. WGM A and WGM B denote lasing WGMs. Inset: Optical microscope image of the trapped lasing droplet.

total duration of the experiment (2 min). For a droplet with the mean radius $a = 4.7 \mu\text{m}$, this translates into the drift of the droplet radius $\Delta a = \Delta\lambda(a/\lambda) = 0.46 \text{ nm}$. Fig. 3.8 displays the intensities of the lasing WGMs A and B indicated in Fig. 3.7 and non-resonant spectral background in the vicinity of these WGMs as a function of the pump laser power. Both lasing and background intensities were determined from Lorentzian fits to WGMs in a series of emission spectra acquired with gradually increasing pump power. Subsequently, two lines were fitted to the respective lasing and background intensity series and the intersection of the fitted lines provided the lasing threshold powers of $19 \mu\text{W}$ and $21 \mu\text{W}$ for WGM A and WGM B, respectively [43]. As expected, the background intensity increased linearly with the pump power; this also indicated that the photobleaching effects during the acquisition of the power-dependent spectral series could be neglected owing to the short exposure time required for recording individual spectra. When the pump power exceeded the threshold, increase of the intensity of the lasing peak with a higher slope relative to the background emission indicated the onset of lasing. The threshold pump power depends on the size of the trapped aerosol particle and the Q-factor of its WGMs [92]. Large radiative losses in smaller droplets result in an exponential decrease of their WGM Q-factors [93]. This sets a

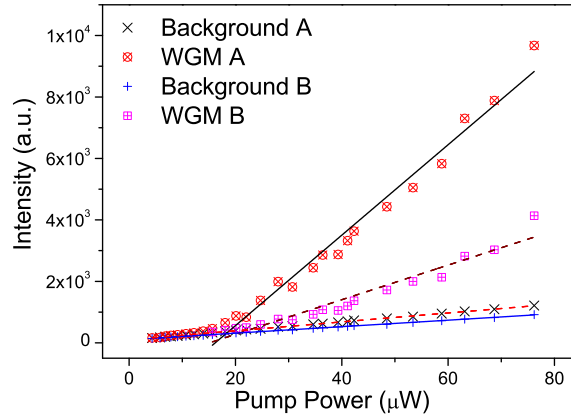


Figure 3.8: Power-dependent intensities of the lasing WGMs and background emissions in a $9.4 \mu\text{m}$ diameter glycerol/water aerosol droplet.

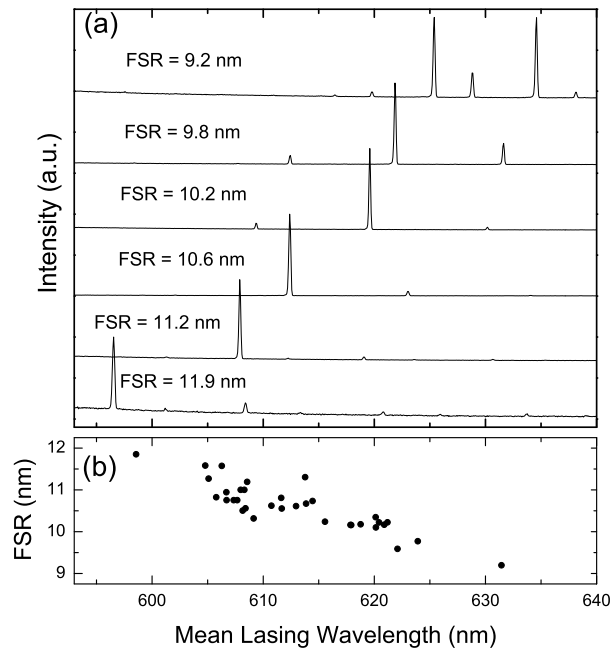


Figure 3.9: (a) Lasing spectra recorded from 6 different aerosols with diameters 7.7 , 8.4 , 9.0 , 9.6 , 10.1 , and $11.0 \mu\text{m}$ (bottom to top) at constant pump laser power of $60 \mu\text{W}$. (b) Free spectral ranges of 34 lasing aerosols as a function of the mean lasing wavelength, $\bar{\lambda}$.

lower limit to the diameter of droplets that display lasing at a given maximal pump power. In our experimental conditions, this lower limit was determined as $7.7 \mu\text{m}$.

With increasing droplet size, spectral position of the emission maximum of lasing aerosols containing constant dye concentration was observed to shift to longer wavelengths. This

trend is illustrated in Fig. 3.9(a) which shows emission spectra of six droplets with different radii recorded at fixed $60 \mu\text{W}$ pump laser power and 3.5 mW trapping laser power. Here, the increasing droplet radius corresponds to the decreasing FSR of the droplet [89]. For the given droplet, spectral location of its overall maximal lasing gain can be quantitatively characterized by the mean lasing wavelength $\bar{\lambda}$ calculated as the intensity-weighted average of the wavelengths of all lasing WGMs from the same mode family observed in the droplet's spectrum. Fig. 3.9(b) summarizes the relationship between $\bar{\lambda}$ and FSR for 34 lasing droplets of varied size. Within the studied range of droplet sizes ($7.7 \mu\text{m}$ to $11.0 \mu\text{m}$), FSR decreased with $\bar{\lambda}$ following an almost linear dependence. A similar spectral shift of the overall lasing gain profile was previously observed in lasing emulsion droplets [45, 43] and explained by the size-dependence of the efficiency of light out-coupling from the droplets and the cross-section of the lasing WGMs.

Chapter 4

SPECTRAL TUNING OF LASING EMISSION FROM DYE-DOPED EMULSION DROPLET LASERS USING OPTICAL STRETCHING

In this chapter, we introduce novel tunable optofluidic dye microlasers that use optical stretching forces for the adjustment of the laser emission wavelength. Our microlasers are based on droplets of immersion oil emulsified in water and confined in a dual-beam optical trap. Since the droplets are stained with a fluorescent dye, they function as active ultrahigh-Q optical resonant cavities that are optically pumped with an independent pulsed green laser. In order to reduce the stretching power required for microlaser tuning, we lower the interfacial tension between the droplets and aqueous host medium to ~ 1 mN/m using a surfactant and sodium chloride. We demonstrate almost reversible spectral tuning of the lasing WGMs with tuning slopes as large as ~ 0.5 nm/W (nm per Watt of the total stretching power). We also show that the direction of wavelength tuning depends on the position of the pump beam focus on the droplet. In addition, we characterize the effects of changes of the droplet and immersion medium temperature on the spectral position of lasing WGMs and show that these thermally induced spectral shifts are caused by simultaneous changes of the droplet size and refractive index of both the droplet and the host medium resulting from the droplet heating by the stretching laser beam.

4.1 *Experimental Setup*

Experimental setup for the observation of tunable lasing from optically trapped and stretched emulsion microdroplets is shown in Fig. 4.1. Studied oil-in-water emulsions were contained within home-made PDMS microfluidic chips featuring a single channel with square cross-section of $160 \times 160 \mu\text{m}^2$. These chips supported two multi-mode optical fibers with $50 \mu\text{m}$ core and $125 \mu\text{m}$ cladding diameters. The faces of the fibers were parallel to the opposite side walls of the channel and their optical axes were precisely aligned to form the dual-beam trap (see inset in Fig. 4.1(a)). The microfluidic channel had one inlet and one outlet with a

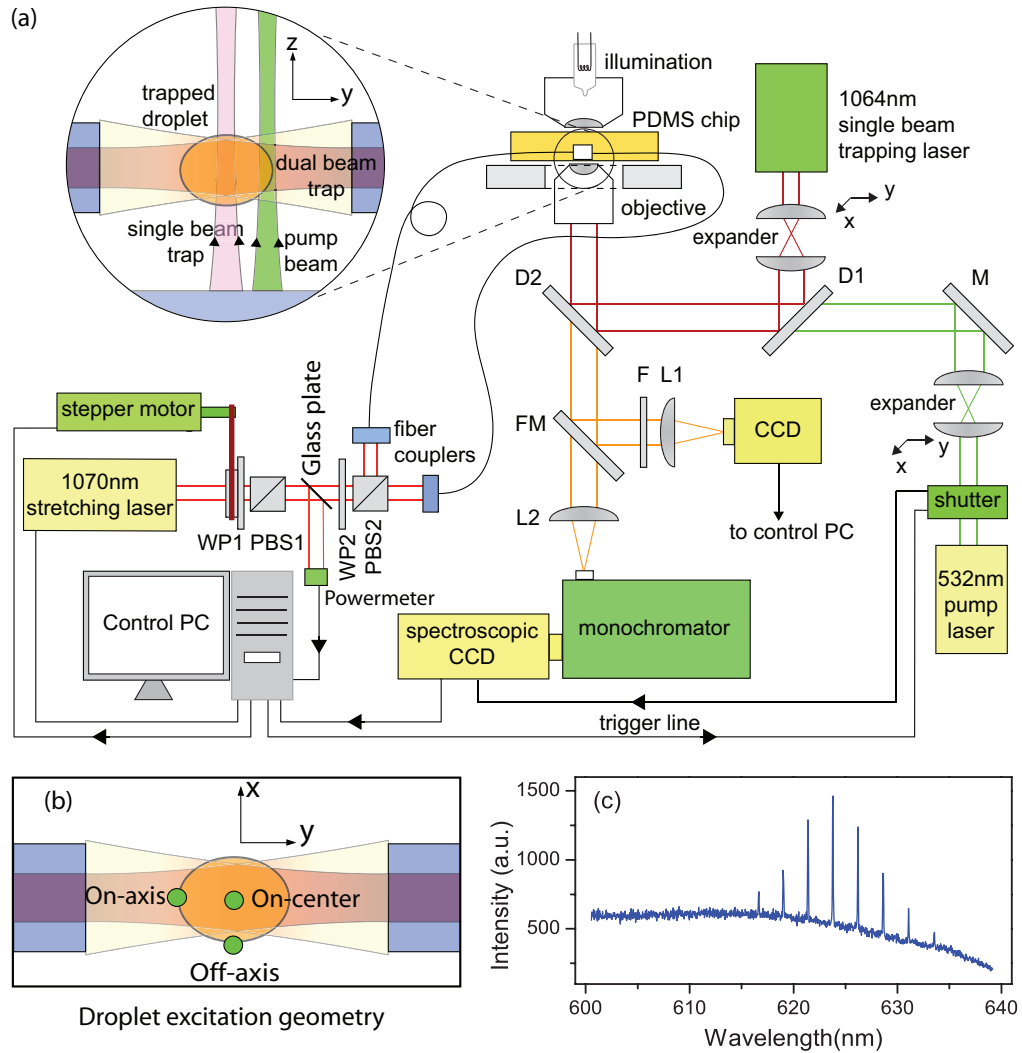


Figure 4.1: (a) Schematics of experimental setup for spectral tuning of droplet-based microlasers by optical stretching. The inset shows the geometry of the single- and dual-beam optical traps and the pump beam. (b) Droplet excitation geometry - view along z -axis, in the propagation direction of the pump beam. (c) A sample lasing spectrum of a $49 \mu\text{m}$ diameter droplet with stretching power of 100 mW.

syringe connected to the inlet via tubing to inject previously prepared microdroplet emulsions and washing solutions. Detailed manufacturing process for the chips is given in the next section. In order to observe the droplets, excite and collect the fluorescence emission from the droplets, and implement single beam optical trap, PDMS chips were mounted on an xyz stage of an inverted optical microscope equipped with a water immersion objective (NA=1.2, 60x; Nikon).

Laser light source for the dual-beam trapping and optical stretching was a 1070 nm Ytterbium fiber laser (YLM-10-LP-SC; IPG Photonics) with 10 W maximum output power. Its output beam was directed to a $\lambda/2$ waveplate (WP1) mounted on a stepper-motor-driven rotary stage and a polarizing beam splitter (PBS1) which together served to adjust the total stretching power coupled into the fibers. Following PBS1, another polarizing beam splitter PBS2 was used to divide the beam into two parts, with $\lambda/2$ waveplate WP2 mounted on a manual rotary stage adjusting the division ratio of the total beam power between the fibers. Subsequently, both beams were coupled to respective single-mode patch cables (P5-980A-PCAPC-1; Thorlabs) using compact fiber couplers (PAF-X-11-C; Thorlabs). The output ports of the patch cables were then connected to the free ends of two multi-mode fibers embedded in the microfluidic chip. In order to measure the total actual power coupled to the fibers, a glass plate with an angle of 45 degrees relative to the laser beam was inserted in the beam path after PBS1; this plate reflected a small fraction of the total power ($\sim 5\%$) towards a power meter. Thus measured power fraction was calibrated by measuring the total output power from the bare fiber ends before inserting them into the chip.

Even though the power balance between the two stretching beams could be adjusted by WP2 for a constant total injected laser power, the power ratio displayed small fluctuations when the total injected power was modified by WP1. Consequently, a droplet confined in the dual-beam optical trap moved in all three directions with respect to the observation focal point when the total stretching power was altered. This phenomenon was further augmented by slight imperfections in the coaxial alignment of the two fibers. In addition, immersion oil used in the experiments was slightly denser than water and, thus, the oil droplets tended to sediment on the bottom of the microchannel. Since the transversal gradient optical force of the dual beam trap that counteracted gravity in our experimental arrangement (gravity pointing in negative z -direction) depends linearly on the total beam power, changes of the dual beam trapping power led to additional vertical displacement of the trapped droplet from the observation focal plane. Such unwanted droplet displacements changed the efficiency of the droplet pumping by the pulsed laser beam (see below) and, subsequently, the intensity of lasing emission from the trapped droplet. To overcome these issues and fix the position of the droplet in the axial and transversal directions during the droplet stretching, an additional infrared laser beam from a cw solid state laser (wavelength 1064 nm, maximum

power 300 mW; CrystaLaser) was introduced to create an independent single beam trap (optical tweezers) perpendicular to the dual beam trap (see inset in Fig. 4.1(a)). This laser beam was sent through a 3x beam expander and reflected from two dichroic mirrors D1, D2 before being focused into the sample chamber by the water immersion microscope objective. The overall transmission of all optical elements in the single beam trapping path was measured to be about 20%, resulting in the average trapping power of ~ 60 mW at the specimen. Using the single beam trap, the studied droplet could be brought exactly to the position of the dual beam trap by adjusting the xyz stage of the inverted microscope. Furthermore, in order to change the position of the single beam trap in the objective focal plane xy , the first lens of the beam expander was mounted on an xy stage that could be steered in x and y directions (perpendicular to the beam axis).

A 532 nm pulsed laser beam generated by frequency-doubling the output of a home-built passively Q-switched Nd – YVO₄ laser (20 ns pulse width, 33 kHz repetition rate, maximal average output power 20 mW) was used as the pump light source to excite fluorescently-stained trapped droplets. The pump laser beam was focused by the same microscope objective as the optical tweezers laser beam, after being transmitted through the dichroic mirror D1 and reflected from the dichroic mirror D2. The diameter of the pump beam focal spot was estimated from the beam spot images acquired after the beam reflection from the cover glass to be $1.24\ \mu\text{m}$. A 2x beam expander with the first lens mounted on an xy stage was added to the optical path of the pump beam to steer the beam focus position in 3-D (xy stage was used to steer the focus of the beam in xy direction and the distance between the two lenses of the beam expander was used to adjust its focal point position relative to the objective lens in the axial direction). This way, focusing points of the optical tweezers beam and the pump beam could be independently adjusted relative to each other and also relative to the imaging focal plane of the objective. Before the experiments, the droplet position was adjusted by moving the optical tweezers in the focal plane so that the focal spot of the pump laser lied near the droplet's rim for the maximal efficiency of the WGM excitation.

Fluorescence from a trapped microdroplet was collected using the same microscope objective as used for focusing the optical tweezers and pump beams, and dispersed by a monochromator (focal length 500 mm; Acton Research) on the chip of a cooled CCD detector (Pixis 100; Princeton Instruments) controlled by WinSpec application software (Prince-

ton Instruments). In Fig. 4.1(c), a typical fluorescence spectrum of a trapped microdroplet is shown. The high-intensity WGMs located in the spectral interval 620 - 630 nm indicate droplet lasing. In order to prevent fast photobleaching of dye molecules inside the droplets, a shutter was added to the pump laser beam path; this shutter was only opened during the spectrum acquisition time and provided trigger signal for the spectroscopic detector to synchronize the data recording. To observe and take an image of the sample, the light in the imaging path of the microscope could be diverted to an ordinary CCD camera via a flippable mirror (FM).

In order to automate the change of the stretching power and synchronize it with the collection of the droplet fluorescence spectra at each level of the stretching power, a LabVIEW code was developed to rotate the stepper motor, open the shutter for 8 ms, and record the stretching laser power while, at the same time, externally triggered WinSpec software was collecting the droplet emission spectra with an exposure time of 8 ms. This way, the droplet deformation cycle could be carried out as fast as possible to minimize the effects of the droplet heating during the spectrum recording interval.

4.2 Microfluidic Chip Fabrication

Microfluidic chips for fiber-based dual-beam optical trapping and stretching were manufactured from PDMS elastomer by casting liquid PDMS precursor into a home-made reusable mold (master). The chip master was prepared in the following manner: first, a piece of optical fiber stripped of the plastic jacket with a diameter of 125 μm was glued onto a cleaned glass substrate with a UV activated adhesive (Loctite 3922 or 3494). This fiber fragment served to form insertion ports for the dual-beam trap fibers in the chip. In the middle of the fiber length, two square capillary tubes (external width of 160 μm) were aligned coaxially with each other and perpendicularly to the fiber, one from each side of the fiber, and glued to the substrate. These capillary tubes defined the liquid channel in the chip. Central openings of the capillary tubes adjacent to the fiber were connected by UV activated adhesive. Resultant cross-like structure with a stalk formed by the capillary tubes and arms in the middle formed by the stripped optical fiber was placed into a plexiglass casting frame that was filled with liquid PDMS precursor and cured at the temperature of $\sim 85^\circ\text{C}$ for 2 hours. After solidification, the resulting PDMS block was peeled off the mold and the PDMS sur-

face was activated together with a 150 μm thick microscope cover slip in an oxygen-argon microwave-excited plasma (oxygen-argon 1:1, total pressure 500 mTorr, microwave power 50 W). Subsequently, the activated PDMS chip was pressed against the activated cover slip, thus sealing the chip permanently. The resulting chip featured one straight channel with square cross-section of $160 \times 160 \mu\text{m}^2$ and two perfectly aligned cylindrical slots for optical fibers in the middle. The liquid inlet and outlet of the channel were realized during PDMS casting with a wire inserted into the mold or after PDMS solidification by a hole-punch.

In order to achieve optimal stretching forces for droplets with diameters around 50 μm , beam diameters at the droplet stable trapping position need to be comparable with the droplet size. This requirement was addressed by using multimode optical fibers (AFS50/125Y, NA=0.22; Thorlabs) with core diameters of 50 μm . These fibers were stripped of their plastic jacket, cleaved, and inserted into the slots in the chip with the help of two small 3-D translational stages, one for each fiber. When the optimal positions of the fibers were reached, connections between the chip and the fibers were sealed using epoxy glue applied to the fiber slots from outside. In order to enable cleaning of the fibers, separation distance between the front faces of the fibers was chosen a little smaller than the width of microfluidic channel, equal to 134 μm .

4.3 Immersion Oil/Water Emulsion System

The emulsion system selected for our study consisted of microdroplets of dye-doped microscope immersion oil ($\eta = 1.515, \rho = 1.02 \text{ g/cm}^3$, Merck) dispersed in deionized water ($\eta = 1.334, \rho = 1.00 \text{ g/cm}^3$). This emulsion system of virtually immiscible liquids provides a high refractive index contrast together with a low density contrast between the droplet and the surrounding medium. This implies a good confinement of WGMs inside the trapped microdroplet, strong optical trapping force, and a small buoyancy that further facilitates the optical trapping of the droplets. The dye DiI(3) (1,1'-Diocetadecyl-3,3,3',3'-tetramethylindol carbocyanine perchlorate, Sigma Aldrich) that has a hydrophilic chromophore and hydrophobic side chains was selected as the laser gain medium. This dye has its excitation peak at $\sim 560 \text{ nm}$ and emission peak at $\sim 575 \text{ nm}$, and is well suited for the efficient excitation of the WGMs due to its surfactant nature that ensures its localization at the oil-water interface where WGMs also reside [43, 88]. In our experiments

Dil(3) was dissolved in chloroform at 10 mM concentration and the dye solution was subsequently added to the immersion oil in 2 to 100 ratio. This solution was put in the oven at $\sim 80^\circ\text{C}$ and evacuated for 10 min to remove the chloroform content. Hence, the final solution contained only immersion oil with the dye concentration of $200\mu\text{M}$.

4.4 Surfactants and Surface Tension Engineering

The term surfactant is made up from a mixture of three words: surface active agent. Surfactants are relatively big molecules that lower the surface tension (or interfacial tension) between two liquids or between a solid and a liquid. Surfactants can be used as detergents, wetting agents, emulsifiers, foaming agents, and dispersant agents.

Water-insoluble molecules are called hydrophobic or lipophilic or oil-soluble and water-soluble molecules are called hydrophilic. Surfactants are usually big organic molecules that are amphiphilic (i.e. they contain both hydrophobic groups as their tails and hydrophilic groups as their heads). Surfactants can diffuse in water and adsorb at interfaces of air/water or oil/water. By dissolving a surfactant in water, its hydrophobic group extends out of the bulk water phase, into the air or into the oil phase, while the hydrophilic head group remains in the water phase. Finely divided solids with amphiphilic properties such as soot, silica and clay, may also act as emulsifying surfactant agents.

4.4.1 Structure of Surfactant Phases in Water

When the surfactants are dissolved in the bulk aqueous phase, they form aggregates such as micelles where the hydrophilic heads are in contact with the surrounding liquid and the hydrophobic tails form the core of the aggregates. Depending on the chemical structure of the surfactants and the balance in size between hydrophilic head and hydrophobic tail, different types of aggregates can be formed, such as spherical or cylindrical micelles or lipid bilayers.

There are two dimensionless parameters that are defined to characterize the shape and type of surfactant aggregates. The first one is critical packing parameter (CPP) that is defined as $\text{CPP} = V_{\text{tail}}/(l_{\text{tail}}a_{\text{head}})$, where V_{tail} , l_{tail} and a_{head} are hydrophobic tail volume, hydrocarbon chain length and effective head group area, respectively. The second one is Hydrophile-lipophile balance (HLB) defined by $\text{HLB} = 20 \times M_{\text{head}}/M_{\text{total}}$, where M_{head} is

Table 4.1: CPP and HLB number meanings for surfactants [94]

CPP Range	HLB Range	Application
2 – 1.5	2 – 6	Antifoaming and W/O emulsifying agents
1.4 – 1	7 – 9	Wetting and spreading agents
1.2 – 0.67	8 – 16	O/W emulsifying agents
0.75 – 0.5	13 – 15	Detergents
0.5 – 0.33	15 – 18	Solubilizing agents

the molecular mass of the hydrophilic portion of the molecule, and M_{total} is the molecular mass of the whole molecule, giving a result on a scale of 0 to 20. An HLB value of 0 corresponds to a completely hydrophobic (lipophilic) molecule, and a value of 20 corresponds to a completely hydrophilic (lipophobic) molecule. HLP=10 is the midpoint and corresponds to equal affinity for oil and water for the surfactant. The phase in which the surfactant is more soluble constitutes the continuous phase. In table. 4.1 the range of HLP values and their corresponding CPP value together with the application for each range of the numbers are given [94].

4.4.2 Classification of Surfactants

The tails of most surfactants are similar and they can be branched or linear hydrocarbon chains, aromatic hydrocarbons, fluorocarbon chains in Fluorosurfactants, or siloxane chains in siloxane surfactants. An important category of surfactants include a polyether chain terminating in a highly polar anionic group. Polyether groups often include ethoxylated (polyethylene oxide-like) sequences to increase the hydrophilic character of a surfactant. Conversely, polypropylene oxides may be inserted to increase the lipophilic character of a surfactant.

Generally, surfactants are classified according to their polar head group. Non-ionic surfactants have no charged groups in their heads: examples include polyglycol, fatty acid esters, lecithin. The heads of ionic surfactants carry a net charge. Surfactants with negative charge in their heads are more specifically called anionic surfactants, such as sodium stearate, potassium laurate, sodium dodecylsulfate (SDS), sodium sulfosuccinate; the ones

with positive charges are called cationic surfactants, such as quaternary ammonium salts, amine hydrochlorides. If a surfactant contains a head with two oppositely charged groups, it is termed zwitterionic.

4.4.3 Critical Micelle Concentration and Minimum Surface Tension

The critical micelle concentration (CMC) is defined as the amount of surfactant concentration in the solution above which micelles start to build up and all additional surfactant molecules added to the solution go to micelles. Before reaching the CMC, the surface tension decreases strongly with the concentration of the surfactant. After reaching the CMC, the surface tension remains almost constant or changes with a lower slope. At CMC the surface tension can be further decreased by adding some ionic agents like NaCl. The value of the CMC for a given dispersant in a given medium depends on temperature, pressure, and on the presence and concentration of other surface active substances and electrolytes. Moreover micelles only form above critical micelle temperature. For example, the value of CMC for sodium dodecyl sulfate in water (no other additives or salts) at 25°C, atmospheric pressure, is 8 mM.

4.4.4 Characterization and Adjustment of Interfacial Tension of Emulsion Droplets

Interfacial tension (γ) between two immiscible liquids can be determined using Wilhelmy plate method [95]. In this method, contacting planar layers of studied liquids are formed in a container and a solid plate from a material that is wetted by the denser liquid is brought into contact with the liquid-liquid interface, perpendicularly to the interface. Subsequently, vertical force acting on the plate is measured that is directly proportional to γ . Since the denser phase in our experimental system was immersion oil, we used Wilhelmy plate made of Teflon that is wetted well by oil. Using Wilhelmy plate method, we measured the value of $\gamma \approx 13.1$ mN/m for the dye-doped immersion oil/water interface.

Tuning of the lasing emission spectra of dye-doped microdroplets by optical stretching requires lowering of surface forces to the level comparable with optical forces. In order to achieve sufficiently low interfacial tensions, we added AOT surfactant (Docusate sodium salt; Sigma-Aldrich) and sodium chloride to the aqueous phase. This surfactant/salt system has been shown to decrease γ to extremely low values (down to 0.001 mN/m) depending

on the concentration of both the surfactant and NaCl [50, 96]. However, such low values of γ are problematic in experiments where the droplets serve as optical resonant cavities since their shape can be easily disturbed by thermal fluctuations which cause degradation of the droplet cavity Q-factor. Here, we used 5 mM AOT surfactant and 40 mM NaCl to decrease the interfacial tension to $\gamma = (1.5 \pm 0.1)$ mN/m. We measured the interfacial tension in the presence of surfactant and salt in a range of temperatures between 25°C and 50°C and found a negligible variation of γ with temperature. Thus, heating of droplets due to residual absorption of the stretching laser light does not cause any appreciable changes of surface forces.

Emulsion microdroplets were obtained by mixing the dye-doped immersion oil with the surfactant-salt-water solution in 1 to 50 ratio, and shaking the obtained mixture by hand. Droplets produced in this way had a large size distribution with diameters ranging from $< 1 \mu\text{m}$ up to $\sim 100 \mu\text{m}$ and the emulsions were stable over ~ 10 hours. Prepared emulsions were subsequently loaded into the PDMS chip using liquid flow controlled by gravitational hydraulic pressure built by the height of water column in a 20 cm long piece of tubing connected to the inlet of the microchip. After loading, microdroplets were observed to float freely within the channel, thanks to their small buoyancy, without sticking to the walls of the sample chamber.

4.5 Simulations of WGM Tuning by Droplet Stretching

In order to calculate the WGM tuning as a function of the stretching power and find out the effects of interfacial tension, droplet size, beam profiles, fiber distance, and refractive index of the used liquids on the tuning range, a simulation of the droplet deformation by optical stretcher was carried out based on a 3-D ray-tracing method developed in [87]. In this method, an incident beam is divided into geometrical rays of variable intensities perpendicular to the wavefront. Each of these rays is then traced through the droplet interface using Snell's law and for each refraction or reflection, the transmitted and reflected powers are calculated for TE and TM polarization by related Fresnel coefficients. Subsequently, the forces acting on the interface as a result of ray reflection or refraction can be calculated from the momentum conservation principle. To calculate the total stretching force ($F_{stretch}$) acting on the droplet, optical forces of all individual rays forming the incident beam are

summed. This ray tracing is continued until the remaining power in the reflected/refracted rays becomes sufficiently small (see the MATLAB codes in Appendix A).

If the fibers are assumed to be coaxial and their output beam profiles and powers to be identical, droplet deformation will be symmetric relative to its equatorial plane xz shown in Fig. 4.2(a). Since the optical stretching forces in moderately focused beams point predominantly along the beam propagation axis y , the droplet will elongate in the y -direction and assume the shape that can be approximated by a prolate spheroid for small deformations. This shape change increases the droplet surface area and, thus, its surface energy. Consequently, a restoring surface force F_{surf} arises that grows with increasing droplet deformation until it exactly balances the optical stretching force $F_{stretch}$. It should be born in mind that $F_{stretch}$ depends on the droplet shape and, thus, it changes with the droplet deformation.

Let us describe the deformed droplet shape by a prolate spheroid $\frac{x^2}{b^2} + \frac{y^2}{a^2} + \frac{z^2}{b^2} = 1$, where a is the polar semi-major axis along the dual beam trap axis y , and b is the equatorial semi-minor axis. The droplet volume is conserved after stretching so $V_0 = 4\pi ab^2/3 = 4\pi r_0^3/3$ and, thus, $b = (r_0^3/a)^{1/2}$, where r_0 is the radius of the unperturbed drop and $a = r_0 + \Delta a$. In equilibrium, $F_{stretch}$ equals to F_{surf} that depends on the droplet elongation Δa along the y -axis as [49]:

$$F_{surf} = -3\pi\gamma\Delta a \quad (4.1)$$

Δa can be found by balancing self-consistently $F_{stretch}$ and F_{surf} . After determining Δa and, subsequently, a and b , droplet circumferences C_e, C_p in the equatorial (xz) and polar (yz) planes, respectively, can be calculated. C_e and C_p then give the wavelength tuning $\Delta\lambda_i$ of WGMs propagating in the equatorial and polar planes: $\Delta\lambda_i = \lambda(C_i - 2\pi r_0)/(2\pi r_0)$, where $i = e, p$, and λ is the WGM wavelength in unperturbed droplet. In the equatorial plane, droplet deformation is rotationally symmetric and $C_e = 2\pi b$. In the polar plane, droplet cross-section is an ellipse and its circumference can be calculated from Ramanujan I approximation [97]:

$$C_p = \pi \left[3(a + b) - \sqrt{10ab + 3(a^2 + b^2)} \right] \quad (4.2)$$

Figure 4.2(b) shows the results of a simulation for a 50 μm diameter oil droplet placed in aqueous surfactant solution with $\gamma = 1.5 \text{ mN/m}$ and located at the center of the dual beam trap. The trap is generated between two multimode fibers with cores of diameter 50 μm

and numerical aperture $NA = 0.22$, and fiber facets are separated by a distance $134 \mu\text{m}$. In this figure we plot the wavelength tuning of WGMs with mean wavelength $\lambda = 625 \text{ nm}$ circulating in the equatorial plane (off-axis excitation) and the polar plane (on-axis excitation) as a function of the stretching laser power ($P_{stretch}$) which corresponds to the total power delivered from the two multimode fibers. For both fibers we assume beam waist diameter equals $50 \mu\text{m}$ and the beam waists are located at the fiber end facets. At the trap center located $67 \mu\text{m}$ away from the fiber end facets, beam diameter of $55 \mu\text{m}$ was found assuming an embedded Gaussian beam with $50 \mu\text{m}$ beam waist diameter propagating with a correction M-factor of 4.0 given by the asymptotic divergence angle of 9.4° that corresponds to the numerical aperture of the fiber output. As we can see, for WGMs propagating in the equatorial plane, tuning slope is negative and equal to -0.96 nm/W , while WGMs propagating in the polar plane are tuned with a positive slope of 0.48 nm/W . Thus, the direction of the lasing wavelength tuning depends on the orientation of the modal path of particular WGM with respect to the droplet planes of symmetry. Due to approximate description of the stretching laser beam profiles and assumption of droplet deforming precisely towards a prolate spheroid, calculated values of the WGM tuning slopes and the tuning slope ratio may differ from the true ones. However, the direction of WGM tuning by optical stretching is predicted correctly.

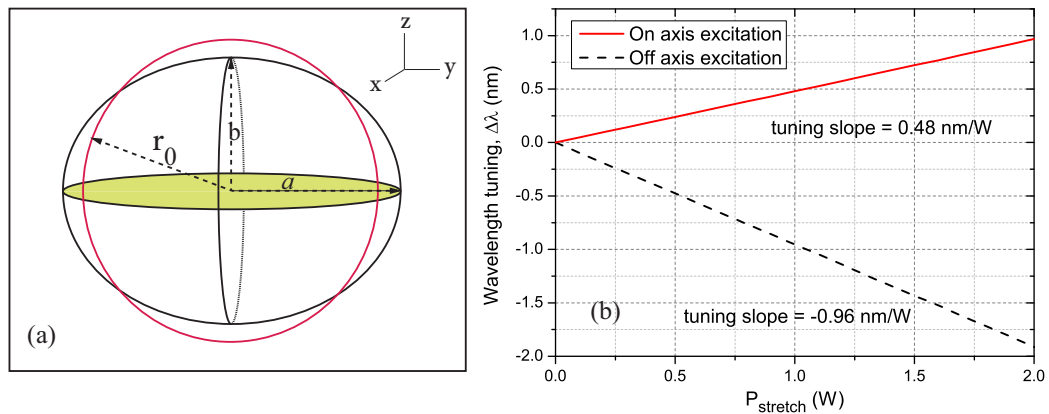


Figure 4.2: (a) Schematic of a prolate spheroid resulting from optical stretching of an originally spherical droplet of identical volume indicated by the red circle. (b) Simulation results showing the tuning of equatorial- and polar-plane WGMs for a $50 \mu\text{m}$ diameter immersion oil droplet in water as a function of $P_{stretch}$.

4.6 Observation of Tunable Dye Lasing in Optically Stretched Microdroplets

Experiments with tunable dye lasing in optically stretched microdroplets were carried out using multimode fibers with parameters identical to those used in the simulations. In order to excite different WGMs in the stretched droplets, the focus of the pump beam was moved to different locations on the droplet.

First, the pump beam was focused at the rim of the droplet in the equatorial plane perpendicular to the dual beam trap axis (off-axis excitation in Fig. 4.1(b)). Figure 4.3(a) illustrates spectral tuning of three consecutive lasing WGMs with off-axis excitation for a droplet with the diameter of $47\text{ }\mu\text{m}$ and $\gamma \approx 1.5\text{ mN/m}$. $P_{stretch}$ was changed from 0 W to 0.88 W in two cycles and the total of 38 spectra were recorded with the minimal values of $P_{stretch}$ corresponding to frame numbers 1, 19, and 38 and the maximal values of $P_{stretch}$ corresponding to frame numbers 10 and 29. Time interval between acquiring consecutive spectra was 50 ms and the droplet was exposed with the pump beam fluence of $\sim 490\text{ mJ/cm}^2$ at the specimen for 8 ms. From Fig. 4.3(a), it is clear that the equatorial plane WGMs experience power-dependent blue tuning consistent with the simulation results presented in Fig. 4.2. As indicated by the white vertical line located near the middle WGM in Fig. 4.3(a), the WGMs do not return back to their initial spectral positions after completing a single tuning cycle and a small blue drift of $\sim 0.04\text{ nm}$ is observed in all lasing WGMs. We interpreted this drift as a result of gradual dissolution of the droplet medium in water triggered by heating of the droplet by the stretching laser beams. This explanation was supported by the fact that the drift amount was directly proportional to the total duration of the tuning cycle and the maximal $P_{stretch}$ (data not shown). During data recording, the effect of the droplet dissolution was minimized by performing the experiments as fast as possible. In order to take the effect of residual droplet dissolution into consideration, we assumed a constant dissolution rate during each tuning cycle resulting in a linear drift of the WGM positions with time. Hence, WGM positions were corrected by subtracting a line connecting the first and last raw WGM position in the tuning cycle corresponding to $P_{stretch} = 0\text{ W}$. This correction was applied to all of the tuning slope calculations presented in this paper. Figure 4.3(b) shows the tuning of the lasing WGM wavelength for the central peak in Fig. 4.3(a) corrected for droplet dissolution as a function of $P_{stretch}$ for two subsequent tuning cycles. The slope of a linear fit to the experimental data is -0.52 nm/W

which is $\sim 54\%$ of the predicted tuning slope of -0.97 nm/W . We address this discrepancy between the experiment and the simulation in the next section.

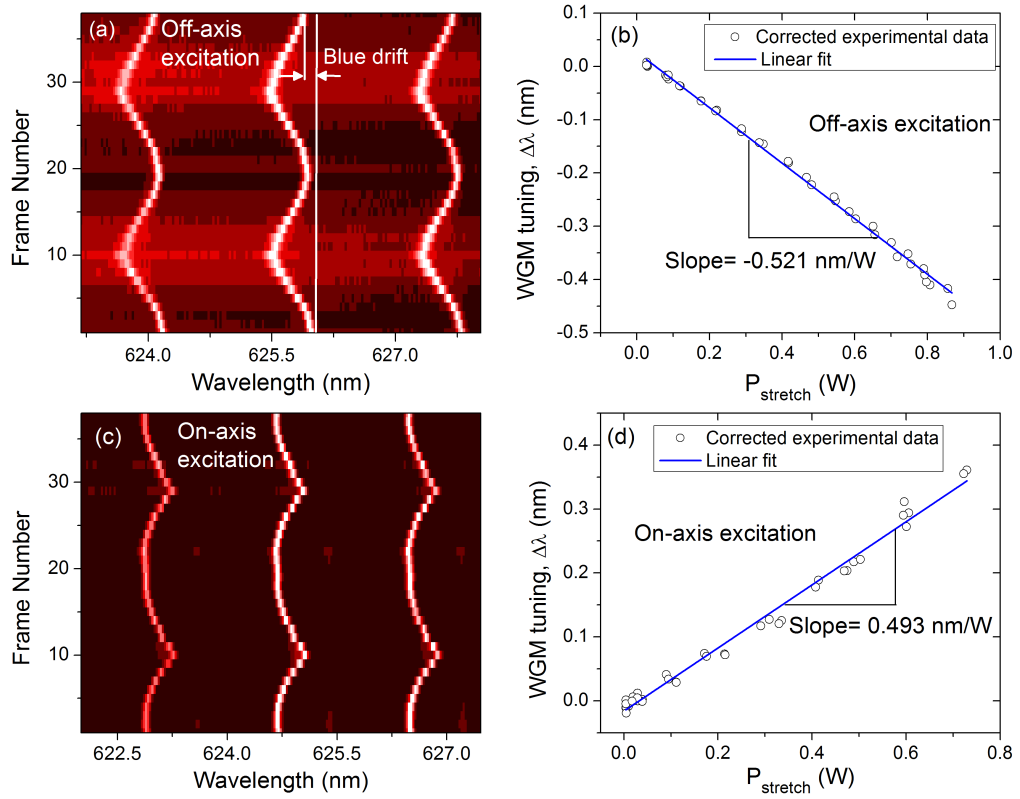


Figure 4.3: (a) Spectral tuning of lasing WGMs of a $47 \mu\text{m}$ diameter droplet in off-axis excitation geometry (see Fig. 4.1(b)) in the presence of surfactant (droplet interfacial tension $\gamma \approx 1.5 \text{ mN/m}$). The white vertical line indicates blue drift caused by droplet dissolution. (b) Dissolution-corrected WGM tuning for the central peak in (a) as a function of the stretching laser power, P_{stretch} . (c) Spectral tuning of lasing WGMs of a $49 \mu\text{m}$ diameter droplet in on-axis excitation geometry (see Fig. 4.1(b)) in the presence of surfactant (droplet interfacial tension $\gamma \approx 1.5 \text{ mN/m}$). (d) Dissolution-corrected WGM tuning for the central peak in (c) as a function of the stretching laser power, P_{stretch} . Intensity values in arbitrary units increase from black to white in (a) and (c).

In the second set of experiments, pump beam was focused at the droplet rim in the polar plane containing the dual beam trap axis (on-axis excitation in Fig. 4.1(b)) and all other experimental parameters were kept fixed. The experiments in both configurations of the pump beam focus were carried out with different droplets since it was not possible to hold the droplet in the trap during the change of the pump beam position. Figure 4.3(c) shows spectral tuning of three consecutive lasing WGMs with on-axis excitation for a droplet with

the diameter of $49\text{ }\mu\text{m}$. $P_{stretch}$ was changed from 0 W to 0.75 W in two cycles and the total of 38 spectra were recorded with the minimal $P_{stretch}$ corresponding to frame numbers 1, 19, and 38 and the maximal $P_{stretch}$ corresponding to frame numbers 10 and 29. As in the previous experiment, time interval between acquiring consecutive spectra was 50 ms and the droplet was exposed with the pump beam fluence of $\sim 490\text{ mJ/cm}^2$ at the specimen for 8 ms. As illustrated in Fig. 4.3(d), for on-axis excitation, lasing WGMs experience red tuning that increases linearly with $P_{stretch}$. Here, a linear fit gives positive tuning slope of 0.49 nm/W that is $\sim 2\%$ larger than the predicted value of 0.48 nm/W .

Tunable lasing experiments with different configurations of the pump beam reveal a systematic shift of experimental tuning slopes with respect to the predictions towards the red end of the spectrum. As argued in the next section, this shift can be explained by simultaneous changes of the droplet size and refractive index of both the droplet and the host medium resulting from heating by the stretching laser beams.

4.7 Influence of Thermal Effects on WGM Tuning

Both the simulations shown in Fig. 4.2 and the asymptotic formula giving the spectral positions of WGMs with different azimuthal mode numbers as a function of the droplet ellipticity [39, 40] predict the ratio of the spectral tuning slopes of the off-axis WGMs (azimuthal mode number = angular momentum index) and the on-axis WGMs (azimuthal mode number = 0) to be -2.0 for droplet sizes studied in this paper. However, in our experiments this ratio was observed to be -1.1 . In order to elucidate this difference, we carried out control experiments with dye-doped immersion oil droplets suspended in pure water without surfactant. As mentioned earlier, interfacial tension for oil/water system $\gamma \approx 13.1\text{ mN/m}$ is almost nine times larger than interfacial tension in the presence of surfactant $\gamma \approx 1.5\text{ mN/m}$. Consequently, one expects nine times smaller tuning slope for the surfactant-free emulsion system in comparison to the data presented in Figs. 4.3(b) and 4.3(d).

In Fig. 4.4(a), spectral tuning of lasing WGMs with off-axis excitation is shown for a $44\text{ }\mu\text{m}$ diameter immersion oil droplet suspended in pure water. The excitation power, exposure time, and time between subsequent frames were identical to the experiments performed with droplets containing surfactant (Fig. 4.3). In the surfactant-free experiments,

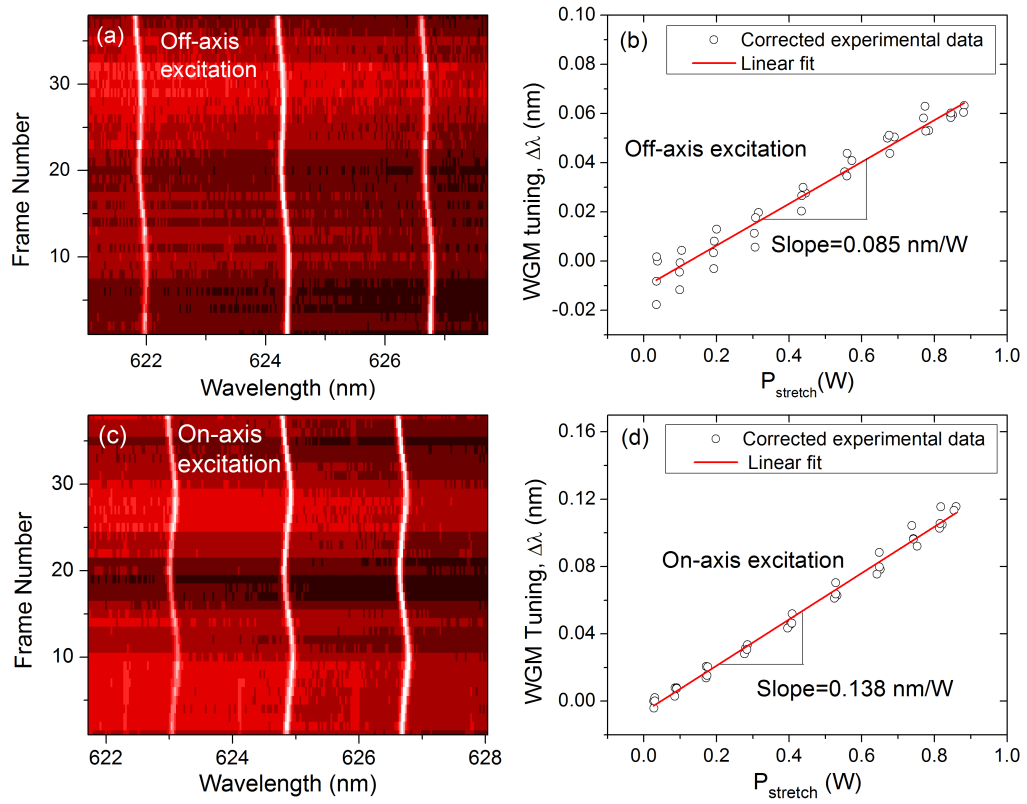


Figure 4.4: (a) Spectral tuning of lasing WGMs of a 44 μm diameter droplet in off-axis excitation geometry (see Fig. 4.1(b)) without surfactant (droplet interfacial tension $\gamma \approx 13.1 \text{ mN/m}$). (b) Dissolution-corrected WGM tuning for the central peak in (a) as a function of the stretching laser power, P_{stretch} . (c) Spectral tuning of lasing WGMs of a 55 μm diameter droplet in on-axis excitation geometry (see Fig. 4.1(b)) without surfactant (droplet interfacial tension $\gamma \approx 13.1 \text{ mN/m}$). (d) Dissolution-corrected WGM tuning for the central peak in (c) as a function of the stretching laser power, P_{stretch} . Intensity values in arbitrary units increase from black to white in (a) and (c).

similarly to the previous cases with surfactant, a monotonous blue drift was observed resulting from the droplet dissolution. In addition, a small cyclic tuning of the WGM positions was also detected with changing P_{stretch} . However, unlike in the previous case with surfactant, spectral tuning for off-axis excitation was towards the red end of the spectrum. A line fit to the dissolution-corrected tuning data shown in Fig. 4.4(b) gives a positive tuning slope of 0.085 nm/W, in contrast to our prediction of a negative slope of -0.11 nm/W from the simulations. In Fig. 4.4(c), spectral tuning of lasing WGMs with on-axis excitation is shown for a 55 μm diameter immersion oil droplet suspended in pure water. Again, a line fit to the dissolution-corrected tuning values in Fig. 4.4(d) shows a positive tuning

slope of 0.138 nm/W that has a proper sign but is 2.6 times larger than the prediction of 0.054 nm/W.

Observation of red-tuning independent of the pump beam position suggests that in the surfactant-free case, WGM tuning is not dominated by droplet stretching which is associated with opposite tuning directions for off-axis and on-axis WGMs. Instead, as we discuss below, heating of the emulsion system by the optical stretching laser beams becomes significant, leading to temperature-induced red shifts observed in WGM spectral positions. Relatively large water absorption at the stretching laser wavelength of 1070 nm leads to an increase in the temperature of water and the droplet by more than 10°C per 1 W of $P_{stretch}$ [98]. For viscous liquids such as immersion oil and water, the dominant mechanism of heat transfer on the scale of hundreds of microns is conduction. For the heat conductivity of water and immersion oil ($\sim 0.5 \text{ Wm}^{-1}\text{K}^{-1}$), steady state is reached within 10 - 20 ms after temperature jumps of 10°C. Since the duration of individual steps of the droplet tuning cycle is > 50 ms, we can assume that the temperature distribution within the droplet reaches equilibrium before each spectral acquisition. Immediate results of such temperature changes are the droplet expansion and the change of the refractive index of the droplet and water. As mentioned in Section 5, interfacial tension does not change appreciably within the temperature range of $\sim 25^\circ \text{C}$ above the room temperature. Therefore, temperature-induced changes of surface forces that could cause additional spectral tuning can be ruled out in the first approximation.

In order to predict the contributions of thermal expansion and refractive index changes to the WGM tuning slopes, we adopted an asymptotic formula which gives the spectral positions of WGMs in terms of oil/water relative refractive index η_1/η_2 and droplet radius r_0 [80]. This asymptotic formula holds for droplets with large size parameters $x = 2\pi r_0/\lambda$ and its use is justified in our case where typical $r_0 \approx 25 \mu\text{m}$ and $\lambda \approx 625 \text{ nm}$ gives $x \approx 251.1$. First derivative of this asymptotic formula with respect to temperature gives the following expression for thermal tuning of WGM positions of spherical droplets:

$$\frac{\Delta\lambda}{\Delta T} = \frac{\lambda\beta}{3} + \lambda\delta_1 - \frac{\lambda^2}{2\pi r_0\eta_1} \left(\frac{\eta_2}{\eta_1}\right)^2 (\delta_1 - \delta_2) \times \left[\left(1 - \left(\frac{\eta_2}{\eta_1}\right)^2\right)^{-\frac{3}{2}} + 2^{-\frac{1}{3}}\alpha_1\nu^{-\frac{2}{3}} \left(1 - \left(\frac{\eta_2}{\eta_1}\right)^2\right)^{-\frac{5}{2}} \right] \quad (4.3)$$

where $\alpha_1 = 2.338$ is the first root of Airy function, $\nu = l + 1/2$ with the angular mode

number $l \approx 2\pi r_0 \eta_1 / \lambda$, $\beta = 3\Delta r / (r\Delta T) = 6.83 \times 10^{-4} \text{ } ^\circ\text{C}^{-1}$ is the volume thermal expansion coefficient of immersion oil, and $\delta_1 = \Delta\eta_1 / (\eta_1 \Delta T) = -2.18 \times 10^{-4} \text{ } ^\circ\text{C}^{-1}$ and $\delta_2 = \Delta\eta_2 / (\eta_2 \Delta T) = -1.02 \times 10^{-4} \text{ } ^\circ\text{C}^{-1}$ are the average thermal coefficients of the refractive index for immersion oil and water, respectively. For our system, $\frac{\Delta\lambda}{\Delta T}$ becomes $\sim 7.8 \text{ pm}/^\circ\text{C}$ which shows a good compensation of the thermal droplet expansion by the refractive index change. Assuming temperature increase of $\sim 10^\circ\text{C}/\text{W}$, the expected thermal tuning slope is approximately $0.078 \text{ nm}/\text{W}$. As thermally induced spectral tuning is isotropic within the droplet, tuning direction does not depend on the position of the pump beam focus on the droplet.

The above simple model of thermally induced tuning shows that in the off-axis excitation geometry, there are two competing mechanisms that tune the WGM spectral positions in opposite directions. While droplet stretching leads to a blue-tuning of WGMs, heating effects tune WGMs to the red end of the spectrum. The overall tuning slopes we observe in the experiments then result from the superposition of these two effects. For emulsions with surfactant, optical stretching dominates and the total wavelength tuning slope is negative (see Figs. 4.3(a) and 4.3(b)) whereas in the surfactant-free emulsions, the total wavelength tuning slope is positive due to the dominance of heating effects (see Figs. 4.4(a) and 4.4(b)). In the on-axis excitation geometry, both thermal and stretching tuning mechanisms lead to positive tuning slopes which explains why the measured tuning slope in Figs. 4.4(c) and 4.4(d) is more than the amount expected solely from the droplet deformation due to optical stretching.

In all experiments in which the excitation beam position was either on-axis or off-axis, we studied only WGMs propagating in a single plane of symmetry of an optically stretched droplet (polar or equatorial, respectively). Thus, it was not possible to monitor simultaneously the spectral positions of both blue-shifting and red-shifting WGMs for a single stretched droplet. However, such information is crucial for determining quantitatively the relative contribution of droplet stretching and thermal effects to the observed WGM tuning. In order to excite simultaneously WGMs propagating along different paths in a single droplet, the excitation beam position was moved to the droplet center (see Fig. 4.1(b)). Figure 5 summarizes experimental results obtained with on-center excitation of a $42 \text{ }\mu\text{m}$ diameter droplet for $\gamma = 1.5 \text{ mN/m}$. With this excitation geometry, WGMs in the droplet

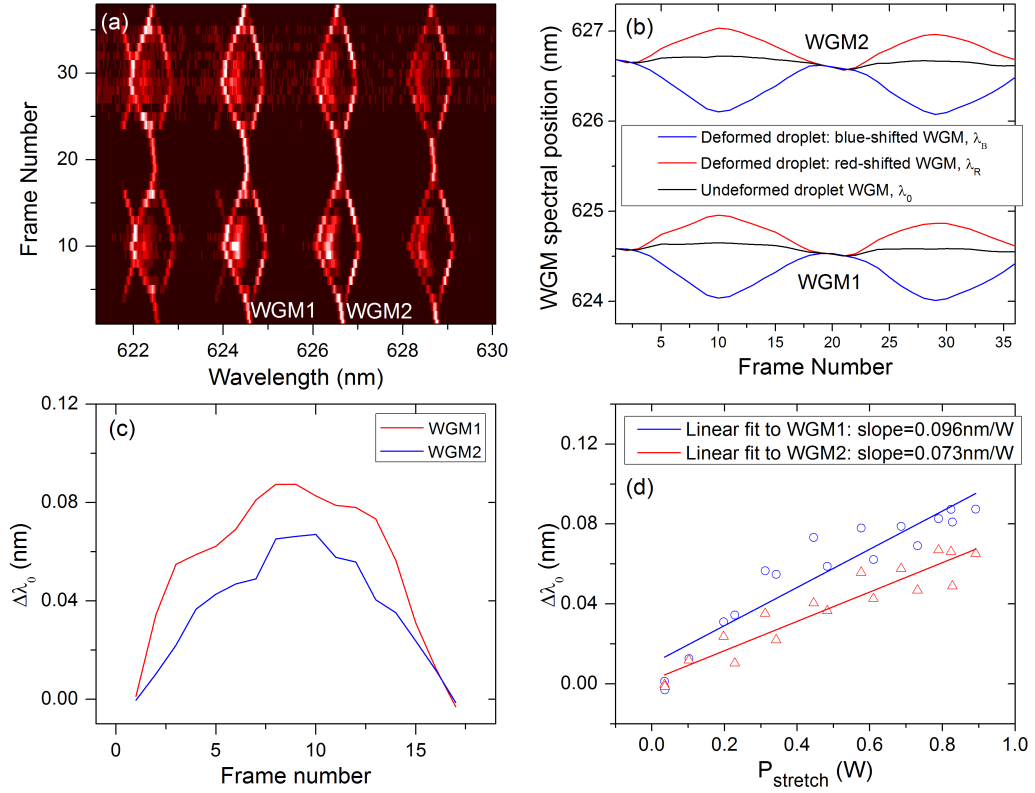


Figure 4.5: (a) Frequency-splitting of WGMs of a 42 μm diameter droplet observed with on-center excitation geometry (see Fig. 4.1(b)). Light intensity in arbitrary units increases from black to white. (b) Dissolution-corrected spectral positions λ_B , λ_R , and λ_0 for WGM1, WGM2 labeled in (a) during two consecutive droplet tuning cycles. (c) Details of changes of spectral position λ_0 for WGM1, WGM2 labeled in (a) within a single droplet tuning cycle. (d) Changes of spectral position λ_0 for WGM1, WGM2 labeled in (a) as a function of the stretching laser power $P_{stretch}$ within a single droplet tuning cycle.

fluorescence spectra display a spectral split $\delta\lambda$ that grows with increasing $P_{stretch}$ (see Fig. 4.5(a)). Within the single frequency-split WGM group, the shortest-wavelength WGM with λ_B propagates in the equatorial plane whereas the longest-wavelength WGM with λ_R propagates in the polar plane. As derived by Chen *et al.* [39], wavelength λ_0 corresponding to the degenerate WGMs propagating in an undeformed spherical droplet is given by $\lambda_0 = \lambda_B + 2\delta\lambda/3$. This formula allows calculating the value of λ_0 for each stretching power from the experimental data. In case of pure stretching deformation of the droplet, λ_0 must be independent of $P_{stretch}$. Non-negligible thermal effects then induce changes of λ_0 with changing $P_{stretch}$. In Fig. 4.5(b), values of λ_B , λ_R , and λ_0 are shown for WGM1, WGM2 labeled in Fig. 4.5(a). Details of changes of λ_0 of the two WGMs with changing $P_{stretch}$

presented in Fig. 4.5(c) then clearly illustrate that the thermal tuning effects cannot be neglected. A linear fit of λ_0 as a function of $P_{stretch}$ given in Fig. 4.5(d) yields the average thermal tuning slope of 0.085 nm/W. This value agrees well with our estimation of 0.082 nm/W obtained from the above presented model of thermal tuning effects for the droplet studied in Fig. 4.5. Measured thermal tuning slope can be used to estimate pure stretching-induced tuning observed in the case of emulsions with surfactants (Fig. 4.3). For off-axis and on-axis excitations, the pure stretching tuning slopes given by the difference between total measured tuning slopes and the average thermal tuning slope become -0.61 nm/W and 0.41 nm/W, respectively. The experimental ratio of the stretching tuning slopes is then -1.5 which is close to the value of -2.0 predicted by the simulations and the analytical formula for deformed droplet WGMs. The remaining difference between the experiments and the prediction may be attributed to several factors. One of them is the fact that individual tuning slopes measured in various excitation geometries were obtained with droplets of different diameters. As the values of both the stretching and thermal tuning slopes depend on the droplet size, experimental ratio of the corrected tuning slopes calculated from measurements carried out with different droplets is generally biased. Also, surfactant concentration in individual droplets is likely not identical which results in variations of the droplet surface tension and, thus, different droplet deformations under otherwise identical experimental conditions. In addition, non-uniform temperature distribution within the droplets heated during stretching [98] induces local variations of refractive index around the droplet circumference. These variations differ for the polar and equatorial WGMs and cause deviations of thermally-induced WGM spectral tuning with respect to the case of a uniformly heated droplet. Finally, despite small magnitude of optical stretching deformations, the exact shape of stretched droplets may differ from a prolate spheroid. For such general droplet shapes, ratio of tuning slopes different from -2.0 is expected.

Chapter 5

IN VITRO AND IN VIVO BIOLASING OF FLUORESCENT PROTEINS SUSPENDED IN LIQUID MICRODROPLET CAVITIES

In this chapter, we study optofluidic biolasers that exploit active liquid optical resonators formed by surface-supported aqueous microdroplets containing purified yellow fluorescent protein or a suspension of live *E. coli* bacterial cells expressing the fluorescent protein. We first demonstrate lasing in fluorescent protein solutions at concentrations as low as 49 μM . Subsequently, we show that a single fluorescent bacterial cell of micrometer size confined in a droplet-based cavity can serve as a laser gain medium.

5.1 Materials and Methods*5.1.1 Expression, Isolation, and Purification of Venus Yellow Fluorescent Protein*

All reagents were obtained from VWR International GmbH (Darmstadt, Germany) and used as received unless otherwise specified. In order to express Venus in BL21 *E. coli* cells, the Venus gene was cloned into the pBTR (Amp^r) expression vector using standard cloning methods and the plasmid was subsequently inserted into the bacteria. After transformation, BL21 cells were cultivated in 1 L of LB-type growth medium for 1 hour at 37 °C. Grown cells were harvested from the medium by centrifugation for 10 minutes at 4500 rpm and then resuspended in 50 mM phosphate buffer at pH 7. Cells in buffered suspensions were homogenized with a probe-tip sonicator. The resulting cell lysate was then ultra-centrifuged at 20000 rpm for 15 minutes and the supernatant was collected and used in all lasing experiments. The emission and excitation fluorescence spectra of 5 μM Venus solution in 50 mM phosphate buffer were measured at 25 °C with a FluoroMax-3 spectrofluorometer. The absorption spectra of the suspended Venus-expressing BL21 cells were collected using a Shimadzu UV-3600 spectrophotometer. For quantitative analysis of the fluorescence intensity of purified Venus solutions and Venus-expressing *E. coli* cells, the samples were imaged with an EMCCD camera (LucaS, Andor) operated in frame-transfer mode at 5 frames per second.

Fluorescence emission data were analyzed using ImageJ (NIH) and MATLAB (MathWorks) software packages.

5.1.2 Generation of Liquid Microdroplets Supported by Superhydrophobic Surfaces

Superhydrophobic surfaces with water contact angles $> 150^\circ$ for droplet deposition were prepared by spin coating hydrophobic silica nanoparticles (Aeroxide LE2; Evonik) dispersed in ethanol on cleaned coverslips [28]. To deposit micron-sized droplets on the surface, liquid aerosols containing the laser gain medium in the form of either purified Venus protein or fluorescent bacteria in a mixture of water and glycerol were generated using a compact ultrasonic nebulizer (JIH50, Beuer) and sprayed over the surface. This procedure provided surface-supported microdroplets with radii ranging from $0.5\ \mu\text{m}$ to $50\ \mu\text{m}$; in case of bacterial suspensions, the mixture was diluted until the droplets contained approximately 5 - 15 bacteria per droplet with $\sim 5\ \mu\text{m}$ radius. The number of bacteria in the selected droplet was estimated by direct counting of the suspended cells. In order to obtain in-focus image of the cells, the position of the microscope focal plane within the droplet was gradually adjusted during counting.

5.2 Experimental Setups

A detailed scheme of the inverted optical microscope system used for recording emission spectra from surface-supported fluorescent microdroplets is shown in Fig. 5.1. The individual surface-supported droplets were optically pumped with a pulsed 488 nm laser beam obtained by frequency-doubling the 976 nm output of an ultrafast Ti:Sa laser (pulse width 140 fs, repetition rate 80 MHz - Chameleon Ultra II; Coherent). Pump laser pulses were sent to the studied droplet in bunches of $5\ \mu\text{s}$ duration separated by 10 ms dark periods. To this end, output beam from the laser was focused through an aspheric lens L1 on a pinhole with $\sim 155\ \mu\text{m}$ diameter located on a chopper wheel rotating with frequency of 100 Hz and then collimated again by a plano-convex lens L2 (see Fig. 5.1). After re-collimation, beam diameter was expanded four times with respect to its original size. The laser repetition rate of 80 MHz corresponds to the separation between the pulses of 12.5 ns and, thus, each $5\ \mu\text{s}$ excitation bunch contains on average 400 pulses (see Fig. 5.2). In order to minimize the distortion of the studied droplet shape by intense pump laser pulses, a single bunch

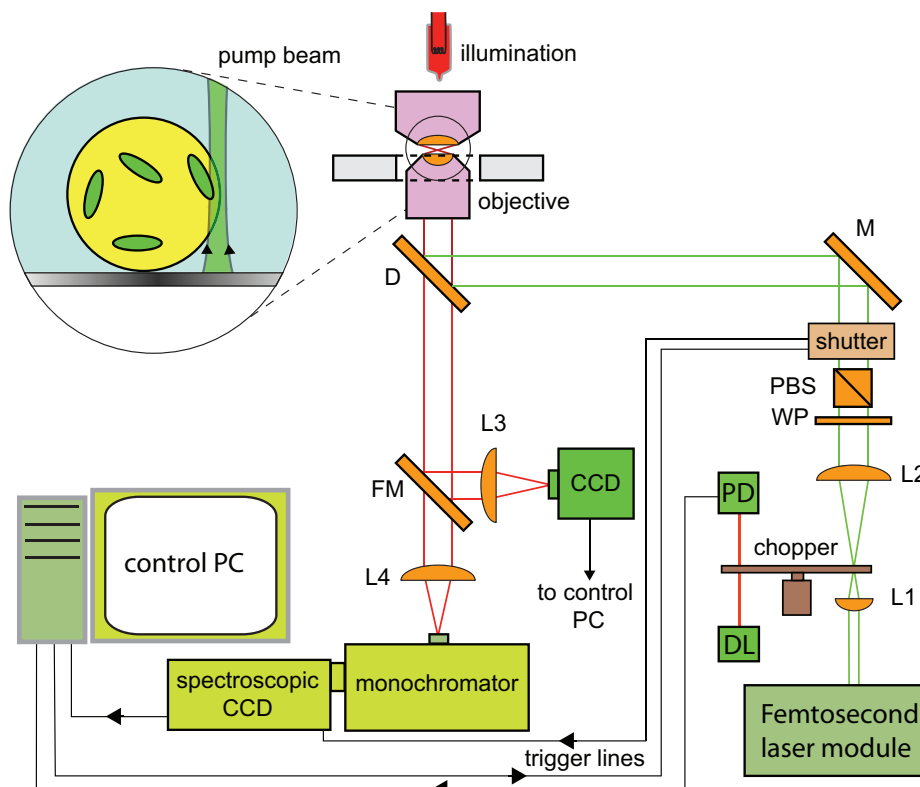


Figure 5.1: Experimental setup for fluorescence spectroscopy of surface-supported lasing microdroplets. D-dichroic mirror, DL-diode laser module, FM-flippable mirror, L1-L4-lenses, M-mirror, PBS-polarizing beam splitter, PD-photodetector, and WP- $\lambda/2$ wave plate.

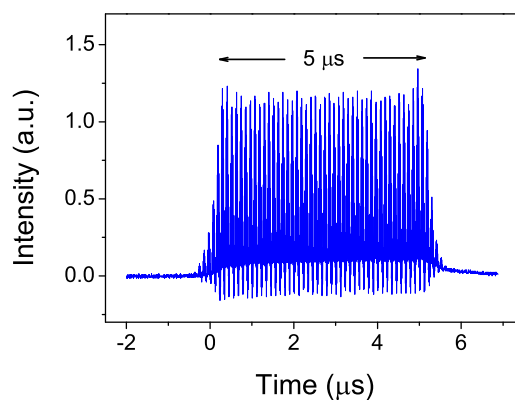


Figure 5.2: A bunch of ~ 400 pulses from the pump laser beam with the pulse repetition rate of 80 MHz after transmission through a rotating chopper wheel with $\sim 155 \mu\text{m}$ diameter pinhole.

of excitation pulses was typically used for recording an emission spectrum of the droplet. Single pulse bunches were selected by adding a mechanical shutter to the optical path of

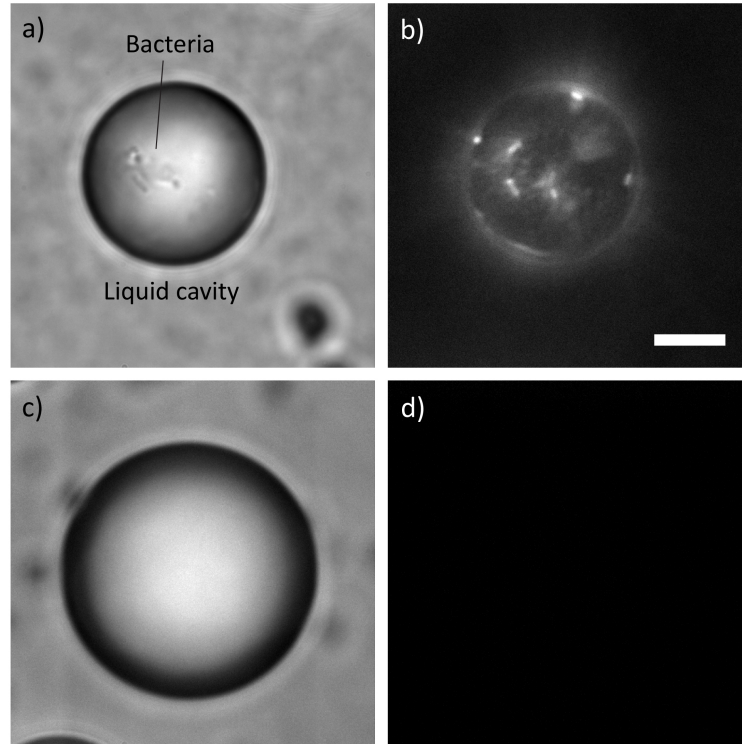


Figure 5.3: (a) DIC image of a surface-supported glycerol-water microdroplet with suspended *E. coli* bacteria expressing Venus fluorescent protein, (b) Fluorescence image of the same microdroplet as shown in (a). (c) DIC image of a surface-supported glycerol-water microdroplet without bacteria. (d) Fluorescence image of the same microdroplet as shown in (c). The scale bar is 10 μm .

the pump beam and synchronizing it with the chopper wheel rotation using an auxiliary diode laser whose power was modulated by the chopper, detected by a photodiode, and fed to the computer controlling the experiment. The overall power of the pump beam could be adjusted by the combination of a half-wave plate and a polarizing beam splitter. After expansion, the excitation beam was reflected from a dichroic mirror and then focused at the rim of the studied droplet using a high NA water-immersion microscope objective lens (60x, NA = 1.2; Nikon) to a diffraction-limited spot with the radius of approximately 0.4 μm . Fluorescence emission from the droplets was collected using the same microscope objective, transmitted through the dichroic mirror, and dispersed by a monochromator (focal length 500 mm; Acton Research) before detection by a cooled spectroscopic CCD camera (Pixis 100; Princeton Instruments). For spectral acquisitions, spectroscopic CCD detector was synchronized with the mechanical shutter using electronic trigger line. Microdroplets de-

posited on the surface were imaged with an independent CCD camera placed at a different exit port of the microscope.

High-resolution images of surface-supported microdroplets with suspended bacteria (see Fig. 5.3) were recorded using an inverted optical microscope (IX83; Olympus) equipped with a high-NA oil-immersion objective lens (UPLSAPO 100x/1.4; Olympus) and an EMCCD camera (iXon3; Andor). In the wide-field fluorescence imaging mode, the bacteria were illuminated through 485/20 (center wavelength/bandwidth in nanometers) excitation filter and the fluorescence emission was collected using 521/25 emission filter. All fluorescence images of bacterial cells suspended in microdroplets were acquired with the integration time of 70 ms.

5.3 Characterization of Venus Fluorescent Protein and Venus-Expressing Bacterial Cells

Venus yellow fluorescent protein has been frequently used as a reporter for the quantification of protein expression levels [99, 100, 101, 102, 103]. Since Venus has a high quantum yield of $\Phi = 0.57$ [104] and it is one of the brightest fluorophores among all fluorescent proteins [105], it is an excellent candidate for the gain medium of optofluidic biolasers. In our experiments, Venus was expressed in BL21 *E. coli* cells using pBTR high-expression vector. The resulting high intracellular concentration of the fluorophore is a prerequisite for observation of live-cell lasing emission with a low pump laser power. In Fig. 5.4(a), an aqueous suspension of Venus-expressing BL21 bacterial cells is shown under white light illumination (left) and UV light illumination (right). In both imaging modes, the bacterial suspension displays intense color (yellow for the transmitted white light image, light green for the fluorescence image) indicative of a high Venus expression level in BL21 cells. Individual fluorescent bacteria deposited on a cover slip surface could be clearly imaged after wide-field illumination with 473 nm laser light [Fig. 5.4(b)]. To determine the maximum absorption wavelength of Venus under in vivo conditions, we acquired the visible absorption spectrum of an aqueous suspension of fluorescent BL21 cells at pH 7.0 [Fig. 5.4(c)]. In this spectrum, the main absorption peak of intracellular Venus at 515 nm is superimposed on the monotonically decreasing spectral background caused by light scattering from the cells. The spectrum also features a secondary absorption shoulder around 488 nm, which was used in the Venus lasing

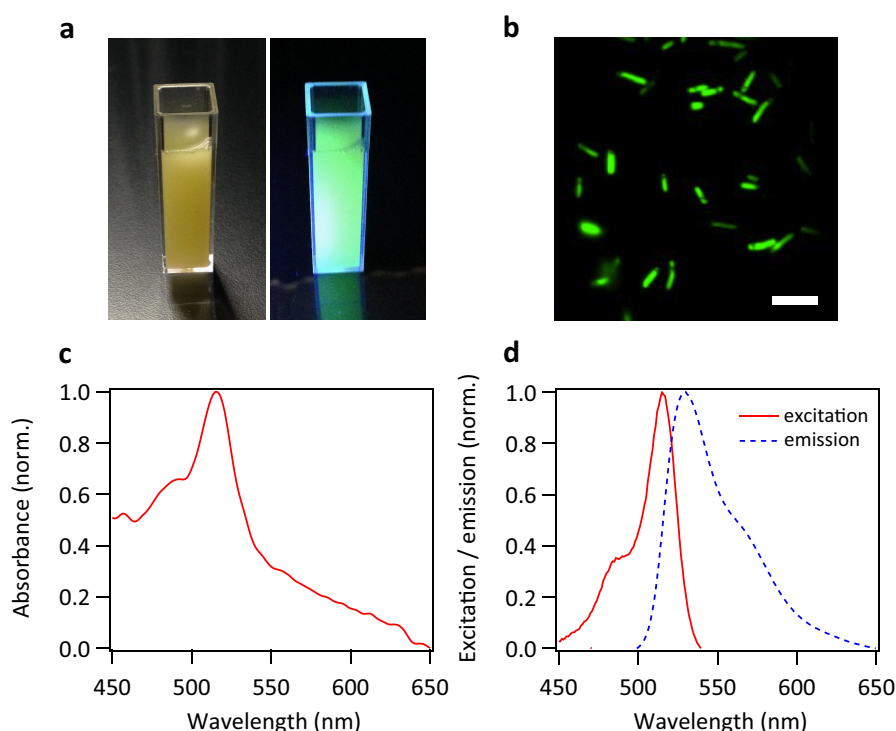


Figure 5.4: Venus-expressing *E. coli* cells as the laser gain medium. (a) Image of aqueous suspension of BL21-strain of *E. coli* bacterial cells expressing Venus variant of the yellow fluorescent protein under white light illumination (left) and UV light illumination (right). (b) Pseudocolor fluorescence image of BL21 cells expressing Venus fluorescent protein. Scale bar is 5 μm . (c) Absorption spectrum of aqueous suspension of BL21 cells expressing Venus fluorescent protein. (d) Excitation and emission spectra of purified Venus fluorescent protein suspended in 50 mM phosphate buffer.

experiments. Further information about the spectral properties of Venus was obtained from the fluorescence excitation and emission spectra of the solutions of purified Venus in 50 mM phosphate buffer [Fig. 5.4(d)]. The concentration of Venus in the buffer solution (5 μM) was determined from its recorded visible absorption spectrum and known molar extinction coefficient [99]. The spectral peak of Venus fluorescence emission recorded with 470 nm excitation light was observed to lie at 530 nm. Identical to the live-cell absorption spectrum of Fig. 5.4(c), the fluorescence excitation spectrum displays a maximum at 515 nm. This suggests that the high expression level of Venus in the bacteria does not have a significant influence on the spectral characteristics and the fluorescence brightness of the protein. In order to estimate the concentration of Venus in living BL21 cells, we compared the intensity of fluorescence from individual cells and Venus solution of a known protein concentration

(see Fig. B.1 in Appendix B). The average intracellular concentration of Venus c_B was found to be approximately 470 μM . Considering a typical *E. coli* cell volume V_B of 0.20-0.77 fl (cell approximated by a cylinder with the diameter of 0.5-0.7 μm and length of 1-2 μm), this corresponds to about $N_A V_B c_B \approx 60,000\text{-}220,000$ copies of Venus per cell (N_A is Avogadro's number).

5.4 Observation of Lasing from Aqueous Solutions of Venus Fluorescent Protein

Liquid microdroplets supported by superhydrophobic (SH) surfaces have been successfully used as optical resonant cavities in the studies of lasing from aqueous solutions of fluorescent dyes [28] and vitamins [61]. Deposition of droplets on an SH surface with a high liquid-solid contact angle preserves the spherical shape of the droplets and stabilizes their position. Moreover, with transparent droplet-supporting substrates, light can be easily coupled into and out of the droplets using an inverted optical microscope [Fig. 5.5(a)]. In our experiments, we obtained transparent SH surfaces by spin-coating a solution of hydrophobic silica nanoparticles on clean glass coverslips. The studies of lasing from aqueous solutions of Venus fluorescent protein were carried out using Venus dissolved in 35% v/v mixture of glycerol and 50 mM phosphate buffer. Presence of low-volatility glycerol in the droplet liquid is essential for stabilizing the droplets exposed to ambient room atmosphere against evaporation [106]. Under typical experimental conditions (temperature 26 °C, relative humidity 64%), the final equilibrium concentration of glycerol in the phosphate buffer solution was estimated to be approximately 64% v/v; this corresponds to the reduction of the droplet volume by a factor of 0.55 and, consequently, the increase of the Venus concentration in the droplets with a factor of 1.81. All concentrations of Venus in droplets reported in this chapter are the final values that take into account partial liquid evaporation after the droplet generation. Venus-containing liquid droplets were deposited on the SH surface using a compact ultrasonic nebulizer. Subsequently, fluorescence from individual droplets was excited by focusing a femtosecond (fs) pulsed laser beam with the wavelength of 488 nm at the droplet rim using a microscope objective of a high numerical aperture. Light emitted from the droplet was collected by the same objective lens and analyzed by a spectrograph (see Fig. 5.1 for details).

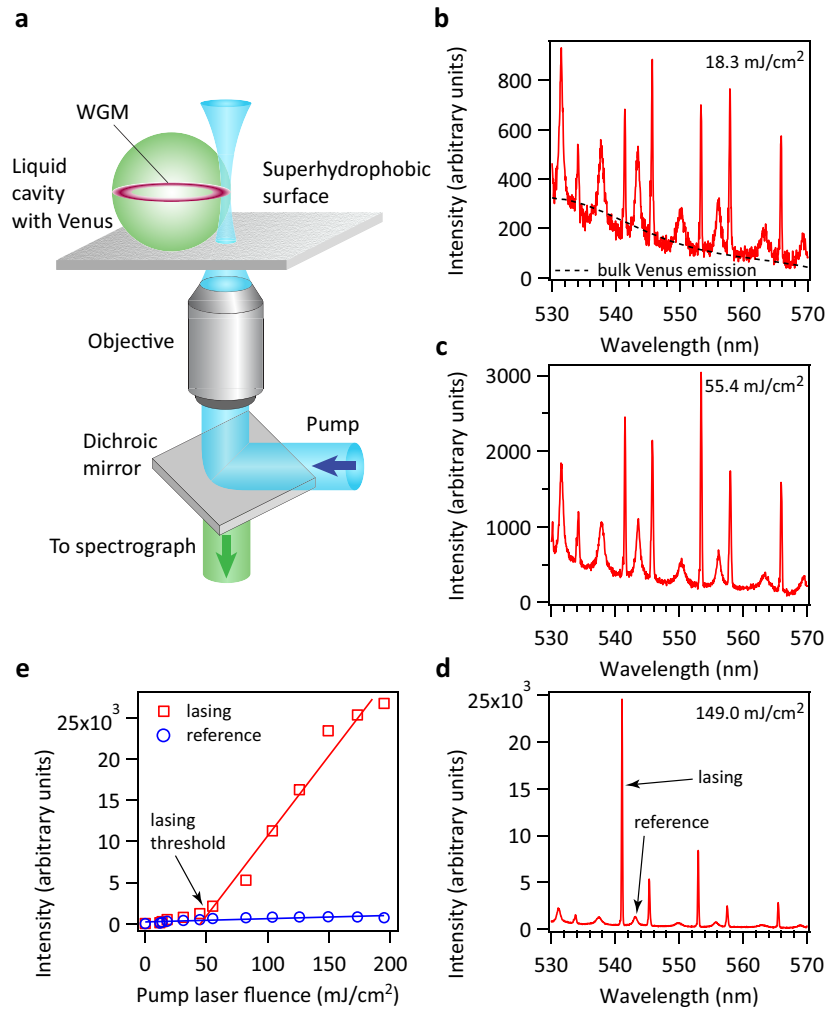


Figure 5.5: Lasing of Venus fluorescent protein in surface-supported microdroplets. (a) Experimental geometry for observation of lasing from the solution of purified Venus fluorescent protein contained in a surface-supported glycerol-water microdroplet acting as a liquid optical resonant cavity. (b) Example of droplet emission spectrum recorded with a pump beam fluence below the lasing threshold. Black dashed line shows the bulk emission spectrum of Venus fluorescent protein solution (no cavity modes). (c) Example of droplet emission spectrum recorded with a pump beam fluence near the lasing threshold. (d) Example of droplet emission spectrum recorded with a pump beam fluence above the lasing threshold. (e) Intensity of the lasing and reference spectral peaks indicated in part (d) as a function of the pump laser fluence. Symbols denote experimental data, solid lines denote linear fits to the data. Droplet radius is $3.2\ \mu\text{m}$.

In Figs. 5.5(b)-(d), emission spectra are presented which were recorded from a single surface-supported droplet with Venus concentration of $49\ \mu\text{M}$ and consecutively increasing fluence of the pump laser beam. At the lowest excitation fluence of $18.3\ \text{mJ}/\text{cm}^2$ [Fig. 5.5(b)],

the pump energy is not sufficient to achieve lasing for the given Venus concentration. The resulting droplet emission spectrum features a number of non-amplified WGMs of comparable intensity and varying width superimposed on a broad non-resonant background of bulk Venus fluorescence. The observed WGMs correspond to different resonant paths of the light in the droplet and can be uniquely identified by their radial, angular, and azimuthal mode numbers and mode polarization (TE or TM) [13]. In general, WGMs with the lowest radial mode number $n = 1$ that circulate closest to the droplet surface display the highest Q-factors and, thus, they are the best candidates for the observation of lasing [107]. When the pump fluence goes up to 55.4 mJ/cm^2 , the intensity of these narrowest WGMs increases by a larger factor than the intensity of broad WGMs and non-resonant spectral background [Fig. 5.5(c)]. Stronger dependence of the intensity of high-Q WGMs on the pump fluence indicates the onset of nonlinear optical phenomena associated with amplified stimulated emission from the droplets. With the pump fluence set to 149 mJ/cm^2 , well above the lasing threshold of the studied droplet, the intensity of lasing WGMs relative to non-lasing optical modes and non-resonant background increases dramatically [Fig. 5.5(d)]. The spectral location of the overall maximum of lasing emission is then determined by the interplay between the Venus absorption and emission profiles, Venus concentration in the droplet, and droplet size. Generally, the strongest lasing peak is shifted to the red from the bulk emission maximum of the fluorophore due to the self-absorption that increases absorptive losses of the cavity at shorter emission wavelengths [43].

In order to quantify the pump threshold required for droplet lasing, we recorded and analyzed a series of droplet emission spectra with gradually increasing fluence of the pump beam. In Fig. 5.5(e), the intensity above background for lasing and reference WGMs annotated in Fig. 5.5(d) is plotted as a function of the pump fluence. From this figure, it is obvious that upon exceeding a certain pump level, intensities of the lasing and reference WGMs start growing with a different rate, which marks the onset of lasing. The actual threshold value of 44.5 mJ/cm^2 was determined from the intersection of line fits to the experimental data points obtained for the reference WGM (over the whole range of studied pump fluences) and lasing WGM (pump fluences above 46 mJ/cm^2). After crossing the threshold, full width at half maximum (FWHM) of the reference WGM remains more or less constant ($\sim 0.65 \text{ nm}$) whereas FWHM of the lasing WGM decreases by approximately

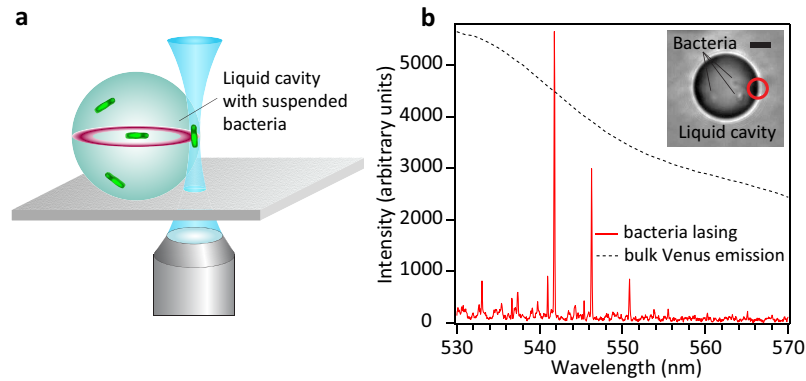


Figure 5.6: Lasing of fluorescent *E. coli* bacterial cells in surface-supported microdroplets. (a) Experimental geometry for observation of lasing from live *E. coli* bacterial cells expressing Venus fluorescent protein. The bacteria are suspended and freely mobile in glycerol-water microdroplets standing on a superhydrophobic surface. The figure is not drawn to scale. (b) Example of lasing emission spectrum recorded from suspended *E. coli* bacterial cells (solid line). For comparison, emission spectrum of purified bulk solution of Venus fluorescent protein is also shown (dashed black line). Inset is the image of the actual droplet [radius 8.4 μm] used for spectral recording that contains ~ 7 bacterial cells. Circle indicates location of the excitation beam spot on the droplet. The scale bar is 5 μm .

20% from 0.22 nm to 0.18 nm (see Fig. 5.8) due to the nonlinear interactions between the amplified resonant light and molecules of the gain medium [28]. Similar to regular fluorescent dyes, the pump threshold of Venus-based microdroplet lasers is a function of the protein concentration in the droplets and droplet radius, as both of these factors influence the overall losses of the cavity [43].

5.5 Observation of Lasing in Suspensions of Bacteria Expressing Venus Fluorescent Protein

After characterizing basic properties of droplet-based microlasers with aqueous solutions of purified Venus fluorescent protein, we carried out experiments in which the laser gain medium was formed by dilute suspensions of living BL21 *E. coli* bacteria stably expressing Venus. To this end, bacterial cells were suspended in 35% v/v mixture of glycerol and 50 mM phosphate buffer (initial glycerol concentration prior droplet generation and partial evaporation-see the discussion in section 5.4. Subsequently, liquid droplets were deposited on SH surface using a nebulizer. Cell concentration in the suspension was adjusted so as to obtain approximately 5-15 bacteria per droplet with $\sim 5 \mu\text{m}$ radius. In order to excite

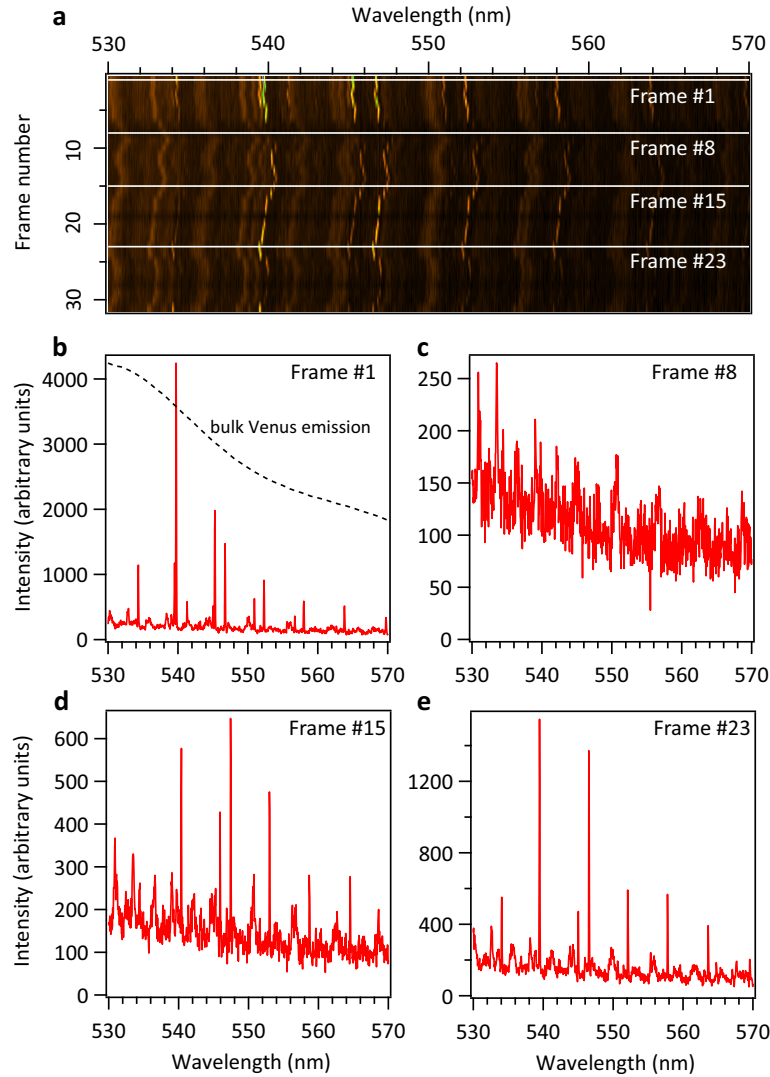


Figure 5.7: Dynamics of lasing from suspended *E. coli* bacterial cells. (a) Time series of emission spectra recorded from a bacteria-containing droplet of $6.8 \mu\text{m}$ radius with a constant pump fluence. The number of bacterial cells in the droplet was ~ 10 . (b)-(e), Droplet emission spectra for frames 1, 8, 15, and 23 indicated by white horizontal lines in part (a). Due to bacteria diffusion and active motion into and out of the excitation volume, droplet emission pattern in different frames switches between lasing and non-lasing emission mode.

fluorescence in the droplets, the pump laser beam was focused at the droplet rim over a suitably positioned bacterial cell (see Fig. 5.6(a) and inset of Fig. 5.6(b) for details of the excitation geometry). Figure 5.6(b) shows an example emission spectrum recorded from an $8.4 \mu\text{m}$ radius droplet containing ~ 7 bacterial cells. The excitation fluence used for recording the spectrum was 312 mJ/cm^2 and the effective acquisition time was $5 \mu\text{s}$. Sharp lasing

WGMs observed between 540-555 nm are shifted to the red with respect to the emission maximum of bulk Venus solution (530 nm) due to self-absorption induced losses at shorter emission wavelengths. FWHM of lasing WGMs in the bacterial suspension (0.13 nm) is comparable to FWHM of the lasing peak in Venus solution [0.18 nm - see Fig. 5.5(d)] which implies comparable Q-factors and, consequently, negligible distortion of the droplet shape and minimal scattering losses due to the presence of bacteria in the liquid.

Unlike in the case of droplets containing purified Venus solution, laser gain medium represented by individual fluorescent bacterial cells is discrete, with random and non-uniform distribution within the liquid cavity. Moreover, the cells can move freely in the liquid due to diffusion and active motion. The size of the effective excitation volume formed in the vicinity of the pump beam focus is comparable to the wavelength of the pump beam and, thus, only a single bacterial cell typically resides within this high-intensity excitation region. Additional restriction on the permissible location of the lasing bacterium within the droplet arises from the requirement of a sufficient overlap of the bacterium with the WGM modal volume, which is a prerequisite for the observation of stimulated emission. As argued in Section 5.4, lasing is associated with the highest-Q WGMs characterized by the lowest radial mode number $n = 1$ [107]. These WGMs are confined to radial distances r from the droplet center of $0.9a < r < a$ where a is the droplet radius [108]. For the typical size of droplets used in our lasing experiments ($a < 10 \mu\text{m}$), the thickness of the spherical shell near the droplet surface within which the stimulated emission can take place lies in the sub-micron range. The limited spatial extent of the excitation region and the modal volume of WGMs together with the random motion of the bacteria into and out of the excitation volume lead to distinctive on-off character of the lasing emission from dilute bacterial suspensions contained in the droplets. Figure 5.7(a) presents time series of fluorescence emission spectra recorded from a droplet with $6.8 \mu\text{m}$ radius containing approximately 10 bacterial cells. A constant pump fluence of 312 mJ/cm^2 was used, with an effective integration time for acquiring each spectrum in the series of $5 \mu\text{s}$, and a total of 32 spectra were recorded with a time delay of 1 s between successive spectra. In the 2-D spectrum of Fig. 5.7(a), random frame-to-frame intensity fluctuations are clearly observable. In addition, small variations in the spectral positions of individual WGMs appear which may be attributed to changes in the WGM resonant path length induced by random diffusion of the cells through the mode

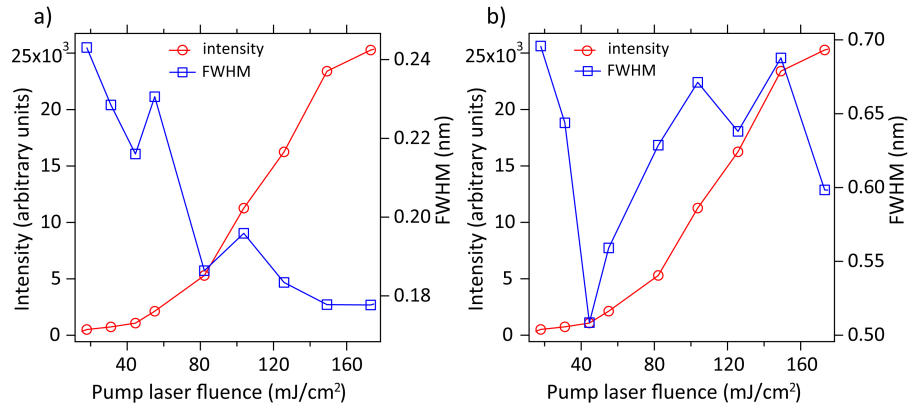


Figure 5.8: (a) FWHM of the lasing WGM studied in Fig. 5.5 as a function of the pump laser fluence (squares). (b) FWHM of the reference WGM studied in Fig. 5.5 as a function of the pump laser fluence (squares). In both figure parts, circles denote the intensity above background of the lasing WGM.

path and fluctuations of the droplet cavity size caused by interplay between the droplet evaporation and condensation during optical pumping [106]. Four selected spectral frames highlighted by white horizontal lines in Fig. 5.7(a) and shown in detail in Figs. 5.7(b)-(e) illustrate the dynamics of the droplet emission pattern. From initial lasing in frame #1, droplet emission progresses to an almost dark state with very low emission intensity in frame #8, as the bacterium forming the laser gain medium tumbles in the liquid. Subsequently, the bacterium approaches the excitation volume again, displaying regular non-amplified WGMs in frame #15, and the droplet then returns back to lasing in frame #23. During the random motion of the selected bacterium through the excitation volume, transitions from amplified stimulated emission to spontaneous emission are marked by large fluctuations of the WGM intensity. Moreover, frame-to-frame changes of the cell position and orientation also result in changes of the relative intensity of individual lasing WGMs since their relative gain and losses are highly sensitive to small perturbations in the liquid cavity.

5.5.1 Dependence of Full Width at Half Maximum of Whispering Gallery Modes on the Pump Fluence and Venus Photobleaching

Due to nonlinear interactions between the amplified resonant light and Venus molecules inside the droplet cavity, full width at half maximum (FWHM) of lasing whispering gallery modes (WGMs) decreases upon crossing the threshold pump fluence required for lasing.

Figure 5.8 shows FWHM of the lasing (part (a)) and reference (part (b)) WGMs studied in Fig. 5.5 as a function of the pump laser fluence. For illustration, intensity above background of the lasing WGM is also displayed. The analysis presented yielded the threshold pump fluence of 44.5 mJ/cm^2 for this particular droplet. From Fig. 5.8(a), it follows that FWHM of the lasing WGM drops by approximately 20%, from 0.22 nm to 0.18 nm, when the pump threshold value is exceeded. This decrease of the mode FWHM correlates with a steeper increase of the WGM intensity with the pump fluence. In contrast, FWHM of the reference WGM which does not experience stimulated emission does not change systematically with increasing pump fluence; instead, it oscillates around the value of $\sim 0.65 \text{ nm}$ [Fig. 5.8(b)].

5.6 Discussion

We have demonstrated and characterized lasing from active liquid optical microcavities formed by surface-supported water/glycerol microdroplets containing purified Venus fluorescent protein or dilute suspension of live *E. coli* bacterial cells expressing stably the Venus protein. Using aqueous Venus solutions, we have shown that lasing can be achieved with Venus concentration in the droplet as low as a few tens of M, which compares favourably to microdroplet lasers that exploit traditional organic dyes [28]. With femtosecond pulsed laser excitation, optofluidic biolasers based on Venus-containing microdroplets can emit several thousand pulses before the fluorophore photobleaches. As suggested by Eggeling *et al.*, detrimental effects of photobleaching on the useful operation time of such droplet-based microlasers can be moderated by using excitation wavelengths closer to the Venus absorption maximum (515 nm) and longer excitation pulses [109]. Alternatively, Venus can be replaced with a different fluorescent protein that displays a better photostability [104]. Our studies of lasing in microdroplets prepared from dilute aqueous suspensions of fluorescent *E. coli* bacteria expressing Venus have provided experimental evidence for the feasibility of such biolasers with active gain medium formed by live cells suspended in a liquid, under environmental conditions compatible with cell survival. Distinctive on-off character of lasing emission from bacterial suspensions supports the notion of single fluorescent bacterium being sufficient as the laser gain medium. Irradiation of the selected bacterial cell serving as the laser gain medium with the high-fluence pump beam raises the question of viability of the cell upon prolonged light exposure. Even though we did not observe any obvious changes

in the integrity of the irradiated cells after recording the spectra, we cannot rule out a more subtle damage of vital organelles of the cell. Daddysman and Fecko studied localized damage of DNA in eukaryotic cells induced by multi-photon absorption of focused fs laser pulses with the pulse width, repetition rate, wavelength, and focal spot radius very similar to our experiments [110]. They found out that the total energy of 100-300 nJ deposited to the specimen (He-La cells or polytene nuclei of *Drosophila* salivary gland cells) is sufficient to cause observable DNA damage. In our experiments with bacteria lasing, the typical energy deposited to the lasing cell for recording a single spectral frame was approximately 600 nJ (120 mW of mean power at the specimen with 5 μ s exposure time). Thus, it is quite likely that the bacterial DNA was at least partially damaged. However, in our case, not all of the pump laser energy reaching the specimen was actually absorbed by the DNA. In *E. coli*, nucleoid (the bacterial chromosome) typically occupies a region with the volume of about 0.23 μm^3 which corresponds to a sphere with the radius of approximately 0.38 μm [111], equal to the radius of the pump beam waist used in our study ($\sim 0.40 \mu\text{m}$). Since the Venus-expressing irradiated cells displayed strong fluorescence, it follows that a significant part of the pump light was absorbed by the fluorescent protein and, thus, it did not reach the DNA. Moreover, even if the originally selected lasing cell is irreversibly damaged by the pump beam, other cells within the same droplet that have not been exposed to the pump light are unaffected and, consequently, they can be used as the gain medium in the next trial.

Chapter 6

SIMULATION OF OPTOFLUIDIC FRET LASERS FOR BIOSENSING PURPOSES

The purpose of this chapter is to carry out a comprehensive analysis of optofluidic FRET lasers using the framework of rate equations for the excited state populations of the donor and acceptor molecules and the corresponding donor and acceptor photon densities. We aim to provide both fundamental understanding of FRET lasers and strategies for constructing optimized FRET lasers for better sensing and photonic performances. To keep the text self-contained, we start with the description and analysis of FRET lasers in which the donor and acceptor molecules are randomly distributed in bulk solution contained within a Fabry-Pérot cavity. Subsequently, we focus on FRET lasers based on molecular constructs linking the donor and acceptor dyes at a predetermined constant distance and stoichiometric ratio. We study the performance of FRET lasers as a function of concentration of the donor and acceptor molecules in the laser cavity, pump fluence, and intermolecular distance between the acceptor and donor molecules. For lasers containing linked donor/acceptor pairs, we analyze the sensitivity of the FRET output signal to changes of donor/acceptor intermolecular spacing and concentration of linked complexes in the laser cavity. We show that when the FRET lasers are operated in an optimal range of pump fluences and linked complex concentrations, for linker lengths around the Förster radius, more than 100 times enhancement can be achieved in output signal sensitivity in comparison to the conventional FRET measurements based on spontaneous fluorescence.

6.1 Mechanisms of Nonradiative Energy Transfer Between Dye Molecules

In general when there is an overlap between donor emission and acceptor absorption spectra, energy can be transferred from donor molecules to acceptor ones. If the average distance between donor and acceptor molecules is more than ~ 10 nm, donor and acceptor do not interact with each other and energy transfer happens radiatively through emission of a

photon by donor and reabsorption by acceptor. This radiative energy transfer strongly depends on the dye concentrations since higher concentrations translate to lower donor-acceptor distances. When donor and acceptor come closer (in the distance range of 2-10 nm) there will be a strong dipole-dipole interaction that will result in non-radiative transfer of energy from donor to acceptor. For distances less than 2 nm other interaction mechanisms are more dominant that also result in non-radiative energy transfer. These mechanisms include intermolecular orbital overlap and multipolar Coulombic interactions that we will not discuss in this thesis.

6.1.1 FRET Between an Isolated Pair of Donor/Acceptor

The dipole-dipole interaction which results in nonradiative energy transfer is known as Förster(or Fluorescence) Resonance Energy Transfer (FRET). FRET rate between a single donor/acceptor pair can be calculated using classical considerations as well as quantum mechanical methods as the following [112]

$$k_{F0} = \frac{1}{\tau_d} \left(\frac{R_0}{R} \right)^6, \quad (6.1)$$

where R and R_0 are the separation distance and Förster radius of the FRET pair, respectively and τ_d is the donor lifetime in the absence of energy transfer. Förster radius R_0 is basically the distance between acceptor and donor at which the spontaneous decay rate and energy transfer rate for donor are equal. R_0 can be determined using the spectroscopic data for the donor and acceptor using the following equation [112]

$$R_0 = \frac{9000 \ln(10) \kappa^2 \varphi_D^0}{128 \pi^5 N_A \eta^4} \int_0^\infty I_D(\lambda) \epsilon_A(\lambda) \lambda^4 d\lambda, \quad (6.2)$$

where φ_D^0 is the fluorescence quantum yield of the donor in the absence of transfer and η is the average refractive index of the medium in the wavelength range where spectral overlap is significant, $I_D(\lambda)$ is the normalized fluorescence spectrum of the donor so that $\int_0^\infty I_D(\lambda) d\lambda = 1$, $\epsilon_A(\lambda)$ is the molar absorption coefficient of the acceptor, N_A is the Avogadro's number, and κ^2 is the orientation factor that in principle can take values from 0 (perpendicular transition moments) to 4 (collinear transition moments). For an isotropic solution of molecules for which the decay rate of donor molecules is much lower than the rotational rate of the molecules, isotropic dynamic averaging of rotation factor results in

$\kappa^2 = 2/3$. Moreover, static isotropic averaging in a rigid medium for an ensemble of acceptors that are statistically randomly distributed about the donor results in $\kappa^2 = 0.476$.

The FRET efficiency is defined as

$$\varphi_{\text{FRET}} = \frac{k_{F0}}{1/\tau_d + k_{F0}} \quad (6.3)$$

Using Eq. 6.1, the FRET efficiency can be written as

$$\varphi_{\text{FRET}} = \frac{1}{1 + (R/R_0)^6} \quad (6.4)$$

This equation shows that for $R = R_0$ the transfer efficiency is 50 %.

6.1.2 FRET for Ensemble of Acceptors Around a Donor

If we assume a donor surrounded by N randomly isotropically distributed acceptor, for the rigid and fixed positions of molecules the probability function $\rho(t)$ for finding the donor at excited state at time t , when it is excited at $t = 0$, is [112]

$$\frac{d\rho(t)}{dt} = - \left[1 + \sum_{p=1}^N \left(\frac{R_0}{R_p} \right)^6 \right] \frac{1}{\tau_d} \rho(t) \quad (6.5)$$

Solving this differential equation by assuming $\rho(0) = 1$ gives

$$\rho(t) = e^{-\left[1 + \sum_{p=1}^N \left(\frac{R_0}{R_p} \right)^6\right] \frac{t}{\tau_d}} = e^{-\frac{t}{\tau_d}} \prod_{p=1}^N e^{-\left(\frac{R_0}{R_p} \right)^6 \frac{t}{\tau_d}} \quad (6.6)$$

Assuming a radially symmetric distribution of acceptor molecules around the donor at continuous distances of R instead of discrete R_p values with a weight function of $w(R)$, we can write the spatial average value for $\rho(t)$ as the following

$$\begin{aligned} \overline{\rho(t)} &= e^{-\frac{t}{\tau_d}} \prod_{p=1}^N \left[\int_0^{R_g} e^{-\frac{t}{\tau_d} \left(\frac{R_0}{R_p} \right)^6} w(R_p) dR_p \right] \\ &= e^{-\frac{t}{\tau_d}} \left[\int_0^{R_g} e^{-\frac{t}{\tau_d} \left(\frac{R_0}{R} \right)^6} w(R) dR \right]^N \\ &= e^{-\frac{t}{\tau_d}} [J(t)]^N \end{aligned} \quad (6.7)$$

Here R_g is the effective range of the dipole-dipole interaction; hence the interaction volume around the donor is $V_i = 4\pi R_g^3/3$. For uniform distribution, the weight function is $w(R)dR = 4\pi R^2 dR/V_i$, so we have

$$J(t) = \frac{4\pi}{V_i} \int_0^{R_g} e^{-\frac{t}{\tau_d} \left(\frac{R_0}{R} \right)^6} R^2 dR \quad (6.8)$$

Using change of variables $\alpha = \left(\frac{R_0}{R}\right)^6 \frac{t}{\tau_d}$ and $\alpha_g = \left(\frac{R_0}{R_g}\right)^6 \frac{t}{\tau_d}$, and assuming a large interaction radius i.e. $R_0 \ll R_g$, during the donor decay time (i.e. $0 \leq t \leq 5\tau_d$), we can conclude that $\alpha_g \ll 1$; hence the solution for the Eq. 6.8 becomes

$$\begin{aligned} J(t) &= \frac{1}{2} \sqrt{\alpha_g} \int_{\alpha_g}^{\infty} \alpha^{3/2} e^{-\alpha} d\alpha \\ &\approx 1 - \sqrt{\pi \alpha_g} \end{aligned} \quad (6.9)$$

By substituting Eq. 6.9 in Eq. 6.7 we have

$$\begin{aligned} \overline{\rho(t)} &= e^{-\frac{t}{\tau_d}} [1 - \sqrt{\pi \alpha_g}]^N = e^{-\frac{t}{\tau_d}} \lim_{N \rightarrow \infty} \left[1 - \frac{1}{N} N \sqrt{\pi \alpha_g} \right]^N \\ &= e^{-\frac{t}{\tau_d}} e^{-N \sqrt{\pi \alpha_g}} = \exp \left(-\frac{t}{\tau_d} - \frac{\sqrt{\pi} N R_0^3}{R_g^3} \sqrt{\frac{t}{\tau_d}} \right) \end{aligned} \quad (6.10)$$

Equation 6.10 shows that spontaneous decay of the donor molecules in the presence of acceptor molecules is not a simple exponential function of time and has an extra \sqrt{t} term that has transient effect on the decay rate in the beginning of the transfer. To obtain a time independent fluorescence yield for donor in the presence and absence of acceptor molecules φ_D and φ_D^0 , respectively, we can perform the following time averaging on Eq. 6.10

$$\varphi_D = C \int_0^{\infty} \overline{\rho(t)} dt \quad (6.11a)$$

$$\varphi_D^0 = C \int_0^{\infty} e^{-\frac{t}{\tau_d}} dt = C \tau_d \quad (6.11b)$$

where C is an unknown normalization constant. By choosing $s = t/\tau_d$ and

$$\beta = \frac{\sqrt{\pi}}{2} \frac{N R_0^3}{R_g^3} = \frac{2}{3} \pi^{\frac{3}{2}} N_a R_0^3 \quad (6.12)$$

where $N_a = N/(\frac{4}{3}\pi R_g^3)$ is the concentration of acceptor molecules; and dividing two equation in Eq. 6.11 we get

$$\begin{aligned} \frac{\varphi_D}{\varphi_D^0} &= \int_0^{\infty} e^{-s-2\beta\sqrt{s}} ds \\ &= 1 - \sqrt{\pi} \beta \exp(\beta^2) \operatorname{erfc}(\beta) \end{aligned} \quad (6.13)$$

where erfc is the complementary error function. Now from the definition of FRET we can calculate the FRET efficiency for a donor chromophore surrounded by an ensemble of

acceptors in a bulk solution of donor/acceptor as the following

$$\begin{aligned}
 \left(\varphi_{\text{FRET}}\right)_{\text{bulk}} &= \frac{\text{fluorescence in absence of acceptors} - \text{fluorescence in presence of acceptors}}{\text{fluorescence in absence of acceptors}} \\
 &= \frac{\varphi_D^0 - \varphi_D}{\varphi_D^0} \\
 &= 1 - \frac{\varphi_D}{\varphi_D^0} \\
 &= \sqrt{\pi} \beta \exp(\beta^2) \operatorname{erfc}(\beta)
 \end{aligned} \tag{6.14}$$

By substituting $\left(\varphi_{\text{FRET}}\right)_{\text{bulk}}$ from Eq. 6.14 to Eq. 6.3 and solving for k_F we get:

$$(k_F)_{\text{bulk}} = \frac{1}{\tau_d} \left(\frac{\sqrt{\pi} \beta \exp(\beta^2) \operatorname{erfc}(\beta)}{1 - \sqrt{\pi} \beta \exp(\beta^2) \operatorname{erfc}(\beta)} \right). \tag{6.15}$$

6.2 Rate Equation Model

Our rate equations are based on those developed previously for a dye laser consisting of a single-dye gain medium [113]. These equations have been expanded to account for the presence of a saturable absorber dye acting as an energy acceptor which is radiatively coupled to the donor dye [114, 115]. Moreover, additional terms describing FRET-based non-radiative energy transfer between the donor and acceptor molecules have been included [116]. The complete energy level diagram of the gain medium and transitions considered in our model is shown in Fig. 6.1(a).

The coupled differential equations used to describe the population dynamics of FRET dye pair serving as the laser gain medium read as:

$$\begin{aligned}
 \frac{dn_d(t)}{dt} &= I_p(t) \sigma_{pd} [N_d - n_d(t)] - \frac{\sigma_{eddC}}{\eta} n_d(t) q_d(t) \\
 &\quad + \frac{\sigma_{addC}}{\eta} [N_d - n_d(t)] q_d(t) - \frac{n_d(t)}{\tau_d} \\
 &\quad - k_F n_d(t),
 \end{aligned} \tag{6.16}$$

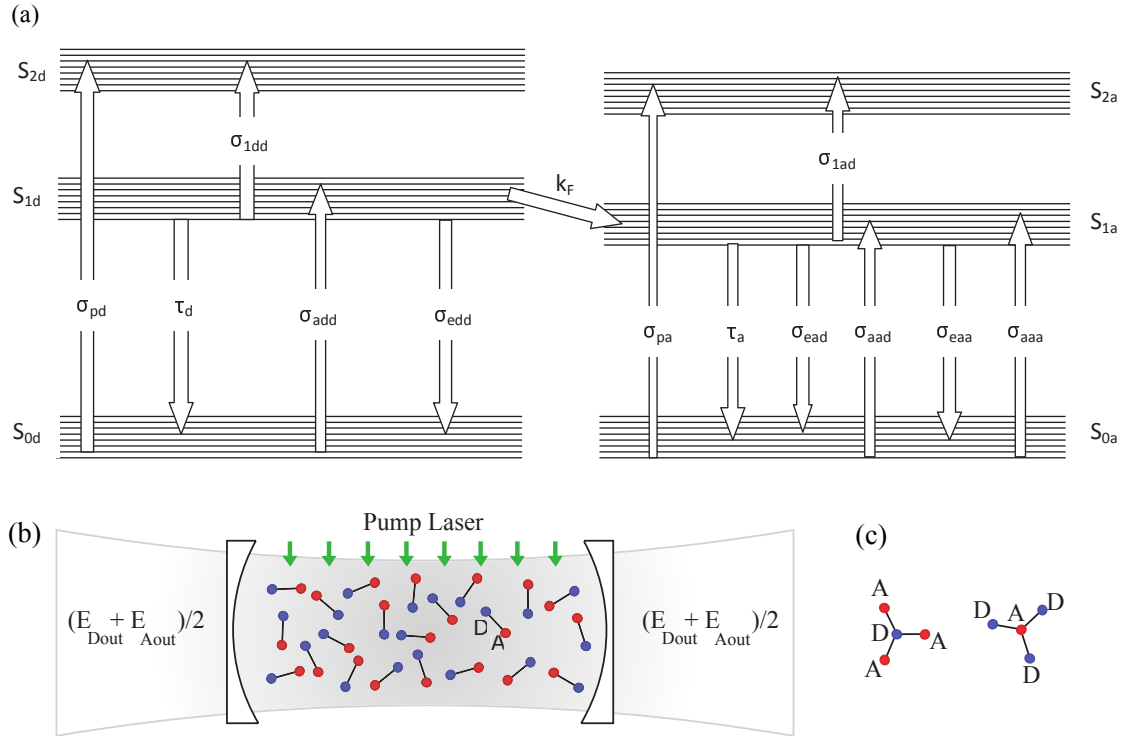


Figure 6.1: (a) Schematic diagram of molecular energy levels for a pair of donor and acceptor dyes showing the lowest three singlet energy levels and their sub-levels for each dye. All relevant electronic transitions that are included in our rate equation model are identified by absorption and emission cross sections specified on the arrows with appropriate transition direction. Non-radiative FRET is assumed to happen between S_{1d} and S_{1a} energy bands. Definitions of individual symbols are given in the text. (b) A simplified Fabry-Pérot laser cavity with two identical output couplers and linked donor/acceptor pairs representing FRET-based active medium. (c) Schematics of molecular constructs with a constant donor-acceptor distance containing one donor linked to three acceptors (1D – 3A) or three donors linked to one acceptor (3D – 1A).

$$\begin{aligned}
 \frac{dq_d(t)}{dt} = & \frac{Fc}{\eta} [\sigma_{edd} - \sigma_{1dd}] n_d(t) q_d(t) + \frac{Fc}{\eta V} \sigma_{edd} n_d(t) \\
 & - \frac{Fc}{\eta} \sigma_{add} [N_d - n_d(t)] q_d(t) - \frac{q_d(t)}{\tau_{cd}} \\
 & + \frac{Fc}{\eta} \sigma_{ead} n_a(t) q_d(t) - \frac{Fc}{\eta} \sigma_{1ad} n_a(t) q_d(t) \\
 & - \frac{Fc}{\eta} \sigma_{aad} [N_a - n_a(t)] q_d(t) ,
 \end{aligned} \tag{6.17}$$

$$\begin{aligned}
\frac{dn_a(t)}{dt} = & I_p(t) \sigma_{pa} [N_a - n_a(t)] - \frac{\sigma_{ead}c}{\eta} n_a(t) q_d(t) \\
& - \frac{n_a(t)}{\tau_a} + \frac{\sigma_{aad}c}{\eta} [N_a - n_a(t)] q_d(t) \\
& - \frac{\sigma_{eaa}c}{\eta} n_a(t) q_a(t) + k_F n_d(t) \\
& + \frac{\sigma_{aaa}c}{\eta} [N_a - n_a(t)] q_a(t) ,
\end{aligned} \tag{6.18}$$

$$\begin{aligned}
\frac{dq_a(t)}{dt} = & \frac{Fc}{\eta} [\sigma_{eaa} - \sigma_{1aa}] n_a(t) q_a(t) + \frac{Fc}{\eta V} \sigma_{eaa} n_a(t) \\
& - \frac{Fc}{\eta} \sigma_{aaa} [N_a - n_a(t)] q_a(t) - \frac{q_a(t)}{\tau_{ca}} .
\end{aligned} \tag{6.19}$$

In these equations, n_d , n_a and q_d , q_a describe the spatially averaged, time-dependent densities of the dye molecules in the first excited states S_{1d} , S_{1a} , and the time-dependent photon densities at a single lasing line for the donor and acceptor dyes, respectively. σ_{pd} , σ_{pa} , σ_{edd} , σ_{eaa} , σ_{ead} , σ_{add} , σ_{1dd} , σ_{1aa} , σ_{1ad} , σ_{aad} , and σ_{aaa} describe different absorption and emission cross-sections of the donor and acceptor molecules, as summarized in Table 6.1. $I_p(t)$ is the time-dependent pump intensity in the units of photons/(cm² · s), N_d and N_a are the total concentrations of donor and acceptor molecules, and k_F is the FRET rate. η is the refractive index of the medium. τ_d and τ_a are the fluorescence lifetimes for donor and acceptor molecules, respectively. τ_{cd} and τ_{ca} denote cavity decay times at the donor and acceptor lasing wavelengths (λ_d and λ_a), respectively. We calculate τ_{cd} and τ_{ca} using the general relation $\tau_c(\lambda) = Q_0\lambda/(2\pi c)$ where Q_0 denotes the quality factor (Q-factor) of an empty cavity and c denotes the speed of light in vacuum. V is the mode volume and F is the fraction of the mode volume occupied by the dye molecules. The second terms on the right-hand side of Eqs. 6.17 and 6.19 describe the photon noise generation or spontaneous emission, indicating the fraction of spontaneously emitted photons coupled into the lasing modes. In accordance with Ref. [113], our calculations are insensitive to the absolute value of the coefficients in these spontaneous emission terms. In this paper, we assume donor and acceptor lasing at a single wavelength (optical mode), although our rate equation model can be extended to multi-mode lasing by adding differential equations describing the rates of changes for photon densities at these additional optical modes [113].

In this paper, we consider gain medium placed into a simple rectangular Fabry-Pérot optical cavity (see Fig. 6.1(b)). Assuming identical out-coupling coefficients for both mirrors of the cavity, the time-dependent total output power emitted from both sides of the cavity from the donor and acceptor dyes can be calculated using the following equations [117]

$$P_{Dout}(t) = \frac{hcq_d(t) V_p}{\lambda_d \tau_{cd}}, \quad (6.20)$$

and

$$P_{Aout}(t) = \frac{hcq_a(t) V_p}{\lambda_a \tau_{ca}}, \quad (6.21)$$

where V_p is the volume of the pumped region of the laser gain medium that can be determined from the pumping beam profile and its illumination geometry and h is the Planck constant. The total output energy of the donor and acceptor pulses (E_{Dout} and E_{Aout} , respectively), can be subsequently calculated by integrating $P_{Dout}(t)$ and $P_{Aout}(t)$ over time. We consider a uniform profile of the pump beam illuminating the gain medium from the top of the Fabry-Pérot cavity (see Fig. 6.1(b)). For simplicity, we further assume that the electromagnetic mode density inside the cavity is uniform and, thus, the mode volume can be represented as $V = dwl$, where d , w , and l are the spatial extents of the electromagnetic mode in individual dimensions. The pump beam penetration depth into the active lasing medium is $d_p = 1/(N_d \sigma_{pd} + N_a \sigma_{pa})$. The condition below can be used for determining the value of V_p depending on the values of d and d_p

$$V_p = \min(FV, Fd_p V/d). \quad (6.22)$$

FRET efficiency, k_F , is influenced by the actual configuration of the donor and acceptor molecules. For the case of the donor and acceptor molecules dissolved in a liquid medium, moving freely relative to each other, k_F is essentially a time-dependent parameter. Depending on the solvent viscosity and the lifetime of the donor excited state, time dependence of k_F can be determined using different methods [118]. For typical organic dyes with large molecules dissolved in typical solvents like ethanol or water at concentrations less than a few mM, the diffusion lengths of the donor and acceptor dye molecules during the donor decay time (typically a few ns) are much smaller than the average separation distance between the donor and acceptor molecules. In such a case, donor and acceptor molecules can be

assumed to be at fixed positions, and an average energy transfer rate can be obtained using Eq. 6.15.

For the case that the donor and acceptor molecules are connected to each other through a linker molecule which ensures a fixed separation distance [69, 71], and under the condition that the overall concentration of linked complexes is low enough so that the donors/acceptors in individual complexes do not transfer energy to other donors/acceptors in the neighboring complexes, k_F can be determined using the basic transfer rate shown in Eq. 6.1. When an individual linked dye complex contains just one donor and one acceptor molecule, the rate of FRET is simply $k_F(1D - 1A) = k_{F0}$. However, when the ratio of donors and acceptors in an individual complex is not unity, k_F will be equal to different fractions of k_{F0} , depending on the actual number of donors and acceptors in the complex. In Fig. 6.1(c), two distinct linked complexes considered in this thesis are shown. The first complex has one donor and three identical acceptors located at equal distances from the donor, $1D - 3A$, and the second complex has one acceptor and three identical donors located at equal distances from the acceptor, $3D - 1A$. For $1D - 3A$, the transfer rate increases threefold and we have $k_F(1D - 3A) = 3k_{F0}$ whereas for $3D - 1A$, the transfer rate for each donor is limited to one acceptor and, thus, $k_F(3D - 1A) = k_{F0}$.

In the simulations presented in this article, we study a model system for optofluidic FRET lasing which consists of Rhodamine 6G (R6G) as the donor and Acid Blue 7 (AB7) as the acceptor. The values of various transition cross-sections and lifetimes describing this FRET pair are summarized in Table 6.1 together with other relevant simulation parameters. The coupled rate equations 6.16 - 6.19 are numerically solved for different excitation pump profiles, $I_p(t)$, using MATLAB [119] stiff ODE solver ODE15s for varying donor/acceptor molecular arrangements and concentrations (see the MATLAB codes in Appendix C). We assume a Gaussian temporal profile of pump intensity, $I_p = I_{p0} \cdot \exp(-4 \cdot \ln 2 \cdot [(t - t_0)/\Delta t]^2)$, with $\Delta t = 5$ ns or $\Delta t = 50$ μ s pulsewidth. Peak intensity of the pulse (I_{p0}) is then calculated using $I_{p0} = \frac{0.94\lambda_p}{hc\Delta t} \Phi_p$, where Φ_p is the pulse energy fluence and λ_p is the pump wavelength. At pump intensities above the lasing threshold, multiple lasing peaks are observed in the temporal profiles of the donor and acceptor emissions due to Q-switching in the gain medium [114, 115, 116]. When reporting the total output lasing energy for a given combination of system parameters (pump fluence, dye concentration, spacing between

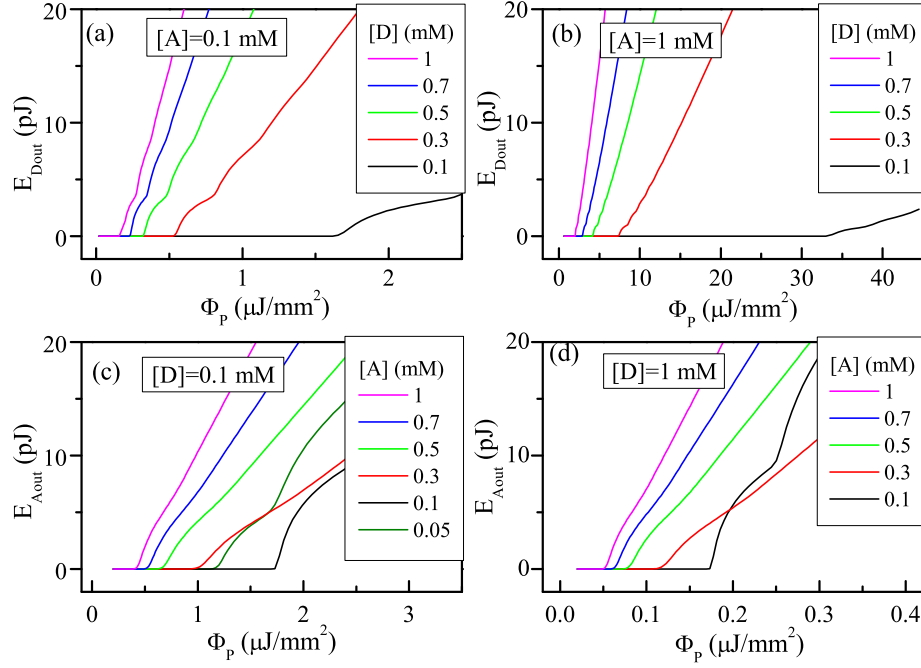


Figure 6.2: Total output emission energy E_{Dout} , E_{Aout} from bulk solutions of R6G/AB7 FRET pair as a function of the pump fluence, Φ_P . (a) Donor lasing with fixed acceptor concentration $[A] = 0.1$ mM and varying donor concentration $[D] = 1$ to 0.1 mM. (b) Donor lasing with fixed acceptor concentration $[A] = 1$ mM and varying donor concentration $[D] = 1$ to 0.1 mM. (c) Acceptor lasing with fixed donor concentration $[D] = 0.1$ mM and varying acceptor concentration $[A] = 1$ to 0.05 mM. (d) Acceptor lasing with fixed donor concentration $[D] = 1$ mM and varying acceptor concentration $[A] = 1$ to 0.1 mM.

donor and acceptor), we always use integral values including all output pulses excited with a single pump pulse.

6.3 Threshold Behavior in Bulk FRET Lasers

We begin our analysis of optofluidic FRET lasers by characterizing the main properties of donor and acceptor lasing for the case of the donor and acceptor molecules dissolved in a bulk solution, without being linked at a fixed separation distance. Figure 6.2 shows the total output energy of donor and acceptor emissions, E_{Dout} and E_{Aout} , calculated for a wide range of donor and acceptor concentrations ($[D]$ and $[A]$) as a function of the pump fluence (Φ_P). In all studied cases, the slope of the curves changes abruptly at a certain threshold value of Φ_P that indicates the onset of lasing. In several cases (such as donor lasing at $[A] = 0.1$ mM

and acceptor lasing at $[D] = 0.1$ mM), the output energy curve displays ripples for Φ_P values larger than the lasing threshold. This is a consequence of multiple lasing peaks appearing in the temporal profile of the output power induced by the gain Q-switching [116]. Figure 6.3 shows detailed views of the donor (Fig. 6.3(a)) and acceptor (Fig. 6.3(b)) output energy curves. Insets in the respective subfigures illustrate the temporal profiles of the donor and acceptor output emission power $P_{\text{Dout}}(t)$ and $P_{\text{Aout}}(t)$ for different Φ_P values. Temporal narrowing of the output pulse and appearance of multiple after-pulses with increasing Φ_P are clearly visible for both donor and acceptor laser emissions.

Threshold values of Φ_P for donor and acceptor lasing extracted from the output energy curves similar to those presented in Fig. 6.2 are shown in Fig. 6.4 for different donor and acceptor concentrations. In order to elucidate the effect of the FRET channel on the overall behavior of the optofluidic lasers using a mixture of two fluorescent dyes as the laser gain medium, we also performed calculations in which the FRET transition was turned off by setting $k_F = 0$. These cases are indicated by dashed lines in Fig. 6.4. With the inactive FRET channel, the donor and acceptor dyes can still couple radiatively through the cavity-enhanced energy transfer (CET) in which the resonant photons emitted by the donor and circulating in the laser cavity are reabsorbed by the acceptor molecules [120, 121, 122].

Figure 6.4(a) shows the threshold Φ_P for donor lasing as a function of acceptor concentration ($[A] = 0.01$ -5 mM) for different fixed donor concentrations ($[D] = 0.01$ mM, 0.1 mM, 1 mM, 5 mM). For $[D]$ between 1-5 mM, donor lasing is observed for all values of $[A]$, while for $[D] = 0.01$ mM and $[D] = 0.1$ mM, donor lasing is not observed for $[A] > 0.2$ mM and $[A] > 2$ mM, respectively, due to the high absorption of acceptor dye in donor emission wavelength and nonradiative FRET depletion of the excited population of the donor to the acceptor dye. Comparison of the solid and dashed lines in the donor threshold curves obtained for $[D] = 0.01$ mM and 0.1 mM suggests that for these cases, FRET channel does not play a significant role and the donor population is depleted mainly by the radiative CET to the acceptor molecules. For the selected range of $[A]$, donor lasing is not observed at all for $[D] \leq 0.001$ mM. For high donor and acceptor concentrations ($[D], [A] > 1$ mM), donor lasing threshold values obtained with active FRET channel are higher than those corresponding to the inactive FRET case (i.e., $k_F = 0$) due to the additional depletion of the excited donor molecules by the FRET transition.

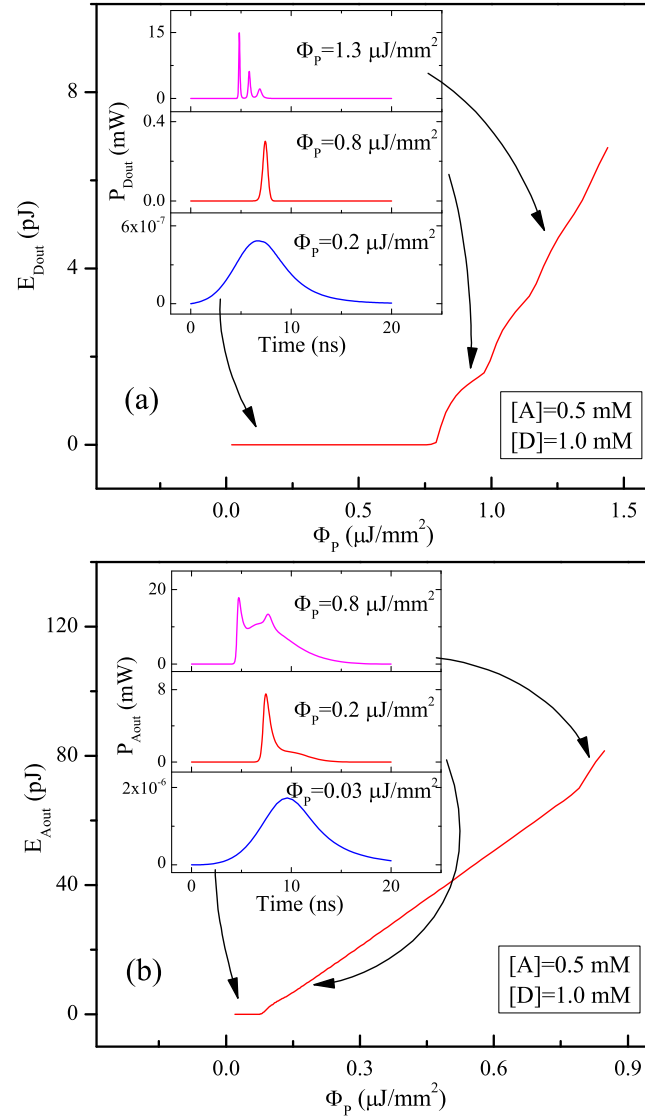


Figure 6.3: Gain Q-switching in optofluidic FRET lasers. (a) Total output emission energy E_{Dout} from the donor as a function of Φ_P . Insets show the time profiles of the donor emission power before reaching the lasing threshold at $\Phi_P = 0.2 \mu\text{J}/\text{mm}^2$, shortly after crossing the threshold at $\Phi_P = 0.8 \mu\text{J}/\text{mm}^2$ (a single output pulse), and well above the threshold at $\Phi_P = 1.3 \mu\text{J}/\text{mm}^2$ (three output pulses corresponding to the third ripple in the output energy curve). (b) Total output emission energy E_{Aout} from the acceptor as a function of Φ_P . Insets show the time profiles of the acceptor emission power before reaching the lasing threshold at $\Phi_P = 0.03 \mu\text{J}/\text{mm}^2$, shortly after crossing the threshold at $\Phi_P = 0.2 \mu\text{J}/\text{mm}^2$ (a single output pulse), and well above the threshold at $\Phi_P = 0.8 \mu\text{J}/\text{mm}^2$ (two output pulses corresponding to the second ripple in the output energy curve).

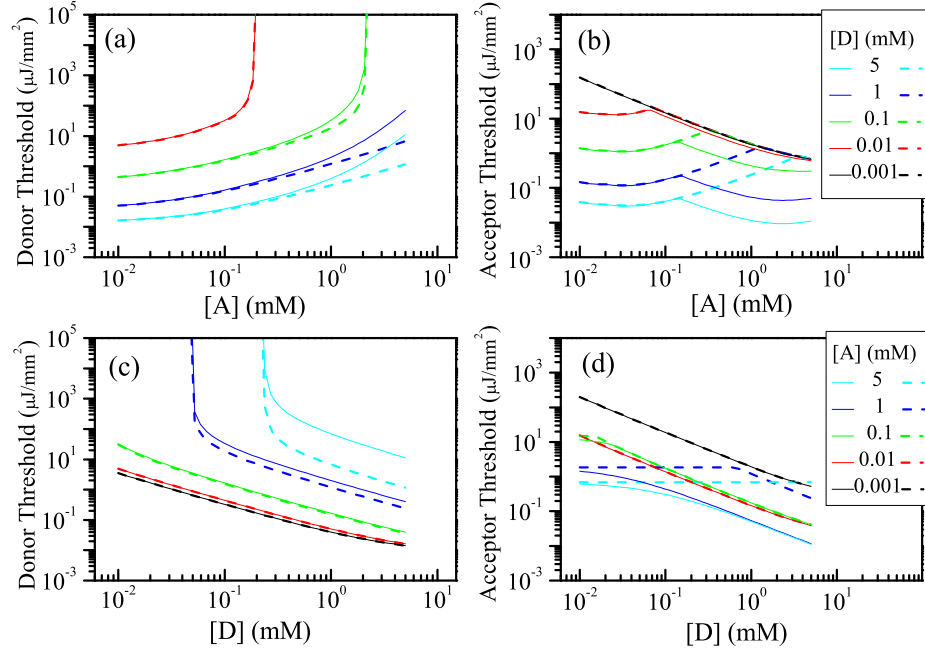


Figure 6.4: Threshold Φ_P of bulk FRET lasing of (a) donor and (b) acceptor as a function of acceptor concentration $[A]$ for several fixed donor concentrations $[D]$. Threshold Φ_P of bulk FRET lasing for (c) donor and (d) acceptor as a function of donor concentration $[D]$ for several fixed acceptor concentrations $[A]$. Solid and dashed curves in (a)-(d) indicate calculations performed assuming active (k_F calculated using Eq. 6.15) and inactive ($k_F = 0$) FRET channels, respectively. The figure legends for (a) and (c) are shown in (b) and (d), respectively.

Threshold values of Φ_P for acceptor lasing are plotted in Fig. 6.4(b) as a function of $[A]$ for different fixed values of $[D]$. In general, higher values of $[D]$ lead to lowering of the acceptor lasing threshold due to more efficient pumping of the acceptor. In the active FRET case (solid curves), dependence of the acceptor lasing threshold on $[A]$ displays two different trends. When donor lasing is dominant, i.e., the donor starts lasing at a lower pump fluence than the acceptor (high $[D]$ and low $[A]$), acceptor lasing threshold shows little change or even a slight increase with increasing $[A]$. In contrast, when acceptor lasing becomes dominant (high $[A]$), acceptor lasing threshold decreases with increasing $[A]$. The effect of FRET can be clearly observed for high $[D]$ and $[A]$ (green, blue and cyan curves for $[A] > 0.2$ mM), when the typical distance between the donor and acceptor molecules becomes comparable to the Förster radius R_0 . In this regime, acceptor lasing threshold with active FRET channel lies significantly below the corresponding value for the inactive

FRET case, indicating efficient pumping of acceptor molecules via the non-radiative energy transfer.

Figure 6.4(c) shows the dependence of the donor lasing threshold on $[D]$ for different fixed values of $[A]$. As expected, the donor lasing threshold decreases with increasing $[D]$ and decreasing $[A]$, corresponding to higher gain and lower loss, respectively. For high acceptor concentrations of $[A] = 1$ mM and $[A] = 5$ mM, donor lasing is completely quenched for $[D] \lesssim 0.05$ mM and $[D] \lesssim 0.2$ mM, respectively. The effect of the FRET channel on the donor lasing threshold curves is well visible for $[A] = 1$ -5 mM (compare solid and dashed curves in blue and cyan color). In this range of acceptor concentrations, the presence of the FRET channel leads to higher overall losses for donor lasing, and, therefore, an increase in the donor lasing threshold.

In Fig. 6.4(d), the acceptor lasing threshold is plotted as a function of $[D]$ for different fixed values of $[A]$. With increasing $[D]$, acceptor molecules are pumped more efficiently via the FRET and/or CET channels. This, consequently leads to a decrease in the acceptor lasing threshold. The effect of FRET on the acceptor lasing threshold is clearly visible for $[A] = 1$ -5 mM (compare corresponding solid and dashed curves). At these acceptor concentrations, donor and acceptor molecules are sufficiently close to each other and, thus, the presence of FRET leads to more efficient acceptor pumping that lowers the acceptor lasing threshold.

In summary, the analysis of lasing threshold presented in Fig. 6.4 indicates that in the case of bulk solutions of donor and acceptor, the efficiency of FRET and, therefore, its contribution to the acceptor pumping is determined solely by the dye concentration. For sufficiently high values of $[A]$ and $[D]$, average distance between the donor and acceptor molecules approaches the Förster radius R_0 of the dye pair. Consequently, FRET rate increases dramatically and non-radiative energy transfer becomes the dominant mechanism for acceptor pumping.

6.4 Threshold Behavior in Molecularly Linked FRET Pair Lasers

After analyzing optofluidic lasers based on energy transfer between donor and acceptor molecules dissolved in bulk solutions, we focus our attention on the situation in which the donor and acceptor molecules are connected to each other using a molecular linker

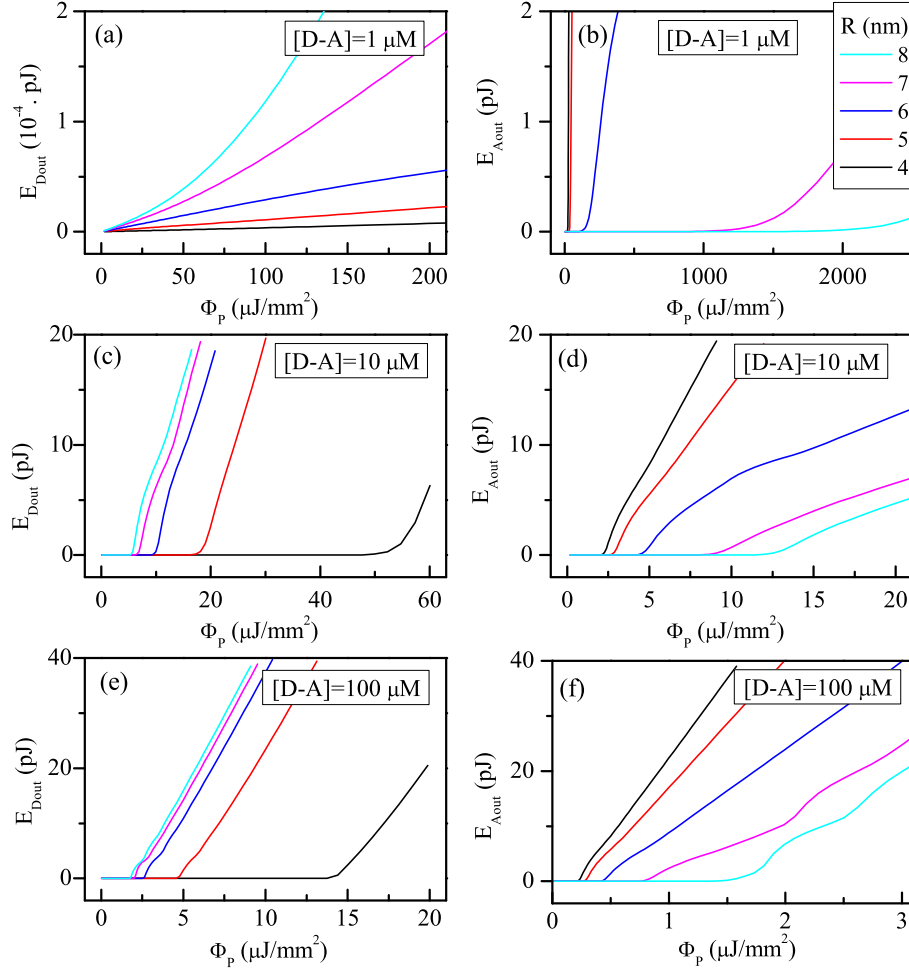


Figure 6.5: Total output emission energy E_{Dout} , E_{Aout} from molecularly linked FRET pair R6G/AB7 (denoted as D-A) as a function of Φ_P for different [D-A] values and linker lengths R . In (a), no lasing is observed in donor emission. Plot legend shown in (b) applies to all sub-figures (a)-(f).

of a fixed length. In this situation, transfer rate k_F describing the efficiency of FRET is a constant independent of the total concentration of linked complexes in the laser gain medium. Figure 6.5 shows the total output energies of the donor and acceptor emissions E_{Dout} and E_{Aout} calculated for the case of a molecularly linked FRET pair (denoted as D-A) for different concentrations of the linked dye complex ([D-A]) and linker lengths (R), as a function of Φ_P . Threshold values of Φ_P obtained from such output energy curves are plotted in Fig. 6.6. With decreasing R which translates into increasing k_F , donor and acceptor lasing threshold fluences are observed to increase and decrease, respectively. In

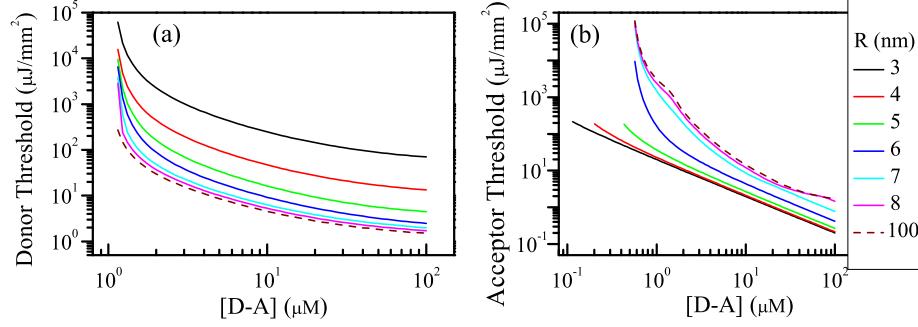


Figure 6.6: (a) Donor lasing threshold as a function of [D-A] for different linker lengths R . (b) Acceptor lasing threshold as a function of [D-A] for different linker lengths R .

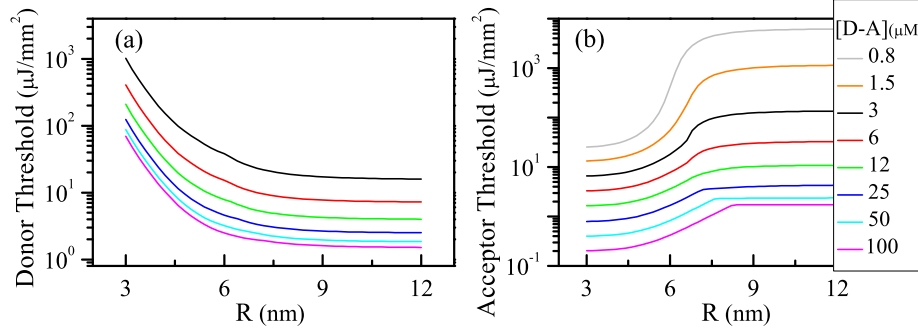


Figure 6.7: (a) Donor lasing threshold as a function of linker length R for different [D-A] values. (b) Acceptor lasing threshold as a function of linker length R for different [D-A] values.

contrast to the bulk case, for the linked case, FRET can be the dominant energy transfer mechanism even at low [D-A] values $\sim 1 \mu\text{M}$, provided that R is comparable to the Förster radius, which is $R_0 = 6.1 \text{ nm}$ for the selected FRET pair. In order to quantify relative contributions of FRET and CET to lasing, we calculated lasing thresholds for a very long linker ($R = 100 \text{ nm}$) where CET becomes the dominant energy transfer mechanism; these calculations are shown as dashed curves in Figs. 6.6(a) and (b). For all [D-A] values studied in Fig. 6.6, when R is comparable to or smaller than R_0 , the donor lasing threshold fluences become significantly higher and the acceptor lasing threshold fluences become significantly lower than the corresponding values for the very long linker case, which are determined solely by CET. Hence, for the range of [D-A] values under study and linker lengths $R \lesssim R_0$, FRET is the dominant mechanism for determining the donor and acceptor lasing properties.

Figure 6.7 shows the donor and acceptor lasing threshold fluences calculated for a molecularly linked FRET pair as a function of R for different $[D-A]$ values. For $[D-A] < 3 \mu\text{M}$, donor lasing is not observed. Hence, in Fig. 6.7, donor lasing threshold values are plotted for $[D-A]$ ranging between $3 \mu\text{M}$ - $100 \mu\text{M}$ while acceptor lasing threshold values are plotted for $[D-A]$ ranging between $0.8 \mu\text{M}$ - $100 \mu\text{M}$. Donor and acceptor threshold fluences follow different dependencies on R . For the values of R much smaller than R_0 , donor energy is almost fully transferred to the acceptor via the very efficient FRET channel. This leads to a very fast depletion of the excited donor molecules, preventing donor lasing. Hence, donor lasing threshold increases indefinitely as $R \rightarrow 0$. In this regime, acceptor lasing threshold is determined solely by the inherent properties of the acceptor dye, similarly to the case of lasing with a single-dye gain medium. When R is much larger than R_0 , donor and acceptor lasing properties follow the trends observed in the bulk lasing case. Thus, for the concentrations considered in Fig. 6.7, CET becomes the dominant energy transfer mechanism. In this limit, donor and acceptor lasing thresholds do not depend on R .

6.5 Sensitivity of Detection of Conformational Changes in Linked FRET Pair Biocomplexes

Analysis performed in the previous section has shown that in the case of a molecularly linked donor-acceptor dye pair, FRET dominates over CET in providing pump energy for lasing of the acceptor dye molecules provided that $R \lesssim R_0$. Hence, this linked-dye configuration is much more suitable for molecular sensing applications than the bulk case with freely diffusing dye molecules, due to the high sensitivity of the FRET rate to the molecular arrangement of the donor and acceptor molecules. In this section, we consider an optofluidic dye laser with a composite gain medium consisting of molecularly linked FRET pair dyes and simulate its lasing properties in order to understand its biosensing potential.

First, we carry out a benchmark analysis that establishes the sensitivity of a simple FRET-based biosensor operated in the absence of lasing, using solely spontaneous fluorescence emission as the measurement signal. Figure 6.8 shows the results of such an analysis performed using our model, assuming $[D-A] = 5 \mu\text{M}$ and a very low Q-factor of the laser cavity ($Q = 1$) to ensure that lasing is prevented. In Figs. 6.8(a) and (b), we present the donor and acceptor output energies E_{Dout} and E_{Aout} as a function of R for different values

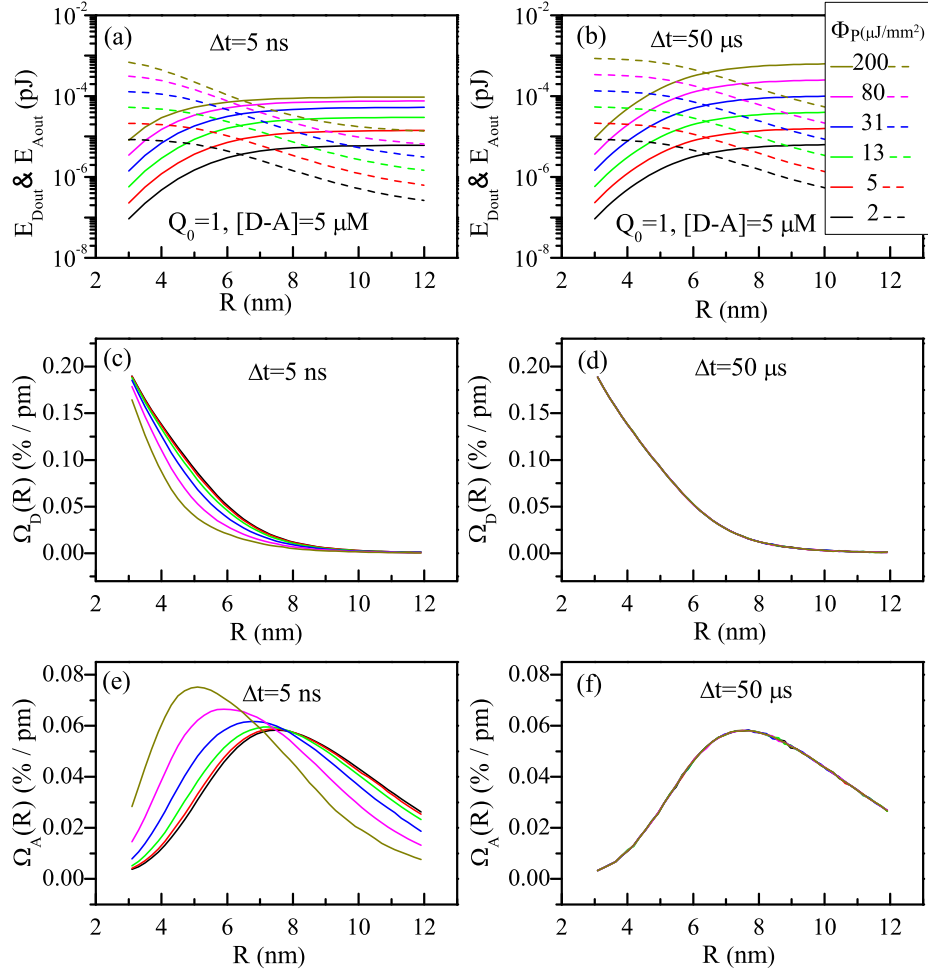


Figure 6.8: Performance of FRET-based biosensors using spontaneous fluorescence emission for $[D - A] = 5 \mu\text{M}$. Donor (solid curves) and acceptor (dashed curves) fluorescence emission energy from linked donor/acceptor pairs versus R at different values of Φ_P for excitation pulsewidth of (a) $\Delta t = 5 \text{ ns}$ and (b) $\Delta t = 50 \mu\text{s}$. Donor emission sensitivity to linker length ($\Omega_D(R)$) versus R for FRET emission from linked donor/acceptor pairs at different values of Φ_P for excitation pulsewidth of (c) $\Delta t = 5 \text{ ns}$ and (d) $\Delta t = 50 \mu\text{s}$. Acceptor emission sensitivity to linker length ($\Omega_A(R)$) versus R for FRET emission from linked donor/acceptor pairs at different values of Φ_P for excitation pulsewidth of (e) $\Delta t = 5 \text{ ns}$ and (f) $\Delta t = 50 \mu\text{s}$. In all these calculations lasing is prevented by assuming $Q = 1$.

of Φ_P at two different excitation pulsewidths, $\Delta t = 5 \text{ ns}$ and $\Delta t = 50 \mu\text{s}$, respectively. In order to quantify the changes in the donor or acceptor emission energies, E_{Dout} , E_{Aout} , triggered by changing the value of a physical parameter X , we define sensitivity, $\Omega(X)$, of emission energy to this parameter using $\Omega(X) = |(100 \times dE_{out}) / (E_{out} dX)|$. In Figs. 6.8(c) and (d), the donor emission sensitivity ($\Omega_D(R) = |(100 \times dE_{Dout}) / (E_{Dout} dR)|$) is plotted

as a function of R for a non-lasing linked donor/acceptor dye pair at different values of Φ_P for $\Delta t = 5$ ns and $\Delta t = 50$ μ s, respectively. Similarly, Figs. 6.8(e) and (f) show the acceptor emission sensitivity ($\Omega_A(R) = |(100 \times dE_{Aout})/(E_{Aout}dR)|$) as a function of R for a non-lasing linked donor/acceptor dye pair at different values of Φ_P for $\Delta t = 5$ ns and $\Delta t = 50$ μ s, respectively.

As illustrated by Figs. 6.8(c) and (e), when Φ_P increases, Ω_D decays faster with increasing R and the maximum of Ω_A shifts toward smaller R values. This behavior is mainly due to the saturation in the absorption of donor molecules. In the absence of the acceptor, output energy of fluorescence emission from the donor dye molecules excited with low pump power depends linearly on the pump power. However, with increasing pump power, output energy of the donor eventually saturates as the number of available dye molecules in the ground state decreases because of the limited decay rate of the donor excited state. In the presence of the acceptor, FRET serves as an additional depletion channel for the excited donor molecules, enabling their faster decay to the ground state and mitigating the effect of saturation. At low pump power when $N_d \gg n_d$, donor absorption represented by the first term on the right-hand side of Eq. 6.16 is virtually independent of R . Hence, the dependence of Ω_D and Ω_A on R derives solely from the changes in FRET efficiency given by Eq. 6.1. However, when the pump power, which is directly proportional to $\Phi_P/\Delta t$, approaches the saturation value of donor absorption, n_d becomes comparable to N_d and, consequently, donor absorption becomes a function of R . Thus, the profiles of $\Omega_D(R)$ and $\Omega_A(R)$ are now determined by the interplay between simultaneously changing FRET efficiency and donor absorption. As the pump power increases toward donor saturation, more assistance from FRET is needed to bring the donor molecules back to the ground state where they can absorb again the pump photons. This leads to a faster decay of Ω_D with increasing R and shifting of maximal values of Ω_A to smaller R where FRET is more efficient.

In order to quantify the donor and acceptor emission sensitivities in a conventional FRET-based bio-sensing assay which typically uses low-power continuous-wave (CW) excitation, we carried out simulations with the pump pulsewidth increased from $\Delta t = 5$ ns to $\Delta t = 50$ μ s. For a constant pump fluence, this translates to the decrease of the average pump power by 4 orders of magnitude, which means the system operates well below the donor saturation level. Consequently, the profiles of $\Omega_D(R)$ and $\Omega_A(R)$ are independent

of the value of Φ_P , following directly the FRET efficiency changes described by Eq. 6.1 (see Figs. 6.8(d) and (f)). In the following, we will use these pump power-invariant linker length sensitivities as a benchmark in quantifying the performance of biosensors based on optofluidic FRET lasers.

Next, in Fig. 6.9, we consider FRET lasing in a high-Q ($Q = 10^6$) cavity and quantify the improvements in sensitivity that can be achieved assuming a linked donor/acceptor pair with $[D - A] = 5 \mu\text{M}$, the same concentration as considered in Fig. 6.8. Figures. 6.9(a) and (b) show the total output energy emitted from the donor and acceptor molecules versus Φ_P for different R values. In Fig. 6.9(a), the donor lasing threshold decreases with increasing linker length because of the lower energy transfer to the acceptor and, thus, lower loss. In contrast, increasing linker length leads to increasing lasing threshold for the acceptor as the pumping efficiency becomes lower due to reduction in FRET rate (see Fig. 6.9(b)). In Figs. 6.9(c) and (d), we present the dependence of E_{Dout} and E_{Aout} , on R at different values of Φ_P . As expected from the above reasoning, at all studied values of Φ_P , E_{Dout} increases monotonously with R whereas E_{Aout} displays the opposite trend.

Figures. 6.9(e) and (f) show $\Omega_D(R)$ and $\Omega_A(R)$ as a function of R at different values of Φ_P . For all values of Φ_P , the profiles of $\Omega_D(R)$ and $\Omega_A(R)$ have Lorentzian-like shapes. With increasing Φ_P , the peak value of $\Omega_D(R)$ increases monotonously and the position of the peak moves toward lower values of R . In contrast, the peak value of $\Omega_A(R)$ reaches maximum for a specific Φ_P which lies around $13 \mu\text{J}/\text{mm}^2$ for the studied Q-factor and FRET complex concentration $[D-A]$. At the same time, peak position of $\Omega_A(R)$ moves toward higher R for increasing Φ_P . The fact that the acceptor sensitivity to the linker length $\Omega_A(R)$ reaches maximum at an intermediate pump fluence Φ_P stems from the combined effect of FRET and CET on the acceptor lasing and it is studied in detail in the next section.

To quantify the enhancement in sensitivity achieved by biosensors based on optofluidic FRET laser as compared to a biosensor using non-lasing FRET, we define the sensitivity enhancement factor Π as the ratio of lasing FRET sensitivity to the regular fluorescence FRET sensitivity, $\Pi = \Omega_{\text{lasing}}(X)/\Omega_{\text{fluorescence}}(X)$. Here, $\Omega_{\text{lasing}}(X)$ is the sensitivity of the output energy of stimulated emission from the donor or acceptor placed inside a high-Q cavity to changes in parameter X characterizing the gain medium whereas $\Omega_{\text{fluorescence}}(X)$ is the corresponding sensitivity of the output energy of regular (non-amplified) fluorescence

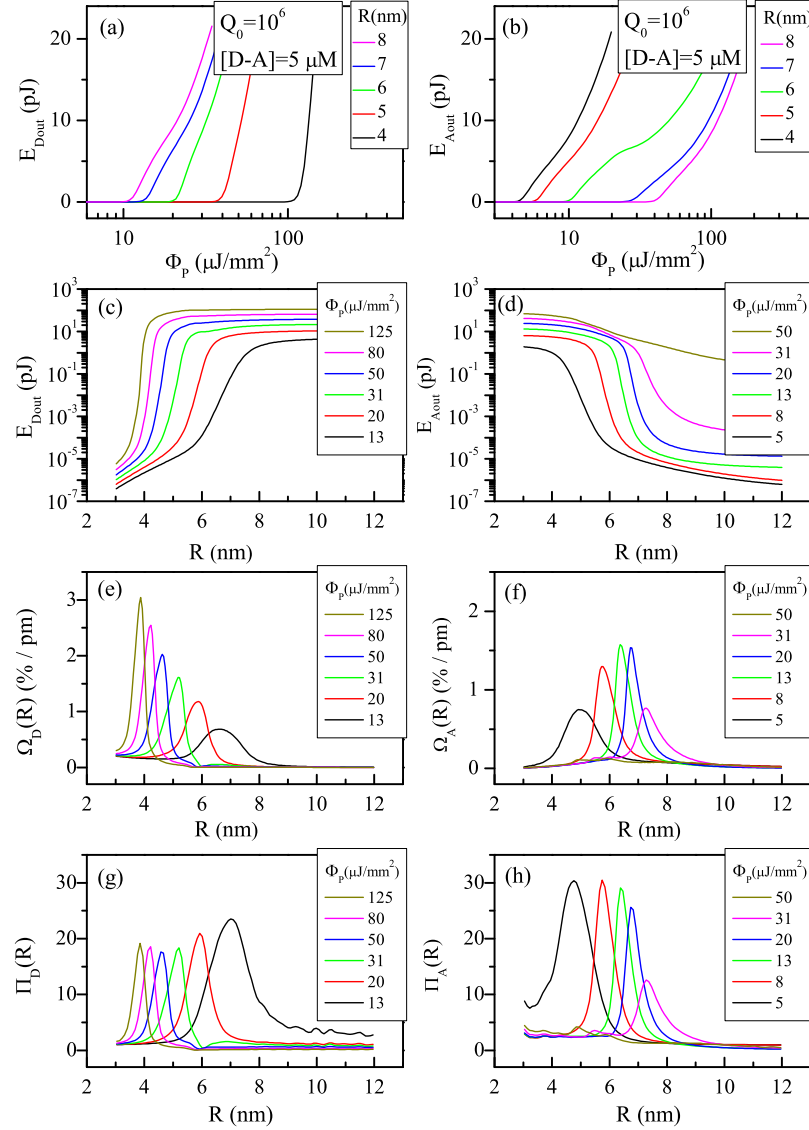


Figure 6.9: Behavior of FRET lasing-based biosensor for changing linker length R . Total output energy of (a) donor and (b) acceptor versus Φ_P for different values of R . Total output energy of (c) donor and (d) acceptor versus R for different values of Φ_P . The linker length sensitivity for (e) donor, $\Omega_D(R)$, versus R and (f) acceptor, $\Omega_A(R)$, versus R , calculated for FRET lasing emission from linked donor/acceptor pairs at different values of Φ_P and a constant value of donor/acceptor complex concentration, $[D-A] = 5 \mu\text{M}$. The sensitivity enhancement factor for (g) donor and (h) acceptor as a function of linker length at different Φ_P values. In all simulations, excitation pulse width was set to $\Delta t = 5 \text{ ns}$ and the cavity Q-factor was 10^6 .

from the donor or acceptor placed inside a cavity with $Q = 1$. Parameter X can be either the donor/acceptor distance R (representing conformational changes in linked dye com-

plex) or the dye complex concentration $[D - A]$. Figures 6.9(g) and (h) show $\Pi_D(R)$ and $\Pi_A(R)$, the donor and acceptor sensitivity enhancement factors, versus R , respectively. In order to calculate $\Pi_D(R)$ and $\Pi_A(R)$, the values of Ω_{lasing} were taken from Figs. 6.9(e) and (f), respectively, whereas the corresponding benchmark values of $\Omega_{\text{fluorescence}}$ come from Figs. 6.8(d) and (f), respectively. As illustrated by Figs. 6.9(g) and (h), maximal enhancement factors of ~ 20 for donor and ~ 25 for acceptor sensitivities are observed for a relatively broad range of R at low pump fluences Φ_P . According to Fig. 6.9(g), the value of $\Pi_D(R)$ reaches maximum for the minimal studied pump fluence $\Phi_P = 13 \mu\text{J}/\text{mm}^2$ and then decreases with increasing Φ_P whereas $\Omega_D(R)$ displays the opposite trend [see Fig. 6.9(e)]. This behavior can be explained by the saturation of donor absorption at high pump fluences which was discussed in detail in Fig. 6.8. In particular, the absorption of lasing donor pumped with $\Delta t = 5 \text{ ns}$ pulses at $\Phi_P > 13 \mu\text{J}/\text{mm}^2$ becomes partially saturated which in turn reduces the effective value of $\Omega_{D,\text{lasing}}(R)$. At the same time, saturation is completely avoided in the benchmark values of $\Omega_{D,\text{fluorescence}}(R)$ which are calculated assuming long pump pulses with $\Delta t = 50 \mu\text{s}$. As a result, $\Pi_D(R) = \Omega_{D,\text{lasing}}(R)/\Omega_{D,\text{fluorescence}}(R)$ is reduced. By lowering Φ_P , the saturation effects are also suppressed in the lasing case and, consequently, the enhancement factor $\Pi_D(R)$ increases. For the case of acceptor, the reason of reduction in $\Pi_A(R)$ for $\Phi_P > 8 \mu\text{J}/\text{mm}^2$ is the progressively increasing magnitude of CET which reduces the sensitivity of the acceptor output energy to the linker length R . For the studied dye complex concentration $[D - A] = 5 \mu\text{M}$, minimal donor lasing threshold corresponding to $R \gg R_0$ is $\Phi_P \approx 13 \mu\text{J}/\text{mm}^2$; upon crossing this value of Φ_P , donor lasing is triggered. Consequently, CET increases dramatically which leads to a drop in $\Pi_A(R)$.

6.6 Effect of Q-factor on Conformational Sensitivities in Linked FRET Pair Biocomplexes

As mentioned briefly in the previous section, sensitivity of the acceptor lasing emission to the linker length $\Omega_A(R)$ is determined by the combined effect of FRET and CET; relative importance of these two mechanisms of acceptor pumping depends on the cavity Q-factor. In this section, we study the influence of Q-factor in a more systematic way. Figure. 6.10 shows emission sensitivities Ω_D and Ω_A for different cavity Q-factors ranging between $10^3 - 10^9$ considering a constant $[D - A] = 5 \mu\text{M}$. For each Q-factor, excitation conditions were fine-

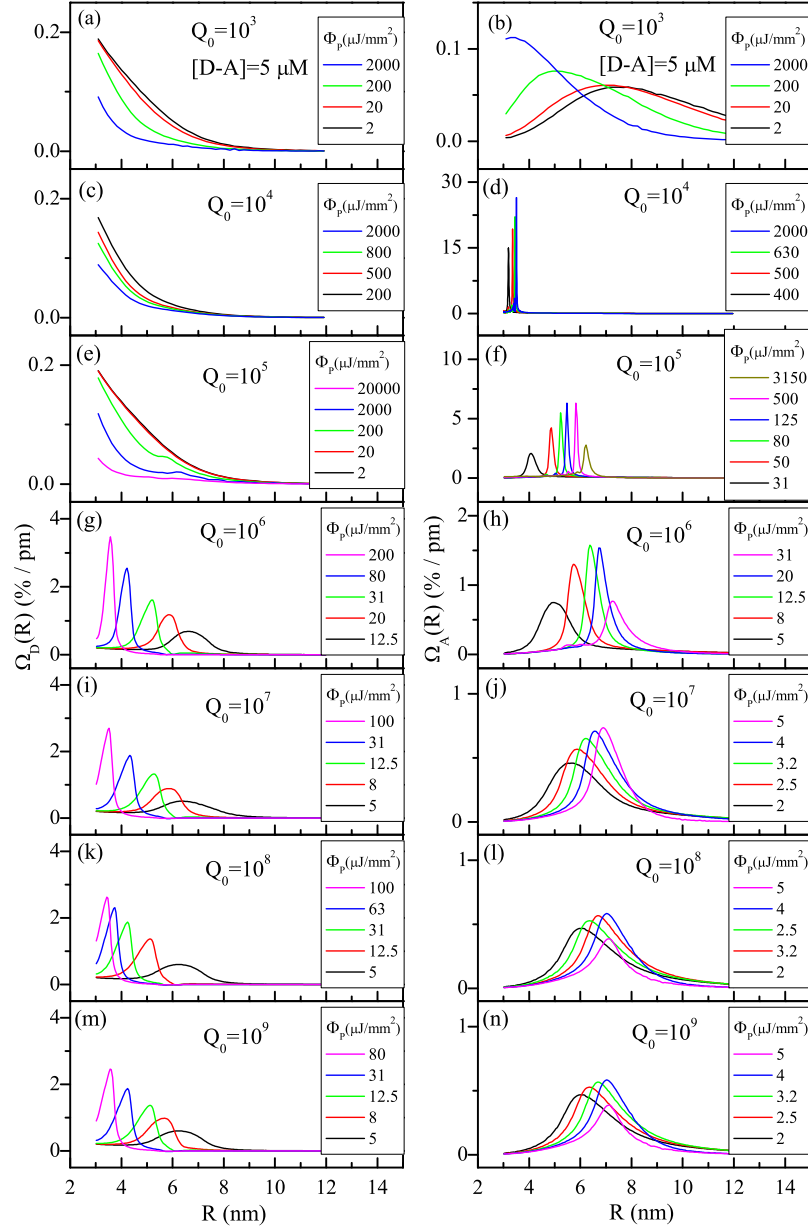


Figure 6.10: Effect of the cavity Q -factor on emission sensitivities of donor, $\Omega_D(R)$, and acceptor, $\Omega_A(R)$, for linked 1D – 1A donor/acceptor complexes at different values of Φ_P and a fixed concentration, $[D - A] = 5 \mu\text{M}$. In (a), (c) and (e) for donor and in (b) for acceptor no lasing is observed.

tuned in order to reveal Φ_P necessary for achieving the maximum FRET sensitivities in donor and acceptor that occur around their respective lasing thresholds. For the case of $Q_0 = 10^3, 10^4$ and 10^5 for donor (Figs. 6.10(a), (c), and (e)) and for $Q_0 = 10^3$ for acceptor (Fig. 6.10(b)), no lasing is observed even at very high Φ_P values. Hence, in these cases, the

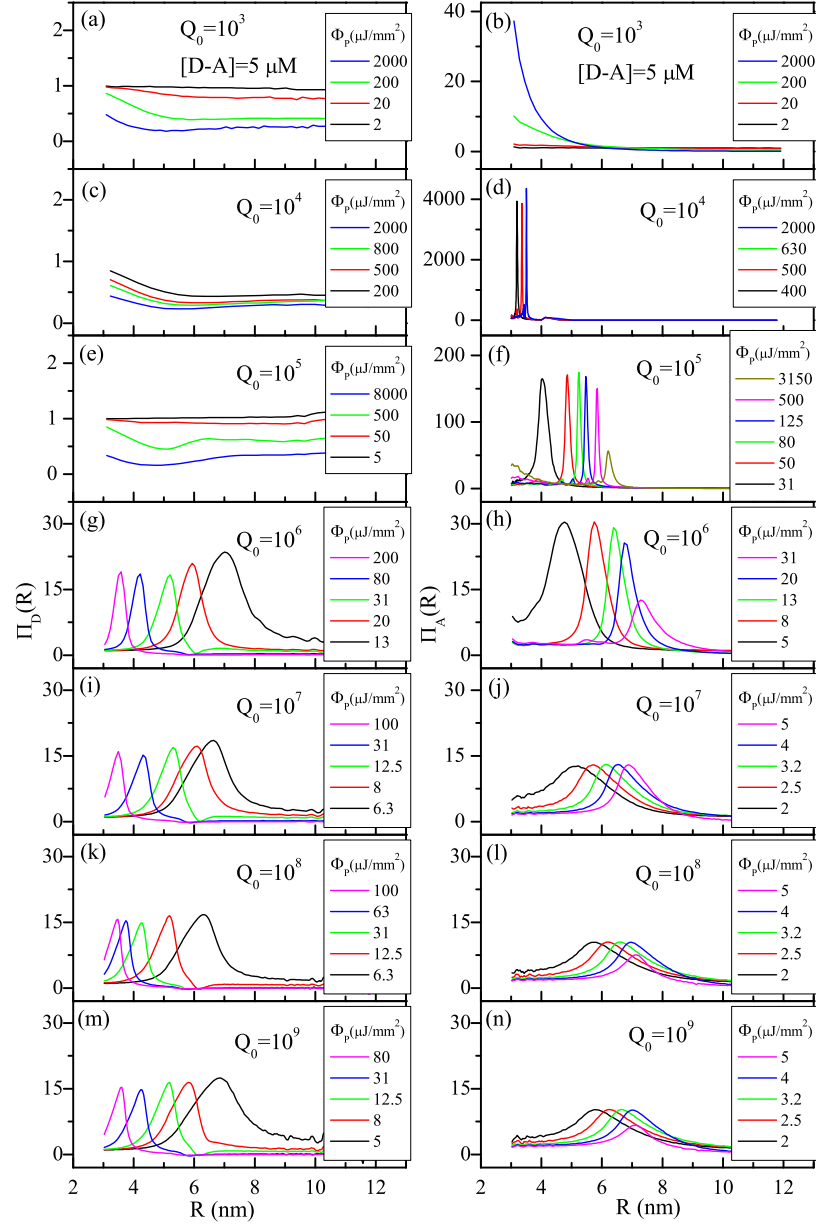


Figure 6.11: Effect of the cavity Q -factor on sensitivity enhancement factors for donor, $\Pi_D(R)$, and acceptor $\Pi_A(R)$ versus R in linked 1D – 1A donor/acceptor complexes at different values of Φ_P and a fixed complex concentration of $[D - A] = 5 \mu\text{M}$.

lasing FRET sensitivity curves are similar to the case of fluorescence FRET sensitivities shown in Figs. 6.8(c) and (e). Figure. 6.11 shows the sensitivity enhancement factors, Π_D and Π_A , obtained for cases considered in Fig. 6.10 using the non-amplified spontaneous FRET sensitivities of Figs. 6.8(d) and (f) as the reference. In Figs. 6.11(a), (c), and (e), we see less than unity enhancement factor for donor molecules, $\Pi_D \lesssim 1$, in the range of

R under study. In contrast, for acceptor molecules, in Figs. 6.11(b), (d), and (f), we see relatively large enhancement factors. In particular, Π_A takes values of more than 30, 4000, and 150 in Figs. 6.11(b), (d), and (f), respectively. In Figs. 6.11(a) and (b), Π_D and Π_A largely deviate from unity, especially at high Φ_P values, despite the absence of both donor and acceptor lasing emissions. This is due to the saturation in donor absorption that effects $\Omega_D(R)$ and $\Omega_A(R)$ curves at high Φ_P values, as we previously explained for Figs 6.8(c) and (e). However, we should note that the high Π_A values in Fig. 6.11(b) do not represent higher absolute sensitivities Ω_A . As we can see in Fig. 6.10(b), for different values of Φ_P values, the maximum value of Ω_A is around 0.05-0.1 %/pm, only the value of R corresponding to the maximum of Ω_A is observed to change. Among the relatively low Q-factor cases ($Q_0 = 10^3$, 10^4 , and 10^5), the results obtained for $Q_0 = 10^5$ are especially noteworthy because for this case, high enhancement of more than 150 is achieved for a broad range of R values around R_0 , the most interesting range of distances used in typical FRET-based biosensor experiments.

For Q-factors larger than 10^6 , donor lasing is observed together with acceptor lasing. As a result, Π_D reaches peak values between 15-20 for Q-factors ranging between $10^6 - 10^9$. With the emergence of donor lasing, a drop is observed in the peak values of Π_A . The peak value of Π_A which is more than 150 for $Q_0 = 10^5$ decreases to around 30 for $Q_0 = 10^6$, as a result of the onset of donor lasing. As Q_0 is further increased from 10^6 in Fig. 6.11(h) up to 10^9 in Fig. 6.11(n), the peak value of Π_A gradually drops from 30 to around 8. This additional drop of the acceptor sensitivity enhancement with increased Q-factor can be attributed to the growing importance of CET, which is insensitive to the donor-acceptor distance, and its eventual dominance over FRET in higher Q-factors. To evaluate the role of CET in the sensitivity reduction at high Q-factors, we use the approach that has been developed by Folan *et al.* [123] for the evaluation of CET effect evaluation in aerosol droplets and that is also applicable to other cavities [121]. In this approach CET is assumed to happen in two steps. In the first step, photons from the donor emission couple to the modes of the resonator with the highest Q-factors. Subsequently, those resonant photons are absorbed by the acceptor chromophores. The CET probability which is the probability of a photon emitted from donor to be absorbed by acceptor molecules with concentration

of ρ_a , can be calculated using [121]:

$$P = \frac{\sigma_{aad}\rho_a c/\eta}{1/\tau_{cd} + \sigma_{aad}\rho_a c/\eta}. \quad (6.23)$$

According to this equation, for $1/\tau_{cd} \gg \sigma_{aad}\rho_a c/\eta$, P is a function of acceptor concentration but for $1/\tau_{cd} \ll \sigma_{aad}\rho_a c/\eta$ which corresponds to a high-Q cavity, P becomes equal to one. The characteristic acceptor concentration at which the full radiative cavity-assisted energy transfer falls by a factor of 2 ($\rho_{a1/2}$) can be determined by $\rho_{a1/2} = \eta/(\tau_{cd}\sigma_{aad}c)$. Using the numerical values from Table 6.1, we find $\rho_{a1/2} = 160 \mu\text{M}$ and $16 \mu\text{M}$, for quality factors of $Q = 10^5$ and 10^6 , respectively. Hence, for 1D – 1A complex structure with $[D - A] = 5 \mu\text{M}$, we expect the CET probabilities to be 3 % and 30 %, respectively, for $Q = 10^5$ and 10^6 . CET probability is independent of R ; hence, when it becomes comparable to or bigger than FRET rate, a dramatic decrease is observed in the R sensitivity of the donor and acceptor lasing emissions. This explains the decrease in the maximum values of Π_D and Π_A with increase in Q-factor from 10^6 to 10^9 in Fig. 6.11. Besides, having a minimum necessary Q-factor to enable acceptor lasing but not donor lasing (as observed for $Q = 10^4$ in Figs. 6.11(c) and (d)) results in a giant jump in the acceptor emission sensitivity. Hence, as a rule of thumb, for a given cavity with a fixed Q-factor, in order to achieve the highest possible sensitivities using optofluidic FRET lasers, CET should be suppressed by choosing sufficiently small acceptor concentrations, i.e. $\rho_a \ll \rho_{a1/2}$.

The total Q-factor Q_0 of the resonator can be found as $Q_0^{-1} = Q_s^{-1} + Q_r^{-1}$ where $Q_s = 2\pi\eta/(\lambda\alpha_s)$ is due to the absorptive losses in a medium with absorption coefficient α_s and $Q_r = 2\pi l/[\lambda(1 - \mathcal{R})]$ is due to the radiative out-coupling by identical cavity mirrors with reflectance \mathcal{R} [124]. For the laser gain medium formed by an aqueous solution of donor and acceptor dyes, the absorption coefficient of water at the donor lasing wavelength is $\alpha_s(\lambda_d) \approx 6 \times 10^{-4} \text{ cm}^{-1}$ which is six times lower than the corresponding value at the acceptor lasing wavelength $\alpha_s(\lambda_a) \approx 35 \times 10^{-4} \text{ cm}^{-1}$ [84]. Assuming $\mathcal{R} \rightarrow 1$ and using water absorption coefficients at the donor and acceptor lasing wavelengths, the corresponding maximal absorption-limited Q-factors are $Q_0(\lambda_d) = 2.5 \times 10^8$ and $Q_0(\lambda_a) = 3.6 \times 10^7$, respectively. Taking this into account, we can conclude that the absorption of water has no effect on the curves of $\Omega(R)$ and $\Pi(R)$ calculated for $Q_0 \leq 10^7$. However, for Q_0 lying between 10^7 and the respective absorption-limited maximal Q-factor values at λ_d and λ_a , the realistic curves of $\Omega(R)$ and $\Pi(R)$ would be slightly different from those presented in

Figs. 6.10 and 6.11.

6.7 Sensitivity of Detection of Conformational Changes in 1D – 3A and 3D – 1A Biocomplexes

When the donor and acceptor dye molecules are connected to each other using a suitable nanometer-scale rigid linker (for example, a DNA fragment or a polypeptide), in addition to the separation distance between the dyes, the donor-to-acceptor ratio can be pre-determined in each dye complex. This opens up new possibilities for tuning of the laser gain in FRET-based optofluidic lasers [70]. Naturally, such control of the donor/acceptor stoichiometry can also be beneficial in sensing applications. To evaluate the performance of FRET lasing-based biosensors with variable donor-to-acceptor ratio, we study two different linked dye complexes which are schematically illustrated in Fig. 6.1(c). In the first one, we assume a single donor molecule attached by three identical linkers to three acceptor molecules (1D – 3A) whereas in the second one, there are three donor molecules linked to a single acceptor molecule by identical linkers (3D – 1A). Figures 6.12 and 6.13 show the total output energy versus Φ_P and also the total output energy, Ω_D , Ω_A , Π_D and Π_A , versus R , for 1D – 3A and 3D – 1A complexes, respectively, for a cavity with $Q = 10^6$. In both studied complexes, the concentration of acceptor is fixed at $[A] = 9 \mu\text{M}$. Consequently, overall concentration of the dye complex is $3 \mu\text{M}$ for 1D – 3A and $9 \mu\text{M}$ for 3D – 1A. Accordingly, the donor concentration is $3 \mu\text{M}$ in case of 1D – 3A and $27 \mu\text{M}$ in case of 3D – 1A. Comparison of Figs. 6.12(b) and 6.13(b) shows that for the values of R varying between 4-8 nm, the acceptor lasing threshold of 3D – 1A complex is 7 to 9 times lower than the corresponding threshold of 1D – 3A complex. This is because of more efficient pumping from the donor side in 3D – 1A complexes in comparison with 1D – 3A complexes since there are more donors in 3D – 1A complexes. This finding is in agreement with our previous experimental results obtained with donor/acceptor complexes linked by tetrahedral DNA scaffold structures and also with theoretical predictions based on an approximate analytical method of lasing threshold estimation [59, 125, 126].

Evaluation of lasing FRET sensitivity curves for donor, Ω_D , and acceptor, Ω_A (see Figs. 6.12(e), (f) and 6.13(e), (f)) and their corresponding spontaneous fluorescence FRET sensitivity curves which are not shown here, results in enhancement factors Π_D and Π_A

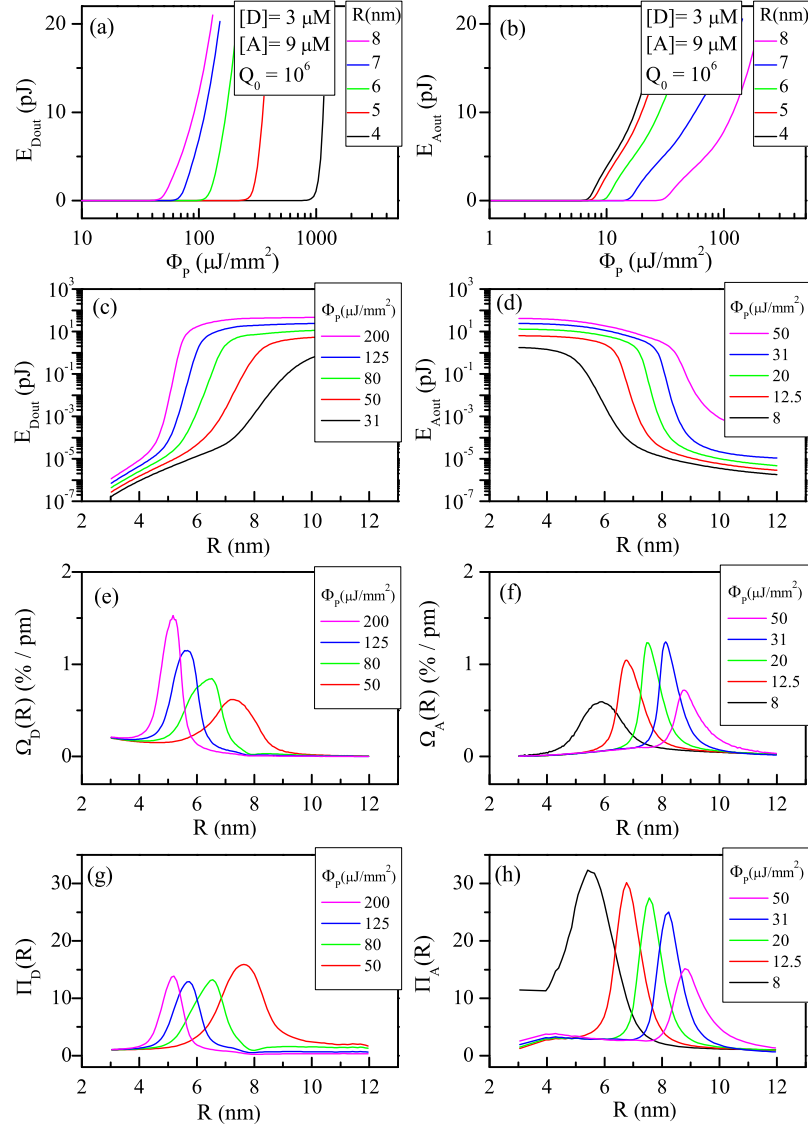


Figure 6.12: Behavior of FRET lasing-based biosensor using 1D – 3A linked dye complexes with changing R . Total output energy of (a) donor and (b) acceptor versus Φ_P for different values of R . Total output energy of (c) donor and (d) acceptor versus R for different values of Φ_P . The emission sensitivity for (e) donor, $\Omega_D(R)$, and (f) acceptor $\Omega_A(R)$, versus R calculated for FRET lasing emission from linked donor/acceptor complexes at different values of Φ_P . Sensitivity enhancement factors for (g) donor, $\Pi_D(R)$, and (h) acceptor $\Pi_A(R)$, versus R calculated for linked donor/acceptor complexes at different values of Φ_P . In all calculations, 1D – 3A linked dye complexes are assumed to have equal link distances between the donor and acceptor molecules. Effective donor concentration is $[D] = 3 \mu\text{M}$, effective acceptor concentration is $[A] = 9 \mu\text{M}$.

shown in 6.12(g), (h) and 6.13(g), (h)). Here, the maximal enhancements Π_D and Π_A for 1D – 3A are around 15 and 30, respectively, while they are both around 30 in 3D – 1A.

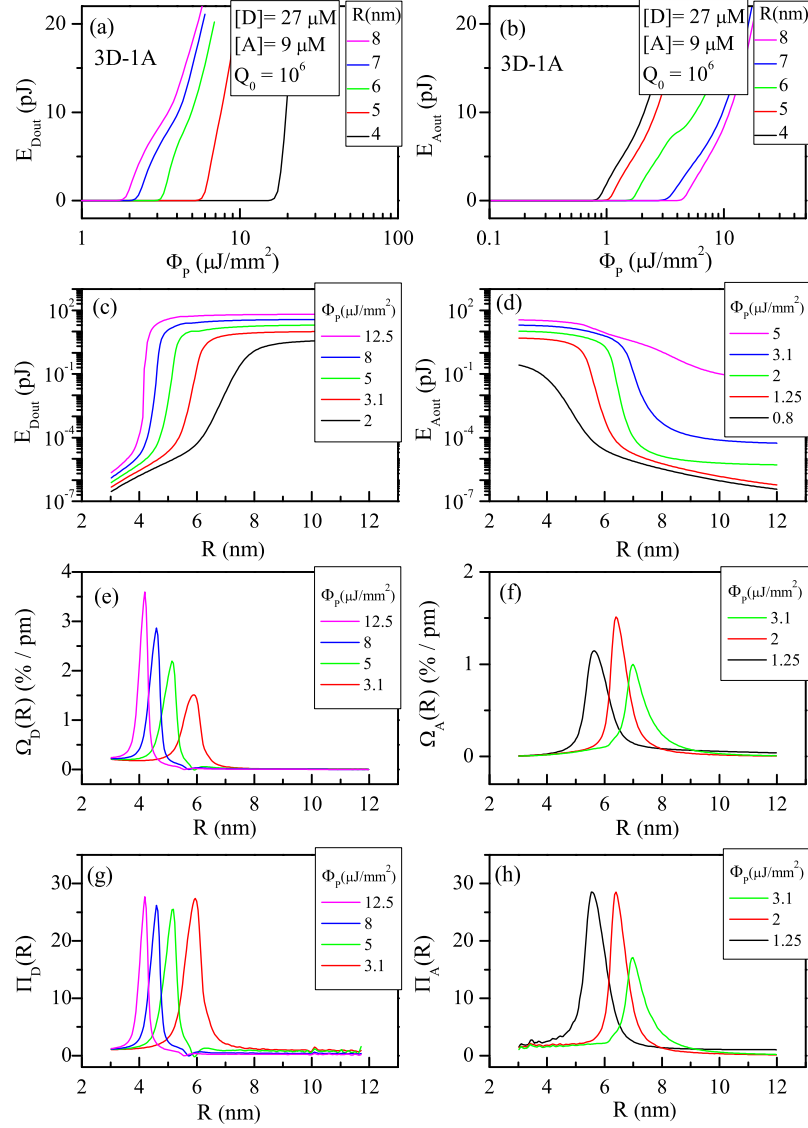


Figure 6.13: Behavior of FRET lasing-based biosensor using 3D – 1A linked dye complexes with changing R . Total output energy of (a) donor and (b) acceptor versus Φ_P for different values of R . Total output energy of (c) donor and (d) acceptor versus R for different values of Φ_P . The emission sensitivity for (e) donor, $\Omega_D(R)$ and (f) acceptor, $\Omega_A(R)$, versus R calculated for FRET lasing emission from linked donor/acceptor complexes at different values of Φ_P . Sensitivity enhancement factors for (g) donor, $\Pi_D(R)$, and (h) acceptor $\Pi_A(R)$, versus R calculated for linked donor/acceptor complexes at different values of Φ_P . In all calculations, 3D – 1A linked dye complexes are assumed to have equal link distances between the acceptor and donor molecules. Effective donor concentration is $[D] = 27 \mu\text{M}$, effective acceptor concentration is $[A] = 9 \mu\text{M}$.

Hence, in 3D – 1A, 2-fold enhancement is observed in donor sensitivity as compared to 1D – 3A case, while acceptor sensitivities are comparable in both linked dye complexes.

This is because of the CET rate dominance over FRET rate at this acceptor concentration.

To increase the enhancement factor even further, the total concentration of the acceptor in the $Q_0 = 10^6$ cavity can be decreased to less than $\sim 1.6 \mu\text{M}$. This value is calculated as $\rho_{a1/2}/10$, based on the rule of thumb ($\rho_a \ll \rho_{a1/2}$) discussed in the previous section. In such small concentrations, the presence of three donor molecules per single acceptor molecule in 3D – 1A compared to one donor in 1D – 1A and 1/3 donor in 1D – 3A, will help the acceptor molecules in 3D – 1A to be pumped more efficiently in comparison to 1D – 1A and 1D – 3A. This in turn allows using lower values of Φ_P and, thus, extending the lifetime of the biochemical sensor by decreasing the risk of chromophore photobleaching.

6.8 Concentration Sensitivity of FRET Laser Biosensors

In addition to analyzing the donor/acceptor sensitivity, Ω_D and Ω_A , to changes in R , it is interesting to study the sensitivity to changes in the complex concentration [D-A], defined by $\Omega_D([D-A]) = \left| \frac{100}{E_{Dout}} \frac{dE_{Dout}}{d[D-A]} \right|$ and $\Omega_A([D-A]) = \left| \frac{100}{E_{Aout}} \frac{dE_{Aout}}{d[D-A]} \right|$ for donor and acceptor, respectively. This situation mimics a biosensing scenario in which FRET dye pairs are removed from or added to the gain medium due to an underlying biological process such as ligand-receptor binding and unbinding. The results of such concentration-dependent study are summarized in Fig. 6.14 which shows the total output energy from the donor and acceptor as a function of Φ_P (parts (a) and (b)) and FRET complex concentration [D-A] (parts (c) and (d)). In all simulations, cavity Q-factor is fixed at 10^6 and the donor-acceptor distance is set to $R = R_0 = 6.1 \text{ nm}$. The dependence of $\Omega_D([D-A])$ and $\Omega_A([D-A])$ on [D-A] for different values of Φ_P , assuming a constant $R = R_0$, is then summarized in Figs. 6.14(e) and (f) for donor and acceptor, respectively. As illustrated in Figs. 6.14(e) and (f), the maximum sensitivity values are reached at lower concentrations [D-A]. This is due to a larger relative change in the lasing pair population by addition or subtraction of individual FRET pairs when [D-A] is smaller. Hence, achieving FRET lasing with minimal FRET pair concentration is critical for maximizing the concentration sensitivity. Here, our calculations show that for $\Phi_P = 200 \mu\text{J}/\text{mm}^2$, remarkable [D-A] concentration sensitivities that are larger than 2 %/nM and 2.5 %/nM can be achieved for donor and acceptor emission, respectively (see Figs. 6.14(e) and (f)). As in the studies of the linker length sensitivity, sensitivity enhancement factors for donor and acceptor, $\Pi_D([D-A])$ and $\Pi_A([D-A])$ are

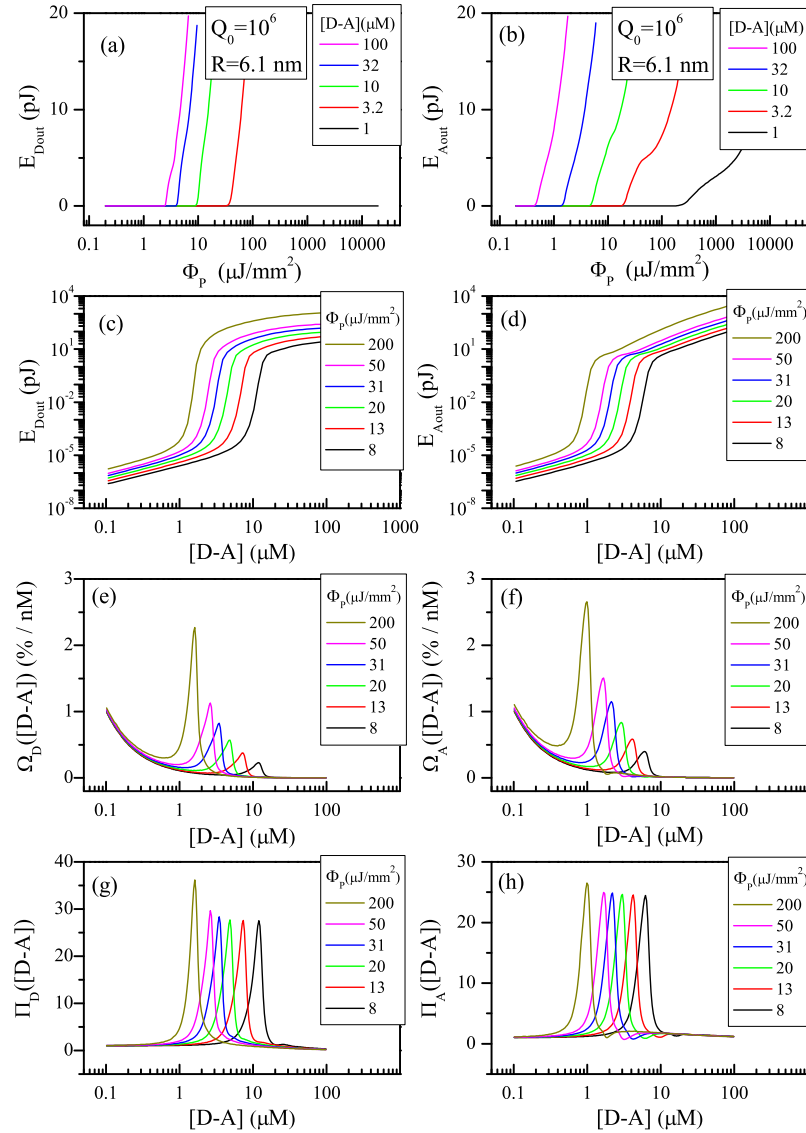


Figure 6.14: Behavior of FRET lasing-based biosensor with changing concentration of linked complex [D-A]. Total output energy of (a) donor and (b) acceptor versus Φ_P for different values of [D-A]. Total output energy of (c) donor and (d) acceptor versus [D-A] for different values of Φ_P . The complex concentration sensitivity of (e) donor and (f) acceptor versus [D-A] calculated for FRET lasing emission from linked donor/acceptor pairs at different values of Φ_P . The complex concentration sensitivity enhancement factor for (g) donor and (h) acceptor versus [D-A] for FRET lasing emission from linked donor/acceptor pairs at different values of Φ_P . In all calculations, R is assumed to be equal to R_0 .

found by dividing the lasing FRET sensitivity with the fluorescence FRET sensitivity and displayed in Figs. 6.14(g) and (h)), versus [D-A]. Depending on the values of Φ_P , maximal sensitivity enhancement are observed at different complex concentrations but their peak

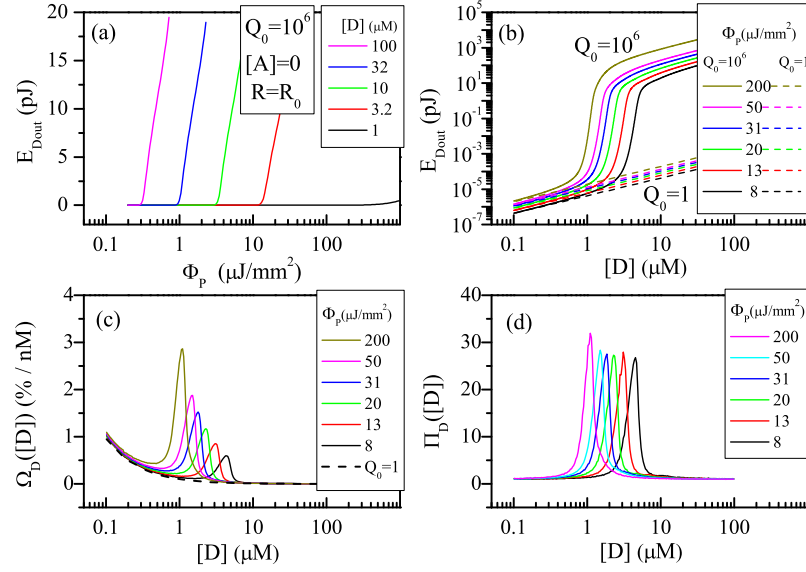


Figure 6.15: Behavior of a single dye laser for changing concentration of the gain medium $[D]$. (a) Total output energy from a single dye, R6G, for $Q_0 = 10^6$ versus Φ_P for different values of $[D]$, (b) Total output energy from a single dye, R6G, for $Q_0 = 10^6$ with solid lines and for $Q_0 = 1$ with dashed lines versus $[D]$ for different values of Φ_P . (c) Concentration sensitivity of emission from a single dye for $Q_0 = 10^6$ with solid lines and for $Q_0 = 1$ with dashed line versus $[D]$ at different values of Φ_P . (d) Concentration sensitivity enhancement factor for single dye versus $[D]$ relative to the nonlasing emission at different values of Φ_P .

values in a wide range of $[D-A]$, from 1 to 10 μM have approximately constant values around 25 that show a 25-times improvement relative to non-lasing FRET sensing. To evaluate the concentration sensitivity for single dye lasing, in Fig. 6.15, we perform the analysis similar to that shown in Fig. 6.14, but just for donor molecules without any acceptors. As shown in Fig. 6.15(a), donor lasing threshold in the absence of acceptor is lower relative to that of FRET lasing shown Fig. 6.14(a) which is caused by depletion of the donor excited state by FRET in the latter case. In Fig. 6.15(b), the total output energies for $Q_0 = 10^6$ and $Q_0 = 1$ are shown respectively by solid and dashed lines versus $[D]$. In Fig. 6.15(c), $\Omega_D([D])$ is shown versus $[D]$ at different values of Φ_P assuming $Q_0 = 10^6$ with solid lines and $Q_0 = 1$ with the dashed line. For the case of spontaneous fluorescence emission ($Q_0 = 1$ i.e. no lasing), concentration sensitivity is independent of the value of Φ_P . In Fig. 6.15(d), the enhancement factor of concentration sensitivity relative to the spontaneous fluorescence measurements shows higher than 25-fold improvement in the maximal sensitivity. In both Figs. 6.15(d) and 6.14(g), the minimum sensible donor or donor/acceptor complex concentration at which

sensitivity enhancement due to lasing can be achieved is limited to about $1\ \mu\text{M}$. However, by using emission of linked acceptor molecules and by choosing linker lengths smaller than R_0 , concentration sensitivity enhancement can be reached at even lower concentrations down to $0.1\ \mu\text{M}$. This can be understood from the linked donor/acceptor threshold curves shown in Fig. 6.6(b). For $R = 3\ \text{nm}$, acceptor can lase down to $0.1\ \mu\text{M}$ which means an order of magnitude expansion toward the nanomolar concentration region.

Table 6.1: Descriptions and numerical values of the constants used in the rate equation model [116]

Constant	Description	Numeric Value
σ_{pd}	Donor absorption cross section at the pump wavelength	$3.42 \times 10^{-16} \text{ cm}^2$
σ_{pa}	Acceptor absorption cross section at the pump wavelength	$0.05 \times 10^{-16} \text{ cm}^2$
σ_{edd}	Donor stimulated emission cross section at λ_d	$3.78 \times 10^{-16} \text{ cm}^2$
σ_{eaa}	Acceptor stimulated emission cross section at λ_a	$6.9 \times 10^{-16} \text{ cm}^2$
σ_{ead}	Acceptor stimulated emission cross section at λ_d	$0.036 \times 10^{-16} \text{ cm}^2$
σ_{add}	Donor absorption cross section at λ_d	$1.00 \times 10^{-16} \text{ cm}^2$
σ_{1dd}	Excited state absorption cross section of donor molecules at λ_d	$0.4 \times 10^{-16} \text{ cm}^2$
σ_{1aa}	Excited state absorption cross section of acceptor molecules at λ_a	$2.00 \times 10^{-16} \text{ cm}^2$
σ_{1ad}	Excited state absorption cross section of acceptor molecules at λ_d	$1.30 \times 10^{-16} \text{ cm}^2$
σ_{aad}	Acceptor absorption cross section at λ_d	$0.156 \times 10^{-16} \text{ cm}^2$
σ_{aaa}	Acceptor absorption cross section at λ_a	$1.00 \times 10^{-16} \text{ cm}^2$
η	Refractive index of the medium	1.33
τ_d	Fluorescence lifetime of donor molecules	4 ns
τ_a	Fluorescence lifetime of acceptor molecules	3.3 ns
τ_{cd}	Fluorescence lifetime of cavity at λ_d	$Q_0 \lambda_d / (2\pi c)$
τ_{ca}	Fluorescence lifetime of cavity at λ_a	$Q_0 \lambda_a / (2\pi c)$
λ_d	Donor lasing wavelength	560 nm
λ_a	Acceptor lasing wavelength	655 nm
R_0	Förster radius	6.1 nm
Q_0	Empty cavity Q-factor	10^6
F	Fraction of mode volume occupied by the dye molecules	1
d	Depth of the electromagnetic mode	30 μm
w	Width of the electromagnetic mode	30 μm
l	Length of the electromagnetic mode	30 μm
V	Volume of the electromagnetic mode	dwl
Δt	Pump laser pulsewidth	5 ns
c	Speed of light in vacuum	$3 \times 10^{10} \text{ cm/s}$
h	Planck's constant	$6.63 \times 10^{-34} \text{ J} \cdot \text{s}$

Chapter 7

FRET LASING FROM SELF-ASSEMBLED DNA TETRAHEDRAL NANOSTRUCTURES SUSPENDED IN OPTOFLUIDIC DROPLET RESONATORS

In this chapter, we demonstrate miniature optofluidic biolasers formed by microdroplets generated from an aqueous solution of fluorescently-labeled DNA complexes and deposited on a superhydrophobic surface which stabilizes the droplet position and shape [36]. Active medium of the presented lasers consists of self-assembled tetrahedral complexes of complementary DNA strands labeled with Cy3 and Cy5 fluorescent dyes which form a donor and acceptor pair for FRET. Moreover we characterize threshold fluence and differential efficiency for DNA complexes droplet lasers containing 1Cy3-3Cy5 and 3Cy3-1Cy5 and we show that the lasing threshold and efficiency of the DNA-FRET biolasers can be efficiently tuned by adjusting the ratio of the donor-to-acceptor dye molecules on an individual tetrahedral DNA complex. Attaching the FRET dye pair to the DNA scaffold with a precisely defined geometry preserves the distance of the donor and acceptor molecules and, thus, fixes the efficiency of FRET, making it independent of the concentration of DNA complex in the droplet liquid [70]. This behavior is different from the behavior of bulk FRET microlasers that display concentration-dependent FRET efficiency [126].

7.1 Materials and Methods

Self-assembled DNA complexes containing Cy3 (donor) and Cy5 (acceptor) dye molecules were prepared by our collaborator in University of Michigan as described in [70]. Two different samples containing either three Cy3 molecules and one Cy5 molecule (3Cy3-1Cy5) or one Cy3 molecule and three Cy5 molecules (1Cy3-3Cy5) per tetrahedron were studied in the experiments. Aqueous microdroplets containing 35% w/w glycerol/water with 1X TAE plus 12.5 mM MgCl_2 and the fluorescent DNA complexes were deposited on cover glasses with superhydrophobic surface layer. These superhydrophobic surfaces were produced by

spin-coating hydrophobic silica nanoparticles (Aeroxide LE1; Degussa AG) dispersed in ethanol on cleaned microscope cover glasses [36] so that the prepared superhydrophobic surfaces were transparent to visible light and they could provide a high contact angle ($> 150^\circ$) for aqueous microdroplets [127].

To deposit micron-sized droplets on the superhydrophobic surface, aerosols of the droplet liquid were generated using a compact ultrasonic nebulizer (JIH50, Beuer) and sprayed over the surface. This procedure provided surface-supported microdroplets with diameters ranging from $1\ \mu\text{m}$ to $100\ \mu\text{m}$. In order to minimize the variation in the observed FRET lasing properties due to the droplet size, we recorded all the presented data from droplets with a narrow size distribution (droplet diameter between $14 - 17\ \mu\text{m}$). Upon droplet deposition, slow evaporation was observed as droplets were exposed to the ambient atmosphere with approximately 50 % relative humidity. To reduce the size variation effects on the recorded data we performed all the experiments during approximately the first 10 minutes after the droplet generation. During this time the reduction in droplet size was measured to be less than 4 %, corresponding to the maximal increase of the dye concentrations by $\sim 12\%$ with respect to the initial values. However, all dye concentrations reported in this chapter refer to those in the initial solutions used for droplet generation.

7.2 Experimental Setup

Experimental setup employed in these lasing studies was similar to Fig. 3.1 and it is described in chapter 3. Since the studied droplets were deposited on a superhydrophobic surface, the trapping beam was removed and the excitation beam was directly coupled to the microscope objective. A relatively large focal spot with $1.6\ \mu\text{m}$ diameter was employed for the excitation beam in order to reduce sensitivity of the observed spectra to the precise position of the excitation beam focus with respect to the microdroplet. A polarizing beam splitter together with a half wave plate mounted on a rotation stepper motor were used to control the green beam pump power.

7.3 Results and discussions

Figure 7.1 illustrates typical FRET lasing spectra recorded from a $15.6\ \mu\text{m}$ diameter droplet containing $8.3\ \mu\text{M}$ 1Cy3-3Cy5 (part a) and a $16.4\ \mu\text{m}$ diameter droplet containing $25\ \mu\text{M}$

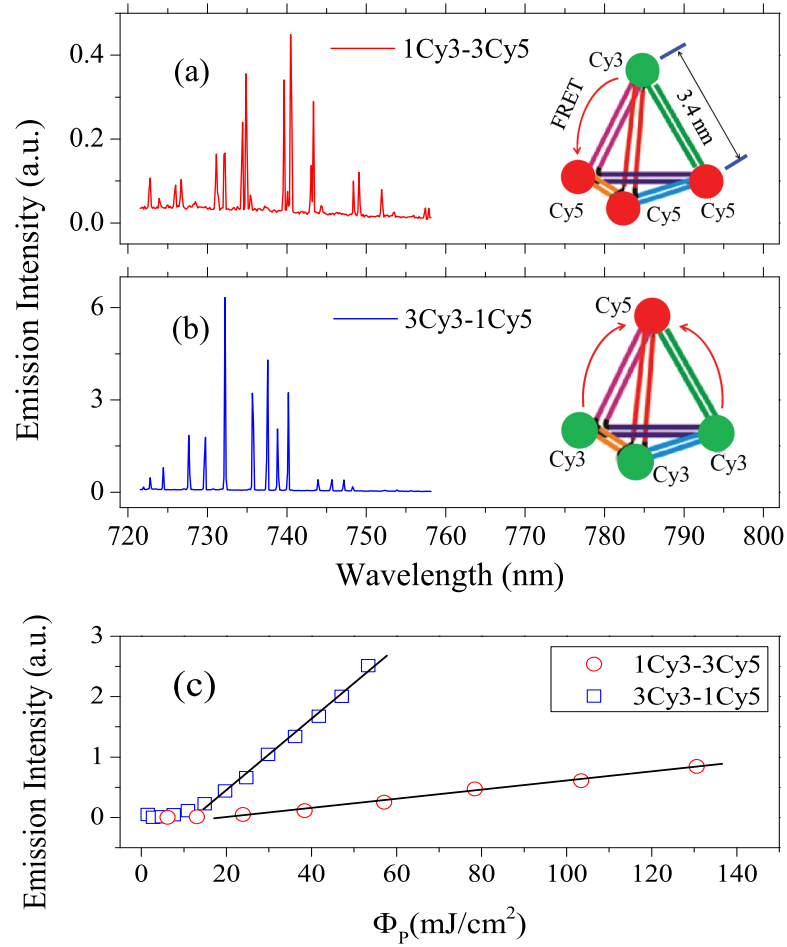
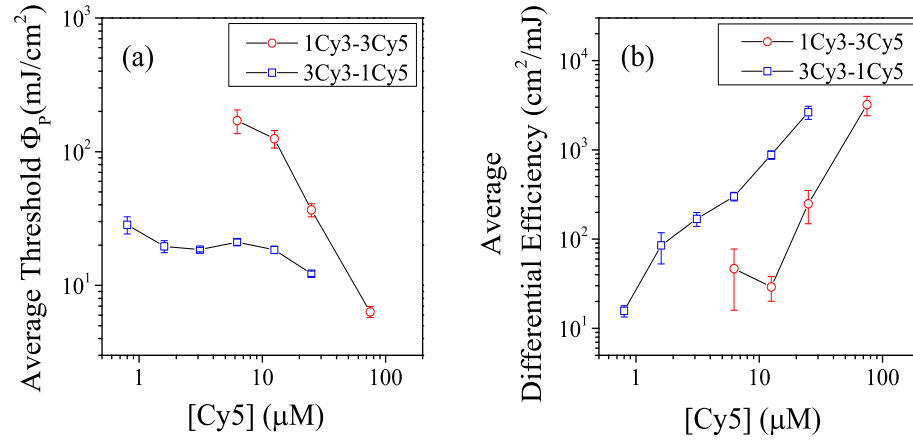


Figure 7.1: (a) Lasing spectrum of a $15.6 \mu\text{m}$ diameter droplet doped with 1Cy3-3Cy5 and (b) lasing spectrum of a $16.4 \mu\text{m}$ diameter droplet doped with 3Cy3-1Cy5 DNA complexes with identical Cy5 concentration of $25 \mu\text{M}$ at a pump fluence of 58 mJ/cm^2 . (c) Integral intensity of the lasing peaks as a function of the pump fluence for the droplet spectra shown in (a) (circles) and (b) (squares). Line fits to both experimental data sets give the lasing threshold fluences of 20 mJ/cm^2 and 11 mJ/cm^2 , and differential efficiencies of $310 \text{ cm}^2/\text{mJ}$ and $3200 \text{ cm}^2/\text{mJ}$, respectively.

3Cy3-1Cy5 (part b). For both microdroplets, the total Cy5 concentration was equal to 25 μM and the spectra were acquired with a constant pump fluence of 58 mJ/cm^2 which was well above the lasing threshold in both cases. The corresponding integral intensity of the lasing emission as a function of the pump beam fluence is shown in Fig. 7.1(c). Here, the integral lasing intensity was obtained by integrating the recorded spectra over the spectral interval from 720 to 760 nm. For the two studied droplets containing 1Cy3-3Cy5 and 3Cy3-1Cy5, respectively, lasing threshold fluences of 20 mJ/cm^2 and 11 mJ/cm^2 , and differential efficiencies (defined as the slope of the linear fit to the integral lasing intensity) of 310 cm^2/mJ and 3200 cm^2/mJ , were measured. The ratio of threshold fluences and differential efficiencies observed for lasing from 1Cy3-3Cy5 and 3Cy3-1Cy5 are 1.8/1 and 1/10.3, respectively. These values are comparable with the theoretical analysis of the DNA FRET lasing and previous experiments carried out using the OFRR. For the studied system of Cy3 and Cy5 fluorescent dyes with the Förster radius of 6 nm and separation distance of 3.4 nm defined by the DNA scaffold, the threshold fluence of 3Cy3-1Cy5 complex is expected to be 8.8 times lower than the threshold fluence of 1Cy3-3Cy5 complex with the same total concentration of Cy5 [70]. In the OFRR experiments, the ratio of lasing threshold fluences and differential efficiencies for 1Cy3-3Cy5 and 3Cy3-1Cy5 with the same total concentration of Cy5 were measured to be 3.8/1 and 1/28, respectively [70]. Quantitative discrepancy between our results and the previously reported data obtained with the OFRR can be attributed to several factors including different geometry of the used active cavity (direct modal field coupling in surface-supported microdroplets vs. evanescent mode coupling in the OFRR) and different total concentration of Cy5 dye in the liquid gain medium. In addition, our experiments with 3Cy3-1Cy5 and 1Cy3-3Cy5 complexes were carried out with different droplets and, thus, we could not prevent variations in the droplet size, precise location of the excitation beam focus on the droplet, and Q-factor of the cavity caused by different contact angles of the droplets.

To demonstrate the dependence of FRET lasing characteristics on the total Cy5 concentration in the droplets, we varied the concentrations of 1Cy3-3Cy5 and 3Cy3-1Cy5 from 25 μM down to the sub- μM range and measured the threshold fluence and differential efficiency. In Fig. 7.2(a), mean threshold fluence of lasing from droplets in the size range of 14-17 μm is shown as a function of the total Cy5 concentration for both 1Cy3-3Cy5



centering

Figure 7.2: (a) Average lasing threshold fluence and (b) average lasing differential efficiency for droplets with diameters 14-17 μm containing 1Cy3-3Cy5 (circles) and 3Cy3-1Cy5 (squares) DNA complexes as a function of Cy5 concentration varying between 0.8 μM and 75 μM .

and 3Cy3-1Cy5. Here, each data point represents an average calculated from at least 10 measurements carried out with different droplets. Error bars indicate the standard error of the mean (i.e. the standard deviation of the measured values divided by the square root of the number of measurements) for each concentration. Due to the highly efficient FRET pumping mechanism in 3Cy3-1Cy5 complexes, lasing is observed even at very low Cy5 concentrations ($\sim 1\mu\text{M}$). For all Cy5 concentrations, average threshold fluence measured for 1Cy3-3Cy5 is 3 to 8 times larger than that recorded for 3Cy3-1Cy5. Figure 7.2(b) shows the lasing differential efficiency of droplets with diameters between 14-17 μm whose lasing threshold fluence was studied in Fig. 7.2(a). Error bars in Fig. 7.2(b) also represent the standard error of the mean. In agreement with the previous work by Chen *et al.* [70], for all Cy5 concentrations, average differential efficiency of 3Cy3-1Cy5 is measured to be larger than that of 1Cy3-3Cy5 by a factor changing between 6 and 30. Hence, we conclude that for the same Cy5 concentration, 3Cy3-1Cy5 displays lower threshold and larger slope efficiency in comparison to 1Cy3-3Cy5. This is due to the high excitation efficiency of a given acceptor molecule when it is surrounded by multiple donor molecules leading to higher overall FRET efficiency. We should note that relatively large variations were observed when the threshold fluences and differential efficiencies were compared for individual studied droplets.

These variations stem mainly from the variations in the droplet cavity Q-factor which is influenced by the droplet size and contact angle and from slight differences in the position of the pump beam focus on the droplet. The presented experimental results in this chapter are not directly comparable to the simulation results in chapter 5 since in simulations we had to use physical specifications of two different dyes. Moreover, the shape of cavities in experiments and simulations were droplet and Fabry-Pérot resonators, respectively that limit the comparison between results to the general trends of simulation and experimental results.

In summary we demonstrated FRET lasing from self-assembled tetrahedral DNA complexes labeled with Cy3 and Cy5 dyes and suspended as a gain medium in aqueous microdroplet cavities deposited on a superhydrophobic surface. We demonstrated that at a constant Cy5 concentration, average threshold fluence is reduced 3 to 8 times and average differential efficiency is enhanced 6 to 30 times for 3Cy3-1Cy5 as compared to 1Cy3-3Cy5. Using 3Cy3-1Cy5 nanostructures, FRET lasing is observed at very low concentrations down to $\sim 1\mu\text{M}$. This work shows that optofluidic microlasers based on droplet resonators can be combined with DNA nanotechnology to explore applications in bio/chemical sensing and novel photonic devices.

Chapter 8

CONCLUSION

In this thesis we used optical forces to control and manipulate lasing microdroplets. To this end we demonstrated lasing from optically trapped dye-doped aerosol and emulsion droplets. Furthermore, we presented tunable laser emission from microdroplet lasers that were deformed by optical forces. By introducing biological samples as laser gain media into microdroplets, we showed biosensing potential of these lasers. Moreover using a comprehensive numerical analysis based on laser rate equations we explored the sensitivity of laser emission from biological FRET lasers to the conformational changes in biomolecules and we proposed proper design parameters to maximize this sensitivity.

In chapter 3, we introduced and characterized optically manipulated dye micro lasers based on liquid droplets immersed in an immiscible host fluid. We demonstrated the stability of laser emission during the droplet positioning within the host liquid and showed that the laser emission wavelength can be tuned by changing the droplet size and/or the concentration of fluorescent dye in the droplet. Emulsion droplet micro-lasers of precise sizes can be easily generated from various fluid combinations using microfluidic chips. This makes them especially attractive for on-chip applications in chemical and biological analysis and sensing. After the droplet bleaches, it can be easily replaced with a fresh droplet generated on demand which is a clear advantage over solid-state spherical microcavities. Moreover, in contrast to the solid-state cavities, shape of the liquid droplets can be easily deformed which provides further potential for reversible tuning of the laser emission spectra.

Also in chapter 3 we demonstrated lasing in the WGMs of dye-doped glycerol/water microdroplets manipulated in air using optical tweezers. By changing the trapped droplet size, we showed that the average lasing wavelength could be tuned between 600-630 nm. Our results are readily adaptable to simultaneous manipulation of large numbers of lasing aerosol particles. They also bring up the possibility of using the high sensitivity of stimulated emission to small perturbations in the shape, size, and material properties of the droplet

cavity for sensitive chemical and biological analysis in airborne particles.

In chapter 4, we presented tunable optofluidic dye microlasers based on active optical resonant cavities formed by optically trapped microdroplets of fluorescently stained immersion oil emulsified in water. All-optical tuning of the laser emission wavelength was achieved by a controlled deformation of the droplet shape using light-induced forces generated by dual-beam optical trap. By lowering interfacial tension between the droplets and the aqueous host medium with a surfactant and sodium chloride, we demonstrated almost reversible spectral tuning of the lasing droplet WGMs with tuning slopes up to ~ 0.5 nm per Watt of the total stretching laser power. These spectral tuning slopes can be increased by further reduction of the droplet interfacial tension. Droplet liquid was observed to slightly dissolve in the host liquid during each tuning cycle, resulting in an irreversible blue-shift in the WGM spectral positions. This can be prevented by further optimization of the emulsion system in order to obtain fully reversible spectral tuning of the WGMs. Tuning direction of our liquid-cavity microlasers could be easily reversed by changing the position of the optical pumping beam on the droplet. Comparison of experimental data with simulations of the WGM tuning revealed an additional mechanism of reversible spectral tuning triggered by thermally induced changes of the droplet size and refractive index of both the droplet and the host medium. Such thermally induced tuning is a consequence of the absorption of the near-infrared optical stretcher light in water; it can be avoided by changing the wavelength of the used laser beam or replacing aqueous host medium with deuterium oxide that has minimal absorption in the near-infrared spectral region. Our droplet-based tunable and disposable optofluidic lasers can be used with a wide choice of fluorescent dyes and they can be easily integrated into microfluidic lab-on-a-chip platforms. Thus, they represent an attractive alternative for tunable sources of light for on-chip applications in chemical and biological analysis and sensing.

In chapter 5 we introduced and systematically studied miniature optofluidic biolasers based on surface-supported liquid microdroplet cavities containing either purified yellow fluorescent protein or live *E. coli* bacteria expressing this protein. Initially, we demonstrated that micromolar protein concentrations in aqueous microdroplets are sufficient for sustained lasing. Subsequently, we showed that a single micron-sized fluorescent bacterial cell can serve as living laser gain medium. Aqueous droplet microcavities allow the maintenance

of the bacterial cells under conditions compatible with unimpeded growth. Therefore, our results also suggest a direct route to microscopic sources of laser light with self-regenerating gain media. Using bacterial strains expressing two different fluorescent proteins that form a FRET donor-acceptor pair, non-radiative energy-transfer mechanism can be used for laser pumping which would further improve lasing efficiency and open up the possibility for emission wavelength tuning. Furthermore, FRET lasing in connection with self-recognition and self-assembly of biological molecules attached to the fluorescent proteins can be exploited to program and modulate the laser characteristics, thus paving the way to new routes of live-cell bio-sensing.

In chapter 6 we presented a comprehensive theoretical analysis of optofluidic lasers with composite active media formed by a pair of donor and acceptor dyes which can participate in radiative and non-radiative (FRET) energy transfer pathways within the laser cavity. We draw the following main conclusions from our analysis:

- Parametric study of the conceptually distinct cases of energy transfer between donor and acceptor molecules diffusing freely in bulk solution and molecules connected by a fixed-length linker showed that the latter arrangement with concentration-independent FRET rate is especially well suited for FRET-based sensing of low-concentration analytes.
- In comparison to conventional FRET sensors using spontaneous fluorescence emission, biochemical sensors based on FRET lasing from linked donor-acceptor complexes can bring about more than 100-fold enhancement of detection sensitivity of conformation changes of the complex for linker lengths comparable to the Forster radius of the donor-acceptor pair. Such high sensitivities can be achieved by choosing the pump fluence near the lasing threshold of the donor or acceptor molecules for a given dye pair concentration.
- Higher Q-factor of the laser cavity does not necessarily result in higher sensitivity to conformational changes in a FRET lasing-based biochemical sensor. At very high Q factors, radiative energy transfer dominates over FRET, thus hampering the performance of FRET laser-based biochemical sensor. Our analysis has revealed that cavities with Q-factors between $10^4 - 10^6$ enable optimal sensing performance.

- Biochemical sensors based on FRET lasing from linked donor-acceptor complexes can provide more than 20-fold enhancement in the sensitivity of FRET signals to dye-pair concentration by choosing an optimal pump fluence and concentration range of the linked complex. Under such experimental conditions, more than 1% change can be observed in donor or acceptor emission intensities for 1 nM change in dye-pair concentration.

Our theoretical findings which are supported by experimental results in chapter 6 and also reported recently in the literature [128] provide a basic set of tools for design and optimization of novel FRET-based biosensors and tunable integrated sources of coherent light.

In chapter 7 we demonstrated miniature optofluidic lasers based on surface-supported liquid microdroplets which use self-assembled DNA complexes labeled with fluorescent dyes forming a FRET donor-acceptor pair as the laser gain medium. We characterized FRET lasing for different concentrations of DNA scaffold structures and showed that the threshold pump fluence and differential efficiency can be tuned over a large range by adjusting the ratio of concentrations of the donor and acceptor dye per single DNA complex and the overall acceptor concentration in the droplet liquid. We demonstrated that at a constant Cy5 concentration, average threshold fluence is reduced 3 to 8 times and average differential efficiency is enhanced 6 to 30 times for 3Cy3-1Cy5 as compared to 1Cy3-3Cy5. Using 3Cy3-1Cy5 nanostructures, FRET lasing is observed at very low concentrations down to $\sim 1\mu\text{M}$. This work shows that optofluidic microlasers based on droplet resonators can be combined with DNA nanotechnology to explore applications in bio/chemical sensing and novel photonic devices. Since the surface-supported droplets can be generated from minute liquid volumes, our technique allows efficient analysis of samples that are only available in small quantities. Thus, the reported work paves the way for using flexible, programmable, and cell-permeable DNA tetrahedral scaffolds together with surface-supported liquid microdroplets as optical resonant cavities for highly sensitive biological and chemical detection, and for the development of novel photonic devices [129].

As an outlook for further studies on biosensing with microdroplet lasers, experiments with conformational changes in biomolecules can be done to evaluate the predictions of simulation results in chapter 5. Following the simulation part of this thesis, droplet resonators

instead of Fabry-Pérot cavities can be included in the modeling to obtain closely comparable simulations with experiments.

Appendix A

MATLAB CODES OF SIMULATION OF OPTICAL STRETCHER

A.1 Optical Force Calculation of a Single Ray

```

function FFF=force(Intensity,Ds,i0,a,b,eta,phi,n1,n2,Num)
%This function calculates the force of a single beam impinging on the
%special point of an ellipsoid and sends back two opposite components of
%forces that one is for the summation on left and the other for right side
N=n2/n1;
%%---- NORMAL VECTOR AND OTHER VECTOR CAL
Csp=[sin(eta)*cos(phi)*b sin(eta)*sin(phi)*b cos(eta)*a];%entrance point
CCsp= Csp./[b^2 b^2 a^2];
N0=CCsp / sqrt(CCsp*CCsp');%entrance point normal
cos_i0=-i0*N0';
if cos_i0<0
%display(cos_i0);
FFF=[0 0 0 0 0 0];
else
Pj=Intensity * Ds * cos_i0 ;
r0=i0 + 2 * cos_i0 * N0;
t0= i0/N - N0 * ( sqrt(1 - (1-(cos_i0)^2) /N^2 ) - cos_i0 / N);
%% ----REFLECTION COEFIECIENT CAL-----
% Reflectances of TE polarization
RTE = ( (i0*N0' - N * t0 * N0') / (i0*N0' + N * t0 * N0'))^2;
% Reflectances of Tm polarization
RTM = ( (N *i0*N0' - t0 * N0') / (N *i0*N0' + t0 * N0'))^2 ;
R0 = ( RTE + RTM )/2;
T0=1-R0;
%%%----FORCE CAL-----
F0= Pj * ( n1* (i0 - R0 * r0) - n2 * T0 * t0);
FMinus = F0;
FPlus=[0 0 0];

```

```

im=t0; %i1=t0 and im starts from i1;
RRR=1;
for m=1:Num
    iim=im ./[b b a];
    CCsp= Csp./[b b a];
    Csp = Csp + (-2 * CCsp * iim') / ( iim*iim' ) * im;
    CCCsp=Csp./[b^2 b^2 a^2];
    Nm=CCCsp / sqrt(CCCsp*CCCsp'); % m'th point normal
    cos_i= im*Nm';
    sin_i2=1-(cos_i)^2;
    rm = im - 2*cos_i * Nm;
    tm= im*N + Nm * (sqrt(1 - sin_i2*N^2) - cos_i * N);
    %----- crictical angle checking
    if sin_i2>N^2
        Rm=1;
    else
        cos_t = tm * Nm';
        % Reflectances of TE polarization
        RTE = ( (N *cos_i - cos_t) / (N *cos_i + cos_t) )^2 ;
        % Reflectances of TM polarization
        RTM = ( (cos_i - N * cos_t) / (cos_i + N * cos_t))^2;
        Rm = ( RTE + RTM )/2;
    end
    %-----
    Fm = Pj* T0* RRR* (n2 *( im - Rm * rm) - n1 * (1-Rm)* tm);
    RRR = RRR * Rm;
    if Fm(3)>0
        FPlus =FPlus + Fm;
    else
        FMinus = FMinus + Fm;
    end
    im = rm;
end
FFF=[FMinus FPlus];
end

```

A.2 Stretching Force Calculation of a Gaussian Beam

```

function F=gaussian(Nr,Nphi,P,w0,a,b,x0,y0,z0,n1,n2,Lambda,alpha,beta,M2)
% This function calculates the stretching forces for a gaussian beam profile
% with given parameters using another function "force" that calculates just
% the force of a single beam.

% a=major axis of the spheriod
% b=minor axis of the spheriod
% z0= distance of fibers to the center of droplet
%w0=fiber core diameter as Gaussian beam waist
% Lambda=trapping beam wavelength
%P=trapping beam power in each fiber
% n1=refractive index of surrounding medium
% n2=refractive index of droplet
Num=5; %Number of tracings in droplet
%Lambda is for free space and correction is made for M2 factor
ZR= pi * w0^2 * n1 / (Lambda *M2);
FF1=[0 0 0];
FF2=[0 0 0];
% Transfer matrix from droplet coordinate to center of mass coordinate
Tr=[cos(alpha)*cos(beta) , -sin(alpha), cos(alpha)*sin(beta)
    sin(alpha)*cos(beta), cos(alpha), sin(alpha)*sin(beta)
    -sin(beta) 0 cos(beta)];

for eta=pi*(.5:Nr-.5) / Nr
    xsp0=sin(eta)*b;
    zsp=a* cos(eta);
    for phi=2*pi*(0:Nphi-1)/Nphi
        xsp=sin(eta)*cos(phi)*b;
        ysp=sin(eta)* sin(phi)*b;
        %----- Transfer from droplet to lab coordinate system
        C = Tr * [xsp;ysp;zsp] + [x0;y0;z0];
        w2=w0^2 * (1 + C(3)^2 / ZR^2);
        Rz= C(3) * (1+ ZR^2 / C(3)^2);
        %---- gaussian entrance beam unit vector at incident point of Csp
        i0 = [C(1) C(2) Rz];
    end
end

```

```

        i0=i0/sqrt(i0*i0');
        %----- inverse transformation for i0 in Lab system to SP system
        i0= (Tr^-1*i0')';
        Ds=(pi/Nr)*(2*pi/Nphi)*xsp0^2*a/b*sqrt(1+b^2*zsp^2/(a^4-a^2*zsp^2));
        Intensity= 2 * exp(-2* (C(1)^2+ C(2)^2) /w2)/pi/w2;
        G=force(Intensity,Ds,i0,a,b,eta,phi,n1,n2,Num);
        Fminus=G(1,1:3);
        Fplus=G(1,4:6);
        FF1=FF1+(Tr^-1 * Fminus')';
        FF2=FF2+(Tr^-1 * Fplus')';
    end
end
c=3e8;
F=2*(FF2(1,3)-FF1(1,3))*P/c;

```

A.3 Calculation of WGM Tuning Versus Stretching Laser Power

```
% This program uses gaussian function to calculate the percentage of change
% in diameter of droplet as a function of given power
clear all
w0=25e-6; % Gaussian beam waist
R0=25e-6; %droplet radius
gama=1.5e-3; % interfacial surface tension
Lambda=1.07e-6; % Wavelength
Lambda2=0.6e-6; % lasing wavelength

x0=0; %--- droplet center in x direction
y0=0; %--- droplet center in y direction
z0=70e-6;% Distance from beam waist to the center of droplet
alpha=0; %-- angle of xsp from x
beta=0; %-- angle of zsp from z
n1=1.324; % Entrance medium refractive index
n2=1.510;% Droplet medium refractive index
Divergence=0.16418; % deivergence angle of beam in far field(rad)
M2=n1*w0*pi*Divergence/Lambda; % Modified M2 factor

Nr=20; % Radial Mesh on droplet
Nphi=20; % Angular Mesh on droplet
M=20;%number of power steps
aa=zeros(1,M);
bb=zeros(1,M);
P=zeros(1,M);

for p=0:M
    P(p+1)=p/M; % Beam power
    F=zeros(1,M+1);
    Fs=zeros(1,M+1);
    for m=0:1000
        e=m/2000;
        a=R0 / (1-e^2)^(1/3);% Semimajor ellipsoid radius
        b=a*sqrt(1-e^2);% Semiminor
```

```

F(m+1)=gaussian(Nr,Nphi,P(p+1),w0,a,b,x0,y0,z0,n1,n2,Lambda,alpha,beta,M2);
Fs(m+1)=-gama * pi * (-b+b^3/a^2);
if m>0
    if (F(m+1)-Fs(m+1)) * (F(m)-Fs(m)) < 0
        aa(p+1)=a;
        bb(p+1)=b;
    end
end
end
end
end

SR0=2*R0;
Sb=2*bb;
% Ramanujan I approximation for ellipse perimeter/pi
Sa=(3*(bb+aa)-sqrt((3*bb+aa).*(bb+3*aa)));
% delta lambda for on axis excitation in prolating direction
D_Lambda_on= Lambda2 * (Sa-SR0)./SR0;
% delta lambda for off axis modes
D_Lambda_off= Lambda2 * (Sb-SR0)./SR0;

plot(2*P,D_Lambda_on *1e9,'r',2*P,D_Lambda_off *1e9,'b')
xlabel('Total incident power (Watt)')
ylabel('Wavelength tuning(nm)')

```


Appendix B

**DETERMINATION OF INTRACELLULAR CONCENTRATION OF
VENUS FLUORESCENT PROTEIN**

Intracellular concentration of Venus fluorescent protein expressed in BL21 *E. coli* cells was determined by comparing the intensity of fluorescence emission from the cells and from a thin layer of Venus solution with a known concentration. To this end, both Venus solution and bacterial suspension samples were loaded into thin flow chambers formed by a glass cover slip and a microscope slide attached together by double-sided tape of 76 μm thickness. The flow chambers were first pre-treated at 100°C for 10 min with 0.5 % poly-L-lysine solution in 50 mM phosphate buffer and, subsequently, 20 μL of Venus and Venus-expressing bacterial suspension were injected into the respective flow chambers. The bacteria were allowed to attach to the poly-L-lysine-coated surface for 20 minutes and the unattached cells were then washed away using 50 mM phosphate buffer. Before recording fluorescence images from the samples, reference background image of a non-fluorescent (blank) sample was acquired with 200 ms exposure time; this image served to correct for the effects of CCD dark current and stray light [Fig. B.1(a), left]. Subsequently, images of Venus solution were recorded using wide-field excitation with 473 nm laser light and the same exposure time as used for the background image acquisition [Fig. B.1(b), left]. Finally, fluorescence images of adherent BL21 cells were recorded using the same excitation laser power and exposure time as for the Venus solution [Fig. B.1(c), left]. After recording the images, histograms of pixel intensity values within an identical region selected in all images were generated [Fig. B.1(a)-(c), right]. For this purpose, all pixel intensity values were normalized with respect to the maximal pixel intensity in the bacteria image. For the case of adherent fluorescent bacteria, individual cells within the region of interest were first identified using particle analysis macro of ImageJ and the pixel intensity was only evaluated within the image areas corresponding to the cells. Total of 100 bacteria were included in the histogram of Fig. B.1(c) which features a relatively narrow peak centered at the normalized fluorescence

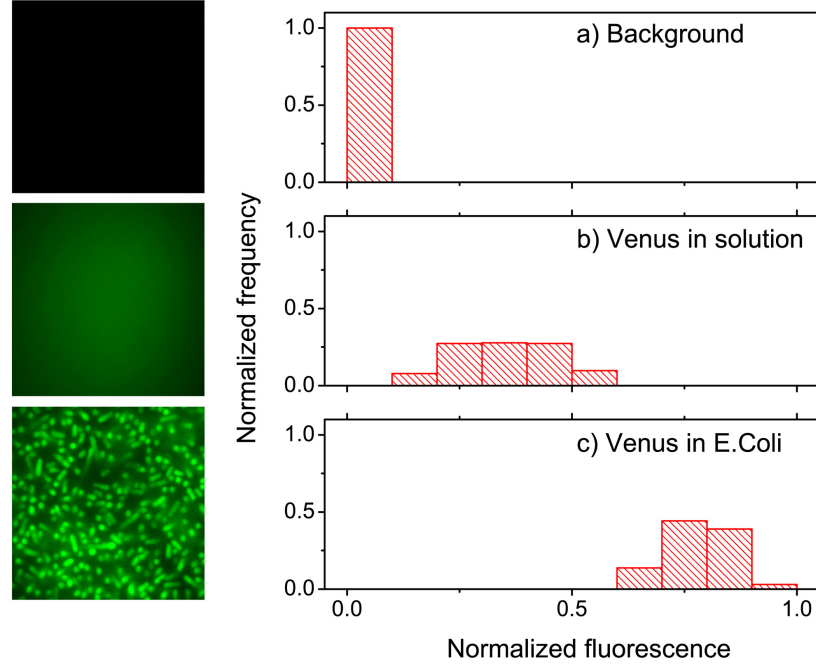


Figure B.1: (a) Background image (left) and histogram of normalized pixel intensity values in this image (right). (b) Fluorescence image of $1.5 \mu\text{M}$ Venus solution (left) and histogram of normalized pixel intensity values in this image (right). (c) Fluorescence image of Venus-expressing BL21 *E. coli* cells adhering to cover slip surface (left) and histogram of normalized pixel intensity values over 100 cells selected in the image (right). Acquisition time for all images was 200 ms. Histograms are normalized such that the sum of frequencies of all bins is equal to 1.

intensity $\nu_B = 0.74$, indicating uniform level of protein expression in the cells. For the Venus solution with concentration $c_V = 1.5 \mu\text{M}$, pixel intensity histogram is centred at $\nu_V = 0.30$, below the emission level of the Venus-expressing BL21 cells [Fig. B.1(b)]. In order to estimate the intracellular concentration of Venus, difference in thickness of the bacteria and the fluorescent protein layer has to be taken into account. In our calculation, we assumed a typical bacteria thickness d_B of $0.6 \mu\text{m}$ and thickness of the Venus layer $d_V = 76 \mu\text{m}$ (thickness of the used double-sided tape). The approximate concentration c_B of Venus in the bacteria was then calculated as

$$c_B = c_v \left(\frac{\nu_B}{\nu_V} \right) \left(\frac{d_V}{d_B} \right) \quad (\text{B.1})$$

For the above given experimental values of c_V , ν_B , ν_V , d_V , and d_B , the concentration of Venus in the cells estimated from Eq. B.1 is $c_B \approx 470 \mu\text{M}$.

Appendix C

MATLAB CODES FOR SIMULATION OF OPTOFLUIDIC FRET LASERS

C.1 FRET Laser Rate Equations for ode15s Solver

```

function dH=Rate(t,h)
dH=zeros(4,1);
global I0 t0 FWHM c Nd Na Tau_d Tau_ca Tau_cd Tau_a n Omega_d Omega_a
global Sigma_pa Sigma_pd Sigma_edd Kf Sigma_add Sigma_aaa
global Sigma_lad Sigma_aad Sigma_ead Sigma_ldd Sigma_eaa Sigma_laa
%=====
Ip= I0*exp(2.3548^2*(-(t-t0).^2)/FWHM^2 /2);%Spatially average pumped power
% for 1D-3A structure put Kf(1D-3A)=3*Kf0
% for 3D-1A structure put Kf(3D-1A)=Kf0
dH(1)=Ip*Sigma_pd*(Nd-h(1))-((Sigma_edd*c*h(1)*h(2))/n)-h(1)/Tau_d -Kf*h(1)+...
    Sigma_add*c*(Nd-h(1))*h(2)/n;
dH(2)= (Sigma_edd-Sigma_ldd)*c*h(1)*h(2)/n - h(2)/Tau_cd + Omega_d*h(1) -...
    Sigma_aad*c*(Na-h(3))*h(2)/n + (Sigma_ead - Sigma_lad)*c*h(3)*h(2)/n-...
    Sigma_add*c*(Nd-h(1))*h(2)/n;
dH(3)= Ip*Sigma_pa*(Na-h(3)) - Sigma_ead*c*(Na-h(3))*h(2)/n - h(3)/Tau_a +...
    Sigma_aad*c*(Na-h(3))*h(2)/n - Sigma_eaa *c*h(3)*h(4)/n +Kf*h(1)+...
    Sigma_aaa*c*(Na-h(3))*h(4)/n;
dH(4)= (Sigma_eaa-Sigma_laa) *c*h(3)*h(4)/n - h(4)/Tau_ca + Omega_a *h(3)-...
    Sigma_aaa*c*(Na-h(3))*h(4)/n;

```

C.2 Lasing Threshold Calculation of Bulk Dye-Pair Solutions

```

% Forster transfer rate is calculated using steady state transfer formula
% demonstrated in Forster's paper 1959
% This code is for threshold calculations in different acceptor molarities
% and a constant donor concentration
clear all
global I0 t0 FWHM c Nd Na Tau_d Tau_ca Tau_cd Tau_a n Omega_d Omega_a
global Sigma_pa Sigma_pd Sigma_edd Kf tt Sigma_add Sigma_aaa
global Sigma_lad Sigma_aad Sigma_ead Sigma_ldd Sigma_eaa Sigma_laa
t0=5e-9; % time location of gaussian pulse center
FWHM=5*10^-9; % %pump pulse FWHM
%=====
hp=6.62606957e-34; %Planck Constant J.s
c=3e10; % cm/s
Sigma_pd=3.42e-16; %Absorption cross section of donor at 532nm,cm^2
Sigma_pa=0.051e-16; %Absorption cross section of absorber at 532nm,cm^2
Sigma_edd=3.78e-16; %donor emission cross-section at donor lasing ...
    wavelength 560nm,cm^2
Sigma_ldd=0.4e-16; %donor S2 excitation cross-section at donor lasing ...
    wavelength 560nm,cm^2
Sigma_aad=0.1558e-16; %absorber absorption cross-section at donor lasing ...
    wavelength 560nm,cm^2
Sigma_ead=0.036e-16; %absorber emission cross-section at donor lasing ...
    wavelength 560nm,cm^2
Sigma_lad=1.30e-16; %absorber S2 excitation cross-section at donor lasing ...
    wavelength 560nm,cm^2
Sigma_eaa=6.9e-16; %absorber emission cross-section at absorber lasing ...
    wavelength 655nm,cm^2
Sigma_laa=2.00e-16; %absorber S2 excitation cross-section at absorber ...
    lasing wavelength 655nm,cm^2
Sigma_add=1.00e-19;
Sigma_aaa=1.00e-19;
lambda_d=560e-7; %Donor Lasing Wavelength cm
lambda_a=655e-7; %Acceptor Lasing Wavelength cm
lambda_p=532e-7; %pump wavelength
Tau_d=4e-9; %Decay time of donor emission

```

```

Tau_a=3.3e-9; %Decay time of absorber
Qf=1e6;
Tau_ca=lambda_a * Qf / (2*pi*c) ; % Cavity lifetime for acceptor lasing
Tau_cd=lambda_d * Qf / (2*pi*c) ; % Cavity lifetime for donor lasing
n=1.33; %Refractive index of the dye solution
R0=61; % Forster distance of donor Angstrom
Width=30e-4; % Width of excited region cm
Length=30e-4; %Length of excited region cm
Height=30e-4; %a=1/(Nd*Sigma_pd+Na*Sigma_pa); %Depth of excited region cm

Omega_d=Sigma_edd*c/(Height*Width*Length*n); % donor spontaneous emission ...
ratio emitted to the lasing mode
Omega_a=Sigma_eaa*c/(Height*Width*Length*n); % acceptor spontaneous emission ...
ratio emitted to the lasing mode
Molarity_a.history=[];
Molarity_d=2; %milimolar acceptor
ss=0;
for Molarity_a=logspace(log10(.01),log10(5),10)
    ss=ss+1;
    display(Molarity_a)
    Molarity_a.history(ss)=Molarity_a;

Nd=Molarity_d*6.022e17; %Density of donor 1/cm3
Na=Molarity_a*6.022e17; %Density of acceptor 1/cm3

Penetration_depth=1/(Nd*Sigma_pd+Na*Sigma_pa); %Depth of excited region cm
if Penetration_depth>Height
    Vp=Height*Width*Length;
else
    Vp=Penetration_depth*Width*Length;
end
Gama=pi^(3/2)*R0^3*(2/3)*Molarity_a*6.023e-7; % Dimensionless value in Kf ...
formula
%(R0 should be in Angstrom and Molarity_a*6.023e-7 is the ...
number of donor per cubic Angstrom volume

Kf=1/(Tau_d * ( 1/ (sqrt(pi)*Gama*exp(Gama^2)*(1-erf(Gama))) - 1 ));
Kf=0;

```

```

%=====
figure(1)
hold off
%   set(gca,'NextPlot','replacechildren');
%   % Preallocate the struct array for the struct returned by getframe
%   F= struct('cdata',[],'colormap',[]);
%=====
Pout_d=0;Pout_a=0;DP=[0 0 0 0 0 0];IP=[18 25 32 18 25 32];

I0 = 10^(IP(1));tt=0;H=0;
[t,H] = ode15s(@Rate,[0 20e-9],[0 0 0 0]);
Pout_d=(hp*c*Vp/lambda_d)*(H(:,2)./Tau_cd); % units J/s or Watt
Pout_a=(hp*c*Vp/lambda_a)*(H(:,4)./Tau_ca); % units J/s or Watt

DP(1)=max(abs(diff(Pout_d)./diff(t)));
DP(4)=max(abs(diff(Pout_a)./diff(t)));
I0 = 10^(IP(3));tt=0;Pout_d=0;Pout_a=0;H=0;
[t,H] = ode15s(@Rate,[0 20e-9],[0 0 0 0]);
Pout_d=(hp*c*Vp/lambda_d)*(H(:,2)./Tau_cd); % units J/s or Watt
Pout_a=(hp*c*Vp/lambda_a)*(H(:,4)./Tau_ca); % units J/s or Watt

DP(3)=max(abs(diff(Pout_d)./diff(t)));
DP(6)=max(abs(diff(Pout_a)./diff(t)));

for kk=1:10
    I0 = 10^(IP(2));tt=0;H=0;Pout_d=0;
    [t,H] = ode15s(@Rate,[0 20e-9],[0 0 0 0]);
    Pout_d=(hp*c*Vp/lambda_d)*(H(:,2)./Tau_cd); % units J/s or Watt
    DP(2)=max(abs(diff(Pout_d)./diff(t)));
    if DP(2)>10^5
        IP(3)=IP(2);
        IP(2)=(IP(1)+IP(2))/2;
        DP(3)=DP(2);
    elseif DP(3)<10^2
        display('nolasing in donor for IP=',IP(3))
    else
        IP(1)=IP(2);
        IP(2)=(IP(2)+IP(3))/2;
    end
end

```

```

        DP(1)=DP(2);

    end

    IO = 10^(IP(5));tt=0;H=0;Pout_a=0;
    [t,H] = ode15s(@Rate,[0 20e-9],[0 0 0 0]);
    Pout_a=(hp*c*Vp/lambda_a)*(H(:,4)./Tau_ca); % units J/s or Watt
    DP(5)=max(abs(diff(Pout_a)./diff(t)));

    if DP(5)>10^5
        IP(6)=IP(5);
        IP(5)=(IP(4)+IP(5))/2;
        DP(6)=DP(5);

    elseif DP(6)<10^2
        display('nolasing in acceptor for IP=',IP(6))
    else
        IP(4)=IP(5);
        IP(5)=(IP(5)+IP(6))/2;
        DP(4)=DP(5);
    end

    plot(kk,IP(2),'*',kk,IP(5),'+')
    title('IP')
    xlabel('iteration')
    ylabel('IP=I0 power')
    hold on
end

Thr_d(ss)=IP(2);
Thr_a(ss)=IP(5);
end

hold off
Thr_d=10.^Thr_d *hp*c*FWHM/lambda_p/0.94*1e4; % uJ/mm2 we have a beam with ...
gaussian temporal profile,J
Thr_a=10.^Thr_a *hp*c*FWHM/lambda_p/0.94*1e4;
%=====

Molarity_a_history=Molarity_a_history';
AAA=[Molarity_a_history,Thr_d',Thr_a'];
loglog(AAA(:,1),AAA(:,2:end))

```

C.3 Lasing Threshold Calculation of Linked Dye-Pair Solutions

```

% Forster transfer rate is calculated using steady state transfer formula
% demonstrated in Forster's paper 1959
% This code is for threshold calculations in different acceptor molarities
% and a constant donor concentration
clear all
global I0 t0 FWHM c Nd Na Tau_d Tau_ca Tau_cd Tau_a n Omega_d Omega_a
global Sigma_pa Sigma_pd Sigma_edd Kf Sigma_add Sigma_aaa
global Sigma_lad Sigma_aad Sigma_ead Sigma_ldd Sigma_eaa Sigma_laa

t0=5e-9; % time location of guassian pulse center
FWHM=5*10^-9; % %pump pulse FWHM
%=====
hp=6.62606957e-34; %Planck Constant J.s
c=3e10; % cm/s
Sigma_pd=3.42e-16; %Absorption cross section of donor at 532nm,cm^2
Sigma_pa=0.051e-16; %Absorption cross section of absorber at 532nm,cm^2
Sigma_edd=3.78e-16; %donor emission cross-section at donor lasing ...
    wavelength 560nm,cm^2
Sigma_ldd=0.4e-16; %donor S2 excitation cross-section at donor lasing ...
    wavelength 560nm,cm^2
Sigma_aad=0.1558e-16; %absorber absorption cross-section at donor lasing ...
    wavelength 560nm,cm^2
Sigma_ead=0.036e-16; %absorber emission cross-section at donor lasing ...
    wavelength 560nm,cm^2
Sigma_lad=1.30e-16; %absorber S2 excitation cross-section at donor lasing ...
    wavelength 560nm,cm^2
Sigma_eaa=6.9e-16; %absorber emission cross-section at absorber lasing ...
    wavelength 655nm,cm^2
Sigma_laa=2.00e-16; %absorber S2 excitation cross-section at absorber ...
    lasing wavelength 655nm,cm^2
Sigma_add=1.00e-19;
Sigma_aaa=1.00e-19;
lambda_d=560e-7; %Donor Lasing Wavelength cm
lambda_a=655e-7; %Acceptor Lasing Wavelength cm
lambda_p=532e-7; %pump wavelength

```



```

Tau_d=4e-9;      %Decay time of donor emission
Tau_a=3.3e-9;   %Decay time of absorber
n=1.33;         %Refractive index of the dye solution
R0=61; % Forster distance of donor Angstrum
Width=30e-4;    % Width of excited region cm
Length=30e-4;   %Length of excited region cm
Height=30e-4;   %a=1/(Nd*Sigma_pd+Na*Sigma_pa); %Depth of excited region cm
Qf=10^6;
Omega_d=Sigma_edd*c/(Height*Width*Length*n); % donor spontaneous emission ...
    ratio emitted to the lasing mode
Omega_a=Sigma_eaa*c/(Height*Width*Length*n); % acceptor spontaneous emission ...
    ratio emitted to the lasing mode
Tau_ca=lambda_a * Qf /(2*pi*c) ; % Cavity lifetime for acceptor lasing
Tau_cd=lambda_d * Qf /(2*pi*c) ; % Cavity lifetime for donor lasing
R.history=[];
Ta=[];Td=[]; ss=0;Slope=4;Thr_d=[];Thr_a=[];Molarity_d_mem=[];
for Molarity_d=[0.8,1.5,3,6,12,25,50,100]*1e-3; %milimolar acceptor
    ss=ss+1;
    display(Molarity_d)
    Molarity_d_mem(ss,1)=Molarity_d;

    Nd=Molarity_d*6.022e17;          %Density of donor 1/cm3
    Na=0;%Molarity_d*6.022e17;      %Density of acceptor 1/cm3
    Penetration_depth=1/(Nd*Sigma_pd+Na*Sigma_pa);%Depth of excited region cm
    if Penetration_depth>Height
        Vp=Height*Width*Length;
    else
        Vp=Penetration_depth*Width*Length;
    end
    pp=0;
    for R=30%:2:120
        pp=pp+1;
        R.history(pp,1)=R/10;
        Kf=0;% (R0/R)^6 / Tau_d;

        %=====
        figure(1)
        hold off

```

```

Pout_d=0;Pout_a=0;DP=[0 0 0 0 0 0];IP=[18 25 32 18 25 32];

I0 = 10^(IP(1));t=[];H=[];
[t,H] = ode15s(@Rate,[0 20e-9],[0 0 0 0]);
Pout_d=(hp*c*Vp/lambda_d)*(H(:,2)./Tau_cd); % units J/s or Watt
Pout_a=(hp*c*Vp/lambda_a)*(H(:,4)./Tau_ca); % units J/s or Watt

DP(1)=max(abs(diff(Pout_d)./diff(t)));
DP(4)=max(abs(diff(Pout_a)./diff(t)));

I0 = 10^(IP(3));t=[];Pout_d=0;Pout_a=0;H=[];
[t,H] = ode15s(@Rate,[0 20e-9],[0 0 0 0]);
Pout_d=(hp*c*Vp/lambda_d)*(H(:,2)./Tau_cd); % units J/s or Watt
Pout_a=(hp*c*Vp/lambda_a)*(H(:,4)./Tau_ca); % units J/s or Watt

DP(3)=max(abs(diff(Pout_d)./diff(t)));
DP(6)=max(abs(diff(Pout_a)./diff(t)));

for kk=1:14
    I0 = 10^(IP(2));t=[];H=[];Pout_d=0;
    [t,H] = ode15s(@Rate,[0 20e-9],[0 0 0 0]);
    Pout_d=(hp*c*Vp/lambda_d)*(H(:,2)./Tau_cd); % units J/s or Watt
    DP(2)=max(abs(diff(Pout_d)./diff(t)));
    if DP(2)>10^Slope
        IP(3)=IP(2);
        IP(2)=(IP(1)+IP(2))/2;
        DP(3)=DP(2);
    elseif DP(3)<10^Slope
        display('nolasing in donor')
    else
        IP(1)=IP(2);
        IP(2)=(IP(2)+IP(3))/2;
        DP(1)=DP(2);
    end
    I0 = 10^(IP(5));t=0;H=0;Pout_a=0;
    [t,H] = ode15s(@Rate,[0 20e-9],[0 0 0 0]);
    Pout_a=(hp*c*Vp/lambda_a)*(H(:,4)./Tau_ca); % units J/s or Watt

```

```

        DP(5)=max(abs(diff(Pout_a)./diff(t)));

        if DP(5)>10^Slope
            IP(6)=IP(5);
            IP(5)=(IP(4)+IP(5))/2;
            DP(6)=DP(5);
        elseif DP(6)<10^Slope
            display('nolasing in acceptor')
        else
            IP(4)=IP(5);
            IP(5)=(IP(5)+IP(6))/2;
            DP(4)=DP(5);
        end

        plot(kk,IP(2),'*',kk,IP(5),'+')
        title('IP')
        xlabel('iteration')
        ylabel('IP=I0 power')
        hold on
    end

    Thr_d(pp)=IP(2);
    Thr_a(pp)=IP(5);
end

hold off
Thr_d=10.^Thr_d *hp*c*FWHM/lambda_p/0.94*1e4; % we have a beam with gaussian ...
        temporal profile,J
Thr_a=10.^Thr_a *hp*c*FWHM/lambda_p/0.94*1e4;
%=====
Td=[Td,Thr_d'];
Ta=[Ta,Thr_a'];
end

figure(2)
semilogy(R_history,Td(:,1:end))
figure(3)
semilogy(R_history,Ta(:,1:end))

Td=[R_history,Td];%nm uJ/mm2
Ta=[R_history,Ta];%nm uJ/mm2
Molarity_d.mem=Molarity_d.mem*1e3;%uM

```

C.4 Output Energy Calculation of FRET Lasers

```

% Forster transfer rate is calculated using steady state transfer formula
% demonstrated in Forster's paper 1959
% This code is input-output calculation in different pair molarities and
% different link length
clear all
global I0 t0 FWHM c Nd Na Tau_d Tau_ca Tau_cd Tau_a n Omega_d Omega_a
global Sigma_pa Sigma_pd Sigma_edd Kf tt Sigma_add Sigma_aaa
global Sigma_lad Sigma_aad Sigma_ead Sigma_ldd Sigma_eaa Sigma_laa
t0=5e-9; % time location of gaussian pulse center
FWHM=5*10^-9; % %pump pulse FWHM
%=====
hp=6.62606957e-34; %Planck Constant J.s
c=3e10; % cm/s
Sigma_pd=3.42e-16; %Absorption cross section of donor at 532nm,cm^2
Sigma_pa=0.051e-16; %Absorption cross section of absorber at 532nm,cm^2
Sigma_edd=3.78e-16; %donor emission cross-section at donor lasing ...
    wavelength 560nm,cm^2
Sigma_ldd=0.4e-16; %donor S2 excitation cross-section at donor lasing ...
    wavelength 560nm,cm^2
Sigma_aad=0.1558e-16; %absorber absorption cross-section at donor lasing ...
    wavelength 560nm,cm^2
Sigma_ead=0.036e-16; %absorber emission cross-section at donor lasing ...
    wavelength 560nm,cm^2
Sigma_lad=1.30e-16; %absorber S2 excitation cross-section at donor lasing ...
    wavelength 560nm,cm^2
Sigma_eaa=6.9e-16; %absorber emission cross-section at absorber lasing ...
    wavelength 655nm,cm^2
Sigma_laa=2.00e-16; %absorber S2 excitation cross-section at absorber ...
    lasing wavelength 655nm,cm^2
Sigma_add=1.00e-19;
Sigma_aaa=1.00e-19;
lambda_d=560e-7; %Donor Lasing Wavelength cm
lambda_a=655e-7; %Acceptor Lasing Wavelength cm
lambda_p=532e-7; %pump wavelength
Tau_d=4e-9; %Decay time of donor emission

```

```

Tau_a=3.3e-9; %Decay time of absorber
Qf=1e6;
Tau_ca=lambda_a * Qf / (2*pi*c) ; % Cavity lifetime for acceptor lasing
Tau_cd=lambda_d * Qf / (2*pi*c) ; % Cavity lifetime for donor lasing
n=1.33;      %Refractive index of the dye solution
R0=61; % Forster distance of donor Angstrom

Width=30e-4; % Width of excited region cm
Length=30e-4; %Length of excited region cm
Height=30e-4; %a=1/(Nd*Sigma_pd+Na*Sigma_pa); %Depth of excited region cm
Omega_d=Sigma_edd*c/(Height*Width*Length*n); % donor spontaneous emission ...
    ratio emitted to the lasing mode
Omega_a=Sigma_eaa*c/(Height*Width*Length*n); % acceptor spontaneous emission ...
    ratio emitted to the lasing mode

Molarity_d=0.1
Nd=Molarity_d*6.022e17;      %Density of donor 1/cm3
Na=Molarity_d*6.022e17;      %Density of acceptor 1/cm3
Penetration_depth=1/(Nd*Sigma_pd+Na*Sigma_pa); %Depth of excited region cm
if Penetration_depth>Height
    Vp=Height*Width*Length;
else
    Vp=Penetration_depth*Width*Length;
end
ss=0; R_mem=[]; BBB1=[]; BBB2=[];
for R=40:10:80
    Kf= (R0/R)^6/ Tau_d;

    ss=ss+1;
    %=====
    figure(1)
    %axis tight
    set(gca, 'NextPlot', 'replacechildren');
    % Preallocate the struct array for the struct returned by getframe
    F= struct('cdata', [], 'colormap', []);
    % Record the movie
    %=====

    pp=0; Pump_Energy=0; Ed.out=0; Ea.out=0;

```

```

for kk=0:0.02:4
    I0 = 10^(22+kk);tt=0;
    [t,H] = ode15s(@Rate,[0 20e-9],[0 0 0 0]);
        % [h(1) h(2) h(3) h(4)]=[nd qd na qa]=
        %=[(donor excited molecules) (donor photons) ...
        (donor excited molecules) (acceptor photons)]

    pp=pp+1;
    Pump_Energy(pp)=I0*hp*c*FWHM/lambda_p/0.94; % we have a beam with ...
        gaussian temporal profile,J
    %=====
    Pout_d=(hp*c*Vp/lambda_d)*(H(:,2)./Tau_cd); % units J/s or Watt
    Pout_a=(hp*c*Vp/lambda_a)*(H(:,4)./Tau_ca); % units J/s or Watt
    Ed_out(pp)=sum(diff(t).*(Pout_d(1:end-1,1)+Pout_d(2:end,1))/2); % Joule, ...
        integrated over all the time
    Ea_out(pp)=sum(diff(t).*(Pout_a(1:end-1,1)+Pout_a(2:end,1))/2); % Joule, ...
        integrated over all the time
    subplot(2,1,1)
    plot(t/1e-9,Pout_d)
    xlabel('Time (ns)')
    ylabel('Donor output power(W)')
    title('Donor output pulse profile')
    subplot(2,1,2)
    plot(t/1e-9,Pout_a)
    title('Acceptor output pulse profile')
    xlabel('Time (ns)')
    ylabel('Acceptor output power(W)')
    F(pp) = getframe;
end

BBB1(:,ss)=Ed_out';
BBB2(:,ss)=Ea_out';
R_mem(ss,1)=R/10;%nm
end

Pump_Energy=Pump_Energy'*1e4;%uJ/mm2
BBB1=BBB1*1e12;%pJ total output
BBB2=BBB2*1e12;%pJ total output
Donor_out=[Pump_Energy,BBB1];
Acceptor_out=[Pump_Energy,BBB2];

```

BIBLIOGRAPHY

- [1] G. Mie. Beitrage zur optik truber meiden speziell kolloidaler metallosungen. *Ann. Phys. (Leipzig)*, 25:377–445, 1908.
- [2] P. Debye. Der lichtdruck auf kugeln von beliebigem material. *Annalen der Physik*, 335(11):57–136, 1909.
- [3] Anatolii N Oraevsky. Whispering-gallery waves. *Quantum Electronics*, 32(5):377, 2002.
- [4] K. J. Vahala. Optical microcavities. *Nature*, 424:839, 2003.
- [5] A. Chiasera, Y. Dumeige, P. Fron, M. Ferrari, Y. Jestin, G. Nunzi Conti, S. Pelli, S. Soria, and G.C. Righini. Spherical whispering-gallery-mode microresonators. *Laser & Photonics Reviews*, 4(3):457–482, 2010.
- [6] Y.P. Rakovich and J.F. Donegan. Photonic atoms and molecules. *Laser & Photonics Reviews*, 4(2):179–191, 2010.
- [7] T. J. Kippenberg and K. J. Vahala. Cavity optomechanics: back-action at the mesoscale. *Science*, 321(5893):1172–1176, 2008.
- [8] P. Del’Haye, A. Schliesser, O. Arcizet, T. Wilken, R. Holzwarth, and T. J. Kippenberg. Optical frequency comb generation from a monolithic microresonator. *Nature*, 450:1214–1217, 2007.
- [9] S. Arnold, M. Khoshhsima, I. Teraoka, S. Holler, and F. Vollmer. Shift of whispering-gallery modes in microspheres by protein adsorption. *Opt. Lett.*, 28(4):272–274, Feb 2003.
- [10] I. S. Grudinin, V. S. Ilchenko, and L. Maleki. Ultrahigh optical q factors of crystalline resonators in the linear regime. *Phys. Rev. A*, 74(6):063806, 2006.

-
- [11] K. Mølhave, A. Kristensen, and N. A. Mortensen. *Advanced Photonic Structures for Biological and Chemical Detection*, chapter Droplet-Based Cavities and Lasers, pages 471–486. Springer, 2009.
 - [12] V. V. Datsyuk. Optics of microdroplets. *J. Mol. Liq.*, 84:1308–1316, 2001.
 - [13] G. C. Righini, Y. Dumeige, P. Feron, M. Ferrari, G. Nunzi Conti, D. Ristic, and S. Soria. Whispering gallery mode microresonators: Fundamentals and applications. *Rivista Del Nuovo Cimento*, 34:435–488, 2011.
 - [14] P. N. Lebedev. Untersuchungen über die druckkräfte des lichtes. *Ann. d. Phys.*, 6:433, 1901.
 - [15] E. F. Nichols and G. F. Hull. A preliminary communication on the pressure of light and heat radiation. *Science*, 14:588, 1901.
 - [16] A. Ashkin. Acceleration and trapping of particles by radiation pressure. *Phys. Rev. Lett.*, 24:156–159, 1970.
 - [17] A. Ashkin and J. M. Dziedzic. Optical levitation of liquid drops by radiation pressure. *Science*, 187:1073, 1975.
 - [18] A. Ashkin and J. M. Dziedzic. Observation of resonances in the radiation pressure on dielectric spheres. *Phys. Rev. Lett.*, 38:1351, 1977.
 - [19] A. Ashkin, J. M. Dziedzic, J. E. Bjorkholm, and S. Chu. Observation of a single-beam gradient force optical trap for dielectric particles. *Opt. Lett.*, 11(5):288–290, 1986.
 - [20] A. Ashkin. Atomic-beam deflection by resonance-radiation pressure. *Phys. Rev. Lett.*, 25(19):1321, 1970.
 - [21] T. W. Hänsch and A. L. Schawlow. Cooling of gases by laser radiation. *Opt. Commun.*, 13(1):68–69, 1975.

-
- [22] A. Ashkin. Trapping of atoms by resonance radiation pressure. *Phy. Rev. Lett.*, 40(12):729, 1978.
- [23] H.-M. Tzeng, K. F. Wall, M. B. Long, and R. K. Chang. Laser emission from individual droplets at wavelengths corresponding to morphology-dependent resonances. *Opt. Lett.*, 9:499–501, 1984.
- [24] S.-X. Qian, J. B. Snow, H. M. Tzeng, and R. K. Chang. Lasing droplets: Highlighting the liquid-air interface by laser emission. *Science*, 231:486, 1986.
- [25] M. Tona and M. Kimura. Novel lasing modes observed in a levitated single dye-doped microdroplet. *J. Phys. Soc. Jpn.*, 69:3533–3535, 2000.
- [26] J. Schäfer, J. P. Mondia, R. Sharma, Z. H. Lu, A. S. Susha, A. L. Rogach, and L. J. Wang. Quantum dot microdrop laser. *Nano Lett.*, 8:1709–1712, 2008.
- [27] H. Azzouz, L. Alkhafadiji, S. Balslev, J. Johansson, N. A. Mortensen, S. Nilsson, and A. Kristensen. Levitated droplet dye laser. *Opt. Express*, 14:4374–4379, 2006.
- [28] A. Kiraz, A. Sennaroglu, S. Doganay, M. A. Dunder, A. Kurt, H. Kalaycioglu, and A. L. Demirel. Lasing from single, stationary, dye-doped glycerol/water microdroplets located on a superhydrophobic surface. *Opt. Commun.*, 276:145–148, 2007.
- [29] M. Tanyeri, R. Perron, and I. M. Kennedy. Lasing droplets in a microfabricated channel. *Opt. Lett.*, 32:2529–2531, 2007.
- [30] N. Kitamura and F. Kitagawa. Optical trapping and chemical analysis of single microparticles in solution. *J. Photochem. Photobiol., C*, 4:227–247, 2003.
- [31] J. P. Reid, H. Meresman, L. Mitchem, and R. Symes. Spectroscopic studies of the size and composition of single aerosol droplets. *Int. Rev. Phys. Chem.*, 26:139–192, 2007.
- [32] R. J. Hopkins, L. Mitchem, A. D. Ward, and J. P. Reid. Control and characterisation of a single aerosol droplet in a single-beam gradient-force optical trap. *Phys. Chem. Chem. Phys.*, 6:4924, 2004.

- [33] D. McGloin, D. R. Burnham, M. D. Summers, D. Rudd, N. Dewar, and Suman Anand. Optical manipulation of airborne particles: techniques and applications. *Faraday Discuss.*, 137:335–350, 2008.
- [34] K. Sasaki, H. Fujiwara, and Hiroshi Masuhara. Optical manipulation of a lasing microparticle and its application to near-field microspectroscopy. *J. Vac. Sci. Technol. B*, 15:2786–2790, 1997.
- [35] K. Sasaki, H. Fujiwara, and H. Masuhara. Photon tunneling from an optically manipulated microsphere to a surface by lasing spectral analysis. *Appl. Phys. Lett.*, 70:2647–2649, 1997.
- [36] A. Kiraz, A. Kurt, M. A. Dündar, and A. L. Demirel. Simple largely tunable optical microcavity. *Appl. Phys. Lett.*, 89:081118, 2006.
- [37] A. Kiraz, Y. Karadağ, and A. F. Coskun. Spectral tuning of liquid microdroplets standing on a superhydrophobic surface using electrowetting. *Appl. Phys. Lett.*, 92:191104, 2008.
- [38] A. Kiraz, Y. Karadag, S. C. Yorulmaz, and M. Muradoglu. Reversible photothermal tuning of a salty water microdroplet. *Phys. Chem. Chem. Phys.*, 11:2597–2560, 2009.
- [39] G. Chen, M. M. Mazumder, Y. R. Chemla, A. Serpengüzel, R. K. Chang, and S. C. Hill. Wavelength variation of laser emission along the entire rim of slightly deformed microdroplets. *Opt. Lett.*, 18:1993–1995, 1993.
- [40] S. C. Yorulmaz, M. Mestre, M. Muradoglu, B. E. Alaca, and A. Kiraz. Controlled observation of nondegenerate cavity modes in a microdroplet on a superhydrophobic surface. *Opt. Commun.*, 282:3024–3027, 2009.
- [41] M. Saito, H. Shimatani, and H. Naruhashi. Tunable whispering gallery mode emission from a microdroplet in elastomer. *Opt. Express*, 16:11915–11919, 2008.
- [42] M. Humar, M. Ravnik, S. Pajk, and I. Muševič. Electrically tunable liquid crystal optical microresonators. *Nat. Photonics*, 3:595–600, 2009.

- [43] M. Aas, A. Jonáš, and A. Kiraz. Lasing in optically manipulated, dye-doped emulsion microdroplets. *Opt. Commun.*, 290:183–187, 2013.
- [44] S. K. Y. Tang, Z. Li, A. R. Abate, J. J. Agresti, D. A. Weitz, D. Psaltis, and G. M. Whitesides. A multi-color fast-switching microfluidic droplet dye laser. *Lab Chip*, 9:2767–2771, 2009.
- [45] S. K. Y. Tang, R. Derda, Q. Quan, M. Loncar, and G. M. Whitesides. Continuously tunable microdroplet-laser in a microfluidic channel. *Opt. Express*, 19:2204–2215, 2011.
- [46] J. Guck, R. Ananthakrishnan, H. Mahmood, T. J. Moon, C. C. Cunningham, and J. Käs. The optical stretcher: A novel laser tool to micromanipulate cells. *Biophys. J.*, 81:767–784, 2001.
- [47] A. Constable, J. Kim, J. Mervis, F. Zarinetchi, and M. Prentiss. Demonstration of a fiber optical light-force trap. *Opt. Lett.*, 18(21):1867–1869, 1993.
- [48] T. Čižmár, O. Brzobohatý, K. Dholakia, and P. Zemánek. The holographic optical micro-manipulation system based on counter-propagating beams. *Laser Phys. Lett.*, 8:50–56, 2011.
- [49] P. C. F. Møller and L. B. Oddershede. Quantification of droplet deformation by electromagnetic trapping. *Europhys. Lett.*, 88:48005, 2009.
- [50] A. D. Ward, M. G. Berry, C. D. Mellor, and C. D. Bain. Optical sculpture: controlled deformation of emulsion droplets with ultralow interfacial tensions using optical tweezers. *Chem. Commun.*, 43:4515–4517, 2006.
- [51] Z. Li and D. Psaltis. Optofluidic dye lasers. *Microfluid. Nanofluid.*, 4:145–158, 2008.
- [52] X. Fan and I. M. White. Optofluidic microsystems for chemical and biological analysis. *Nat. Photonics*, 5:591–597, 2011.

-
- [53] X. Fan and S. H. Yun. The potential of optofluidic biolasers. *Nat. Methods*, 11(2):141–147, Jan 2014.
- [54] S. J. Remington. Green fluorescent protein: a perspective. *Protein Sci.*, 20(9):1509–1519, 2011.
- [55] J. Wiedenmann, F. Oswald, and G. U. Nienhaus. Fluorescent proteins for live cell imaging: opportunities, limitations, and challenges. *IUBMB life*, 61(11):1029–1042, 2009.
- [56] M. Zimmer. Green fluorescent protein (GFP): applications, structure, and related photophysical behavior. *Chem. Rev.*, 102(3):759–782, 2002.
- [57] M. C. Gather and S. H. Yun. Single cell biological lasers. *Nat. Photonics*, 5:406–410, 2011.
- [58] M. C. Gather and S. H. Yun. Lasing from escherichia coli bacteria genetically programmed to express green fluorescent protein. *Opt. Lett.*, 36:3299–3301, 2011.
- [59] Q. Chen, X. Zhang, Y. Sun, M. Ritt, S. Sivaramakrishnan, and X. Fan. Highly sensitive fluorescent protein FRET detection using optofluidic lasers. *Lab Chip*, 13:2679–2681, 2013.
- [60] X. Wu, Q. Chen, Y. Sun, and X. Fan. Bio-inspired optofluidic lasers with luciferin. *Appl. Phys. Lett.*, 102:203706, 2013.
- [61] S. Nizamoglu, M. C. Gather, and S. H. Yun. All-biomaterial laser using vitamin and biopolymers. *Adv. Mater.*, 25:5943–5947, 2013.
- [62] S. Zadran, S. Standley, K. Wong, E. Otiniano, A. Amighi, and M. Baudry. Fluorescence resonance energy transfer FRET-based biosensors: visualizing cellular dynamics and bioenergetics. *Appl. Microbiol. Biotechnol.*, 96(4):895–902, 2012.

-
- [63] I. T. Li, E. Pham, and K. Truong. Protein biosensors based on the principle of fluorescence resonance energy transfer for monitoring cellular dynamics. *Biotechnol. Lett.*, 28(24):1971–1982, Nov. 2006.
- [64] S. I. Shopova, J. M. Cupps, P. Zhang, E. P. Henderson, S. Lacey, and X. Fan. Optofluidic ring resonator lasers based on highly efficient resonant energy transfer. *Opt. Express*, 15(20):12735–12742, 2007.
- [65] M. Berggren, A. Dodabalapur, R. E. Slusher, and Z. Bao. Light amplification in organic thin films using cascade energy transfer. *Nature*, 389(6650):466–469, Oct 1997.
- [66] Y. Sun and X. Fan. Distinguishing DNA by analog-to-digital-like conversion by using optofluidic lasers. *Angew. Chem. Int. Ed.*, 51:1236–1239, 2012.
- [67] W. Lee and X. Fan. Intracavity DNA melting analysis with optofluidic lasers. *Anal. Chem.*, 84:9558–9563, Oct 2012.
- [68] X. Zhang, W. Lee, and X. Fan. Bio-switchable optofluidic lasers based on DNA holliday junctions. *Lab Chip*, 12:3673–3675, 2012.
- [69] Y. Sun, S. I. Shopova, C.-S. Wu, S. Arnold, and X. Fan. Bioinspired optofluidic fret lasers via DNA scaffolds. *PNAS*, 107(37):16039–16042, 2010.
- [70] Q. Chen, H. Liu, W. Lee, Y. Sun, D. Zhu, H. Pei, C. Fan, and X. Fan. Self-assembled DNA tetrahedral optofluidic lasers with precise and tunable gain control. *Lab Chip*, 13(17):3351–3354, 2013.
- [71] Q. Chen, M. Ritt, S. Sivaramakrishnan, X. Sun, and X. Fan. Optofluidic lasers with a single molecular layer of gain. *Lab Chip*, 14(24):4590–4595, 2014.
- [72] Z. S. Wang, H. A. Rabitz, and M. O. Scully. The single-molecule dye laser. *Laser Phys.*, 15(1):118–123, 2005.

-
- [73] Z. Li, Z. Zhang, T. Emery, A. Scherer, and D. Psaltis. Single mode optofluidic distributed feedback dye laser. *Opt. Express*, 14:696–701, 2006.
- [74] S. I. Shopova, H. Zhou, and X. Fan. Optofluidic ring resonator based dye laser. *Appl. Phys. Lett.*, 90:221101, 2007.
- [75] F. Vollmer and L. Yang. Label-free detection with high-Q microcavities: a review of biosensing mechanisms for integrated devices. *J. Nanophotonics*, 1:267–291, 2012.
- [76] J. P. Barton, D. R. Alexander, and S. A. Schaub. Internal and near-surface electromagnetic fields for a spherical particle irradiated by a focused laser beam. *J. Appl. Phys.*, 64:1632–1639, 1988.
- [77] Julius Adams Stratton and Jacques Hebenstreit. *Théorie de l'électromagnétisme*. Dunod, 1961.
- [78] J. D. Jackson. *Classical Electrodynamics*. Wiley, 1998.
- [79] H. M. Nussenzveig. *Diffraction effects in semiclassical scattering*, volume 1. Penguin Group, 2006.
- [80] C. C. Lam, P. T. Leung, and K. Young. Explicit asymptotic formulas for the positions, widths, and strengths of resonances in Mie scattering. *J. Opt. Soc. Am. B*, 9:1585–1592, 1992.
- [81] Colin Pask. Generalized parameters for tunneling ray attenuation in optical fibers. *J. Opt. Soc. Am.*, 68(1):110–116, Jan 1978.
- [82] F. Treussart. *Etude expérimentale de l'effet Laser dans des microsphères de silice dopées avec des ions néodyme*. PhD thesis, Université Paris VI, 1997.
- [83] Maziar Khoshshima. *Perturbation of whispering gallery modes in microspheres by protein adsorption: theory and experiment*. PhD thesis, Polytechnic University, Brooklyn, New York, 2004.

-
- [84] G. M. Hale and M. R. Query. Optical constants of water in the 200-nm to 200- μ m wavelength region. *Appl. Opt.*, 12(3):555–563, Mar 1973.
- [85] M. L. Gorodetsky, A. A. Savchenkov, and V. S. Ilchenko. Ultimate Q of optical microsphere resonators. *Opt. Lett.*, 21:453–455, 1996.
- [86] P. K. Tien. Light waves in thin films and integrated optics. *Appl. Opt.*, 10(11):2395–2413, 1971.
- [87] H. Sosa-Martínez and J. C. Gutiérrez-Vega. Optical forces on a Mie spheroidal particle arbitrarily oriented in a counterpropagating trap. *J. Opt. Soc. Am. B*, 26:2109–2116, 2009.
- [88] S. Holler, N. L. Goddard, and S. Arnold. Spontaneous emission spectra from microdroplets. *J. Chem. Phys.*, 108:6545–6547, 1998.
- [89] P. Chylek, J. T. Kiehl, and M. K. W. Ko. Optical levitation and partial-wave resonances. *Phys. Rev. A*, 18:2229, 1978.
- [90] D. V. Vezenov, B. T. Mayers, D. B. Wolfe, and G. M. Whitesides. Integrated fluorescent light source for optofluidic applications. *Appl. Phys. Lett.*, 86:041104, 2005.
- [91] H.-B. Lin, J. D. Eversole, and A.J. Campillo. Spectral properties of lasing microdroplets. *J. Opt. Soc. Am. B*, 9(1):43–50, 1992.
- [92] A. J. Campillo, J. D. Eversole, and H. B. Lin. Cavity quantum electrodynamic enhancement of stimulated emission in microdroplets. *Phys. Rev. Lett.*, 67:437–440, 1991.
- [93] A. Serpengüzel, J. C. Swindal, R. K. Chang, and W. P. Acker. Two-dimensional imaging of sprays with fluorescence, lasing, and stimulated raman scattering. *Appl. Opt.*, 31:3543–3551, 1992.
- [94] William C. Griffin. Classification of surface-active agents by 'HLB'. *J. Soc. Cosmet. Chem.*, 1949.

-
- [95] J. Drelich, Ch. Fang, and C. L. White. *The Encyclopedia of Surface and Colloid Science: Measurement of Interfacial Tension in Fluid/Fluid Systems*. Marcel- Dekker, 2002.
- [96] R. Aveyard, B.P. Binks, S. Clark, and J. Mead. Interfacial tension minima in oil-water-durfactant systrms. *J. Chem. Soc., Faraday Trans.*, 82:125–142, 1986.
- [97] S. Ramanujan. *Collected papers of Srinivasa Ramanujan*. Cambridge University Press, 1927.
- [98] S. Ebert, K. Travis, B. Lincoln, and J. Guck. Fluorescence ratio thermometry in a microfluidic dual-beam laser trap. *Opt. Express*, 15:15493–15499, 2007.
- [99] T. Nagai, K. Ibata, E. S. Park, M. Kubota, K. Mikoshiba, and A. Miyawaki. A variant of yellow fluorescent protein with fast and efficient maturation for cell-biological applications. *Nat. Biotechnol.*, 20(1):87–90, 2002.
- [100] T. Nagai, S. Yamada, T. Tominaga, M. Ichikawa, and A. Miyawaki. Expanded dynamic range of fluorescent indicators for Ca^{2+} by circularly permuted yellow fluorescent proteins. *PNAS*, 101(29):10554–10559, 2004.
- [101] J. Yu, J. Xiao, X. Ren, K. Lao, and X. S. Xie. Probing gene expression in live cells, one protein molecule at a time. *Science*, 311(5767):1600–1603, 2006.
- [102] M. Drobizhev, N. S. Makarov, S. E. Tillo, T. E. Hughes, and A. Rebane. Two-photon absorption properties of fluorescent proteins. *Nat. Methods*, 8(5):393–399, 2011.
- [103] A. Miyawaki. Development of probes for cellular functions using fluorescent proteins and fluorescence resonance energy transfer. *Annu. Rev. Biochem.*, 80:357–373, 2011.
- [104] N. C. Shaner, P. A. Steinbach, and R. Y. Tsien. A guide to choosing fluorescent proteins. *Nat. Methods*, 2(12):905–909, 2005.
- [105] G.-J. Kremers, S. G. Gilbert, P. J. Cranfill, M. W. Davidson, and D. W. Piston. Fluorescent proteins at a glance. *J. Cell Sci.*, 124(2):157–160, 2011.

-
- [106] A. Kiraz, Y. Karadağ, and M. Muradoğlu. Large spectral tuning of a water/glycerol microdroplet by a focused laser: Characterization and modeling. *Phys. Chem. Chem. Phys.*, 10:6446–6454, 2008.
- [107] J. D. Eversole, H-B. Lin, and A. J. Campillo. Cavity-mode identification of fluorescence and lasing in dye-doped microdroplets. *Appl. Opt.*, 31:1982–1991, 1992.
- [108] J.D. Eversole, H.-B. Lin, C.D. Merritt, and A.J. Campillo. Absorption spectroscopy using microdroplet resonance fluorescence intensities. *Appl. Spectrosc.*, 48(3):373–381, 1994.
- [109] C. Eggeling, A. Volkmer, and C. A. Seidel. Molecular photobleaching kinetics of rhodamine 6g by one-and two-photon induced confocal fluorescence microscopy. *ChemPhysChem*, 6(5):791–804, 2005.
- [110] M. K. Daddysman and C. J. Fecko. DNA multiphoton absorption generates localized damage for studying repair dynamics in live cells. *Biophys. J.*, 101(9):2294–2303, 2011.
- [111] C. L. Woldringh and N. Nanninga. Structural and physical aspects of bacterial chromosome segregation. *J. Struct. Biol.*, 156(2):273–283, 2006.
- [112] T. Förster. Experimentelle und theoretische untersuchung des zwischenmolekularen bergangs von elektronenanregungsenergie. *Z. Naturforsch. B*, 4a:321–327, 1949.
- [113] J. Atkinson and F. Pace. The spectral linewidth of a flashlamp-pumped dye laser. *IEEE J. Quantum Electron.*, 9(6):569–574, Jun 1973.
- [114] J. Hebling. 20 ps pulse generation by an excimer laser pumped double self-Q-switched distributed feedback dye laser. *App. Phys. B*, 47(3):267–272, Nov 1988.
- [115] J. Hebling, J. Seres, ZS. Bor, and B. Racz. Dye laser pulse shortening and stabilization by Q-switching. *Opt. Quantum Electron.*, 22(4):375–384, Jul 1990.

- [116] M. Basheer Ahamed and P.K. Palanisamy. Nd:YAG laser pumped energy transfer distributed feedback dye laser in Rhodamine 6G and Acid blue 7 dye mixture. *Opt. Commun.*, 213(1-3):67–80, 2002.
- [117] Z. Bor and A. Muller. Picosecond distributed feedback dye lasers. *IEEE J. Quantum Electron.*, 22(8):1524–1533, 1986.
- [118] B. Valeur and M.N. Berberan-Santos. *Molecular Fluorescence: Principles and Applications*, chapter 9, pages 247–273. Wiley-VCH, Weinheim, Germany, 2nd edition edition, Apr. 2012.
- [119] *The MathWorks, Inc. - MATLAB R2006b*. Natick, MA, USA.
- [120] S. Arnold and L. M. Folan. Energy transfer and the photon lifetime within an aerosol particle. *Opt. Lett.*, 14:387–389, 1989.
- [121] P. T. Leung and K. Young. Theory of enhanced energy transfer in an aerosol particle. *J. Chem. Phys.*, 89(5):2894–2899, 1988.
- [122] S. Götzinger, L. de S. Menezes, A. Mazzei, S. Kühn, V. Sandoghdar, and O. Benson. Controlled photon transfer between two individual nanoemitters via shared high-Q modes of a microsphere resonator. *Nano Lett.*, 6(6):1151–1154, Jun 2006.
- [123] L. M. Folan, S. Arnold, and S. D. Druger. Enhanced energy transfer within a microparticle. *Chem. Phys. Lett.*, 118(3):322–327, Jul 1985.
- [124] B. E. A. Saleh and M. C. Teich. *Fundamentals of Photonics*, chapter 10, pages 365–400. Wiley, Hoboken, NJ, USA, 2nd edition edition, 2007.
- [125] M. Aas, E. Özelci, A. Jonáš, A. Kiraz A., H. Liu, C. Fan, Q. Chen, and X. Fan. FRET lasing from self-assembled DNA tetrahedral nanostructures suspended in optofluidic droplet resonators. *Eur. Phys. J-Spec. Top.*, 223(10):2057–2062, Sep. 2014.
- [126] E. Özelci, M. Aas, A. Jonáš, and A. Kiraz. Optofluidic FRET microlasers based on surface-supported liquid microdroplets. *Laser Phys. Lett.*, 11(4):045802, Feb 2014.

-
- [127] M. Y. Yüce, A. L. Demirel, and F. Menzel. Tuning the surface hydrophobicity of polymer/nanoparticle composite films in the wenzel regime by composition. *Langmuir*, 21:5073, 2005.
- [128] M. Aas, Q. Chen, A. Jonas, A. Kiraz, and X. Fan. Optofluidic FRET lasers and their applications in novel photonic devices and biochemical sensing. *IEEE J. Sel. Top. Quantum Electron.*, PP(99):1–1, 2015.
- [129] I. M. White, H. Oveys, and X. Fan. Liquid-core optical ring-resonator sensors. *Opt. Lett.*, 31(9):1319–1321, May 2006.

VITA

Mehdi Aas was born in Iran and he got his B.Sc. and M.Sc. in Applied Physics from the University of Tabriz and Shahid Beheshti University in 2002 and 2005, respectively. In 2006 he moved to University of Bonab as an instructor for five years. During this time he worked on different subjects such as digital holography and design and construction of gas lasers. In 2011 he received a scholarship for pursuing Ph.D degree in Physics at Koç University in Turkey and he accomplished his studies on the optics of microdroplet lasers and their potential biosensing applications.

List of Publications

1. **M. Aas**, Q. Chen, A. Jonás, A. Kiraz, and X. Fan. Optofluidic FRET lasers and their applications in novel photonic devices and biochemical sensing. *IEEE J. Sel. Top. Quantum Electron.*, 1–15,22(4), 2016 (available online).
2. A. Jonás, **M. Aas**, Y. Karadag, Selen Manioglu, S. Anand, D. McGloin, H. Bayraktar and, and A. Kiraz. In vitro and in vivo biolasing of fluorescent proteins suspended in liquid microdroplet cavities. *Lab Chip*, 3093:3100–14, 2014.
3. **M. Aas**, E. Özelci, A. Jonás, A. Kiraz, H. Liu, C. Fan, Q. Chen, and X. Fan. FRET lasing from self-assembled DNA tetrahedral nanostructures suspended in optofluidic droplet resonators. *Eur. Phys. J. Special Topics*, 2057:2062–223, 2014.
4. S. Manioglu, M. Atis, **M. Aas**, A. Kiraz, and H. Bayraktar. Direct conversion of Cytochrome c spectral shifts to fluorescence using photochromic FRET. *Chem. Comm.*, 12333:12336–50, 2014.
5. E. Özelci, **M. Aas**, A. Jonás, and A. Kiraz. Optofluidic FRET microlasers based on surface supported liquid microdroplets. *Laser Phys. Lett.*, 11(4):045802, 2014.

6. Y. Karadag **M. Aas**, A. Jonás, S. Anand, D. McGloin, and A. Kiraz. Dye lasing in optically manipulated liquid aerosols. *Opt. Lett.*, 1669:1671–38, 2013.
7. **M. Aas**, A. Jonás, A. Kiraz., O. Brzobohatý, J. Jezek, Z. Pilát, and P. Zemánek. Spectral tuning of lasing emission from optofluidic droplet microlasers using optical stretching. *Opt. Express*, 21380:21394–21, 2013.
8. **M. Aas**, A. Jonás, and A. Kiraz. Lasing in optically manipulated, dye-doped emulsion microdroplets. *Opt. Commun.*, 290:183–187, 2013.